

LANCASTER UNIVERSITY

**Numerical Simulation of Wave-Plasma
Interactions in the Ionosphere**

by

Patrick David Cannon

A thesis submitted in partial fulfillment for the
degree of Doctor of Philosophy

in the
Faculty of Science and Technology
Department of Physics

June 2016

Declaration of Authorship

I, Patrick David Cannon, declare that this thesis titled, '*Numerical Simulation of Wave-Plasma Interactions in the Ionosphere*' and the work presented in it are my own. I confirm that:

- This work was done wholly or mainly while in candidature for a research degree at this University.
- Where any part of this thesis has previously been submitted for a degree or any other qualification at this University or any other institution, this has been clearly stated.
- Where I have consulted the published work of others, this is always clearly attributed.
- Where I have quoted from the work of others, the source is always given. With the exception of such quotations, this thesis is entirely my own work.
- I have acknowledged all main sources of help.
- Where the thesis is based on work done by myself jointly with others, I have made clear exactly what was done by others and what I have contributed myself.

Signed:

Date:

*“‘Its damned picturesque,’
said Lymond bitterly,
‘but it doesn’t alter facts.’”*

Queen’s Play

Dorothy Dunnett

Abstract

Ionospheric modification by means of high-power electromagnetic (EM) waves can result in the excitation of a diverse range of plasma waves and instabilities. This thesis presents the development and application of a GPU-accelerated finite-difference time-domain (FDTD) code designed to simulate the time-explicit response of an ionospheric plasma to incident EM waves. Validation tests are presented in which the code achieved good agreement with the predictions of plasma theory and the computations of benchmark software.

The code was used to investigate the mechanisms behind several recent experimental observations which have not been fully understood, including the effect of 2D density inhomogeneity on the O-mode to Z-mode conversion process and thus the shape of the conversion window, and the influence of EM wave polarisation and frequency on the growth of density irregularities.

The O-to-Z-mode conversion process was shown to be responsible for a strong dependence of artificially-induced plasma perturbation on both the EM wave inclination angle and the 2D characteristics of the background plasma. Allowing excited Z-mode waves to reflect back towards the interaction region was found to cause enhancement of the electric field and a substantial increase in electron temperature.

Simulations of O-mode and X-mode polarised waves demonstrated that both are capable of exciting geomagnetic field-aligned density irregularities, particularly at altitudes where the background plasma frequency corresponds to an electron gyroharmonic. Inclusion of estimated electrostatic fields associated with irregularities in the simulation algorithm resulted in an enhanced electron temperature. Excitation of these density features could address an observed asymmetry in anomalous absorption and recent unexplained X-mode heating results reported at EISCAT.

Comparing simulations with ion motion allowed or suppressed indicated that a parametric instability was responsible for irregularity production. Simulation of EM wave fields confirmed that X-mode waves are capable of exceeding the threshold for parametric instability excitation under certain conditions.

Acknowledgements

The PhD process is a journey that cannot be made alone; I am indebted to many heroic individuals who have helped me immeasurably along the way:

Firstly I would like to thank my supervisor, Prof. Farideh Honary, for giving me an opportunity to study at Lancaster University and for being a constant source of support, guidance and good advice throughout my PhD.

I am grateful to those with whom I have collaborated during my PhD research, particularly to Prof. Nikolay Borisov for taking the time to read and contribute to my article manuscript, and to the staff at the Lancaster University High-End Cluster for their patience and technical assistance. I would also like to thank all members, past and present, of the research group formerly known as SPEARS, who have helped make working at Lancaster a thoroughly enjoyable experience.

That my sanity has been maintained during the past few years is in part thanks to Rowan, Richy and Tom (and around 30,726 unfortunate zombies).

Special thanks are due to those back in the Shire, family and faithful hounds all: it has been a great comfort to know that there is always an unlocked door, a warm fire and a healthy dram waiting just up the road.

Finally, especially, I would like to thank Janette Mill, who would have carried me all the way to Mordor on her own if necessary; without her encouragement and companionship this thesis could have never have been written.

Contents

Declaration of Authorship	i
Abstract	iii
Acknowledgements	iv
List of Figures	viii
List of Tables	xix
Abbreviations	xx
1 Introduction: Plasma Physics and the Ionosphere	1
1.1 Plasma Fundamentals	2
1.1.1 Quasi-neutrality and the Debye Length	2
1.1.2 Plasma Parameter	5
1.1.3 Cold Plasma Oscillation	6
1.2 Single-Particle Motion	9
1.2.1 Lorentz Motion and Gyration	9
1.2.2 Guiding Centre Drift	11
1.3 Plasma Dynamics	16
1.3.1 Kinetic Formulation	16
1.3.2 Fluid Formulation	18
1.4 Waves in Plasma	19
1.4.1 Electromagnetic Waves	21
1.4.1.1 Unmagnetised Plasma	21
1.4.1.2 Magnetised Plasma	23
1.4.1.3 EM Waves in a Vertically-Stratified Magnetised Plasma .	29
1.4.2 Electrostatic Electron Waves	32
1.4.3 Ion Waves	36
1.4.4 Kinetic Waves	40
1.4.4.1 Landau Damping	41
1.4.4.2 Cyclotron Damping	43
1.4.4.3 Bernstein Waves	44
1.5 Earth's Ionosphere and Near-Space Environment	47
1.5.1 The Sun-Earth System: Basic Structure	47

1.5.2	The Ionosphere	50
1.6	Ionospheric Modification Experiments	53
1.6.1	E-Field Amplitude Swelling	54
1.6.2	Linear Mode Conversion	56
1.6.3	Plasma Modification	57
1.6.4	Parametric Instabilities	60
1.6.5	Thermal Resonance Instabilities	63
1.6.6	Self-Focusing Instabilities	64
2	Introduction: Numerical Simulation	65
2.1	The Finite-Difference Time-Domain Method	66
2.1.1	Discretisation and the Yee Cell	67
2.1.2	Finite-Difference Approximation	69
2.1.3	Update Equations for Electromagnetic Waves	71
2.2	Dispersion and Stability	75
2.2.1	Dispersion in the FDTD Domain	75
2.2.2	Stability Criteria and the Courant-Friedrichs-Lowy Condition	82
2.2.3	Choosing Simulation Parameters	84
2.3	Boundary Conditions	85
2.3.1	Mur Absorbing Boundary Conditions	86
2.3.2	Perfectly-Matched Layer	89
2.4	FDTD Advantages and Limitations	94
3	Development of a GPU-Accelerated FDTD Scheme for Electromagnetic Wave Interaction with Plasma	98
3.1	Introduction	98
3.2	Methodology	101
3.2.1	Governing Equations	101
3.2.2	Discretisation Scheme	102
3.2.2.1	Update Equation for Magnetic Field	103
3.2.2.2	Update Equation for Electric Field	103
3.2.2.3	Update Equation for Fluid Velocity	103
3.2.2.4	Update Equation for Plasma Density and Temperature .	107
3.2.2.5	Full Update Algorithm	109
3.2.3	Stability and Accuracy	109
3.3	Computational Performance	116
3.4	Validation	121
3.4.1	Wave Propagation Through Homogeneous Plasma	121
3.4.2	Wave Propagation Through Inhomogeneous Plasma	129
3.5	Summary and Conclusions	133
4	Simulation of the Radio Window and Magnetic Zenith Effect	135
4.1	Introduction	135
4.2	Methodology	139
4.3	Numerical Simulation of Radio Window	142
4.4	Impact of Z-mode on Heating Effects	155
4.5	Magnetic Zenith Effect with the Inclusion of Density Structures	169

4.6	Summary and Conclusions	176
5	Simulation of Density Irregularity Growth During O-Mode and X-Mode Heating	182
5.1	Introduction	182
5.2	Methodology	188
5.3	Excitation of Density Irregularities	190
5.4	Contribution of Electrostatic Fields to Temperature	212
5.5	Summary and Conclusions	217
6	Comparison of Simulated X-mode Wave Fields with Theoretical Parametric Instability Thresholds	221
6.1	Introduction	222
6.2	Threshold Calculation and Comparison to Experiment and Observation .	223
6.3	Numerical Simulation Results	228
6.4	Summary and Conclusions	232
7	Summary and Conclusions	234
7.1	Development of a GPU-Accelerated FDTD Scheme	235
7.2	Simulation of the Radio Window and Magnetic Zenith Effect	236
7.3	Simulation of Density Irregularity Growth During O-Mode and X-Mode Heating	239
7.4	Comparison of Simulated X-mode Wave Fields with Theoretical Parametric Instability Thresholds	240
7.5	Further Investigation	242
	Bibliography	245

List of Figures

1.1	Schematic diagram of the fundamental cold plasma oscillation in response to the displacement of electrons by an external field.	7
1.2	Schematic diagram of an electron moving in a uniform, time-invariant B-field, $\mathbf{B} = B\hat{\mathbf{z}}$. Presence of a magnetic field causes the electron to rotate in a plane perpendicular to the field direction. Motion parallel to the magnetic field combined with simultaneous gyrorotation in the perpendicular plane leads to helical motion of the particle following the field direction. A positive ion would rotate in the opposite sense to the electron due to their opposing polarities.	11
1.3	Schematic diagram of electron and ion drift motion for the cases of no perpendicular field, a perpendicular E-field and a perpendicular B-field gradient. (note that this is a cartoon only: the gyroradii are not to scale)	13
1.4	Dispersion relation for electromagnetic waves in a cold, collisionless, unmagnetised plasma (red). There is a frequency cut-off at $\omega = \omega_{pe}$, below which there is no wave propagation. The relationship asymptotically approaches the $\omega = ck$ vacuum expression as frequency is increased (indicated by dashed-black line).	23
1.5	Dispersion relation for electromagnetic waves in a cold, collisionless, magnetised plasma for a range of propagation angles between $\theta = 0$ (parallel) and $\theta = \pi/2$ (perpendicular). The effect of the anisotropy introduced by the static background magnetic field is to split EM wave propagation into several distinct modes determined by polarisation and direction. The solid lines show the “+” solutions from the Appleton-Hartree equation (1.73) (referred to in this thesis as O-modes), while the dashed lines show the “-” solutions (referred to in this thesis as X-modes).	27
1.6	Real part of the refractive index $n = n_r + in_i = c^2 k^2 / \omega^2$ for EM waves in a cold, collisionless, magnetised plasma where the electron density gradient increases linearly along the magnetic field direction, plotted for a range of propagation angles. The O-mode branch is indicated by the solid lines, and shows a clear cut-off at $X = 1$. The X-mode branches are indicated by dashed lines and show cut-offs at $X = 1 \pm Y$, and a resonance at $X = 1 - Y^2 / (1 - Y^2 \cos^2 \theta)$. Here, $X = \omega_{pe}^2 / \omega^2$ and $Y = \omega_{ce} / \omega$	30

1.7	Dispersion relation for electrostatic electron plasma-fluid waves in a warm (non-zero temperature), collisionless, magnetised plasma, shown for a range of propagation angles between $\theta = 0^\circ$ (parallel) and $\theta = 90^\circ$ (perpendicular). Electron cyclotron wave modes can be seen at low frequencies ($\omega < \omega_{ce}$). High-frequency modes range from Langmuir waves (plasma oscillations drifting with a non-zero thermal velocity) with propagation parallel to the static magnetic field ($\theta = 0^\circ$), to upper-hybrid waves with propagation perpendicular to the field ($\theta = 90^\circ$). For oblique angles in between, the high-frequency plasma wave is a hybrid of the Langmuir and UH wave. The thermal velocity limit, $\omega = \sqrt{\frac{\gamma}{2}v_{Te}k}$ is indicated by the dashed line. For the case of unmagnetised $\mathbf{B}_0 = 0$ plasma, the hybrid modes disappear and only the Langmuir plasma wave remains.	35
1.8	Dispersion relation for electrostatic plasma-fluid waves in a warm, collisionless, magnetised plasma. In both plots the ion acoustic relationship $\omega = c_{is}k$ is indicated by the dashed line. The lower panel shows that the ion acoustic branch is modified by the appearance of electrostatic ion-cyclotron waves at low frequencies close to the resonance at $\omega = \omega_{ci}$. The upper panel shows parallel and perpendicular dispersion for the cases of $T_i \simeq 0$ (dashed lines) and $T_i \simeq \frac{1}{2}T_e$ (solid lines) at higher frequencies. For perpendicular propagation, a new hybrid resonance appears at ω_{lh} corresponding to lower-hybrid waves. For $T_e \gg T_i$, both the ion-cyclotron and lower-hybrid branches of the acoustic wave asymptotically tend towards the constant-frequency ion plasma oscillation, $\omega^2 = \omega_{pi}^2$ for large k	39
1.9	Dispersion relation for kinetic perpendicular ES electron waves in a magnetised, collisionless plasma, plotted for several values of the ratio $(\omega_{pe}/\omega_{ce})^2$. Several successive bands of electrostatic Bernstein modes can be seen located close to the gyroharmonic frequencies. For each value of $(\omega_{pe}/\omega_{ce})^2$, the upper-hybrid branch is preserved and can be identified as the mode crossing $k_\perp = 0$ between gyroharmonic resonance frequencies (the cold-plasma upper-hybrid frequency $\omega_{UH}^2 = \omega_{pe}^2 + \omega_{ce}^2$ is indicated for each $\omega_{pe}^2/\omega_{ce}^2$ by a circular marker). The dispersive behaviour of the Bernstein waves can be seen to differ depending on whether the wave frequency is below or above the UH band.	46
1.10	Schematic representation of the plasma and magnetic field structure of the Sun-Earth system. Solid lines indicate the magnetic field. <i>Image credit: [Baumjohann and Treumann, 1996]</i>	48
1.11	Schematic representation of the main current systems existing in the Earth's magnetosphere. <i>Image credit: [Baumjohann and Treumann, 1996]</i>	49
1.12	Typical ionospheric vertical electron density profile at moderate solar activity, shown for day-time and night-time conditions, for the cases of solar-cycle maximum (solid lines) and solar-cycle minimum (dashed lines). <i>Image credit: [Hunsucker and Hargreaves, 2002]</i>	50
1.13	Typical vertical temperature profiles for ionospheric electrons, ions and neutral species <i>Image credit: [Brekke, 1997]</i>	51

1.14 Calculated growth of a high-amplitude E-field standing wave produced as an O-mode pump wave approaches the reflection height at $x_{3,0}$ in a vertically-inhomogeneous ionosphere. From top to bottom, the panels show the fields calculated by [Lundborg and Thidé, 1986] for the cases of EM wave frequencies $f_0 = 5.13, 5.423$, and 3.515 MHz , electron cyclotron frequencies $f_{ce} = 1.1, 1.3$, and 1.4 MHz and magnetic dip angles $\alpha = 42^\circ, 13^\circ$, and 13° . Indicated in the plots are the parallel E-field amplitude (solid line), the perpendicular amplitudes (bold-ish lines) and the E-field pattern for the case of no geomagnetic field (dot-dashed line). <i>Image credit: [Lundborg and Thidé, 1986]</i>	55
1.15 Electron temperature enhancement variation with time as reported by [Honary et al., 2011] for an O-mode heating experiment performed at EISCAT on 27 September 2007. For the results shown in the upper panel, the heater pump wave was directed along the local geomagnetic field direction; for the results in the lower panel, it was directed vertically along the electron density gradient. The large variation in perturbed temperature with heater direction demonstrates the <i>Magnetic Zenith Effect</i> . <i>Image credit: [Honary et al., 2011]</i>	58
1.16 Parametric wave-matching conditions for the following instabilities: (A) decay of a Langmuir electron plasma wave to an ion-acoustic wave plus a frequency-downshifted Langmuir wave (EDI / LDI); (B) decay of an EM pump wave to a Langmuir wave and an ion-acoustic wave (PDI); (C) decay of an EM pump wave to a frequency-downshifted EM wave plus an ion-acoustic wave (SBS); (D) decay of an EM pump wave to a pair of plasma waves propagating in opposite directions (TPD). <i>Image credit: [Chen, 1984]</i>	61
2.1 Schematic diagram of the fundamental Yee cell [Yee, 1966]. E-field and H-field component nodes are offset in both space and time, enabling the simulation to be advanced in time using a leapfrog-style update algorithm.	68
2.2 Variation of numerical phase velocity \tilde{c}_p with the number of grid cells per wavelength λ_0/Δ_x for the case of a plane wave propagating along one of the principle gird axes. As the Courant number is reduced, the magnitude of the numerical dispersion error can be seen to increase, particularly at low resolutions.	79
2.3 Variation in numerical phase velocity error with wave propagation angle, for a range of grid resolutions. The Courant ratio was fixed at $S_c = 0.5$. The ideal case of $\tilde{c}_p = c$ is indicated by a dotted line.	80
2.4 Variation in numerical phase velocity error with wave propagation angle, for a range of Courant ratios. The resolution was fixed at $\Delta_x = \lambda_0/16$. The ideal case of $\tilde{c}_p = c$ is indicated by a dotted line. For cases where $S_c > 1/\sqrt{2}$, the numerical phase velocity is superluminal at some or all propagation angles.	81
2.5 Comparison between 1 st -order (red) and 2 nd -order (blue) Mur-style ABCs when a Gaussian pulse signal is incident from the left, for the case of $S_c = 1/\sqrt{3}$.	88
3.1 The basic computational grid unit cell, with the positions of field nodes indicated. <i>Image reproduced from [Cannon and Honary, 2015] © 2015 IEEE.</i>	102

3.2	Dispersion curves (upper) and relative errors when compared to the continuous-world regime (lower) for a range of dimensionless parameter $\omega_p \Delta_t$ shown for the ordinary mode (left) and extraordinary mode (right) branches of (3.25). Positive root shown only. <i>Image reproduced from [Cannon and Honary, 2015] © 2015 IEEE.</i>	114
3.3	Dissipation curves (upper) and relative errors when compared to the continuous-world regime (lower) for a range of dimensionless parameter $\omega_p \Delta_t$ shown for the ordinary mode (left) and extraordinary mode (right) branches of (3.25). Positive root shown only. <i>Image reproduced from [Cannon and Honary, 2015] © 2015 IEEE.</i>	115
3.4	Variation in code performance with the number of work groups per device compute unit, for a constant work group size. <i>Image reproduced from [Cannon and Honary, 2015] © 2015 IEEE.</i>	118
3.5	Variation in code performance with the number of wavefronts in a work group, for a constant total number of work groups. <i>Image reproduced from [Cannon and Honary, 2015] © 2015 IEEE.</i>	119
3.6	Code performance for varying offsets of the z-direction work item index. Offset multiples of 32 correspond to coalesced memory access. <i>Image reproduced from [Cannon and Honary, 2015] © 2015 IEEE.</i>	120
3.7	E_x signal for an EM pulse of form (3.29) propagating through a free-space simulation, recorded at a point 128 cells from the $z = 0$ launch plane. Upper panel shows time domain comparison of signals measured using the FDTD algorithm described in this work (red) and an equivalent VORPAL simulation (black). Lower panel shows the frequency domain form of the signals, which peak at $\omega_{peak} = 4.55 \times 10^6 \text{ rad s}^{-1}$. Computational grid parameters of $\Delta_t = 1.939 \times 10^{-8} \text{ s}$ and $\Delta_x = 11.626 \text{ m}$ were used in these simulations. <i>Image reproduced from [Cannon and Honary, 2015] © 2015 IEEE.</i>	123
3.8	Time domain E_x signal for pulse propagating through an unmagnetised plasma simulation. Upper panel shows FDTD signal (red), VORPAL signal (blue) and the expected result from plasma theory (black). Central panel shows the error between the simulated signals and the predictions of plasma theory. Lower panel shows the error between FDTD and VORPAL signals. Computational grid parameters of $\Delta_t = 1.939 \times 10^{-8} \text{ s}$ and $\Delta_x = 11.626 \text{ m}$ were used in these simulations. <i>Image reproduced from [Cannon and Honary, 2015] © 2015 IEEE.</i>	124
3.9	Frequency domain E_x signal for pulse propagating through an unmagnetised plasma simulation. Upper panel shows discrete Fourier transform of FDTD signal (red), VORPAL signal (blue) and the expected result from plasma theory (black). A clear cutoff can be seen at simulation plasma frequency $\omega_p = 2.5 \times 10^6 \text{ rad s}^{-1}$. Central panel shows the error between the simulated signals and the predictions of plasma theory. Lower panel shows the error between FDTD and VORPAL signals. Computational grid parameters of $\Delta_t = 1.939 \times 10^{-8} \text{ s}$ and $\Delta_x = 11.626 \text{ m}$ were used in these simulations. <i>Image reproduced from [Cannon and Honary, 2015] © 2015 IEEE.</i>	125

3.10 Time domain E_x signal for pulse propagating through a magnetised plasma simulation. Upper panel shows FDTD signal (red) and VORPAL signal (blue). Lower panel shows the error between FDTD and VORPAL signals. Computational grid parameters of $\Delta_t = 1.939 \times 10^{-8} s$ and $\Delta_x = 11.626 m$ were used in these simulations. <i>Image reproduced from [Cannon and Honary, 2015] © 2015 IEEE.</i>	127
3.11 Frequency domain E_x signal for pulse propagating through a magnetised plasma simulation. Upper panel shows discrete Fourier transform of FDTD signal (red) and VORPAL signal (blue). Clear cutoffs can be seen due to the different propagation characteristics of the right- and left-hand circularly polarised components. The expected positions of the cutoffs are indicated in black. Lower panel shows the error between FDTD and VORPAL signals. Computational grid parameters $\Delta_t = 1.939 \times 10^{-8} s$ and $\Delta_x = 11.626 m$ were used in these simulations. <i>Image reproduced from [Cannon and Honary, 2015] © 2015 IEEE.</i>	128
3.12 Upper panel shows the numerical refractive index curves for a magnetised plasma of density profile (3.33). Lower panel shows a comparison of the time averaged O- and X-mode E-field amplitudes measured along the central axis of the computational domain. Computational grid parameters $\Delta_t = 1.939 \times 10^{-8} s$ and $\Delta_x = 11.626 m$ were used in the O-mode and X-mode propagation simulations. <i>Image reproduced from [Cannon and Honary, 2015] © 2015 IEEE.</i>	130
3.13 Comparison between standing wave pattern developed in FDTD simulation and theoretical calculation following the method of [Lundborg and Thidé, 1986]. Computational grid parameters $\Delta_t = 1.939 \times 10^{-8} s$ and $\Delta_x = 11.626 m$ were used in the simulation of the O-mode E-field standing wave pattern. <i>Image reproduced from [Cannon and Honary, 2015] © 2015 IEEE.</i>	131
4.1 Angular dependence of O-mode to Z-mode conversion for linear vertical density gradient. Upper panel shows E-field amplitude averaged over $9.17 \times 10^{-4} s$ (1×10^5 time steps) for a selection of inclination angles. Penetration beyond the O-mode reflection height 4.1 km above the lower plane of the computational domain can be seen to occur most effectively for angles close to the Spitzé at 5.5° . Lower panel shows the simulated radio transmission window (red points, dashed black Gaussian fit) and the theoretical prediction from [Mjølhus, 1984] (blue). Computational grid parameters $\Delta_t = 9.17 \times 10^{-9} s$ and $\Delta_x = 5.50 m$ were used in these simulations.	144

4.2 Simulated Z-mode window for varying horizontal slope scale size L_x when background density profile (4.9) is used as a background density profile (smaller L_x implies a steeper slope). It can be seen that increasing the steepness of the slope shifts the centre of the radio window away from the Spitzer direction and towards the magnetic zenith. This effect is most pronounced in the case of the 20 km curve (the steepest horizontal gradient considered here), with no radio window peak seen in the range of angles between vertical (0°) and field-aligned (12°); from the shape of the curve, it appears likely that the peak in this case occurs just beyond the zenith direction. The background plasma density, magnetic field direction (dashed line), vertical direction (dotted line) and position of the O-mode reflection height (solid black line) used for each L_x are shown in upper panels.	148
4.3 Simulated Z-mode window for varying duct width L_{width} when density perturbation of (4.10) is included in the background density profile. Initial amplitude of perturbation was set as 5% of the unperturbed background density given by (4.7). Smaller-width structures with $L_{width} \leq 0.1\text{km}$ can be seen to shift the distribution away from the Spitzer direction towards vertical by $(0.5 - 1)^\circ$. As the irregularity width increases, the window broadens and loses its Gaussian shape. For widths $\geq 0.2\text{km}$, a significant fraction of incident wave amplitude was transmitted at all sampled angles, leading to a dramatic widening and flattening of the window. The background plasma density, magnetic field direction (dashed line), vertical direction (dotted line) and position of the O-mode reflection height (solid black line) used for each L_{width} are shown in upper panels. Computational grid parameters $\Delta_t = 9.17 \times 10^{-9}\text{s}$ and $\Delta_x = 5.50\text{m}$ were used in these simulations.	151
4.4 Time-averaged E-field amplitude for pump wave inclination angles of 0.6° , 2.9° , 5.2° , 7.4° , 9.7° and 12.0° when density perturbations of the form (4.10) and with L_{widths} of 0.08, 0.10, 0.20, 0.50 and 0.80 km are included in the background density profile. The position of the $X = 1$ O-mode reflection contour marked by a solid line. The colour range has been logarithmically-normalised to more clearly show the transmitted Z-mode waves passing beyond the O-mode reflection height. Upper panels show the background electron density, position of the O-mode reflection layer (solid black line), magnetic field direction (dashed black line) and vertical direction (dotted black line) for each L_{width} condition. Computational grid parameters $\Delta_t = 9.17 \times 10^{-9}\text{s}$ and $\Delta_x = 5.50\text{m}$ were used in these simulations.	152

- 4.5 Time-averaged E-field amplitude for pump wave inclination angles of 0.6° , 2.9° , 5.2° , 7.4° , 9.7° and 12.0° when periodic density perturbations of the form (4.11) and with L_{widths} of 0.08, 0.10, 0.20, 0.50 and 0.80 km are included in the background density profile. The position of the $X = 1$ O-mode reflection contour is marked by a solid line. The colour range has been scaled to more clearly show the transmitted and scattered Z-mode waves beyond the O-mode reflection height. Upper panels show the background electron density, position of the O-mode reflection layer (solid black line), magnetic field direction (dashed black line) and vertical direction (dotted black line) for each L_{width} condition. Computational grid parameters $\Delta_t = 9.17 \times 10^{-9} s$ and $\Delta_x = 5.50 m$ were used in these simulations. 156
- 4.6 Upper panels show comparison of the E-field amplitude averaged over 1×10^5 time steps ($9.17 \times 10^{-4} s$) for the case that the upwards boundary of the computational domain is terminated with an absorbing PML (blue) or a reflecting layer (red-dashed). Traces are shown for a selection of initial pump wave inclination angles. Lowermost panel shows the variation of maximum averaged E-field amplitude with inclination angle. It can be seen that allowing the Z-mode wave to reflect enhances the amplification of E-field around the interaction region, particularly for waves directed towards the centre of the radio window around 5.5° . Computational grid parameters $\Delta_t = 9.17 \times 10^{-9} s$ and $\Delta_x = 5.50 m$ were used in these simulations. The critical density for reflection of O-mode waves z_c was set to occur 4.1 km above the lower edge of the computational domain. . . 157
- 4.7 Change in the simulated E-field amplitude, electron density perturbation (expressed as a fraction of the background density N_{e0}), density irregularity amplitude $(N_e - \langle N_e \rangle_x)/N_{e0}$, and electron temperature perturbation with time, when Z-mode reflection was suppressed. Spatial snapshots of each quantity are shown for times $1.83 \times 10^{-4} s$, $1.83 \times 10^{-2} s$, $9.17 \times 10^{-2} s$, $1.83 \times 10^{-1} s$, $2.93 \times 10^{-1} s$ and $1.10 s$. Background conditions are shown in the uppermost panel. Computational grid parameters $\Delta_t = 1.83 \times 10^{-8} s$ and $\Delta_x = 11.0 m$ were used in this simulation. Field-aligned density irregularities with scale-sizes of approximately $30 - 40 m$ ($\sim 3 - 4 \Delta_x$) perpendicular to the geomagnetic field can be seen to grow with time around the upper-hybrid resonance height. 160
- 4.8 Change in the simulated E-field amplitude, electron density perturbation (expressed as a fraction of the background density N_{e0}), density irregularity amplitude $(N_e - \langle N_e \rangle_x)/N_{e0}$, and electron temperature perturbation with time, when Z-mode reflection was allowed. Spatial snapshots of each quantity are shown for times $1.83 \times 10^{-4} s$, $1.83 \times 10^{-2} s$, $9.17 \times 10^{-2} s$, $1.83 \times 10^{-1} s$, $2.93 \times 10^{-1} s$ and $1.10 s$. Background conditions are shown in the uppermost panel. Computational grid parameters $\Delta_t = 1.83 \times 10^{-8} s$ and $\Delta_x = 11.0 m$ were used in this simulation. 161

- 4.9 Variation of electron density and electron temperature perturbation with pump wave inclination angle, for the cases that Z-mode reflection is allowed and Z-mode reflection is suppressed. In the reflection-allowed scenario, the strongest electron temperature enhancement was found to occur for the pump wave inclined an angle of 5.2° (close to the Spitze angle), supporting the argument that the pump wave that is most effectively converted the Z-mode excites the greatest temperature perturbation. In the reflection-suppressed scenario, the wave launched in a near-vertical direction produced the greatest temperature enhancement. The lowermost panels show the variation of the maximum value of electron temperature enhancement and electron density depletion in the simulation domain with time, for the Z-mode reflection allowed (solid lines) and suppressed (dashed lines) scenarios. Background conditions are shown in the uppermost panel. Computational grid parameters $\Delta_t = 1.83 \times 10^{-8} s$ and $\Delta_x = 11.0 m$ were used in these simulations. 166
- 4.10 Right-hand three columns show the simulated growth of small-scale field-aligned density irregularities with time in a narrow band of altitude below the UH resonance level for pump waves directed along 0.0° , 5.2° and 8.6° to the vertical. The UH resonance height is indicated by a dashed line. Panels in the leftmost column show the 1D spatial discrete Fourier transform (DFT) of $\delta N/N_{e0}$ sampled along the horizontal axis of the simulation domain at the height at which the irregularities begin to develop ($\sim 2.8 km$ above the lower boundary of the simulation). Amplitude of spatial frequency components around this value increases with time corresponding to the growth of irregularities and is greater by a factor of 2 or more in the case of the 5.2° -directed wave. Computational grid parameters $\Delta_t = 1.83 \times 10^{-8} s$ and $\Delta_x = 11.0 m$ were used in these simulations. 168
- 4.11 Variation in electron density perturbation and electron temperature perturbation with pump wave inclination angle when horizontal density slopes of the form (4.9) with $L_x = 20 km$ and $L_x = 50 km$ were included in the background density profile. Uppermost panels show the background conditions for each L_x case. Lowermost panels show the variation of minimum density perturbation and maximum temperature perturbation recorded in the simulation with time for $L_x = 20 km$ (solid line) and $L_x = 50 km$ (dashed line). The inclination angle responsible for the greatest temperature enhancement shifts from the Spitz position towards the magnetic zenith direction with decreasing L_x , consistent with the modification of the Z-mode window simulated in Section 4.3 (shown in Figure 4.2). Computational grid parameters $\Delta_t = 1.22 \times 10^{-8} s$ and $\Delta_x = 7.33 m$ were used in these simulations. 171
- 4.12 Variation in electron density perturbation and electron temperature perturbation with pump wave inclination angle when single density-depleted field-aligned irregularities of the form (4.10) with $L_{width} = 0.08 km$ and $L_{width} = 0.8 km$ were included in the background density profile. Uppermost panels show the background conditions for each L_{width} . Lowermost panels show the variation of minimum density perturbation and maximum temperature perturbation recorded in the simulation with time, for $L_{width} = 0.08 km$ (solid line) and $L_{width} = 0.8 km$ (dashed line). Computational grid parameters $\Delta_t = 1.22 \times 10^{-8} s$ and $\Delta_x = 7.33 m$ were used in these simulations. 173

- 4.13 Variation in electron density perturbation and electron temperature perturbation with pump wave inclination angle when periodic density-depleted field-aligned irregularities of the form (4.11) with $L_{width} = 0.08 \text{ km}$ and $L_{width} = 0.8 \text{ km}$ were included in the background density profile. Uppermost panels show the background conditions for each L_{width} . Lowermost panels show the variation of minimum density perturbation and maximum temperature perturbation recorded in the simulation with time, for $L_{width} = 0.08 \text{ km}$ (solid line) and $L_{width} = 0.8 \text{ km}$ (dashed line). Computational grid parameters $\Delta_t = 1.22 \times 10^{-8} \text{ s}$ and $\Delta_x = 7.33 \text{ m}$ were used in these simulations. 174
- 5.1 Variation of background electron plasma frequency (red) and background electron temperature (blue) with vertical distance from lower edge of the computation domain. From left to right these represent the profiles used in the case of simulated pump wave frequency in the ranges $\omega_0 = (2 - 3)\omega_{ce}$, $\omega_0 = (3 - 4)\omega_{ce}$, and $\omega_0 = (4 - 5)\omega_{ce}$ respectively. The points where the electron plasma frequency matches one of the electron gyroharmonics are indicated by 'x' symbols. 194
- 5.2 Evolution of density perturbation with time for the case of an O-mode pump wave with frequency $\omega_0 = 4.8\omega_{ce}$. Top panel shows spatial variation of ω_{pe} and ω_{UH} with altitude in the simulation domain. Lower panels show density perturbation snap-shots at various simulation times (increasing downwards). Large-amplitude density depletion can be seen at the O-mode reflection height. Below this, several populations of small-scale density irregularities can be seen to emerge and grow with time, particularly when ω_{pe} and ω_{UH} approach an electron gyroharmonic. Computational grid parameters $\Delta_t = 1.51 \times 10^{-8} \text{ s}$, $\Delta_x = 8.82 \text{ m}$ were used in this simulation. The particularly clear irregularities which form just above $\omega_{pe} = 3\omega_{ce}$ have horizontal spatial scales in the range $\sim 20 - 40 \text{ m}$ ($\sim 3 - 5\Delta_x$). 196
- 5.3 Evolution of density perturbation with time for the case of an X-mode pump wave with frequency $\omega_0 = 4.8\omega_{ce}$. Top panel shows spatial variation of ω_{pe} and ω_{UH} with altitude in the simulation domain. Lower panels show density perturbation snap-shots at various simulation times (increasing downwards). Large-amplitude density depletion can be seen at the X-mode reflection height. As in the O-mode case depicted in Figure 5.2, several populations of small-scale density irregularities can be seen to emerge and grow with time, located close to the layers where ω_{pe} and ω_{UH} approach an electron gyroharmonic. Computational grid parameters $\Delta_t = 1.51 \times 10^{-8} \text{ s}$, $\Delta_x = 8.82 \text{ m}$ were used in this simulation. 199

5.4 Examples of the density perturbations developed in the simulation using pump wave frequencies in the range $(2 - 3)\omega_{ce}$. For each frequency, the upper panel displays the spatial snapshot of the electron density perturbation developed after 0.75 s . Note that the colour-map has been logarithmically-normalised. The gyroharmonic heights are indicated by dotted lines. The lower panel for each frequency shows horizontally-averaged vertical profiles of the density perturbation for a range of heights (solid lines). The horizontally-averaged profile from the corresponding O-mode simulation is indicated by the dotted line (recorded after 0.75 s simulated time). Computational grid parameters used in these simulations can be found in Table 5.1.	201
5.5 Examples of the density perturbations developed in the simulation using pump wave frequencies in the range $(3 - 4)\omega_{ce}$. For each frequency, the upper panel displays the spatial snapshot of the electron density perturbation developed after 0.72 s . Note that the colour-map has been logarithmically-normalised. The gyroharmonic heights are indicated by dotted lines. The lower panel for each frequency shows horizontally-averaged vertical profiles of the density perturbation for a range of heights (solid lines). The horizontally-averaged profile from the corresponding O-mode simulation is indicated by the dotted line (recorded after 0.72 s simulated time). Computational grid parameters used in these simulations can be found in Table 5.1.	203
5.6 Examples of the density perturbations developed in the simulation using pump wave frequencies in the range $(4 - 5)\omega_{ce}$. For each frequency, the upper panel displays the spatial snapshot of the electron density perturbation developed after 0.56 s . Note that the colour-map has been logarithmically-normalised. The gyroharmonic heights are indicated by dotted lines. The lower panel for each frequency shows horizontally-averaged vertical profiles of the density perturbation for a range of heights (solid lines). The horizontally-averaged profile from the corresponding O-mode simulation is indicated by the dotted line (recorded after 0.56 s simulated time). Computational grid parameters used in these simulations can be found in Table 5.1.	205
5.7 Comparison of the electron density perturbation simulated after 0.4 s for the cases of dynamic O^+ ions with time-varying density (upper panels) and static ions with no variation in density with time (lower panels) for the case of an X-mode polarised pump wave with $\omega_0 = 4.8\omega_{ce}$. In the static-ion case, plasma waves that rely on oscillation of the ion fluid such as lower-hybrid or ion-acoustic waves cannot exist in the simulation. Similar results were found for the O-mode case. Computational grid parameters $\Delta_t = 1.51 \times 10^{-8}\text{ s}$, $\Delta_x = 8.82\text{ m}$ were used in this simulation.	207

- 5.8 Top panel shows an example of the anomalous absorption asymmetry for pump wave frequencies $\omega_0 \simeq 3\omega_{ce}$ measured at EISCAT (plot adapted from the upper panel in Figure 10 of [Stubbe et al., 1994]). Central panel shows the variation of the mean-squared irregularity amplitude $\langle|\delta N|^2\rangle/N_0^2$ with ω_{pe} close to the third gyroharmonic height, sampled at similar frequency steps to those used in the upper panel. Bottom panel shows the temporal evolution of $\langle|\delta N|^2\rangle/N_0^2$, averaged over the altitude range $z_c \geq z \geq z_c - 2\text{ km}$. The greatest irregularity amplitude, and hence the greatest expected anomalous absorption, can be seen to occur for $3.1\omega_{ce}$. Computational grid parameters used in these simulations can be found in Table 5.1. *Image credit (upper panel): [Stubbe et al., 1994]. . . . 209*
- 5.9 Comparison of the electron temperature perturbations developed in the simulation domain with and without the inclusion of estimated E-fields due to excited density irregularities in the electron temperature update calculation. Spatial snap-shots of temperature perturbation with and without E_{ES} are shown for example pump wave frequencies $\omega_0 = 3.8\omega_{ce}$, $\omega_0 = 4.2\omega_{ce}$ and $\omega_0 = 4.8\omega_{ce}$ (from top to bottom respectively). The gyroharmonic heights are indicated by dotted lines. The more coarsely-dashed line indicates the X-mode reflection layer for each case. Computational grid parameters used in these simulations can be found in Table 5.1. . . . 215
- 6.1 The simulated $E_{||}$ amplitude around the X-mode reflection height for each set of experimental conditions, averaged over 2×10^5 timesteps ($\sim 2.67\text{ ms}$). The field amplitude corresponding to 3% of the pump wave ERP is indicated by a dashed line for the cases of the 19 October 2012 and 22 October 2013 experiments. For the remaining experiment, the PDI threshold corresponded to $\sim 50\%$ of EPR and therefore was much higher than the maximum simulated E-field amplitude shown here. 230
- 6.2 The variation of maximum simulated $E_{||}$ amplitudes with irregularity perpendicular scale-size when field-aligned density depletions with amplitude 5% of background density were included in the simulation. Results are shown for the pump wave conditions of 22 October 2013 (blue), 19 October 2012 (red) and 8 March 2010 (black). For the cases of the 19 October 2012 and 22 October 2013 experiments, the maximum simulated $E_{||}$ for most irregularity scale sizes is well in excess of the amplitude corresponding to $\sim 12\%$ EPR ($\sim 0.25\text{ V/m}$) threshold required for the OTSI. 231

List of Tables

1.1	Parameters typical to the daytime ionosphere	53
3.1	Table comparing the performance of a serial implementation of the FDTD code running on a single CPU with parallel implementations running on a single GPU and on two networked GPUs. <i>Table reproduced from [Cannon and Honary, 2015] © 2015 IEEE.</i>	121
5.1	List of computational grid parameters used for each simulated pump wave frequency ω_0	192

Abbreviations

ABC	Absorbing Boundary Condition
ADI	Alternating-Direction Implicit
BUM	Broad Upshifted Maximum
CPU	Central Processing Unit
CFL	CourantFriedrichsLewy
DFT	Discrete Fourier Transform
DM	Downshifted Maximum
EDI	Electron Decay Instability
EM	Electromagnetic
ES	Electrostatic
FDTD	Finite-Difference Time-Domain
FFT	Fast Fourier Transform
GPU	Graphical Processing Unit
LDI	Langmuir Decay Instability
LH	Lower Hybrid
MZE	Magnetic Zenith Effect
PDI	Parametric Decay Instability
PIC	Particle-in-Cell
PML	Perfectly-Matched Layer
OTSI	Oscillating Two-Stream Instability
SBS	Stimulated Brillouin Scattering
SFI	Self-Focusing Instability
TPD	Two-Plasmon Decay
UH	Upper Hybrid
UHR	Upper Hybrid Resonance

Chapter 1

Introduction: Plasma Physics and the Ionosphere

Plasma can be defined as a gas in which a fraction of the constituent molecules have non-zero electrical charges. Typically consisting of large numbers of electrons and ionised atoms or molecules moving freely against a background of neutral, un-ionised gas particles, plasmas occur naturally when a neutral gas is subjected to extreme conditions; plasma can be created through raising the temperature of a gas sufficiently high such that increased thermal motion of particles causes collisional ionisation, by bombarding a gas with energetic particles, by illuminating a gas with high-frequency UV or X-ray radiation, or via any other process that can strip electrons from the constituent particles to leave a partially- or fully-ionised gaseous state. Unlike a neutral gas, charged plasma particles can interact with each other through their mutual Coulomb force and will respond to external electrical stimuli such as applied magnetic fields or incident electromagnetic radiation. As such, the dynamical behaviour of even a weakly-ionised plasma is determined by these electric and electromagnetic interactions, resulting in a diverse range of complicated and collective behaviour not found in neutral gases. The particles in a plasma must be *unbound*: thermal kinetic energy must dominate over electric potential energy, allowing the plasma to conduct and sustain electrical currents, and redistribute in response to external electrical stimuli. Several other criteria that must

be met for an ionised gas to be considered a plasma are outlined in Section 1.1 below. Despite the relatively extreme circumstances required for their formation, plasmas make up 99% of all observable matter in the Universe and form a crucial component of almost every aspect of space physics.

This Chapter introduces the fundamental plasma physics principles that form the basis of the numerical simulation code and research studies presented in Chapters 3-6 of this thesis. The structure of the ionosphere and several important observations made by ionospheric modification experiments are also reviewed briefly below. The descriptions and derivations in this Chapter draw from number of source textbooks, primarily [Baumjohann and Treumann, 1996], [Chen, 1984], [Inan and Golkowski, 2011], [Kelley, 1989] and [Kivelson and Russell, 1995]; further detail on any of the topics discussed here can be found within these reference texts.

1.1 Plasma Fundamentals

In this section, the basic properties and collective dynamics of a plasma are derived from simple theory, and the conditions that distinguish a plasma as a specific class of ionised gas, as defined by [Baumjohann and Treumann, 1996], are outlined.

1.1.1 Quasi-neutrality and the Debye Length

A fundamental property of the plasma state is *quasineutrality*: over large scales, the net charge on an element of plasma is zero; the number of positively-charged plasma particles is roughly equal to the number of negatively-charged plasma particles in a unit volume. Transient regions of non-zero charge may exist over short timescales, however a true plasma will respond to any charge imbalance by attempting to reassert neutrality. The most common model of a plasma interaction considers relatively fast-moving electrons and a slow-moving or static background of heavy, positive, singly-ionised ions. In this scheme, a local charge separation will result in a electrostatic attraction between the oppositely-charged species that acts to restore neutrality and smooth out any charge

perturbations. In response to an applied electric field, the plasma particles will naturally redistribute in order to shield as much of the bulk plasma as possible from the effects of the field. This collective response to external disturbances is known as *Debye Shielding* and is an intrinsic and important property of all plasma.

Consider a quasineutral plasma consisting of electrons with number density N_e at equilibrium with singly-ionised positive ions with number density N_i . The quasineutrality condition dictates that $N_e \simeq N_i \simeq N_0$. A stationary test point-charge Q located at the origin of a spherically-symmetric coordinate system would induce an electrostatic potential ϕ at a radial distance r given by:

$$\phi = \frac{Q}{4\pi\epsilon_0 r} \quad (1.1)$$

Over time, the constituent plasma particles will rearrange to form a new equilibrium distribution which takes into consideration the perturbing presence of the test charge. In this simple model, electron motion is assumed to be sufficiently fast compared to the ion motion such that the ions can be considered to be stationary; the plasma can be described by a population of fast-moving electrons immersed in a neutralising bath of static ions. When the plasma has established thermal equilibrium in the presence of applied potential ϕ , the ion density is thus unchanged and the perturbed electron number density can be expressed using a Boltzmann distribution:

$$N_e(r) = N_0 \exp \left[\frac{e\phi(r)}{k_B T_e} \right] \quad (1.2)$$

where e is the fundamental electric charge, T_e is the electron temperature and k_B is Boltzmann's constant. The new potential due to the rearranged particle distribution can be evaluated using Poisson's equation:

$$\nabla^2 \phi(r) = -\frac{\rho}{\epsilon_0} = -\frac{N_i - N_e}{\epsilon_0} \quad (1.3)$$

where ρ is the charge density. In spherically-symmetric coordinates, (1.3) can be expressed as:

$$\begin{aligned} \frac{1}{r^2} \frac{d}{dr} \left[r^2 \frac{d\phi}{dr} \right] &= -\frac{1}{\epsilon_0} \left\{ eN_0 - eN_0 \exp \left[\frac{e\phi(r)}{k_B T_e} \right] \right\} \\ &\simeq -\frac{eN_0}{\epsilon_0} \left\{ 1 - \left[1 + \frac{e\phi(r)}{k_B T_e} \right] \right\} \\ &\simeq \frac{e^2 N_0}{\epsilon_0 k_B T_e} \phi(r) \end{aligned} \quad (1.4)$$

Solving this differential equation for $r > 0$ results in the solution:

$$\phi(r) = \phi_0(r) \exp \left(-\frac{r}{\lambda_D} \right) \quad (1.5)$$

where $\phi_0(r)$ is the potential from the perturbing test charge as shown by (1.1) and λ_D is the *Debye shielding length*:

$$\lambda_D = \left[\frac{\epsilon_0 k_B T_e}{N_0 e^2} \right]^{\frac{1}{2}} \quad (1.6)$$

The collective response of the plasma to the perturbation is therefore to rearrange such that the potential due to the test charge is exponentially attenuated with distance. At short distances from the charge ($r \rightarrow 0$) the potential tends to that of the unshielded test charge ($\phi(r) \rightarrow \phi_0(r)$). As the distance from the charge increases, the potential falls more rapidly than the free-space Coulomb potential, until at long distances ($r \gg \lambda_D$) the test charge is effectively completely shielded ($\phi(r) \rightarrow 0$). Thus, the Coulomb force due to the test charge is able to extend only $\sim \lambda_D$ into the plasma. As the electron temperature increases, λ_D increases as electrons have a greater thermal kinetic energy and can more easily resist the attractive / repulsive effect of the test charge. λ_D decreases as plasma density increases as there are more particles available to contribute to the shielding process. In a more realistic case, where the ions are not static, the T_e term in (1.6) is replaced by an effective temperature $T_e + T_i$.

The Debye Length defines one of the key criteria for an ionised gas to be classified as a plasma, as defined by [Baumjohann and Treumann, 1996]: the spatial length scale of

the plasma L must be much greater than the Debye scale ($L \gg \lambda_D$) otherwise shielding cannot take place and quasineutrality cannot be established.

1.1.2 Plasma Parameter

The shielding of excess charge in plasma takes place over radial distance scale λ_D , in a volume known as the *Debye Sphere*. The number of particles of a single species involved in the shielding process, n_D , can be expressed as:

$$n_D \simeq \frac{4}{3}\pi\lambda_D^3 N_0 \quad (1.7)$$

where N_0 is the unperturbed density of electrons or ions. This allows the *plasma parameter*, Λ , to be defined as:

$$\Lambda \equiv N_0\lambda_D^3 \quad (1.8)$$

Substituting the definition of λ_D , (1.6):

$$\Lambda \propto \frac{(k_B T_e)^{3/2}}{N_0^{1/2}} \quad (1.9)$$

In a plasma, the constituent particles must be unbound and free to move. For this to be the case, the thermal kinetic energy of the particles ($\propto k_B T$) must dominate over the Coulomb potential energy (\propto interparticle distance, $N_0^{-1/3}$). Thus the plasma parameter can be used to define a second key condition for an ionised gas to be considered a plasma [Baumjohann and Treumann, 1996]:

$$\Lambda = N_0\lambda_D^3 \gg 1 \quad (1.10)$$

In essence, this criteria requires that there must be a sufficient number of freely-moving plasma particles within a Debye sphere volume to adequately shield a charge disturbance.

1.1.3 Cold Plasma Oscillation

In the simplified model of cold plasma described above, low-mass, fast electrons move against a background of heavy, slow ions. In response to an external force, the electrons will be displaced while the position of the ions will remain relatively unchanged; the mutual attraction between the stationary ions and displaced electrons provides the restoring force in a simple harmonic oscillator system, in which the displacement of plasma electrons fluctuates periodically around an equilibrium position with a frequency defined by the plasma conditions. The periodic oscillation of plasma particles in response to an applied electric field is a fundamental property of a plasma: the *plasma frequency*. To demonstrate this, consider an isolated block of cold plasma of dimensions $L \times L \times L$, at equilibrium at time $t = 0$, shown schematically in Figure 1.1 (a). If an externally-applied force was to suddenly displace all electrons from their equilibrium positions by a distance $+x$, this would leave an excess charge of $+eN_0L^2x$ on one edge of the plasma due to all the stationary ions left behind, as shown in 1.1 (b). From Gauss's Law, the E-field between the displaced electrons and the un-moved ions is given by:

$$\oint_S \mathbf{E} \cdot d\mathbf{S} = \frac{1}{\varepsilon_0} Q_{\text{enclosed}}$$

where surface S surrounds the volume of excess positive charge.

$$\begin{aligned} \Rightarrow E_x L^2 &= \frac{eN_0 L^2 x}{\varepsilon_0} \\ E_x &= \frac{eN_0}{\varepsilon_0} x \end{aligned} \quad (1.11)$$

The force exerted on the electrons due to this induced E-field is given by:

$$\begin{aligned} F &= m_e \frac{d^2 x}{dx^2} = -eE_x \\ \Rightarrow \frac{d^2 x}{dx^2} &= -\frac{e^2 N_e}{\varepsilon_0 m_e} x \end{aligned} \quad (1.12)$$

This is merely an expression of the form $\ddot{x} = -\omega^2 x$ describing simple harmonic oscillation at frequency ω . Thus the fundamental oscillation period of an electron in plasma, ω_{pe} ,

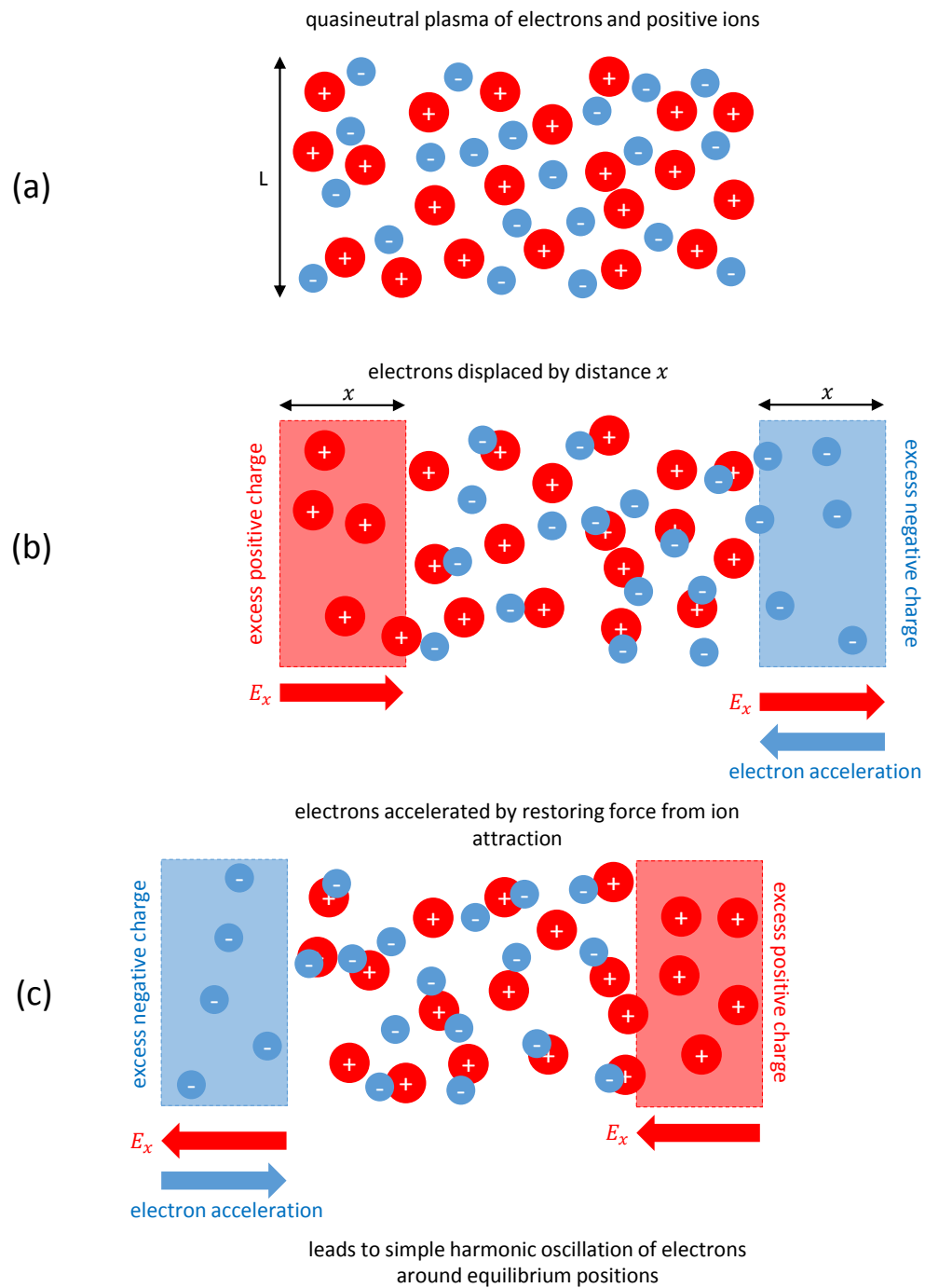


FIGURE 1.1: Schematic diagram of the fundamental cold plasma oscillation in response to the displacement of electrons by an external field.

can be expressed as a function of the plasma density:

$$\omega_{pe} = \left[\frac{e^2 N_e}{\varepsilon_0 m_e} \right]^{\frac{1}{2}} \quad (1.13)$$

In reality, the ions are unlikely to be completely motionless, and will oscillate around their equilibrium position in response to an applied E-field with frequency ω_{pi} :

$$\omega_{pi} = \left[\frac{Z_i^2 e^2 N_i}{\varepsilon_0 m_i} \right]^{\frac{1}{2}} \quad (1.14)$$

where Ze is the total charge on the ionised particle. This leads to a to an overall fundamental frequency of plasma oscillation given by:

$$\omega_p^2 = \omega_{pe}^2 + \sum_{ion species} \omega_{pi}^2 \quad (1.15)$$

Due to the significant mass difference between electrons and ions, $m_e \ll m_i$, the electron plasma frequency usually dominates the ion plasma frequency, meaning that $\omega_p \simeq \omega_{pe}$ under most conditions.

Any perturbation to a cold plasma resulting in small displacements of the plasma particles from their displacement positions; for example, the effect of a propagating radio wave will cause the plasma to oscillate at a frequency entirely determined by the local plasma properties. Most plasmas are only partially-ionised, with the charged species moving against a background of un-ionised neutral particles: plasma oscillations can only be sustained if the collision rate between electrons and neutrals, ν_{en} , is sufficiently small compared to the plasma oscillation frequency. From this, a third criterion required for an ionised gas to be classified as a plasma can be defined [Baumjohann and Treumann, 1996]:

$$\frac{\omega_p}{\nu_{en}} \gg 1 \quad (1.16)$$

If this condition is not met, the charged species will attain equilibrium with the neutral medium and no longer exhibit any of the dynamic collective behaviours of a plasma. This criterion holds for an ideal plasma, however in practice it is not always satisfied in

the case of imperfectly-ionised, collisional plasmas.

From the definition of the Debye length:

$$\lambda_D = \left[\frac{\varepsilon_0 k_B T_e}{N_0 e^2} \right]^{\frac{1}{2}} = \left[\frac{k_B T_e}{m_e} \right]^{\frac{1}{2}} \frac{1}{\omega_{pe}} \simeq \frac{v_{Te}}{\omega_{pe}} \quad (1.17)$$

where v_{Te} is the electron thermal velocity. The Debye length can be defined as approximately the distance an electron can travel via thermal motion during one plasma oscillation period.

1.2 Single-Particle Motion

Much of the plasma behaviour discussed in this thesis is in the context of the plasma as a fluid; the collective, bulk response of the plasma medium to externally-applied forces or perturbations, such as illumination via high-power electromagnetic waves. The root of this macroscopic behaviour, however, arises from the microscopic dynamics of individual charged particles in the presence of applied electric or magnetic fields. In this Section, the basic motion of a single charged particle due to external applied forces is discussed.

1.2.1 Lorentz Motion and Gyration

The motion of a single non-relativistic particle of charge q and mass m is governed by the Lorentz force:

$$\mathbf{F} = m \frac{d\mathbf{v}}{dt} = q(\mathbf{E} + \mathbf{v} \times \mathbf{B}) + \mathbf{F}_{other} \quad (1.18)$$

where \mathbf{v} is the particle velocity and \mathbf{F}_{other} bundles together of all the non-electromagnetic forces acting on the particle, for example pressure or gravity.

In the presence of an electric field only ($\mathbf{B} = 0$), the particle simply experiences a constant acceleration $q\mathbf{E}$ parallel to the applied E-field. The direction of acceleration is dictated by the polarity of the particle's charge: positive ions follow the E-field direction; electrons and negative ions travel anti-parallel to the E-field. Under an applied E-field, $|\mathbf{v}|^2$, and as such the kinetic energy of the particle, will increase.

In the presence of a magnetic field only ($\mathbf{E} = 0$), the particle is accelerated in a direction perpendicular to both \mathbf{B} and \mathbf{v} . The kinetic energy of the particle will remain unperturbed, as demonstrated by taking the dot-product of \mathbf{v} with (1.18) (assuming $\mathbf{F}_{other} \simeq 0$):

$$\begin{aligned} m\mathbf{v} \cdot \frac{d\mathbf{v}}{dt} &= q\mathbf{v} \cdot (\mathbf{v} \times \mathbf{B}) \\ \Rightarrow \frac{d}{dt} \left(\frac{1}{2}m|\mathbf{v}|^2 \right) &= 0 \end{aligned} \quad (1.19)$$

No work is done on the particle by the applied B-field, and the particle therefore can receive no acceleration along the field direction. Instead, the particle rotates conservatively in the plane perpendicular to the B-field, as shown in Figure 1.2; this orbit around \mathbf{B} is known as *gyromotion*. Assuming an externally-applied B-field along the z -direction, $\mathbf{B} = B\hat{\mathbf{z}}$, the particle acceleration can be expressed as:

$$m \frac{d\mathbf{v}}{dt} = m \begin{bmatrix} \dot{v}_x \\ \dot{v}_y \\ \dot{v}_z \end{bmatrix} = \begin{bmatrix} qBv_y \\ -qBv_x \\ 0 \end{bmatrix} \quad (1.20)$$

Note that v_x and v_y are $\pi/2$ out of phase. Taking the second derivative of (1.20) and substituting in expressions for $\ddot{v}_{x,y}$ yields:

$$\begin{bmatrix} \ddot{v}_x \\ \ddot{v}_y \\ \ddot{v}_z \end{bmatrix} = \begin{bmatrix} \frac{qB}{m}\dot{v}_y \\ -\frac{qB}{m}\dot{v}_x \\ 0 \end{bmatrix} = \begin{bmatrix} -\omega_c^2 v_x \\ -\omega_c^2 v_y \\ 0 \end{bmatrix} \quad (1.21)$$

From this equation it is clear that, provided the particle initially has a non-zero component of velocity in the plane perpendicular to the B-field, circular motion in this plane will occur with an orbital frequency defined as the *gyrofrequency* or *cyclotron frequency*, ω_c :

$$\omega_c = -\frac{q|\mathbf{B}|}{m} \quad (1.22)$$

The direction of rotation is dependent on the charge of the rotating particle; electrons and negative ions will rotate in a right-handed sense (counter-clockwise around a field

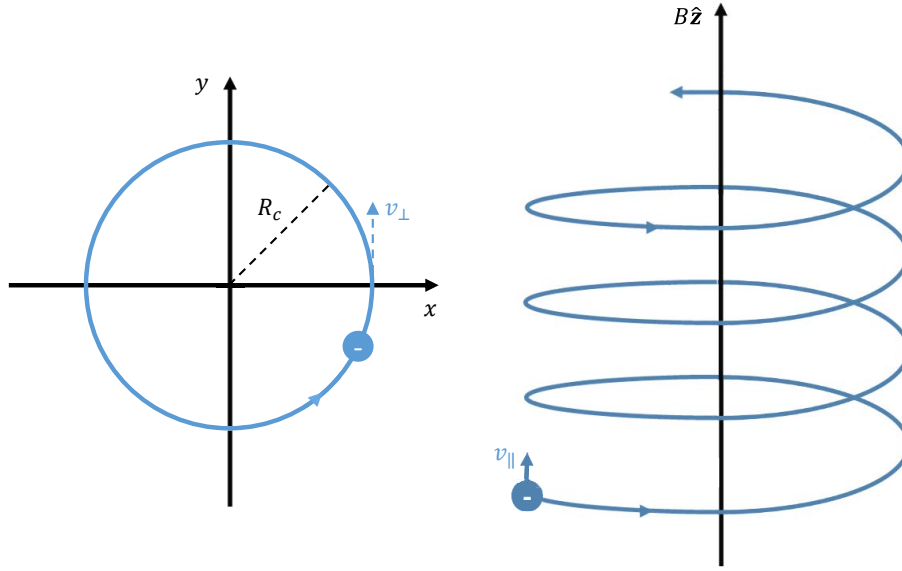


FIGURE 1.2: Schematic diagram of an electron moving in a uniform, time-invariant B-field, $\mathbf{B} = B\hat{\mathbf{z}}$. Presence of a magnetic field causes the electron to rotate in a plane perpendicular to the field direction. Motion parallel to the magnetic field combined with simultaneous gyrorotation in the perpendicular plane leads to helical motion of the particle following the field direction. A positive ion would rotate in the opposite sense to the electron due to their opposing polarities.

pointing towards the observer); positive ions will rotate in the opposite sense. Due to the large mass difference ($m_e \ll m_i$), the gyrofrequency for electrons is generally much greater than for ions ($\omega_{ce} \gg \omega_{ci}$).

1.2.2 Guiding Centre Drift

In the presence of an applied magnetic field, a charged plasma particle will orbit in the plane perpendicular to the field with frequency ω_c , with the parallel component of velocity unperturbed; non-zero parallel motion combined with simultaneous gyrorotation in the perpendicular plane leads to helical motion of the particle following the magnetic field line, as shown in Figure 1.2. In more complex situations, perhaps with the inclusion of an electric field, or where the magnetic field is not uniform, it is useful to consider the average motion of the particle's *guiding centre*: following the centre of the gyromotion allows the motion of the particle to be followed as if it were time-averaged over several gyrorotational periods.

To illustrate this, consider the case of a time-independent force acting on the particle in addition to a constant B-field. A force aligned with the magnetic field, \mathbf{F}_{\parallel} , will simply accelerate the particle such that its parallel velocity component can be described by:

$$\frac{d\mathbf{v}_{\parallel}}{dt} = \frac{\mathbf{F}_{\parallel}}{m} \quad (1.23)$$

$$\Rightarrow \mathbf{v}_{\parallel}(t) = \mathbf{v}_{\parallel}(0) + \frac{\mathbf{F}_{\parallel}}{m}t \quad (1.24)$$

More interesting is a force lying in the plane perpendicular to the magnetic field, \mathbf{F}_{\perp} , which may act such that the position of the guiding centre is not necessarily constant in this plane. In this case, the perpendicular velocity will be described by:

$$\frac{d\mathbf{v}_{\perp}}{dt} = \boldsymbol{\omega}_c \times \mathbf{v}_{\perp} + \frac{\mathbf{F}_{\perp}}{m} \quad (1.25)$$

where $\boldsymbol{\omega}_c = -q\mathbf{B}/m$. Differentiating (1.25) with respect to time and rearranging yields:

$$\begin{aligned} \frac{d^2\mathbf{v}_{\perp}}{dt^2} &= \boldsymbol{\omega}_c \times \frac{d\mathbf{v}_{\perp}}{dt} \\ &= \boldsymbol{\omega}_c \times \left(\boldsymbol{\omega}_c \times \mathbf{v}_{\perp} + \frac{\mathbf{F}_{\perp}}{m} \right) \\ &= \underbrace{-\omega_c^2 \mathbf{v}_{\perp}}_{\text{gyromotion}} + \underbrace{\frac{\boldsymbol{\omega}_c \times \mathbf{F}_{\perp}}{m}}_{\text{drift}} \end{aligned} \quad (1.26)$$

using $\boldsymbol{\omega}_c \times \boldsymbol{\omega}_c \times \mathbf{v}_{\perp} = \boldsymbol{\omega}_c (\boldsymbol{\omega}_c \cdot \mathbf{v}_{\perp}) - \omega_c^2 \mathbf{v}_{\perp} = -\omega_c^2 \mathbf{v}_{\perp}$. The first term is simply the harmonic gyromotion derived in Section 1.2.1 above. The second term causes the guiding centre of the particle's rotation to drift in a direction perpendicular to both the force direction and the magnetic field direction, with a constant drift velocity $\mathbf{v}_{F_{\perp}}$:

$$\mathbf{v}_{F_{\perp}} = \frac{\boldsymbol{\omega}_c \times \mathbf{F}_{\perp}}{m\omega_c^2} = \left(\frac{1}{q} \right) \frac{\mathbf{F}_{\perp} \times \mathbf{B}}{B^2} \quad (1.27)$$

Thus, in the presence of a constant E-field in the plane perpendicular to the B-Field, plasma particles will drift with an average velocity $\mathbf{v}_{E_{\perp}}$ in a direction perpendicular to

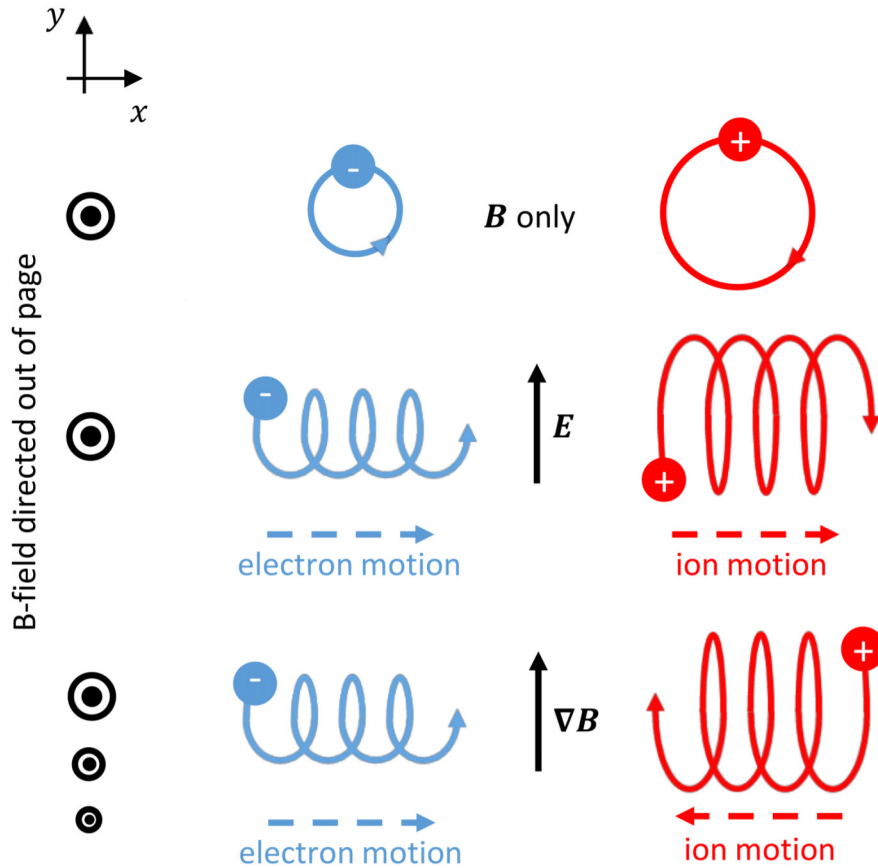


FIGURE 1.3: Schematic diagram of electron and ion drift motion for the cases of no perpendicular field, a perpendicular E-field and a perpendicular B-field gradient.
(note that this is a cartoon only: the gyroradii are not to scale)

both the applied E-field and applied B-field:

$$\mathbf{v}_{E\perp} = \left(\frac{1}{q}\right) \frac{(q\mathbf{E}_\perp) \times \mathbf{B}}{B^2} = \frac{\mathbf{E}_\perp \times \mathbf{B}}{B^2} \quad (1.28)$$

This drift velocity is in the same direction for both positively- and negatively-charged particles (*ambipolar*), and is independent of both particle mass and charge magnitude. The process can be explained physically by considering a single positive ion processing around a static magnetic field in the presence of a perpendicular E-field, as shown in Figure 1.3. Over part of its gyrorotation, the particle moves against the E-field and is decelerated. As the radius of gyrorotation is given by $r_c = |\mathbf{v}_\perp|/w_c$, decelerating

the particle in the plane of rotation will reduce r_c . Over the remaining part of its gyrorotation, the particle moves in the same direction as the E-field and is accelerated, increasing its radius of rotation. The combination of wide loops as the particle moves with the field and tight corners as it moves against the field leads to a net constant drift in the $\mathbf{E} \times \mathbf{B}$ direction. An electron rotates in the opposite sense, but also gains and loses velocity with the field in the opposite direction (accelerates moving against the field, decelerates moving with the field), and thus the drift motion occurs in the same direction as for the positive ion.

An additional *polarisation drift* term emerges when the E-field is allowed to vary slowly with time. In this context, *slowly-varying* implies slow compared to the particle cyclotron frequency. To evaluate this, the cross-product of (1.25) with \mathbf{B}/B^2 is taken, for the case that perpendicular force \mathbf{F}_\perp is a time-dependent E-field perpendicular to \mathbf{B} :

$$\frac{d\mathbf{v}_\perp}{dt} \times \frac{\mathbf{B}}{B^2} = \boldsymbol{\omega}_c \times \mathbf{v}_\perp \times \frac{\mathbf{B}}{B^2} + \frac{q\mathbf{E}_\perp(t) \times \mathbf{B}}{mB^2}$$

Using the expansion $\boldsymbol{\omega}_c \times \mathbf{v}_\perp \times \frac{\mathbf{B}}{B^2} = \mathbf{v}_\perp \underbrace{\left(\frac{\boldsymbol{\omega}_c \cdot \mathbf{B}}{B^2} \right)}_{\frac{q\mathbf{B}}{m} \cdot \frac{\mathbf{B}}{B^2}} - \frac{\mathbf{B}}{B^2} \underbrace{(\boldsymbol{\omega}_c \cdot \mathbf{v}_\perp)}_0 = -\frac{q}{m}\mathbf{v}_\perp$:

$$\begin{aligned} \mathbf{v}_\perp &= \frac{\mathbf{E}_\perp(t) \times \mathbf{B}}{B^2} - \left(\frac{m}{q} \right) \frac{d\mathbf{v}_\perp}{dt} \times \frac{\mathbf{B}}{B^2} \\ \mathbf{v}_\perp &= \mathbf{v}_E - \left(\frac{m}{qB^2} \right) \frac{d}{dt} \mathbf{v}_\perp \times \mathbf{B} \end{aligned} \quad (1.29)$$

Averaging over many gyrorotation periods, $\mathbf{v}_\perp \times \mathbf{B} \simeq -\mathbf{E}_\perp$. Thus, the slowly-varying solution can be expressed as:

$$\Rightarrow \mathbf{v}_\perp = \mathbf{v}_E + \underbrace{\frac{1}{\omega_c B} \frac{d\mathbf{E}_\perp}{dt}}_{\text{polarisation drift velocity } \mathbf{v}_P} \quad (1.30)$$

The effect of a time-varying electric field is therefore to introduce a polarisation particle drift, \mathbf{v}_P , along the direction of the applied field. Unlike the $\mathbf{E} \times \mathbf{B}$ drift given by (1.28), the polarisation drift direction is dependent on particle charge, with positive ions drifting with the E-field and electrons drifting against it. The magnitude of the velocity

is proportional to particle mass, and as such is much greater in the case of ions than electrons. The differential motion of electric charges induces a polarisation current, \mathbf{J}_P , carried mostly by the ions in an electron/positive ion plasma due to the large mass ratio $m_e \ll m_i$.

$$\mathbf{J}_P = eN_i\mathbf{v}_{Pi} - eN_e\mathbf{v}_{Pe} \simeq \frac{N_0(m_i + m_e)}{B^2} \frac{d\mathbf{E}_\perp}{dt} \quad (1.31)$$

for a quasineutral plasma with $N_i \simeq N_e \simeq N_0$.

From the general drift equation (1.27), particle guiding centre velocities can easily be found for any time-invariant applied force using the same technique as above, for example the force due to gravity leads to:

$$\mathbf{F}_G = -mg\mathbf{g}_\perp \Rightarrow \mathbf{v}_G = -\frac{1}{\omega_c} \frac{\mathbf{g}_\perp \times \mathbf{B}}{B} \quad (1.32)$$

where \mathbf{g}_\perp is the component of gravitational acceleration perpendicular to the applied B-field. Unlike in the static E-field case, particles of different polarities will drift in different directions and the magnitude of velocity is no longer invariant between particle types.

The above scenarios all assume that the magnetic field is uniform in space. A further class of drifts occur due to inhomogeneities in the magnetic field. Consider a particle in the presence of a weak gradient in the magnetic field, where *weak* in this context implies that the scale size of spatial variation of the field is much greater than the particle's radius of gyrorotation. The variation in the field will cause the radius of gyromotion to change over the course of one orbit, leading to a net drift of the guiding centre, in a similar manner to that described for $E \times B$ drift above. This corresponds to a force of the form $\mathbf{F}_{\nabla B} = -\Theta_M \nabla B$ acting on the particle, where $\Theta_M = mv_\perp^2/2B$ is the magnetic moment of the gyrorotation. Substituting this force into the general drift equation (1.27) yields a particle drift of:

$$\mathbf{v}_{\nabla B} = \frac{mv_\perp^2}{qB^3} (\nabla B) \times \mathbf{B} \quad (1.33)$$

This drift causes electrons and positive ions to move in opposing directions and will hence induce a grad-B current. The velocity increases with the particle's energy in

the drift plane, $\frac{1}{2}mv_{\perp}^2$, as faster particles will experience more of the field variation, as illustrated schematically in Figure 1.3.

A further drift due to B-field inhomogeneity occurs when the field lines are curved. In this case, the particles trying to move along the field line experience a centrifugal force corresponding to $\mathbf{F}_C = mv_{\parallel}^2 \mathbf{R}_C / R_C^2$, where \mathbf{R}_C is the radius of curvature. From (1.27) this leads to a drift of:

$$\mathbf{v}_C = \frac{mv_{\parallel}^2}{qR_C^2 B^2} \mathbf{R}_C \times \mathbf{B} \quad (1.34)$$

Again, this drift induces differential motion of electrons and positive ions, and increases in magnitude with kinetic energy along the field line, as particles moving faster in this direction will experience more of the field line curvature.

1.3 Plasma Dynamics

The above Section 1.2.2 describes the motion of a single charged particle under the influence of external stimuli, however to describe the dynamic behaviour of plasma a more collective approach is required. As every pair of particles in a plasma share a mutual interaction, an analytical approach that involves tracking the time-dependent motion of every individual particle is impossible, and numerical computation of the motion of individual particles is far too computationally-intensive to be feasible. To allow the dynamics of a plasma system to be described and modelled, several schemes of approximations can be made; two commonly-used formulations of this nature are described below.

1.3.1 Kinetic Formulation

The kinetic formulation of plasma dynamics is a way of statistically representing the behaviour of a large population of coupled particles through the evolution of their distribution in 6-dimensional position-velocity *phase space* [Inan and Golkowski, 2011]. This scheme assumes that each particle can be described at time t by independent position and velocity vectors, given by $\mathbf{r}(t) = x(t)\hat{\mathbf{x}} + y(t)\hat{\mathbf{y}} + z(t)\hat{\mathbf{z}}$ and $\mathbf{v}(t) = v_x(t)\hat{\mathbf{x}} + v_y(t)\hat{\mathbf{y}} + v_z(t)\hat{\mathbf{z}}$

respectively. The probability of a particle having a particular \mathbf{r} and \mathbf{v} at time t is described by the particle distribution function $f(\mathbf{r}, \mathbf{v}, t)$. Plasma quantities such as particle count or number density can be evaluated by integrating over this function:

$$\text{Number of particles: } \mathcal{N} = \int \int_{-\infty}^{\infty} f(\mathbf{r}, \mathbf{v}, t) d\mathbf{r} d\mathbf{v} \quad (1.35)$$

$$\text{Number density: } N = \int_{-\infty}^{\infty} f(\mathbf{r}, \mathbf{v}, t) d\mathbf{v} \quad (1.36)$$

There is no restriction on the form of distribution function f ; in the case of cold plasma a delta function is appropriate, while a Maxwellian distribution is often adopted for the case of a warm plasma with non-zero temperature.

To investigate the behaviour of the particle distribution function under the influence of an applied force \mathbf{F} , consider an element of phase space with volume $dV = d\mathbf{r} d\mathbf{v}$, and surface areas in position- and velocity-space $d\mathbf{S}_r$ and $d\mathbf{S}_v$ respectively. Assuming conservation of particles, the net flux of particle into the volume in both position- and velocity-space balances the rate of change of particle count within the volume:

$$\frac{d}{dt} \int f dV + \int f \mathbf{v} \cdot d\mathbf{S}_r + \int f \frac{d\mathbf{v}}{dt} \cdot d\mathbf{S}_v = 0 \quad (1.37)$$

Using the divergence theorem $(\nabla \cdot \mathbf{A}) dV = \mathbf{A} \cdot d\mathbf{S}$ and rearranging gives an expression for the *collisionless Boltzmann equation*:

$$\begin{aligned} \frac{d}{dt} f d\mathbf{r} d\mathbf{v} + \nabla_r \cdot (f \mathbf{v}) d\mathbf{r} d\mathbf{v} + \nabla_v \cdot \left(f \frac{d\mathbf{v}}{dt} \right) d\mathbf{r} d\mathbf{v} &= 0 \\ \Rightarrow \frac{df}{dt} + (\mathbf{v} \cdot \nabla_r) f + \left(\frac{\mathbf{F}}{m} \cdot \nabla_v \right) f &= 0 \end{aligned} \quad (1.38)$$

where \mathbf{F} is assumed to be independent of \mathbf{v} , $\nabla_r = \hat{\mathbf{x}} \frac{\partial}{\partial x} + \hat{\mathbf{y}} \frac{\partial}{\partial y} + \hat{\mathbf{z}} \frac{\partial}{\partial z}$ and $\nabla_v = \hat{\mathbf{v}}_x \frac{\partial}{\partial v_x} + \hat{\mathbf{v}}_y \frac{\partial}{\partial v_y} + \hat{\mathbf{v}}_z \frac{\partial}{\partial v_z}$. In a cold, magnetised plasma, the external force term is provided by the Lorentz equation to give the *Vlasov equation*:

$$\frac{df_a}{dt} + (\mathbf{v} \cdot \nabla_r) f_a + \frac{e_a}{m_a} [(\mathbf{E} + \mathbf{v} \times \mathbf{B}) \cdot \nabla_v] f_a = 0 \quad (1.39)$$

for plasma species a . The Vlasov equation can then be evaluated for a given set of

conditions to determine the time dependent, kinetic behaviour of the plasma population. Physical quantities such as density or energy can be deduced taking moments of the distribution function. In the case of a collisional plasma, an additional term $(\partial f / \partial t)_{coll}$ must be included on the right-hand side of equation (1.39) [Inan and Golkowski, 2011].

1.3.2 Fluid Formulation

The fluid formulation of plasma dynamics follows directly from the kinetic approach: bulk-averaged quantities representing observable parameters such as momentum or energy can be obtained by taking moments of the Vlasov equation (1.39). The fluid average for any parameter A at position \mathbf{r} and time t can be found via:

$$A(\mathbf{r}, t) = \langle A \rangle = \frac{1}{N(\mathbf{r}, t)} \int A(\mathbf{r}, t) f(\mathbf{r}, \mathbf{v}, t) d\mathbf{v} \quad (1.40)$$

where the number density $N(\mathbf{r}, t)$ is given by (1.35). For example, the plasma bulk-fluid velocity can be expressed as:

$$\mathbf{U}(\mathbf{r}, t) = \langle \mathbf{v} \rangle = \frac{1}{N(\mathbf{r}, t)} \int \mathbf{v}(\mathbf{r}, t) f(\mathbf{r}, \mathbf{v}, t) d\mathbf{v} \quad (1.41)$$

In the multiple-fluid formulation, each plasma species can be represented as a separate fluid. For each component, fluid equations describing the dynamical behaviour of momentum, number density and energy can be found by multiplying the Vlasov equation by these parameters and integrating over velocity space. These can be combined with Maxwell's equations to give a coupled set of multiple-fluid equations that completely describe the time-dependent evolution of bulk-fluid quantities in an ionospheric plasma, as given by equations (1.42)-(1.48) [Inan and Golkowski, 2011, Gurevich, 1978]:

$$\nabla \cdot \mathbf{E} = \frac{1}{\epsilon_0} \underbrace{\sum_a N_a e_a}_{\text{charge density } \rho} \quad (1.42)$$

$$\nabla \cdot \mathbf{B} = 0 \quad (1.43)$$

$$-\mu_0 \frac{\partial \mathbf{H}}{\partial t} = \nabla \times \mathbf{E} \quad (1.44)$$

$$\varepsilon_0 \frac{\partial \mathbf{E}}{\partial t} = \nabla \times \mathbf{H} - \underbrace{\sum_{a=e,i} N_a e_a \mathbf{U}_a}_{\text{current density } \mathbf{J}} \quad (1.45)$$

$$N_a m_a \left[\frac{\partial \mathbf{U}_a}{\partial t} + (\mathbf{U}_a \cdot \nabla) \mathbf{U}_a \right] = N_a e_a (\mathbf{E} + \mathbf{U}_a \times \mathbf{B}) - \dots \\ \dots - N_a m_a \nu_a \mathbf{U}_a - \underbrace{\nabla (\gamma k_B N_a T_a)}_{\text{pressure gradient } \nabla p} \quad (1.46)$$

$$\frac{\partial N_a}{\partial t} + \nabla \cdot (N_a \mathbf{U}_a) = 0 \quad (1.47)$$

$$\frac{3}{2} k_B \frac{\partial}{\partial t} (N_a T_a) + \underbrace{\nabla \cdot \mathbf{Q}_a}_{\text{heat flux transport}} = \underbrace{N_a e_a \mathbf{E} \cdot \mathbf{U}_a}_{\text{ohmic heating}} + \underbrace{\Delta \varepsilon_a}_{\text{collisional heating}} \quad (1.48)$$

where $a = e, i$ for electrons and ion species, and ν_a is the effective collision frequency. These equations will form the basis of the plasma-fluid finite-difference time-domain simulation algorithm developed in Chapter 3.

1.4 Waves in Plasma

The plasma medium is able to support a diverse assortment of waves arising from the plasma's response to artificial or natural perturbations, each possessing a distinct and often complicated range of properties and behaviours. Further, due to its electrically-sensitive nature, plasma is able to interact strongly with electromagnetic waves, significantly affecting their propagation characteristics and coupling to stimulate a variety of instabilities and wave-conversion effects. In this section the properties of some common plasma waves are described. As the focus of this thesis is primarily centred around the F-Region of the Earth's ionosphere, this section will be limited to a description of waves commonly found in this plasma regime. The theory of wave propagation and dynamics in plasma forms a crucial background to the processes investigated in Chapter 3 and beyond. To simplify the analysis, it is usually assumed that the wave perturbations are small compared to the background conditions. Further approximations (for example limiting the calculation to specific propagation angles) can be made to make the algebra manageable; in reality, the conditions are never so well-defined and simplistic: wave processes rarely occur in isolation and it is often impossible to disentangle a distinct wave

flavour from a superposition of competing interactions. The need for a way to model the time dependent evolution of many mutually-interacting complicated and often non-linear plasma phenomena is one of the prime motivations behind the development of the time-explicit numerical code described in Chapter 3.

A plasma wave can be described through a medium-dependent dispersion relation, which defines how the wave frequency ω varies with its propagation vector \mathbf{k} . To construct a dispersion relation, Maxwell's Equations (1.42)-(1.45) are converted from the time-domain to the frequency-domain assuming plane-wave solutions of the form $e^{i(\omega t - \mathbf{k} \cdot \mathbf{r})}$ and thus using the Fourier transform pairs $\nabla \rightarrow -i\mathbf{k}$ and $\partial/\partial t \rightarrow i\omega$ to give:

$$\mathbf{k} \cdot \boldsymbol{\varepsilon} \cdot \mathbf{E} = 0 \quad (1.49)$$

$$\mathbf{k} \cdot \mathbf{B} = 0 \quad (1.50)$$

$$\mathbf{k} \times \mathbf{E} = \omega \mathbf{B} \quad (1.51)$$

$$\mathbf{k} \times \mathbf{B} = -\omega \mu_0 \boldsymbol{\varepsilon} \cdot \mathbf{E} \quad (1.52)$$

In these expressions, the dispersive effects of the plasma have been wrapped up into the dielectric permittivity tensor $\boldsymbol{\varepsilon}$, defined such that:

$$\boldsymbol{\varepsilon} \cdot \mathbf{E} = \frac{1}{i\omega\varepsilon_0} \mathbf{J} + \mathbf{E} = \left(\mathbf{1} + \frac{\boldsymbol{\sigma}}{i\omega\varepsilon_0} \right) \cdot \mathbf{E} \quad (1.53)$$

where $\boldsymbol{\sigma}$ is the plasma conductivity tensor. Taking the frequency-domain curl of (1.51) and (1.52) and rearranging gives the basic plasma dispersion relation (1.54):

$$\mathbf{k} (\mathbf{k} \cdot \mathbf{E}) - k^2 \mathbf{E} + \left(\frac{w}{c} \right)^2 \boldsymbol{\varepsilon} \cdot \mathbf{E} = 0 \quad (1.54)$$

In the following descriptions, the term *transverse* will refer to wave modes with \mathbf{k} perpendicular to \mathbf{E} ($\Rightarrow \mathbf{k} \cdot \mathbf{E} = 0$), while *longitudinal* will refer to waves with \mathbf{k} parallel to \mathbf{E} ($\Rightarrow \mathbf{k} \times \mathbf{E} = 0$). *Perpendicular* propagation will refer to waves with \mathbf{k} perpendicular to the background magnetic field \mathbf{B}_0 , while *parallel* propagation will refer to waves with \mathbf{k} parallel to \mathbf{B}_0 . The term *electrostatic* (ES) will be used to describe any wave

where $\mathbf{B} = 0$. From (1.51), this condition implies that these waves are longitudinal with $\mathbf{k} \times \mathbf{E} = 0$. The term *Electromagnetic* (EM) will refer to waves with $\mathbf{B} \neq 0$.

1.4.1 Electromagnetic Waves

In a vacuum, an electromagnetic wave travels at a constant speed of light and obeys the simple dispersion relation given by (1.55):

$$\omega^2 = c^2 k^2 \quad (1.55)$$

However a plasma acts as a dispersive and often anisotropic medium that can significantly influence the propagation of the wave. Below, the dispersive behavior for electromagnetic waves under various plasma conditions are summarised, treating the wave fields \mathbf{E} and \mathbf{B} as small perturbations to the medium. As EM waves require $\mathbf{B} \neq 0$, dispersion relations can be found by using equation (1.54) with the appropriate expression for ϵ . The derivations outlined below can be found in more detail in [Inan and Golkowski, 2011] and other textbooks.

1.4.1.1 Unmagnetised Plasma

The simplest case of plasma is a uniform, cold, collisionless and unmagnetised combination of electrons and singly-ionised positive ions at thermal equilibrium, as encountered in Section 1.1 above. The oscillating electric field of an EM wave travelling through this plasma will displace the plasma particles from their equilibrium positions, causing them to attempt to oscillate at the plasma frequency as described in Section 1.1.3. The restoring electric field induced by the plasma oscillations interferes with the EM field, introducing frequency-dependent dispersive effects. In the cold, collisionless case with $\mathbf{B}_0 = 0$ and $\nu_c = 0$, the electron momentum equation (1.46) can be expressed in the frequency domain as:

$$i\omega \mathbf{U}_e = -\frac{e}{m_e} \mathbf{E} \quad (1.56)$$

Assuming that the ions are stationary on the timescale of electron oscillations, the induced current can be described by:

$$\mathbf{J}_e = -eN_e \mathbf{U}_e = \frac{e^2 N_e}{i\omega m_e} \mathbf{E} \quad (1.57)$$

where the unmagnetised and thus isotropic condition implies scalar values for the conductivity and permittivity. The EM dispersion relation can be obtained by using equation (1.54) in conjunction with the transverse condition $\mathbf{k} \cdot \mathbf{E} = 0$ to give:

$$\frac{c^2 k^2}{\omega^2} \mathbf{E} = \boldsymbol{\varepsilon} \cdot \mathbf{E} \quad \text{or} \quad \left(1 - \frac{c^2 k^2}{\omega^2}\right) \mathbf{E} = -\frac{1}{i\omega \varepsilon_0} \mathbf{J} \quad (1.58)$$

Finally, substitution of (1.57) into (1.58) gives:

$$\left(1 - \frac{c^2 k^2}{\omega^2}\right) \mathbf{E} = -\frac{1}{i\omega \varepsilon_0} \left(\frac{e^2 N_e}{i\omega m_e}\right) \mathbf{E} \quad (1.59)$$

which simplifies to give a dispersion relation for EM waves in a cold unmagnetised plasma:

$$\omega^2 = \omega_{pe}^2 + k^2 c^2 \quad (1.60)$$

using expression (1.13) for the electron plasma frequency ω_{pe} .

The EM dispersion relation for unmagnetised plasma is plotted in Figure 1.4. From this it is clear an unmagnetised plasma is completely opaque to EM waves with a frequency below the characteristic frequency of electron oscillation. This corresponds to a frequency cut-off at $\omega = \omega_{pe}$, and a critical value of electron number density, N_{eCrit} , above which the wave cannot propagate:

$$N_{eCrit} = \frac{\varepsilon_0 m_e}{e^2} \omega_0^2 \quad (1.61)$$

As the frequency is increased beyond ω_{pe} , the expression converges to the vacuum dispersion relation (1.55).

Inclusion of collisional terms in the cold plasma model causes a damping term to arise in

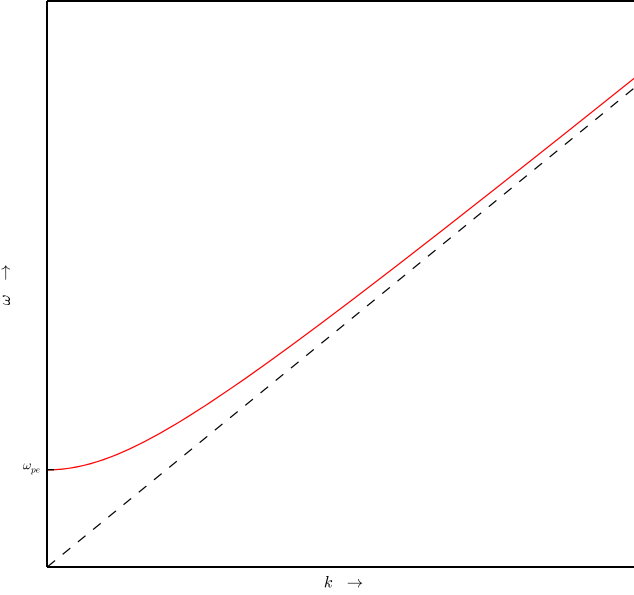


FIGURE 1.4: Dispersion relation for electromagnetic waves in a cold, collisionless, unmagnetised plasma (red). There is a frequency cut-off at $\omega = \omega_{pe}$, below which there is no wave propagation. The relationship asymptotically approaches the $\omega = ck$ vacuum expression as frequency is increased (indicated by dashed-black line).

the dispersion relation. With effective collision frequency $\nu_c \neq 0$, the frequency-domain momentum expression (1.56) becomes:

$$i\omega \left(1 - i\frac{\nu_c}{\omega}\right) \mathbf{U}_e = -\frac{e}{m_e} \mathbf{E} \quad (1.62)$$

Addition of collisions effectively corresponds to the substitution $m \rightarrow m(1 - i\nu_c/\omega)$ [Inan and Golkowski, 2011]. This leads to the appearance of a frequency-dependent negative-imaginary damping term in the dispersion relation, which manifests physically as an exponential attenuation of the wave with distance:

$$\omega^2 = \omega_{pe}^2 + k^2 c^2 + i\nu_c \omega \left(1 - \frac{k^2 c^2}{\omega^2}\right) \quad (1.63)$$

1.4.1.2 Magnetised Plasma

In this unmagnetised plasma scheme above, the components of the propagating electric field are uncoupled: propagation is not sensitive to the wave polarisation; dispersive characteristics are equivalent for any direction of travel in the infinite, uniform plasma.

The addition of a background magnetic field introduces an anisotropy to the plasma properties and significantly influences the behaviour of a propagating EM wave. Transverse E-field components are now coupled through the $\mathbf{U} \times \mathbf{B}_0$ term in (1.46), leading to elliptical polarisation. The dispersive behaviour of a propagating EM wave is now heavily dependent on the orientation of wavevector \mathbf{k} with respect to the magnetic field direction. Unlike in unmagnetised conditions, multiple distinct modes of EM propagation exist in a magnetised plasma, corresponding to different regimes of polarisation and orientation. The theory of how electromagnetic waves behave in a magnetised plasma is crucial to understanding the interaction of a radio wave in the F-region of the ionosphere under the influence of the Earth's geomagnetic field.

Again, a spatially-homogeneous, collisionless, equilibrium cold plasma of electrons and non-moving positive singly-ionised ions is assumed. A static background magnetic field of magnitude B_0 is assumed to lie along the z -direction ($\mathbf{B}_0 = B_0\hat{\mathbf{z}}$). Wave propagation is assumed, with no loss of generality, to lie within the xz -plane with propagation vector \mathbf{k} at an angle θ to the field-aligned z -axis ($\mathbf{k} = k \sin \theta \hat{\mathbf{x}} + k \cos \theta \hat{\mathbf{z}}$). From (1.46) and $\mathbf{J} = \mathbf{J}_i - \mathbf{J}_e \simeq -eN_e \mathbf{U}_e$, the $\mathbf{J}/i\omega\varepsilon_0$ term in (1.53) can be expressed as (1.64):

$$\frac{1}{i\omega\varepsilon_0} \begin{bmatrix} J_x \\ J_y \\ J_z \end{bmatrix} = \frac{-eN_e}{i\omega\varepsilon_0} \begin{bmatrix} U_{ex} \\ U_{ey} \\ U_{ez} \end{bmatrix} = \left(\frac{-eN_e}{i\omega\varepsilon_0} \right) \left(\frac{-e}{i\omega m_e} \right) \begin{bmatrix} E_x + U_{ey}B_0 \\ E_y - U_{ex}B_0 \\ E_z \end{bmatrix} = - \begin{bmatrix} \frac{\omega_{pe}^2}{\omega^2} E_x + \frac{\omega_{ce}}{\omega^2\varepsilon_0} J_x \\ \frac{\omega_{pe}^2}{\omega^2} E_y - \frac{\omega_{ce}}{\omega^2\varepsilon_0} J_y \\ \frac{\omega_{pe}^2}{\omega^2} E_z \end{bmatrix} \quad (1.64)$$

This set of coupled equations can be rearranged as shown by (1.65):

$$\frac{1}{i\omega\varepsilon_0} \begin{bmatrix} J_x \\ J_y \\ J_z \end{bmatrix} = \begin{bmatrix} \frac{-X}{1-Y^2} E_x - \frac{iXY}{1-Y^2} E_y \\ \frac{-X}{1-Y^2} E_y + \frac{iXY}{1-Y^2} E_x \\ -XE_z \end{bmatrix} \quad (1.65)$$

where, by convention:

$$X = \omega_{pe}^2/\omega^2 \quad (1.66)$$

and

$$Y = \omega_{ce}/\omega \quad (1.67)$$

Thus from (1.53) and (1.65), the permittivity tensor $\boldsymbol{\varepsilon}$ can be expressed as (1.68):

$$\boldsymbol{\varepsilon} \cdot \mathbf{E} = \begin{bmatrix} 1 - \frac{X}{1-Y^2} & -\frac{iXY}{1-Y^2} & 0 \\ \frac{iXY}{1-Y^2} & 1 - \frac{X}{1-Y^2} & 0 \\ 0 & 0 & 1-X \end{bmatrix} \begin{bmatrix} E_x \\ E_y \\ E_z \end{bmatrix} = \begin{bmatrix} \varepsilon_{\perp} & -i\varepsilon_{\times} & 0 \\ i\varepsilon_{\times} & \varepsilon_{\perp} & 0 \\ 0 & 0 & \varepsilon_{\parallel} \end{bmatrix} \begin{bmatrix} E_x \\ E_y \\ E_z \end{bmatrix} \quad (1.68)$$

where the perpendicular, parallel and transverse-coupling permittivities are given by:

$$\varepsilon_{\perp} = 1 - \frac{X}{1-Y^2} \quad (1.69)$$

$$\varepsilon_{\parallel} = 1 - X \quad (1.70)$$

$$\varepsilon_{\times} = \frac{XY}{1-Y^2} \quad (1.71)$$

As expected from the analysis in Section 1.2.2 above, the component of wave E-field propagating directly along the background magnetic field direction is unaffected and behaves in the same manner as it would in an unmagnetised plasma. The magnetic field couples the transverse components of the wave E-field through ε_{\times} , causing the wave polarisation vector to describe an ellipse in the transverse xy -plane. If the magnetic field is reduced such that $\omega_{ce} \ll \omega$, the unmagnetised permittivity expression is recovered for all field components ($\varepsilon \rightarrow \varepsilon_{\parallel}$). The dispersion relation can be obtained using (1.68) in conjunction with (1.54) as described in [Inan and Golkowski, 2011] to give:

$$\underbrace{\begin{bmatrix} k^2 \sin^2 \theta & 0 & k^2 \cos \theta \sin \theta \\ 0 & 0 & 0 \\ k^2 \cos \theta \sin \theta & 0 & k^2 \cos^2 \theta \end{bmatrix}}_{\mathbf{k}(\mathbf{k} \cdot \mathbf{E})} \cdot \mathbf{E} + \underbrace{\begin{bmatrix} -k^2 & 0 & 0 \\ 0 & -k^2 & 0 \\ 0 & 0 & -k^2 \end{bmatrix}}_{-k^2} \cdot \mathbf{E} + \left(\frac{w}{c}\right)^2 \underbrace{\begin{bmatrix} \varepsilon_{\perp} & -i\varepsilon_{\times} & 0 \\ i\varepsilon_{\times} & \varepsilon_{\perp} & 0 \\ 0 & 0 & \varepsilon_{\parallel} \end{bmatrix}}_{\boldsymbol{\varepsilon}} \cdot \mathbf{E} = 0$$

$$\Rightarrow \begin{bmatrix} \varepsilon_{\perp} - \frac{c^2 k^2}{\omega^2} \cos^2 \theta & -i\varepsilon_{\times} & \frac{c^2 k^2}{\omega^2} \cos^2 \theta \sin^2 \theta \\ i\varepsilon_{\times} & \varepsilon_{\perp} - \frac{c^2 k^2}{\omega^2} & 0 \\ \frac{c^2 k^2}{\omega^2} \cos^2 \theta \sin^2 \theta & 0 & \varepsilon_{\parallel} - \frac{c^2 k^2}{\omega^2} \sin^2 \theta \end{bmatrix} \cdot \mathbf{E} = 0 \quad (1.72)$$

Non-trivial solutions to (1.72) can be found by setting the determinant of the simultaneous-equation matrix to zero, to give the well-known *Appleton-Hartree* equation [Ginzburg, 1970] describing the dispersion of an EM plane wave propagating at angle θ to the static B-field in a magnetised, homogeneous plasma:

$$1 - \frac{c^2 k^2}{\omega^2} - \frac{2X(1-X)}{2(1-X) - Y^2 \sin^2 \theta \pm \left[Y^4 \sin^4 \theta + 4(1-X)^2 Y^2 \cos^2 \theta \right]^{1/2}} = 0 \quad (1.73)$$

In the limit that $\omega_{ce} \ll \omega$, $Y \rightarrow 0$, this expression reduces to that of the unmagnetised case, (1.60).

Figure 1.5 shows the Appleton-Hartree dispersion relationship plotted for a range of propagation angles between $\theta = 0$ (propagation parallel to the background magnetic field) and $\theta = \pi/2$ (propagation perpendicular to the background magnetic field). Here and in all following descriptions, it is assumed that $\omega_{pe} > \omega_{ce}$, as is the case for the F-region ionosphere. It can be seen that the anisotropy introduced by the static background magnetic field has the effect of splitting the EM wave propagation into several distinct modes determined by polarisation and direction, and introducing an extra frequency cut-offs and resonances not encountered in the unmagnetised case. The main source of splitting arises from the “ \pm ” in the denominator of (1.73): the dispersion relation has two solutions at any given frequency and propagation direction. The principal wave modes that emerge for the case that wave propagation is parallel to the background magnetic field ($\mathbf{k} \parallel \mathbf{B}_0$) are commonly referred to as the L-mode and the R-mode, corresponding respectively to the “+” and “-” solution in (1.73) for $\theta = 0$. In the case of both these modes, the E-field vector exists in a plane perpendicular to both the wave propagation and background magnetic field vectors ($\mathbf{E} \perp \mathbf{k}$, $\mathbf{E} \perp \mathbf{B}_0$), with the L-mode wave polarised in a left-handed-circular sense and the R-mode wave polarised in a right-handed-circular sense (see, for example, Figure 4-38 of [Chen, 1984] for a schematic

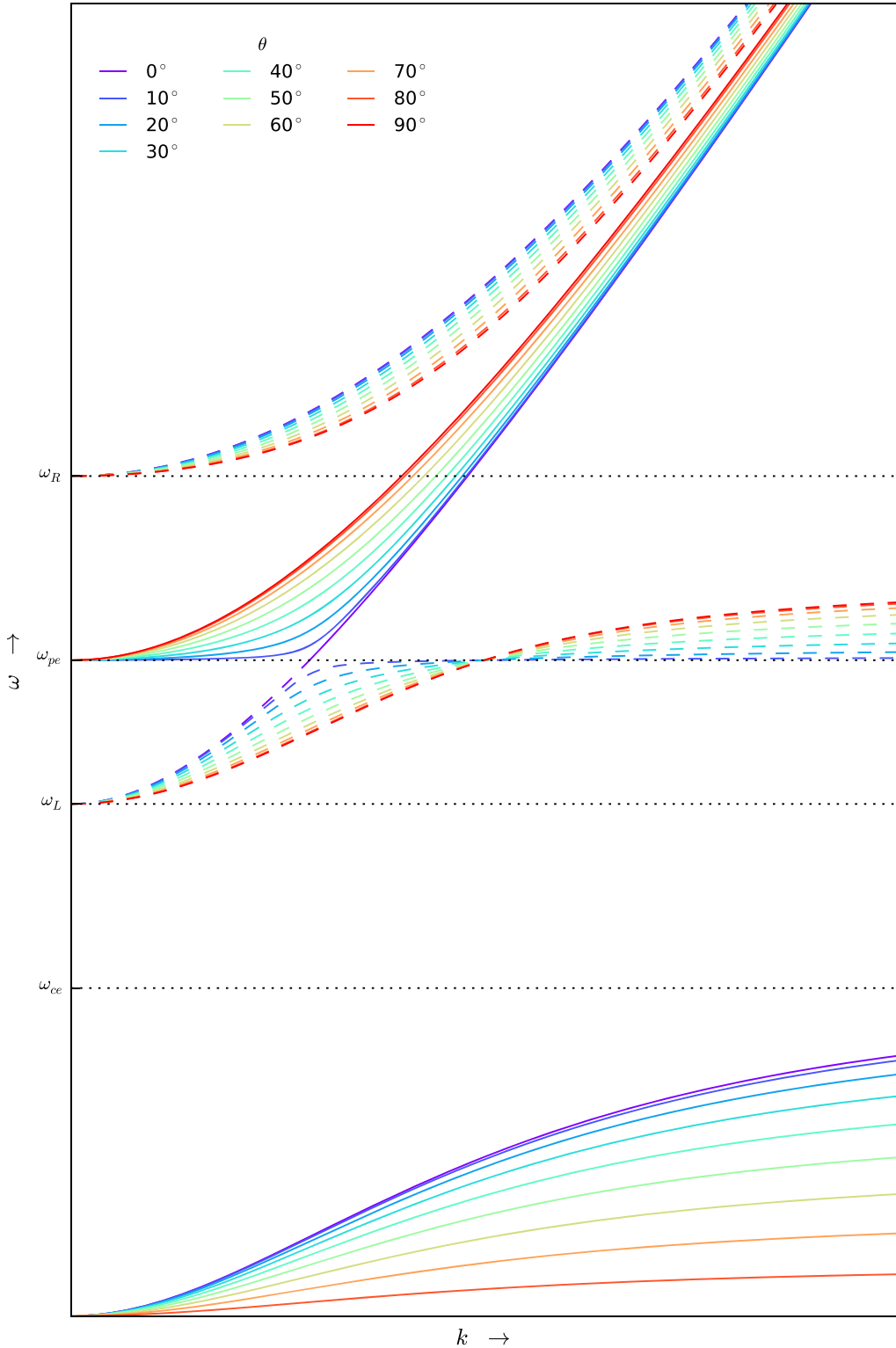


FIGURE 1.5: Dispersion relation for electromagnetic waves in a cold, collisionless, magnetised plasma for a range of propagation angles between $\theta = 0$ (parallel) and $\theta = \pi/2$ (perpendicular). The effect of the anisotropy introduced by the static background magnetic field is to split EM wave propagation into several distinct modes determined by polarisation and direction. The solid lines show the “+” solutions from the Appleton-Hartree equation (1.73) (referred to in this thesis as O-modes), while the dashed lines show the “-” solutions (referred to in this thesis as X-modes).

illustration of the difference between L- and R-mode polarisation). In the limit of wave propagation perpendicular to the background magnetic field ($\mathbf{k} \perp \mathbf{B}_0$), the principal wave modes are defined as the O-mode, for which the E-field vector is aligned with the background magnetic field ($\mathbf{E} \parallel \mathbf{B}_0$), and the X-mode, for which the E-field vector exists in the plane perpendicular the background magnetic field ($\mathbf{E} \perp \mathbf{B}_0$). These correspond respectively to the “+” and “−” branches of (1.73) for $\theta = \pi/2$. Obliquely-propagating modes with can be described as linear combinations of these limiting cases. For the purposes of this thesis, the following naming convention will be adopted, to match the convention employed in much of the artificial ionospheric modification literature cited in later Chapters: the “+” solution of the Appleton-Hartree equation (indicated by solid lines in Figure 1.5) is referred to hereafter as the *ordinary mode* (O-mode); this mode corresponds to left-handed circular polarisation for the case of parallel propagation and purely-transverse polarisation for the case of perpendicular propagation. The “−” solution (indicated by dashed lines) is referred to hereafter as the *extraordinary mode* (X-mode); this mode corresponds to right-handed circular polarisation for the case of parallel propagation and an elliptical mixture of transverse and longitudinal polarisation for the case of perpendicular propagation. The $\omega < \omega_{ce}$ low-frequency solution is referred to as the *whistler mode*. In essence, for O-mode waves the polarisation vector rotates around \mathbf{B}_0 in a left-handed sense, while for X-mode waves the rotation is in a right-handed sense, irrespective of the alignment of the wavevector with the magnetic field.

The frequency cut-offs for EM waves in a magnetised plasma correspond to the points where the refractive index, $n = n_r + in_i = c^2 k^2 / \omega^2$, is equal to zero (group velocity $\rightarrow 0$: reflection of wave energy). These can be calculated from (1.73), and are shown clearly as the $k = 0$ solutions in Figure 1.5. The O-mode branch has a single cut-off, equivalent to that found in the unmagnetised case, corresponding to $\omega = \omega_{pe}$ and $X = 1$. The X-mode branch has twin cut-offs, known commonly as the left- and right-handed cut-off frequencies, given by (1.74) and (1.75) [Inan and Golkowski, 2011] below:

$$\omega_L = \frac{1}{2} \left([\omega_{ce}^2 + 4\omega_{pe}^2]^{\frac{1}{2}} - \omega_{ce} \right); \quad X_L = 1 - Y \quad (1.74)$$

$$\omega_R = \frac{1}{2} \left([\omega_{ce}^2 + 4\omega_{pe}^2]^{\frac{1}{2}} + \omega_{ce} \right); \quad X_R = 1 + Y \quad (1.75)$$

Resonances corresponding to the refractive index tending to infinity (group velocity $\rightarrow \infty$: absorption of wave energy) can be found by setting the denominator of (1.73) to zero. A resonance of the low-frequency “whistler” branch occurs at $\omega = \omega_{ce} \cos \theta$. An X-mode resonance corresponding to the upper-hybrid wave frequency (see 1.4.2 below) also occurs at $\omega = \omega_H$ and $X = 1 - Y^2 / (1 - Y^2 \cos^2 \theta)$.

It can be seen that for the special case of $\theta = 0^\circ$, the ordinary mode branch is coincident in $\omega - k$ space with one of the extraordinary mode branches, allowing mode conversion between the two polarisation regimes. The mechanics of this process and its impact on artificial heating on the F-region of the ionosphere will be investigated in Chapter 4.

As in the unmagnetised scenario, the inclusion of collisions adds a complex damping term to the dispersion relation, which implies that wave energy is dissipated in the plasma due to collisional processes. Following the above procedure, but with $\nu_c \neq 0$, yields the complex-valued dispersion relation [Inan and Golkowski, 2011]:

$$1 = \frac{c^2 k^2}{\omega^2} + \frac{2X(1-X-iZ)}{2(1-X)(1-X-iZ)-Y^2 \sin^2 \theta \pm \left[Y^4 \sin^4 \theta + 4(1-X-iZ)^2 Y^2 \cos^2 \theta \right]^{1/2}} \quad (1.76)$$

The effect of finite temperature (“warm”) plasma fluids or mobile, magnetised ions does not have a significant impact on high-frequency ($> \omega_{ce}$) EM wave propagation, but will be discussed below for the case of ES waves.

1.4.1.3 EM Waves in a Vertically-Stratified Magnetised Plasma

The above calculation considers only the case of uniform, spatially-homogeneous plasma where the fundamental plasma frequencies are constant. In the ionosphere, this is not the case: as will be discussed in more detail in Section 1.5.2 below, the electron density gradient in the ionosphere, and therefore the fundamental frequency of plasma oscillation, varies strongly with height; the geomagnetic field is not constant in orientation or magnitude, thus the anisotropy and cyclotron frequencies change; the temperature and ionic/neutral composition also varies leading to inhomogeneity in parameters such

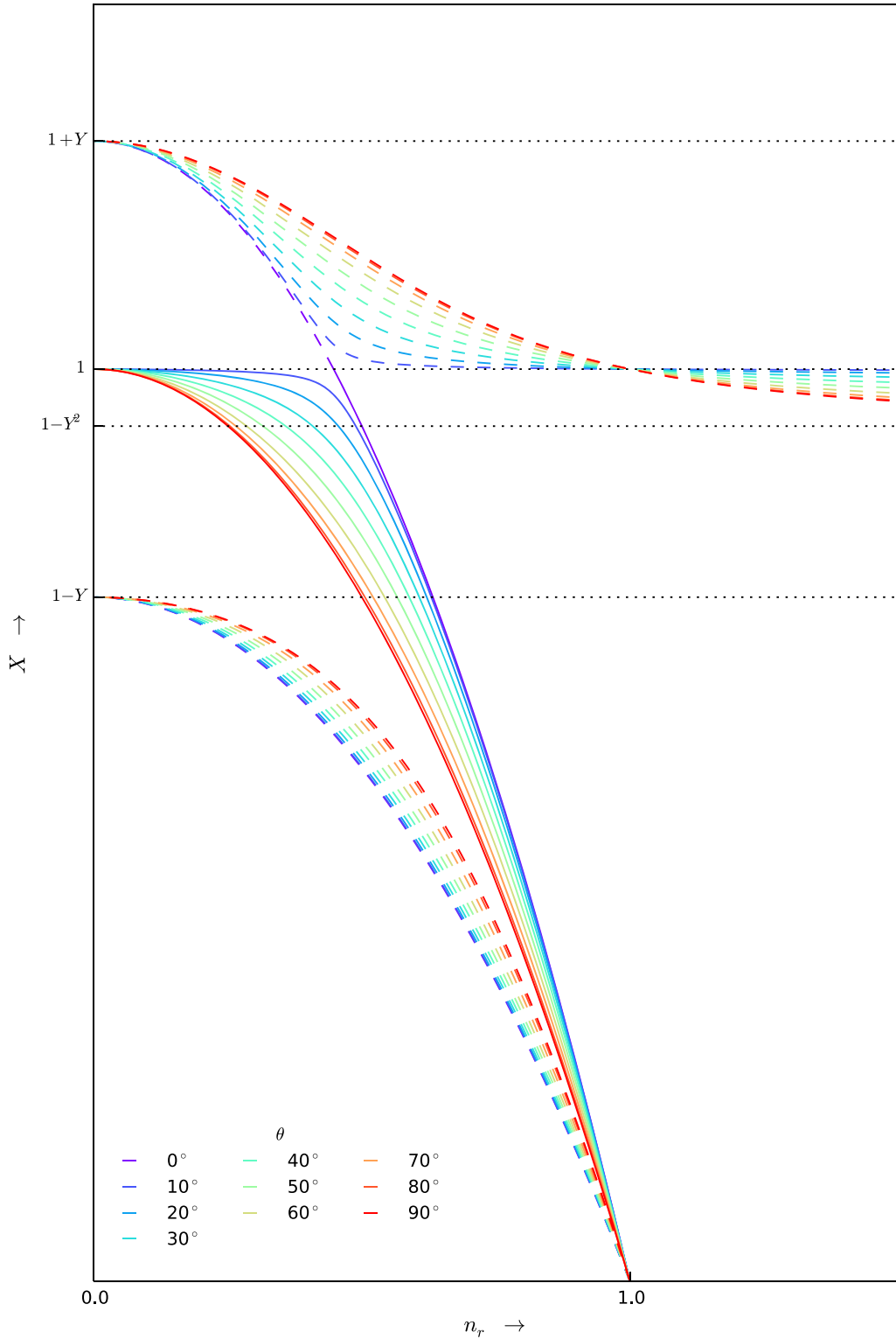


FIGURE 1.6: Real part of the refractive index $n = n_r + in_i = c^2 k^2 / \omega^2$ for EM waves in a cold, collisionless, magnetised plasma where the electron density gradient increases linearly along the magnetic field direction, plotted for a range of propagation angles. The O-mode branch is indicated by the solid lines, and shows a clear cut-off at $X = 1$. The X-mode branches are indicated by dashed lines and show cut-offs at $X = 1 \pm Y$, and a resonance at $X = 1 - Y^2 / (1 - Y^2 \cos^2 \theta)$. Here, $X = \omega_{pe}^2 / \omega^2$ and $Y = \omega_{ce} / \omega$.

as the collision frequency. In this thesis, the effects of a varying \mathbf{B}_0 will not be considered as the geomagnetic field is approximately uniform in strength and direction over the areas of interest, as is the chemical composition of ion and neutral species. The effects of finite-temperature plasma fluid are incorporated into the simulation code described in Chapter 2 but do not have a significant impact on EM wave propagation. The variation in ω_{pe} however is of crucial importance to the behaviour of a radio wave propagating in the ionosphere. Figure 1.6 shows the real part of the refractive index $n = n_r + in_i = c^2 k^2 / \omega^2$ for the case of an EM plane wave of single frequency propagating in an inhomogeneous magnetised plasma, where the electron density gradient (and hence the parameter X) is linearly increasing with altitude. The O-mode branch is indicated by the solid lines, and shows a clear cut-off at $X = 1$. The consequence of this is that as the vertically propagating wave ascends to higher altitudes its group velocity decreases, tending to zero when the electron plasma frequency matches with the EM wave frequency. The wave cannot propagate beyond this level (known in the ionosphere as the *O-mode reflection height*) and is reflected, a process which may lead to the formation of a reflection-standing wave and effective transfer of wave energy to the plasma (see Section 1.6). The X-mode branches are indicated by dashed lines and show cut-offs at $X = 1 \pm Y$, and a resonance at $X = 1 - Y^2 / (1 - Y^2 \cos^2 \theta)$. Like the O-mode wave, the X-mode wave slows and is reflected as it approaches electron plasma densities corresponding to its cut-off frequencies. As an X-mode wave approaches the resonance close to the upper-hybrid height at $1 - Y^2$, its wavevector tends to infinity and the wave energy is very efficiently absorbed, potentially leading to the excitation of high-amplitude plasma waves and electron temperature enhancement (see [Gondarenko et al., 2006] and references within). A ground-launched X-mode wave in a vertically-increasing plasma density gradient will however be reflected at the lower altitude corresponding to $1 - Y$ and hence can never access the resonance; for an X-mode wave to reach the resonance height, a mode conversion process such as that indicated by the $\theta = 0^\circ$ trace in Figure 1.6 must proceed. As the O- and X-mode refractive index branches coexist at $X = 1$ for wavevectors aligned with \mathbf{B}_0 , the wave can convert from an O-mode to the high-frequency X-mode branch (referred to hereafter as the *Z-mode*) and potentially access the resonance. This process and its consequences for artificial plasma modification will

be investigated in more detail in Chapter 4.

One important point to note is that, for a given wave, the orientation of the propagation vector will not be constant as the wave moves through the plasma: the refractive effects of the plasma will act to bend the wave direction as it propagates, particularly for the case where the background magnetic field direction is not aligned with the direction of plasma density gradient. As shown by Figure 1.6 and others, the orientation of the wavevector has a significant influence on the behaviour of the wave, and computing the three-dimensional dynamics of an EM wave in an inhomogeneous plasma when the orientation is constantly in flux is not a trivial problem. To do so, one could use an analytic technique such as geometric optics (see [Budden, 1961] or [Ginzburg, 1970]), however these require somewhat-constraining regimes of approximation, and are unable to treat complicated multi-dimensional inhomogeneity features accurately. A more powerful solution is to use a numerical simulation code to fully compute the effects of an inhomogeneous plasma on wave dynamics; one of the main motivations behind the work in this thesis was to produce a computational code that could accurately simulate the multi-dimensional dispersive and refractive behaviour of a EM wave propagating through an ionospheric plasma medium containing complicated and highly-inhomogeneous density profiles, as will be discussed in detail in Chapter 3 and beyond.

1.4.2 Electrostatic Electron Waves

Unlike the electromagnetic waves described above, electrostatic waves do not involve an oscillating magnetic field ($\mathbf{B} = 0$, $\nabla \times \mathbf{E} = 0$), but always involve a longitudinal component corresponding to a non-zero space charge ($\nabla \cdot \mathbf{E} \neq 0$). The derivations outlined below were drawn mainly from the calculations in [Chen, 1984] and [Baumjohann and Treumann, 1996], more details can be found in these and other textbooks.

The simplest form of ES wave is the *Langmuir* wave, often referred to as the *electron plasma wave* (see, for example, [Chen, 1984]). It was shown in Section 1.1.3 above that any displacement of the plasma electrons from their equilibrium positions will cause them to oscillate with a characteristic frequency, ω_{pe} . In an idealised cold plasma,

this behaviour is merely an *oscillation*, non-propagating and static in space about the equilibrium position. In a more realistic plasma with finite non-zero temperature, the particle vibrations can travel with a small thermal velocity and can be properly termed a plasma *wave*. With the addition of a magnetic field, the plasma oscillations can also couple with the electron cyclotron motion resulting in hybrid electrostatic plasma waves and resonant cyclotron modes.

The dispersion relation for ES waves in a collisionless, magnetised plasma-fluid can be calculated from (1.49) using the longitudinal condition, which implies that \mathbf{E} lies along \mathbf{k} . With wave propagation again restricted to the xz -plane and the background magnetic field directed along the z -axis, the wave E-field and wavevector can be expressed as $\mathbf{E} = E \sin \theta \hat{\mathbf{x}} + E \cos \theta \hat{\mathbf{z}}$ and $\mathbf{k} = k \sin \theta \hat{\mathbf{x}} + k \cos \theta \hat{\mathbf{z}}$ respectively, where θ is the propagation angle relative to the z -axis. Associated with these ES waves is an oscillating space charge which manifests as a periodic variation of the electron density $N = N_0 + N_1 e^{-i(\omega t - \mathbf{k} \cdot \mathbf{r})}$ where the perturbation density is assumed to be small compared to the background density ($N_1 \ll N_0$). The plasma is assumed to have a non-zero, uniform temperature, T_0 . Under these assumptions (1.49) becomes:

$$\mathbf{k} \cdot \boldsymbol{\varepsilon} \cdot \mathbf{E} = \mathbf{k} \cdot \left(\mathbf{E} + \frac{ieN_0}{\omega\varepsilon_0} \mathbf{U} \right) = 0 \quad \Rightarrow \quad E = -\frac{ieN_0}{\omega\varepsilon_0} (U_x \sin \theta + U_z \cos \theta) \quad (1.77)$$

From (1.46), the fluid velocity components can be expressed as:

$$U_x = \frac{ie}{\omega m_e} E_x + \frac{i\omega_{ce}}{\omega} U_y + \frac{\gamma k_x}{2\omega} \left(\frac{2k_B T_0}{m_e} \right) \frac{N_1}{N_0} \quad (1.78)$$

$$U_y = -\frac{i\omega_{ce}}{\omega} U_x \quad (1.79)$$

$$U_z = \frac{ie}{\omega m_e} E_z + \frac{\gamma k_z}{2\omega} \left(\frac{2k_B T_0}{m_e} \right) \frac{N_1}{N_0} \quad (1.80)$$

which can be rearranged to give:

$$U_x = \left[\frac{ie}{\omega m_e} E + \frac{\gamma k v_{Te}^2}{2\omega} \left(\frac{N_1}{N_0} \right) \right] \frac{\sin \theta}{1 - Y^2} \quad (1.81)$$

$$U_z = \left[\frac{ie}{\omega m_e} E + \frac{\gamma k v_{Te}^2}{2\omega} \left(\frac{N_1}{N_0} \right) \right] \cos \theta \quad (1.82)$$

where the electron thermal velocity is defined as $v_{Te} = \sqrt{2k_B T_0/m_e}$ [Chen, 1984]. Combining (1.81) and (1.82) with (1.77) and $i\varepsilon_0 \mathbf{k} \cdot \mathbf{E} = i\varepsilon_0 k E \simeq eN_1$ yields:

$$\begin{aligned} E &= -\frac{ieN_0}{\omega\varepsilon_0} \left\{ \left[\frac{ie}{\omega m_e} + \frac{\gamma k^2 v_{Te}^2}{2\omega} \left(\frac{i\varepsilon_0}{eN_0} \right) \right] \frac{\sin^2 \theta}{1 - Y^2} + \left[\frac{ie}{\omega m_e} + \frac{\gamma k^2 v_{Te}^2}{2\omega} \left(\frac{i\varepsilon_0}{eN_0} \right) \right] \cos^2 \theta \right\} E \\ 1 &= \left[\frac{e^2 N_0}{\omega^2 \varepsilon_0 m_e} + \frac{\gamma k^2 v_{Te}^2}{2\omega^2} \right] \frac{\sin^2 \theta}{1 - Y^2} + \left[\frac{e^2 N_0}{\omega^2 \varepsilon_0 m_e} + \frac{\gamma k^2 v_{Te}^2}{2\omega^2} \right] \cos^2 \theta \end{aligned} \quad (1.83)$$

which allows the ES dispersion relation for oblique propagation to be expressed as:

$$\Rightarrow 1 = \left[X + \frac{\gamma k^2 v_{Te}^2}{2\omega^2} \right] \left[\cos^2 \theta + \frac{\sin^2 \theta}{1 - Y^2} \right] \quad (1.84)$$

This dispersion relation is plotted in Figure 1.7 for a range of propagation angles between $\theta = 0^\circ$ (parallel) and $\theta = 90^\circ$ (perpendicular). The dispersion relation is multivalued, with a low-frequency mode and a high-frequency mode existing simultaneously at each propagation angle. The low frequency modes at $\omega < \omega_{ce}$ correspond to resonant electron cyclotron waves. This wave mode requires some component of the wave E-field to be in the plane of electron gyrorotation, and hence only exists for $\theta \neq 0^\circ$. For the case of purely-parallel propagation, the high-frequency mode corresponds to the Langmuir wave: electron plasma oscillations drifting with a non-zero thermal velocity along the magnetic field direction with a dispersion relation given by (1.85) [Chen, 1984]:

$$\omega_{Langmuir}^2 = \omega_{pe}^2 + \frac{\gamma}{2} v_{Te}^2 k^2 \quad (1.85)$$

As the E-field is aligned with \mathbf{B}_0 , the wave experiences no perturbation due to the magnetic field and behaves as if the plasma was unmagnetised. In the purely-perpendicular case, the electron plasma oscillations can couple with the electron cyclotron oscillations to produce the upper-hybrid wave mode (see, for example, [Chen, 1984]), which has a dispersion relation given by (1.86):

$$\omega_{UH}^2 = \omega_H^2 + \frac{\gamma}{2} v_{Te}^2 k^2 \quad (1.86)$$

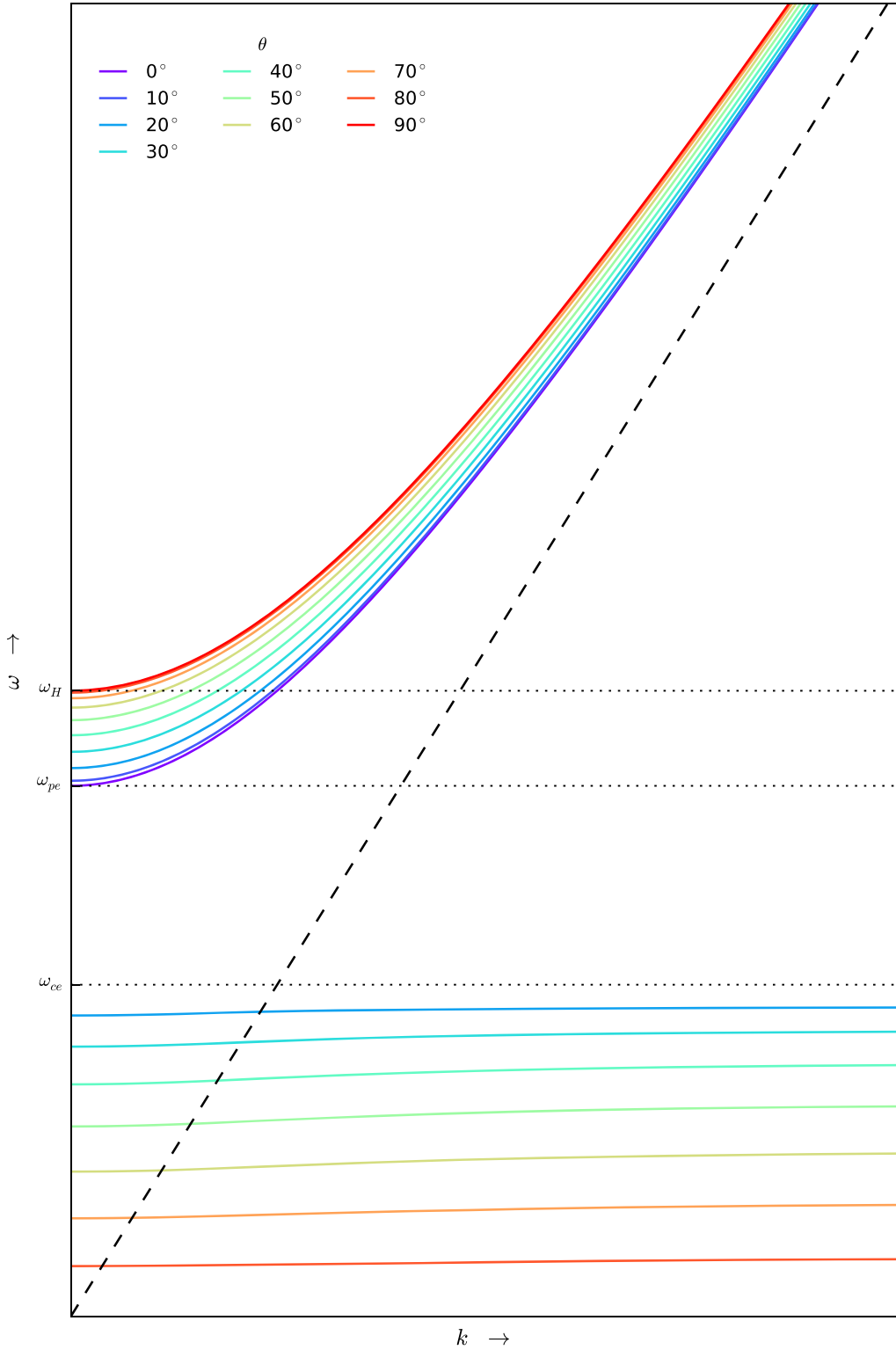


FIGURE 1.7: Dispersion relation for electrostatic electron plasma-fluid waves in a warm (non-zero temperature), collisionless, magnetised plasma, shown for a range of propagation angles between $\theta = 0^\circ$ (parallel) and $\theta = 90^\circ$ (perpendicular). Electron cyclotron wave modes can be seen at low frequencies ($\omega < \omega_{ce}$). High-frequency modes range from Langmuir waves (plasma oscillations drifting with a non-zero thermal velocity) with propagation parallel to the static magnetic field ($\theta = 0^\circ$), to upper-hybrid waves with propagation perpendicular to the field ($\theta = 90^\circ$). For oblique angles in between, the high-frequency plasma wave is a hybrid of the Langmuir and UH wave. The thermal velocity limit, $\omega = \sqrt{\frac{T}{2}}v_{Te}k$ is indicated by the dashed line. For the case of unmagnetised $\mathbf{B}_0 = 0$ plasma, the hybrid modes disappear and only the Langmuir plasma wave remains.

where ω_H is the upper hybrid oscillation frequency defined by (1.87):

$$\omega_H = [\omega_{pe}^2 + \omega_{ce}^2]^{\frac{1}{2}} \quad (1.87)$$

For oblique propagation directions ranging between parallel and perpendicular, the high-frequency mode smoothly varies between the Langmuir wave and the upper-hybrid wave. As the frequency increases, the high-frequency modes tend towards the thermal velocity limit, $\omega = \sqrt{\frac{\gamma}{2}}v_{Te}k$. For the case of an unmagnetised plasma, clearly there is no cyclotron motion present and the hybrid modes disappear leaving only the Langmuir wave.

1.4.3 Ion Waves

The above calculations have assumed that all ions are stationary and provide only a restorative, neutralising background against which the electrons oscillate. At low frequencies approaching the characteristic ion plasma frequency (ω_{pi}) or cyclotron frequency (ω_{ci}) however, this assumption is no longer valid and the effect of ion dynamics must be included in the dispersion relations. The derivations outlined below were drawn primarily from the calculations in [Chen, 1984] and [Baumjohann and Treumann, 1996], more details can be found in these and other textbooks.

In a neutral gas, the propagation of acoustic pressure-waves requires collisions between particles, however in a plasma the particles can also transfer momentum via electric interaction and thus an acoustic wave can exist in a collision free plasma. If a region of ions becomes compressed, the electrons in the plasma will quickly move to mask the excess charge through a Debye-shielding process as described in 1.1.1, however this will not be perfect, particularly on short distance scales, and the ions will experience electrostatic repulsion causing the concentration in the region to be smoothed back towards the equilibrium neutral concentration. For non-zero ion temperatures, the random thermal motion of the ions will also tend to reduce the compression. Due to their high mass, the inertia of the ions can lead them to overshoot the neutral distribution, leading to a region of rarefaction. By this process, oscillating regions of compression and rarefaction known

as *ion-acoustic waves* can propagate at low frequencies, analogous to a pressure-driven sound wave.

The pure ion-acoustic wave exists in an unmagnetised plasma and is independent of propagation direction. In response to the potential, ϕ , caused by a region with an excess or deficit of ions, the perturbation to the electron density can be described by a Boltzmann distribution:

$$N_e = N_0 + N_{e1} = N_0 e^{\frac{e\phi}{k_B T_e}} \simeq N_0 \left(1 + \frac{e\phi}{k_B T_e} \dots \right) \Rightarrow N_{e1} \simeq N_0 \frac{e\phi}{k_B T_e} \quad (1.88)$$

Considering plane-wave perturbations to both the ion and electron densities (N_{i1} and N_{e1}), Poisson's equation (1.42) can be expressed in the frequency domain as:

$$-i\varepsilon_0 k E = \varepsilon_0 k^2 \phi = e(N_{i1} - N_{e1}) \quad (1.89)$$

Thus the perturbation to the ion density is given by:

$$N_{i1} = N_0 \frac{e\phi}{k_B T_e} + \varepsilon_0 \frac{k^2 \phi}{e} = \frac{\varepsilon_0 k^2 \phi}{e} \left(\frac{1}{k^2 \lambda_D^2} + 1 \right) \quad (1.90)$$

For a 1D perturbation in the x -direction (for the non-magnetised case, this can be assumed with no loss of generality), the linearised frequency-space ion continuity and momentum equations are given by:

$$i\omega m_i N_0 U_{ix} = \underbrace{i k e N_0 \phi}_{e N_0 E_x} + \underbrace{i k \gamma_i k_B T_i N_{i1}}_{-\gamma_i k_B T_i \frac{\partial N_{i1}}{\partial x}} \quad (1.91)$$

$$i\omega N_{i1} = \underbrace{i k N_0 U_{ix}}_{-\frac{\partial}{\partial x}(N_i U_{ix})} \quad (1.92)$$

Using (1.92) to eliminate U_{ix} from (1.91) and substituting in N_{i1} from (1.90) yields an expression for the ion-acoustic dispersion relation:

$$\left(\frac{\omega}{k} \right)^2 = \frac{e^2 N_0}{k^2 m_i \varepsilon_0} \left(\frac{1}{\frac{1}{k^2 \lambda_D^2} + 1} \right) + \frac{\gamma_i k_B T_i}{m_i}$$

$$\Rightarrow \frac{\omega}{k} = \left[\frac{k_B T_e}{m_i} \left(\frac{1}{1 + k^2 \lambda_D^2} \right) + \frac{\gamma_i k_B T_i}{m_i} \right]^{\frac{1}{2}} = c_{is} \quad (1.93)$$

Note that, unlike in the neutral gas, ion sound waves can propagate even if $T_i = 0$ and there is no ion thermal pressure. At long wavelengths where $k^2 \lambda_D^2 \ll 1$, the ion acoustic wave is a constant-velocity wave where the group velocity is equivalent to the phase velocity. At short wavelengths where $k^2 \lambda_D^2 \gg 1$, the ion acoustic wave becomes the constant-frequency ion plasma oscillation, which is non-propagating with dispersion relation $\omega^2 = \omega_{pi}^2$ for the case $T_i = 0$. This is in direct contrast to the Langmuir electron plasma wave (1.85) investigated above: the electron plasma wave transitions from a constant-frequency oscillation at small k to a constant-velocity wave at large k , whereas the ion-acoustic wave transitions from a constant-velocity sound wave at small k to a constant-frequency oscillation at large k .

In a magnetised plasma, the vibrations associated with ion-acoustic sound waves and ion plasma and cyclotron motions modify the electrostatic dispersion relation at low frequencies. The perturbed densities can be expressed in terms of the plasma fluid velocity components in frequency space using the linearised form of continuity equation (1.47):

$$i\omega N_{a1} = N_0 (k_x U_{ax} + k_z U_{az}) \quad \text{where } a = e, i \quad (1.94)$$

Substituting electron velocities (1.81) and (1.82) and the ion equivalents, then combining with the frequency-domain Poisson's equation (1.89) and rearranging gives the dispersion relation for oblique propagation of ES waves with the inclusion of ion dynamics:

$$1 = \frac{X_e \left(\cos^2 \theta + \frac{\sin^2 \theta}{1 - Y_e^2} \right)}{1 - \frac{\gamma_e k^2 v_{Te}^2}{2\omega^2} \left(\cos^2 \theta + \frac{\sin^2 \theta}{1 - Y_e^2} \right)} + \frac{X_i \left(\cos^2 \theta + \frac{\sin^2 \theta}{1 - Y_i^2} \right)}{1 - \frac{\gamma_i k^2 v_{Ti}^2}{2\omega^2} \left(\cos^2 \theta + \frac{\sin^2 \theta}{1 - Y_i^2} \right)} \quad (1.95)$$

This relationship is shown for low frequencies in Figure 1.8. Due to the fact that ion gyromotion is now taken into account, the ion-acoustic dispersion branch can be seen to be modified by the appearance of ion cyclotron waves at low frequencies close to the resonance at $\omega = \omega_{ci}$. These represent the case when low frequency acoustic vibrations disturb the ions from their equilibrium positions and the Lorentz force acts as a restoring

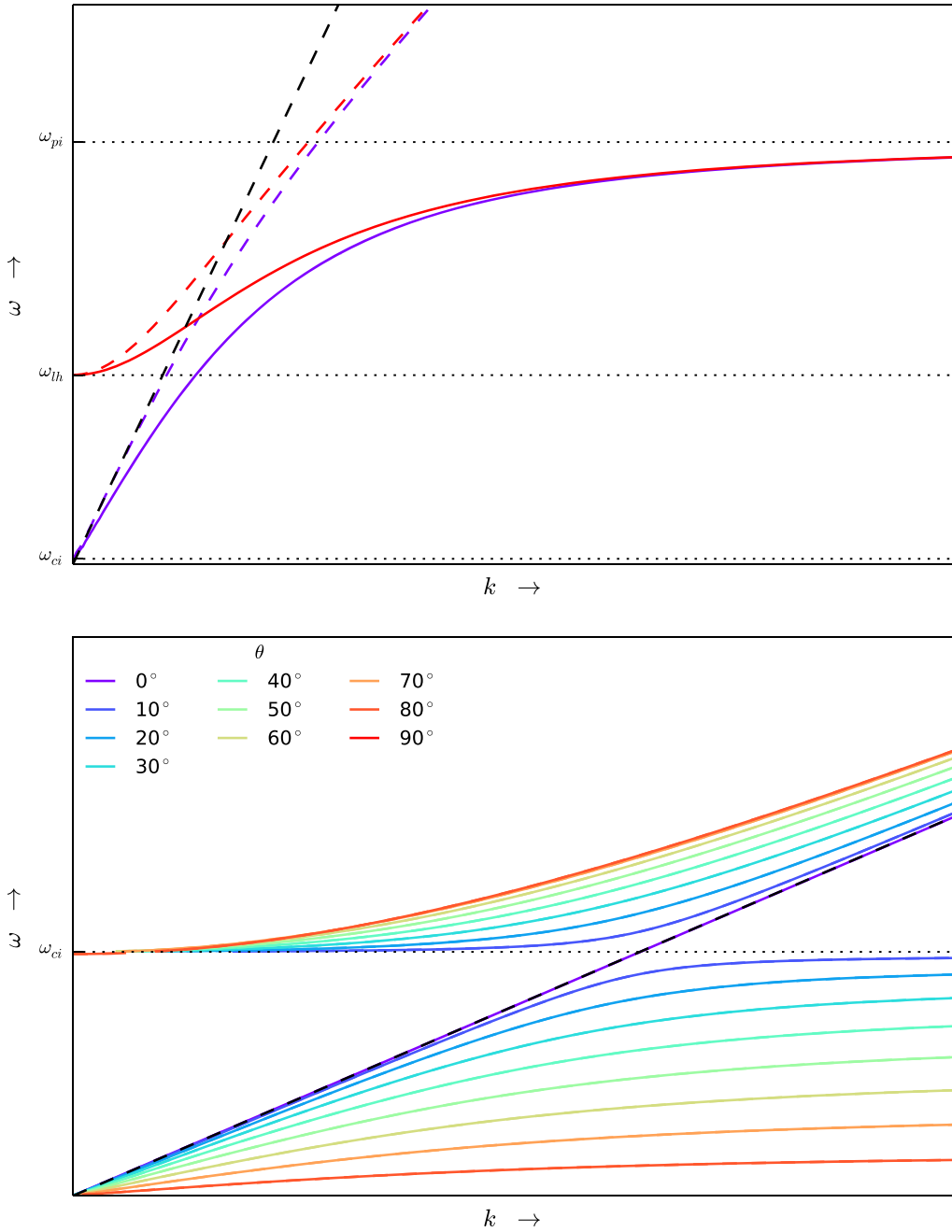


FIGURE 1.8: Dispersion relation for electrostatic plasma-fluid waves in a warm, collisionless, magnetised plasma. In both plots the ion acoustic relationship $\omega = c_i k$ is indicated by the dashed line. The lower panel shows that the ion acoustic branch is modified by the appearance of electrostatic ion-cyclotron waves at low frequencies close to the resonance at $\omega = \omega_{ci}$. The upper panel shows parallel and perpendicular dispersion for the cases of $T_i \simeq 0$ (dashed lines) and $T_i \simeq \frac{1}{2}T_e$ (solid lines) at higher frequencies. For perpendicular propagation, a new hybrid resonance appears at ω_{lh} corresponding to lower-hybrid waves. For $T_e \gg T_i$, both the ion-cyclotron and lower-hybrid branches of the acoustic wave asymptotically tend towards the constant-frequency ion plasma oscillation, $\omega^2 = \omega_{pi}^2$ for large k .

force, leading to cyclotron motion coupled with drift close to the ion sound speed. For perpendicular or very close to perpendicular propagation, a new resonant oscillation is produced known as the *lower-hybrid* (LH) oscillation, with a frequency given by (1.96) [Chen, 1984]:

$$\omega_{LH} = \left[\frac{\omega_{pi}^2 + \omega_{ci}^2}{1 + \left(\frac{\omega_{pe}}{\omega_{ce}} \right)^2} \right]^{\frac{1}{2}} \quad (1.96)$$

This is similar to the upper-hybrid electron oscillation, however it also contains an electron contribution; the electrons respond to the low-frequency transverse E-field associated with the oscillation by drifting perpendicular to the magnetic field, leading to the extra terms in the denominator of (1.96). At large k , both the LH and ion-cyclotron branches of the acoustic wave tend towards the constant-frequency ion plasma oscillation for the case of $T_e \gg T_i$. For larger ion temperatures, this wave becomes the propagating ion plasma wave drifting at the ion thermal velocity; an ionic version of the Langmuir electron plasma wave.

A further set of waves corresponding to transverse or electromagnetic modes, including ion-whistler branches, magnetosonic and hydrodynamic waves (for example the Alfvén wave family) can be found by including magnetised ion dynamics as additive perturbations to the permittivity tensor (1.68). These waves, while of great importance in the magnetosphere and beyond, are not so relevant to the ionospheric studies presented later in this thesis and so will not be discussed here. More information on these wave modes can be found in, for example, [Baumjohann and Treumann, 1996] or [Chen, 1984].

1.4.4 Kinetic Waves

In some cases, the multi-fluid plasma scheme used above is not sufficient to describe all of the dynamic behaviour of a plasma and instead a kinetic approach is required. In a fluid scheme, only the bulk-average of physical plasma quantities at a point in space and time are considered; the exact form of the particle distribution function in velocity space is neglected. Two populations of plasma particles may have entirely different distribution functions $f(\mathbf{v})$ at a particular location - and hence different kinetic behaviours - however

both would be treated equivalently by a fluid scheme provided that the integrals over the $f(\mathbf{v})$ s in velocity space in each case were equal. A kinetic treatment is also required in situations for which the spatial scales under consideration were close to or less than the gyrorotational radii for the plasma species, meaning that the guiding-centre approach is no longer valid. Several kinetic effects which make an important contribution to ionospheric F-region wave dynamics are outlined below. The derivations for these are rather long and involved and so are only briefly described here, but can be found in more detail in [Chen, 1984] and other textbooks.

1.4.4.1 Landau Damping

Landau damping is a collisionless transfer of energy from an electromagnetic wave to particles in the plasma or *vice-versa*, and occurs when the phase velocity of the wave is close to the thermal velocity of the particles. Such wave-particle interaction is not well-described by a fluid formulation and must be evaluated using a kinetic scheme. To analyse this effect, the collisionless Vlasov equation (1.39) for electrons is linearised such that any perturbation to the particle distribution function due to wave propagation is assumed to be small compared to the undisturbed background distribution ($f_{e,i} = f_{e,i0} + f_{e,i1}$ where $|f_{e,i0}| \gg |f_{e,i1}|$) to give:

$$\frac{\partial}{\partial t} f_1 [\mathbf{r}(t), \mathbf{v}(t), t] = \frac{e}{m} \mathbf{E} [\mathbf{r}(t), t] \cdot \frac{\partial f_0 [\mathbf{v}(t)]}{\partial \mathbf{v}(t)} \quad (1.97)$$

where \mathbf{E} is the electric field of the EM wave and the plasma is assumed to be unmagnetised for simplicity. In the limit that the ions are static and any plasma perturbations are plane waves propagating in the x -direction only, such that $f \propto e^{-i(\omega t - kx)}$, the time-harmonic version of equation (1.97) becomes:

$$-i\omega f_1 + ikv_x f_1 = \frac{e}{m} \mathbf{E}_x \cdot \frac{\partial f_0}{\partial v_x} \quad (1.98)$$

The 1D perturbation to the electron distribution can then be expressed as:

$$f_1 = \frac{ieE_x}{m} \frac{\partial f_0}{\partial v_x} \left(\frac{1}{\omega - kv_x} \right) \quad (1.99)$$

This distribution can then be integrated over velocity space to give the electron number density, and combined with the frequency-domain Poisson equation $ik\varepsilon_0 E_x = -eN$ to yield a dispersion relation:

$$ik\varepsilon_0 E_x = -eN = -e \int_{-\infty}^{\infty} f_1 dv_x \quad (1.100)$$

$$\Rightarrow 1 = \frac{\omega_{pe}^2}{k^2} \int_{-\infty}^{\infty} \frac{\partial f_0}{\partial v_x} \left(\frac{1}{v_x - \omega/k} \right) dv_x \quad (1.101)$$

This expression demonstrates a resonance when the particle is moving at the phase velocity of the EM wave and $v_x = \omega/k$; in this situation the Doppler-shifted wave frequency experienced by the particle corresponds to $\omega' = \omega - kv_x = 0$. Resonant particles travelling in-phase with the wave therefore see a constant electric field amplitude rather than a rapidly-fluctuating oscillation, allowing ready and efficient exchange of energy between the particles and the wave. Physically, this means that a population of electrons with velocities slightly lower than the phase speed of an EM wave will receive energy from the wave as it propagates, causing an attenuation of the wave energy. Conversely, a beam of electrons travelling at a slightly higher velocity than the wave will lose energy to the wave, leading to a reduction of the particle energies. Though in principle this exchange of energy can happen in both directions, a Maxwellian distribution has a greater population of particles towards the low-velocity end of the distribution; on average an EM wave will lose more energy to the slow bulge of the distribution than it will gain from the fast tail, thus this interaction generally leads to *damping* of the wave under ionospheric conditions. Mathematically, the damping effect arises from the singularity in velocity space found at $v_x = \omega/k$ in (1.101). By treating the integral as an initial-value problem, Landau demonstrated that, under the conditions of weak damping and large phase velocity, the effect of this singularity was to introduce a negative-imaginary component to the wave frequency, hence leading to collisionless damping of the wave. A more in-depth description of this calculation can be found in the original paper [Landau, 1946], or, for example, in [Chen, 1984].

1.4.4.2 Cyclotron Damping

Additional kinetic effects appear under the influence of a magnetic field. Particles with a non-zero perpendicular velocity can experience effects connected with resonant cyclotron motion: in the case of waves of wavelength comparable to the cyclotron radius r_L , the **E** and **B** fields associated with the wave can distort the gyrorotational orbits of the particles and lead to resonant damping, or the excitement of harmonic cyclotron plasma waves known as *Bernstein modes*. In the fluid limit, kr_L is small and these gyroharmonic effects disappear.

To analyse this effect, the collisionless Vlasov equation for magnetised plasma (1.39) is linearised to give:

$$\frac{\partial}{\partial t} f_{a1} [\mathbf{r}(t), \mathbf{v}_a(t), t] = -\frac{e_a}{m_a} \{ \mathbf{E}_1 [\mathbf{r}(t), t] + \mathbf{v}_a(t) \times \mathbf{B}_1 [\mathbf{r}(t), t] \} \cdot \frac{\partial f_{a0} [\mathbf{v}_a(t)]}{\partial \mathbf{v}_a(t)} \quad (1.102)$$

where \mathbf{E}_1 and \mathbf{B}_1 are the EM fields associated with the wave, and $a = e, i$ for electrons and ions. As it has been assumed that perturbations to the distribution functions are small, particle displacement due to gyromotion can be approximated by that experienced in uniform magnetic field \mathbf{B}_0 , thus velocities and positions can be expressed as:

$$r_\perp(t) = r_L \sin(\omega_c t + \psi) \quad r_\parallel(t) = v_\parallel t \quad (1.103)$$

$$v_\perp(t) = -v_\perp \cos(\omega_c t + \psi) \quad v_\parallel(t) = v_\parallel \quad (1.104)$$

where gyroradius $r_L = v_\perp/\omega_c$ and ψ is a phase constant. Assuming plane wave solutions and looking only at ES waves with $\mathbf{B}_1 = 0$ gives:

$$f_{a1} [\mathbf{v}_a] = -\frac{e_a \mathbf{E}_1 (\mathbf{k}, \omega)}{\omega m_a} \cdot \int_0^\infty dt' e^{i[\omega t' - \frac{k_\perp v_{a\perp}}{\omega c a} \sin(\omega c a t' + \psi') - k_\parallel v_{a\parallel} t']} \frac{\partial f_{a0} [\mathbf{v}_a(t)]}{\partial \mathbf{v}_a(t)} \quad (1.105)$$

where the integration is over the whole time history of the system (i.e. t between $-\infty$ and τ , followed by the substitution $t' = \tau - t$). This expression for the particle distribution can then be integrated over velocity phase space to find an expression for the plane-wave current density perturbation, assuming a two-component electron/ion plasma:

$$\mathbf{J}_1 (\mathbf{k}, \omega) = \sum_{a=e,i} e_a N_a \int_0^\infty \int_{-\infty}^\infty \int_0^{2\pi} v_{a\perp} dv_{a\perp} dv_{a\parallel} d\psi' f_{a1} (\mathbf{v}_a) \quad (1.106)$$

Combining (1.106) with equation (1.53) yields (after much algebra: see [Baumjohann and Treumann, 1996] Appendix A.6 for details) a kinetic expression for the dielectric permittivity:

$$\varepsilon(\mathbf{k}, \omega) = 1 - \sum_a \sum_{j=-\infty}^{+\infty} \frac{2\pi\omega_{pa}^2}{N_{0a}k^2} \int_0^\infty \int_{-\infty}^\infty v_{a\perp} dv_{a\perp} dv_{a\parallel} \left(k_\parallel \frac{\partial f_{0a}}{\partial v_{a\parallel}} + \frac{j\omega_{ca}}{v_{a\perp}} \frac{\partial f_{0a}}{\partial v_{a\perp}} \right) \frac{J_j^2 \left(\frac{k_\perp v_{a\perp}}{\omega_{ca}} \right)}{k_\parallel v_{a\parallel} + j\omega_{ca} - \omega} \quad (1.107)$$

where J_j are the Bessel functions of the first kind. As this derivation assumes ES waves ($\mathbf{B}_1 = 0$), the permittivity tensor cross terms drop out leaving only a scalar quantity.

This expression demonstrates a resonance at $\omega - k_\parallel v_\parallel - j\omega_{ca}$, where j is an integer. In the non-magnetised case, this corresponds to the Landau resonance at $\omega = kv$: a resonance that occurs for particles with velocities matching the phase velocity of the wave. In the magnetised case, resonances also occur when the Doppler-shifted frequency experienced by a particle travelling parallel to the field, ω' , matches one of the gyroharmonic frequencies, such that $\omega' = (\omega - k_\parallel v_\parallel) = j\omega_c$. Physically, this represents a particle travelling in phase with the wave such that perpendicular component of the wave's E-field ($\mathbf{E}_{1\perp}$) as experienced by the particle, oscillates at a harmonic of the appropriate cyclotron frequency. This can lead to efficient transfer of the wave energy to the particles and *cyclotron damping*. Unlike in the Landau damping case, the transfer of energy is in a direction perpendicular to the component of velocity responsible for meeting the resonance condition.

1.4.4.3 Bernstein Waves

Dispersion relations for kinetic ES plasma waves can be derived by setting the permittivity expression (1.107) to zero and assuming a form for the distribution function f_0 . Here a thermal-equilibrium Maxwellian function is used, however the dispersion relation would still be valid for any appropriate distribution. In the limit of parallel propagation ($k_\perp = 0$ and $k_\parallel = k$), the dispersion relation simply returns the Langmuir electron plasma wave and ion-acoustic wave encountered in the fluid description above, albeit with kinetic corrections at short wavelengths. In perpendicular propagation limit

however, a new flavour of electrostatic wave modes emerges: kinetic cyclotron-harmonic *Bernstein* waves. Using $k_{\parallel} = 0$ and $k_{\perp} = k$ and assuming static ions allows (1.107) to be manipulated (see [Chen, 1984] for the steps) to give a dispersion relation for perpendicular kinetic ES electron waves:

$$1 - \left(\frac{\omega_{pe}}{\omega_{ce}} \right)^2 \sum_{j=1}^{\infty} \frac{2je^{-b} I_j(b)}{\frac{b}{\omega_{ce}^2} (\omega^2 - j^2 \omega_{ce}^2)} = \varepsilon(\mathbf{k}, \omega) = 0 \quad (1.108)$$

where I_j are the modified Bessel functions and $b = k_{\perp}^2 v_{Te}^2 / 2\omega_{ce}^2 = k_{\perp}^2 r_L^2 / 2$. In the fluid limit of $k_{\perp}^2 r_L^2 \rightarrow 0$ only the $j = 1$ term survives, leaving the cold plasma upper-hybrid oscillation expression.

This dispersion relation is plotted in Figure 1.9 for several values of the ratio $(\omega_{pe}/\omega_{ce})^2$. Where in the fluid case the only perpendicular electron mode was the upper-hybrid wave, the kinetic approach reveals successive bands of electrostatic modes located close to the gyroharmonic frequencies. For each value of $(\omega_{pe}/\omega_{ce})^2$, the upper-hybrid branch is preserved and can be identified as the mode crossing $k_{\perp} = 0$ between gyroharmonic resonance frequencies (the cold-plasma upper-hybrid frequency $\omega_{UH}^2 = \omega_{pe}^2 + \omega_{ce}^2$ is indicated for each $\omega_{pe}^2/\omega_{ce}^2$ by a circular marker). The dispersive behaviour of the Bernstein waves differs depending on whether the wave frequency is below or above the upper-hybrid band: below the UH band, the Bernstein mode dispersion branch approaches the gyroharmonic frequency from beneath as $k_{\perp} \rightarrow 0$; while conversely, branches lying at higher frequencies than the UH band tend towards the gyroharmonic from above as $k_{\perp} \rightarrow 0$. This banded configuration leads to frequency cut-out regions at each $(\omega_{pe}/\omega_{ce})^2$ for which Bernstein modes cannot propagate. The dispersion relation for individual electron Bernstein waves can be expressed as (1.109) [Chen, 1984]:

$$\omega_{EB_j} = j\omega_{ce} \left[1 + 2 \left(\frac{\omega_{pe}}{\omega_{ce}} \right)^2 \frac{e^{-b} I_j(b)}{b} \right]^{\frac{1}{2}} \quad (1.109)$$

where index j refers to the mode associated with the j^{th} cyclotron harmonic.

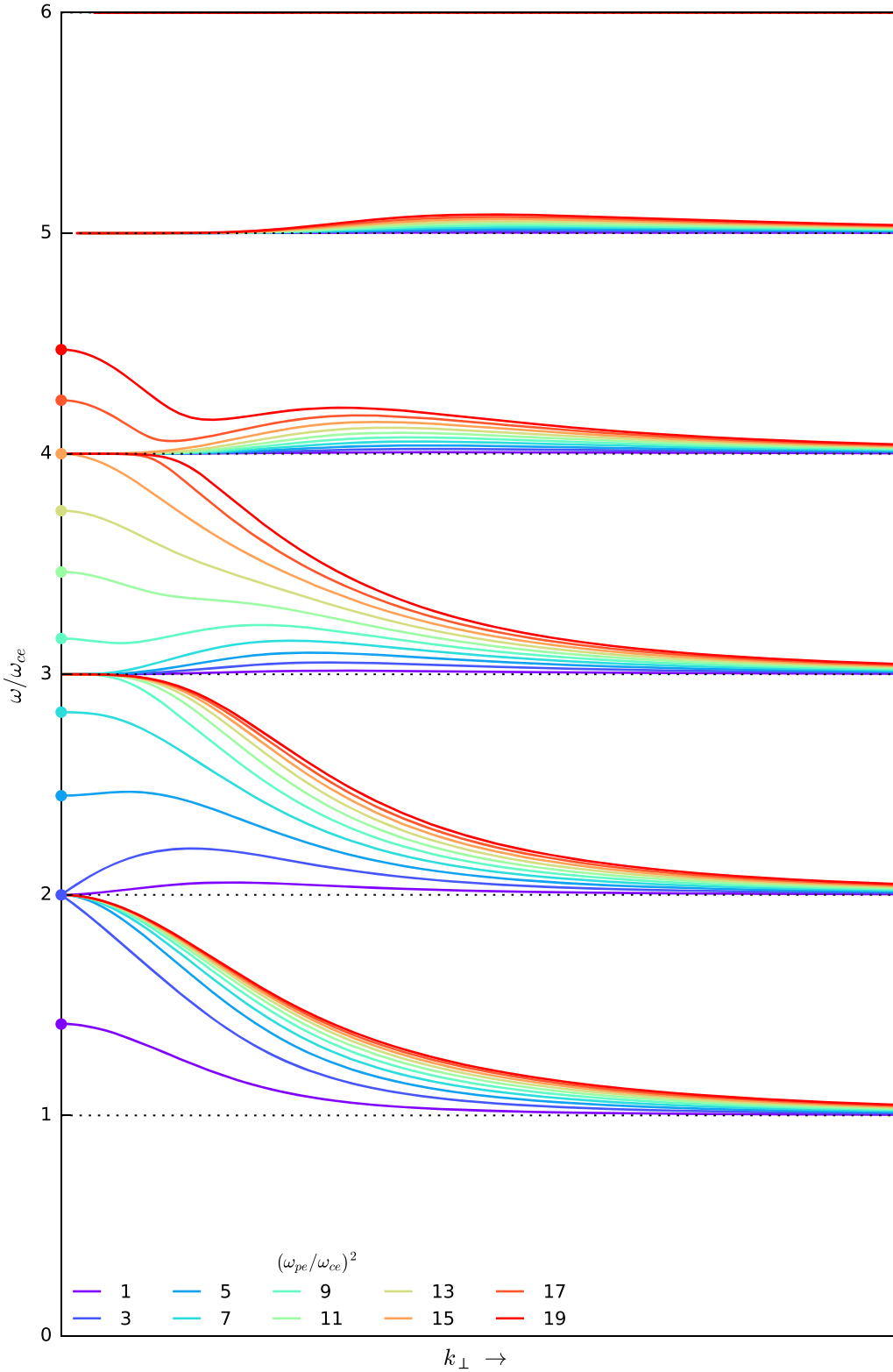


FIGURE 1.9: Dispersion relation for kinetic perpendicular ES electron waves in a magnetised, collisionless plasma, plotted for several values of the ratio $(\omega_{pe}/\omega_{ce})^2$. Several successive bands of electrostatic Bernstein modes can be seen located close to the gyroharmonic frequencies. For each value of $(\omega_{pe}/\omega_{ce})^2$, the upper-hybrid branch is preserved and can be identified as the mode crossing $k_\perp = 0$ between gyroharmonic resonance frequencies (the cold-plasma upper-hybrid frequency $\omega_{UH}^2 = \omega_{pe}^2 + \omega_{ce}^2$ is indicated for each $\omega_{pe}^2/\omega_{ce}^2$ by a circular marker). The dispersive behaviour of the Bernstein waves can be seen to differ depending on whether the wave frequency is below or above the UH band.

1.5 Earth’s Ionosphere and Near-Space Environment

Plasma mechanics are crucial to understanding near-Earth space physics, governing processes that range from high-energy interactions in the Sun to the dynamics of the Earth’s ionosphere. In this section, the geophysical plasmas that constitute the Sun-Earth system and the plasma morphology of the Earth’s ionosphere are described briefly, to give some background context for the simulation studies outlined in subsequent Chapters.

1.5.1 The Sun-Earth System: Basic Structure

The Sun ejects a high-velocity plasma consisting mostly of electrons and ionised protons into the interplanetary space as a consequence of supersonic expansion of the solar corona: this is known as the *Solar Wind* (SW). The SW plasma is highly conductive, and as a result the magnetic field lines from the Sun are “frozen-in” to the plasma and transported outwards from the Sun along with the SW outflow to form the *Interplanetary Magnetic Field* (IMF). The plasma is emitted in an approximately radial direction, which, when combined with the axial rotation of the Sun, produces a characteristic spiral configuration of solar wind propagating outwards from the Sun into interplanetary space (first described in [Parker, 1958]). Typical SW conditions close to Earth (as reported in [Baumjohann and Treumann, 1996], Chapter 1.2) are $N_e \simeq 5 \times 10^6 m^{-3}$ and $T_e \simeq 10^5 K$, with an IMF magnitude of $|B_{SW}| \simeq 5 \times 10^{-9} T$.

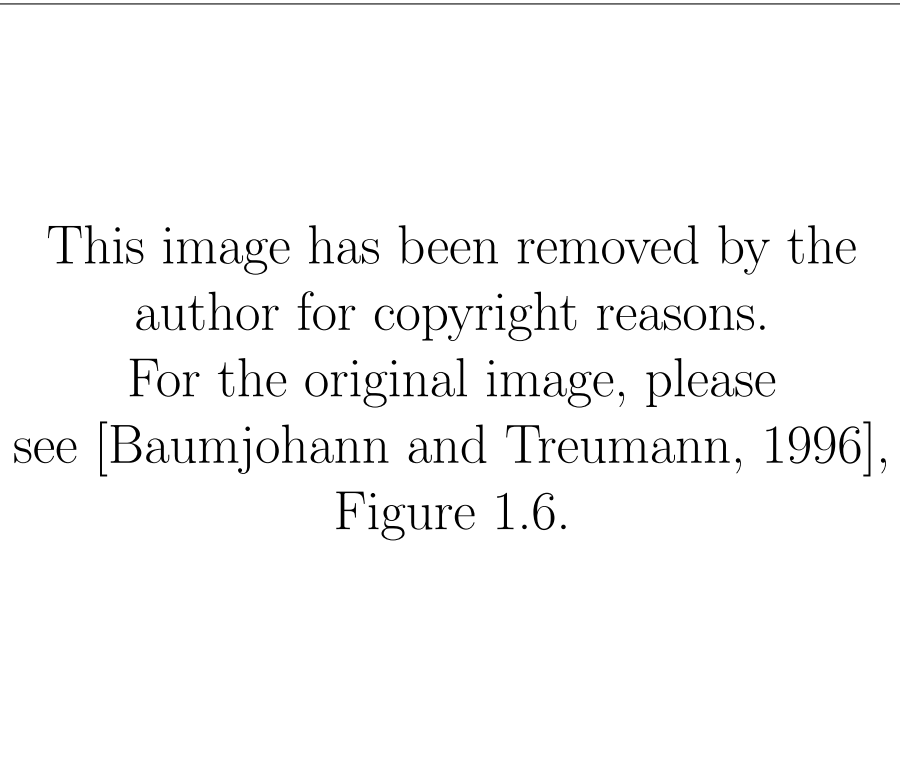
The Earth produces an intrinsic magnetic field as a result of dynamo-like effect of its molten-fluid outer core. Free from external perturbation, this field would take a dipolar configuration, tilted with respect to the Earth’s axis of rotation. In reality, the spatial distribution of this field is heavily influenced through interaction with the IMF, as shown schematically in Figure 1.10. As the IMF is carried towards the Earth via the solar wind, it is unable to pass directly over the dipole field but is instead slowed down or deflected around it, causing a compression of the day-side (sun-facing) dipole field and an stretching of the night-side dipole field lines (leading to an elongated dipole “tail” structure). The rapid deceleration of the supersonic solar wind plasma to subsonic velocities and resultant compression of field lines where the IMF meets the dipole field

This image has been removed by the author for copyright reasons.
For the original image, please see [Baumjohann and Treumann, 1996], Figure 1.4.

FIGURE 1.10: Schematic representation of the plasma and magnetic field structure of the Sun-Earth system. Solid lines indicate the magnetic field.
Image credit: [Baumjohann and Treumann, 1996]

causes a shock region to develop known as the *bow shock*. Beyond the bow shock is a region of slow plasma where a significant fraction of the incident SW kinetic energy has been converted to thermal energy on encountering the shock region, known as the *magnetosheath*. The thermalised plasma in this region is of greater temperature and density than the incoming SW plasma [Baumjohann and Treumann, 1996].

The SW plasma and frozen-in IMF cannot easily penetrate the Earth's dipole field and is instead deflected around it, leading to the distorted dipole and elongated *magnetotail* structure shown in Figure 1.10. The magnetic boundary between the solar wind and the region dominated by the Earth's magnetic field (the *magnetosphere*) is known as the *magnetopause*. Within the magnetosphere, the plasma is non-uniform and organised into distinct structures, including: the energetic *radiation belts* which consist of trapped electrons and ions drifting along field lines and oscillating between the hemispherical poles, with typical parameters $N_e \simeq 1 \times 10^6 m^{-3}$ and $T_e \simeq 5 \times 10^7 K$ [Baumjohann and Treumann, 1996]; the concentrated *plasma sheet* running along the magnetotail central plane and extending to the high-latitude ionosphere close to the magnetic poles (typical



This image has been removed by the author for copyright reasons.

For the original image, please see [Baumjohann and Treumann, 1996], Figure 1.6.

FIGURE 1.11: Schematic representation of the main current systems existing in the Earth's magnetosphere.

Image credit: [Baumjohann and Treumann, 1996]

parameters $N_e \simeq 5 \times 10^5 m^{-3}$ and $T_e \simeq 5 \times 10^6 K$ [Baumjohann and Treumann, 1996]); and the less dense surrounding *lobe* material (typical parameters $N_e \simeq 1 \times 10^4 m^{-3}$ and $T_e \simeq 5 \times 10^5 K$ [Baumjohann and Treumann, 1996]). Closer to the Earth, over an altitude range of $\sim 60 - 1000 km$, incident ultraviolet solar radiation and energetic particles ionise the neutral atmosphere at a higher rate than the recombination rate for charged particles, creating a permanent weak plasma layer known as the *ionosphere* with typical parameters $N_e \simeq 1 \times 10^8 - 10^{12} m^{-3}$ and $T_e \simeq 1 \times 10^3 K$ [Baumjohann and Treumann, 1996].

Exchange of material between the solar wind and the inner magnetosphere occurs via reconnection in the dayside magnetosphere and in the tail. Energetic particles injected into the plasma sheet can travel along field lines to the high-latitude poles and precipitate into the ionosphere; collisions between high-energy precipitant particles and ionospheric plasma can cause intense electromagnetic emission in the visual spectrum and leads to the observed *aurora*. The magnetosphere supports an intricate range of coupled currents

This image has been removed by the author for copyright reasons.
For the original image, please see [Hunsucker and Hargreaves, 2002], Figure 1.4.

FIGURE 1.12: Typical ionospheric vertical electron density profile at moderate solar activity, shown for day-time and night-time conditions, for the cases of solar-cycle maximum (solid lines) and solar-cycle minimum (dashed lines).

Image credit: [Hunsucker and Hargreaves, 2002]

due to the differential drift motions of electrons and positive ions under certain stimuli, as shown schematically in Figure 1.11. Exchange of energy and momentum between the ionosphere and the outer plasma layers can occur via field-aligned currents. These currents close in the high-latitude region of the ionosphere, where geomagnetic field lines associated with the plasma sheet and lobe penetrate the ionospheric plasma, and connect the magnetospheric current systems with those in the polar ionosphere.

1.5.2 The Ionosphere

The Earth's neutral upper atmosphere ($\gtrsim 60\text{km}$) is dominated by the molecules N_2 , O_2 and atomic O, along with minor contributions from He, Ar, NO, CO_2 and others, each with a vertical density structure and relative abundance arising largely as a result of the interplay between the gravity-driven pressure balance, thermal energy input from the sun and various chemical interactions between species. Neutral species can be ionised by incoming solar radiation, primarily in the UV ($\lambda = 100 - 200 \times 10^{-9}\text{m}$), EUV ($\lambda = 10 - 100 \times 10^{-9}\text{m}$) and X-ray ($\lambda = 0.1 - 10 \times 10^{-9}\text{m}$) bands of the spectrum

This image has been removed by the author for copyright reasons.

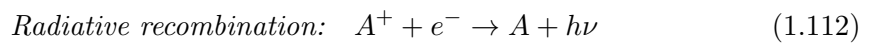
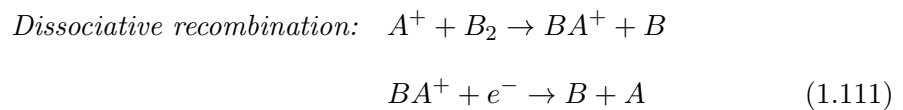
For the original image, please see [Brekke, 1997].

FIGURE 1.13: Typical vertical temperature profiles for ionospheric electrons, ions and neutral species *Image credit: [Brekke, 1997]*

through a *photoionisation* process [Kelley, 1989]:



where A is a neutral species and $h\nu$ represents a photon of frequency ν . Ion production can also occur via collisional ionisation of a neutral particle by incident energetic particles injected from the solar wind or magnetosphere. Free electrons and ions can subsequently recombine by a variety of processes, the most favourable of which under ionospheric conditions being *dissociative recombination* and *radiative recombination* [Kelley, 1989]:



Over altitudes around $\sim 60 - 1000\text{ km}$, ionisation occurs more rapidly than recombination and leads to the formation of the quasineutral layer of free electrons and positive ions that comprises the ionosphere. The ionisation fraction of the ionospheric layer is small compared to that found in the magnetosphere or solar wind, with the plasma

dominated by the neutral component. The ratio of electron (or ion) density to neutral density in the ionosphere varies greatly with altitude, as can be inferred from, for example, Figure 1.2 of [Kelley, 1989], and would also be expected to vary with solar conditions and latitude, but is typically far lower than 1%. In Figure 1.2 of [Kelley, 1989], the International Solar Quiet Year daytime composition of ionospheric electrons, ions and neutral species as measured at White Sands, New Mexico, is plotted - under these conditions the ionisation ratio to ranges from around 10^{-8} or less at lower altitudes (D-region) to approximately 10^{-4} at the F-region peak. Nevertheless, the weak ionospheric plasma has a great influence on the propagation of electromagnetic waves in the upper atmosphere; the fundamental frequency of plasma oscillation in the ionosphere is typically in the radio-frequency range, meaning that incident radio waves can experience strong reflection or refractive effects. The fine-structure morphology of the ionosphere is governed by the delicate balance between plasma production and loss processes, leading to the layered vertical structure shown in Figure 1.12. There is an excess energy associated with photoionisation process (1.110) which is translated to the reaction products as kinetic energy, and causes heating of the ionospheric plasma and in particular the electrons. Collisions between the energised species and other plasma or neutral particles acts to increase the temperature of both the plasma and neutral background; this heating is balanced by cooling processes such as thermal transport, plasma convection and radiative cooling to produce the typical vertical temperature structure depicted in Figure 1.13. As the plasma production mechanisms are highly dependent on incident radiation from the Sun, the ionospheric density and temperature profiles vary on a daily cycle, with greater plasma densities and temperatures generally occurring during the daytime conditions when the solar radiation is most intense. Seasonal variations and a longer-term variability connected with the 11-year solar cycle have also been observed.

The ionospheric layers shown in Figure 1.12 are typically referred to, in ascending altitude, as the *D*, *E*, *F1* and *F2* layers. Typical values of the plasma parameters characteristic to each layer are listed in Table 1.1. A detailed discussion of the various chemical and transport processes responsible for this distinctive structure can be found in, for example: [Kelley, 1989] or [Hunsucker and Hargreaves, 2002].

Layer	Altitude	Electron Density
<i>D</i>	60 – 90 km	$10^8 – 10^{10} \text{ m}^{-3}$
<i>E</i>	90 – 150 km	$10^{10} – 10^{11} \text{ m}^{-3}$
<i>F1</i>	150 – 180 km	$10^{11} – 10^{12} \text{ m}^{-3}$
<i>F2</i>	180 – 500+ km; peak at ~ 250 km	$> 10^{12} \text{ m}^{-3}$

TABLE 1.1: Parameters typical to the daytime ionosphere

The *D-region* occurs over an altitude range of 60 – 90 km and generally consists of plasma at a lower density and temperature than the upper layers. The neutral density is comparatively high, meaning that plasma-neutral collisions are more frequent, and consequently this region can be very effective at absorbing incident EM waves.

The ionospheric plasma density generally increases with altitude to a peak in the *F2-region* at an altitude between $\sim 200 – 300$ km. For a ground-launched radio wave to escape the ionosphere, it must have a frequency greater than the electron plasma frequency at the peak; any waves with a frequency below the peak will be reflected at a lower altitude.

1.6 Ionospheric Modification Experiments

Understanding the mechanics of the ionosphere is crucial to the communications industry: radio waves must cope with its reflective and refractive properties, satellite signals must pass through it; without a thorough understanding of the way the ionosphere affects EM wave propagation, technology such as GPS would not be viable. Study of the ionosphere also presents the opportunity to investigate fundamental plasma physics over huge scale lengths and observe the myriad of diverse waves and instabilities the ionosphere is capable of supporting. The ionosphere can be treated effectively as a vast plasma laboratory where experiments can be performed without the scale length limitations or edge effects of an artificial lab-plasma. To this end, facilities such as

Sura, EISCAT (European Incoherent Scatter), HAARP (High Frequency Active Auroral Research Program), Aricebo, and others have been used to conduct artificial ionospheric modification (“heating”) campaigns. In these experiments, high-power electromagnetic waves are launched from ground-based transmitters to perturb the ionosphere and exploit its natural suitability as an unbounded laboratory in which to study plasma physics. Wave frequencies in the radio band are most often used, as these correspond most closely to the various wave and oscillation modes occurring at ionospheric plasma densities. The resulting interaction between the EM “pump” wave and the ionospheric plasma can then be observed via a number of channels: UHF/VHF incoherent scatter radar is used to measure the plasma density and temperature; optical instruments are used to measure the visible-spectrum airglow produced via high-energy particle collisions; spectrum analysers are used to monitor the *stimulated electromagnetic emission* (SEE) signal emerging from the heated region. Below are summarised a selection of the many plasma phenomena and instabilities observed over several decades of ionospheric F-region heating experiments, with a focus on those which will be explored in through numerical simulation later in this thesis. This summary focuses on the high-latitude northern-hemisphere region, and as its main sources draws from the EISCAT-focused review papers by [Rietveld et al., 1993] and [Robinson, 1989].

1.6.1 E-Field Amplitude Swelling

As shown in Section 1.4.1.3, the altitude at which an EM wave reflects is dependent on the wave polarisation and its frequency relative to the electron oscillation frequency in the ionospheric plasma. An O-mode polarised wave will reflect at the altitude corresponding to $X = 1$, while an X-mode polarised wave will reflect at $X = 1 \pm Y$ (a ground-launched X-mode wave will thus not be able to penetrate beyond $X = 1 - Y$). Heating for which the ionosphere peak density is sufficiently low that the pump wave never reflects is referred to as *underdense*. As the wave approaches its reflection height, its group velocity tends to zero and thus its energy density approaches infinity, causing significant swelling of the wave amplitude. This amplitude swelling effect, combined

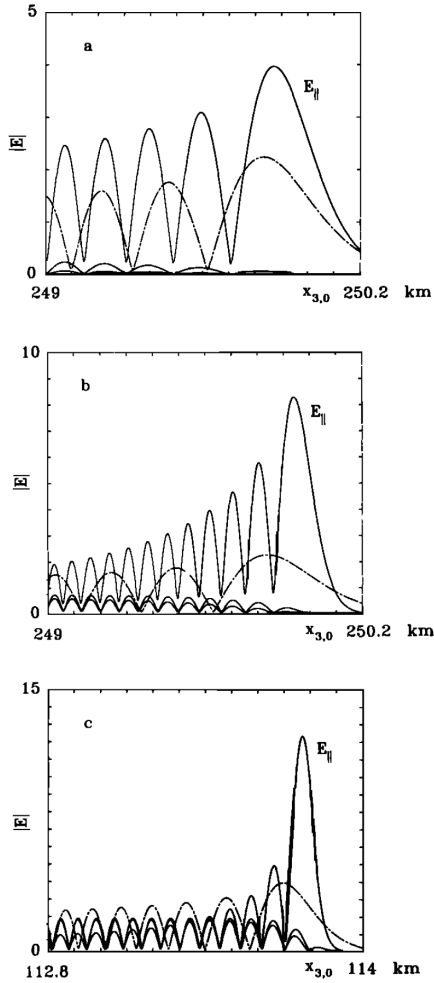


FIGURE 1.14: Calculated growth of a high-amplitude E-field standing wave produced as an O-mode pump wave approaches the reflection height at $x_{3,0}$ in a vertically-inhomogeneous ionosphere. From top to bottom, the panels show the fields calculated by [Lundborg and Thidé, 1986] for the cases of EM wave frequencies $f_0 = 5.13, 5.423$, and 3.515 MHz , electron cyclotron frequencies $f_{ce} = 1.1, 1.3$, and 1.4 MHz and magnetic dip angles $\alpha = 42^\circ, 13^\circ$, and 13° . Indicated in the plots are the parallel E-field amplitude (solid line), the perpendicular amplitudes (bold-ish lines) and the E-field pattern for the case of no geomagnetic field (dot-dashed line).

Image credit: [Lundborg and Thidé, 1986]

with the field of the reflected pump wave, leads to the formation of a Airy-like spatially-periodic standing wave in the region just below the reflection level, with a maximum amplitude well in excess of the incident pump wave amplitude. This effect is demonstrated by the examples in Figure 1.14, which show the standing wave amplitude as calculated by [Lundborg and Thidé, 1986] for the conditions of Aricebo (top), Tromsø F-region (centre), and Tromsø E-region (bottom). The swollen amplitude due to reflection is an important factor in artificial ionospheric modification, as the increased E-field

allows for significant perturbation of the plasma through collisional Ohmic heating processes, and may allow the threshold for several instabilities which contribute greatly to heating-induced modifications to be exceeded. Formation of the standing wave in accordance with the theoretical calculations of [Lundborg and Thidé, 1986] will be used to validate the newly-developed numerical simulation code in Chapter 3.

Particles may also experience a nonlinear drift force due to the non-uniformity of the electric field known as the *ponderomotive force*, effectively a nonlinear coupling of the radiation-induced pressure with the plasma motion. This force is proportional to $-\frac{\omega_p^2}{\omega^2} \nabla |E|^2$ [Chen, 1984] and acts independently of charge. A consequence of this effect is that in regions of sharply increasing E-field, the ponderomotive force acts to expel plasma from the local area, causing depletion of the plasma medium and acceleration of electrons (the force acts more strongly on electrons than ions due to the ω_p^2 dependence; the effects of the force are mostly translated to the ions via the electron response).

1.6.2 Linear Mode Conversion

As shown in Section 1.4.1.3, Figure 1.6, at plasma densities corresponding to the O-mode wave reflection height ($X = 1$) the O-mode wave can convert to the upper branch of the X-mode wave, often referred to as the *Z-mode* wave or *slow X-mode* (see, for example, [Mjølhus, 1984], [Gondarenko et al., 2003]). This phenomenon is an example of *linear mode conversion*, and can only occur for incident wave propagation vectors which are close to parallel to the geomagnetic field as the wave reaches the $X = 1$ conversion region. The term “linear” conversion refers to the fact that energy is transferred linearly from one mode to the other (in this case from the O-mode to the Z-mode) and does not rely on feedback from the plasma in order to proceed. In a non-linear conversion process such as a parametric instability (see 1.6.4 below), the conversion process often relies on the response of the plasma to an initial perturbation to create a feedback loop, leading to conditions that encourage the growth of an instability and efficient transferal of energy from the initial wave mode(s) to one or more daughter modes. This non-linear process can require the fulfillment of wavenumber- and frequency-matching criteria before it can

proceed efficiently. In the linear case, no such mechanism is required; conversion can occur when the dispersion curves for the modes intersect, as is the case for the O-mode and Z-mode branches for waves with \mathbf{k} parallel to the geomagnetic field at $X = 1$ (see Figure 1.6).

A ground-launched O-mode wave will experience refraction as it propagates through the inhomogeneous, anisotropic ionosphere, bending its path and altering the direction of its propagation vector as it travels upwards. For linear mode conversion to occur, the wave must be launched at a critical angle, θ_{Sp} known as the *Spitze angle* [Mjølhus, 1990]:

$$\theta_{Sp} = \arcsin \left[\left(\frac{Y}{Y+1} \right)^{\frac{1}{2}} \sin(\alpha) \right] \quad (1.113)$$

which takes into account the refraction of the upwards-travelling pump wave assuming a one-dimensional electron density variation in the vertical ($\theta = 0^\circ$) direction only and a magnetic field dip angle α . The dependence of mode propagation on pump wave angle leads to the observable *radio window*: a range of inclination angles for which a ground-launched O-mode wave, rather than reflecting, will be able to penetrate beyond $X = 1$ and reach normally-inaccessible regions of the ionosphere. When the electron density varies in more than one dimension (for example, when field-aligned density irregularities are present), the range of critical angles comprising the radio window is almost impossible to calculate analytically without resorting to a heavy regime of approximation, and instead must be analysed numerically; this process will be investigated for the case of several types of two-dimensional density irregularities as part of the simulation work presented in Chapter 4. The term “linear conversion” can also be used to refer to the direct conversion of any pump wave to an electrostatic wave mode, such as the conversion of the O-mode wave to upper-hybrid waves in the presence of density striations discussed in 1.6.5 below.

1.6.3 Plasma Modification

F-region heating experiments have been shown to cause significant large-scale perturbation to the plasma medium. As defined by [Gurevich, 1978, Robinson, 1989], the term

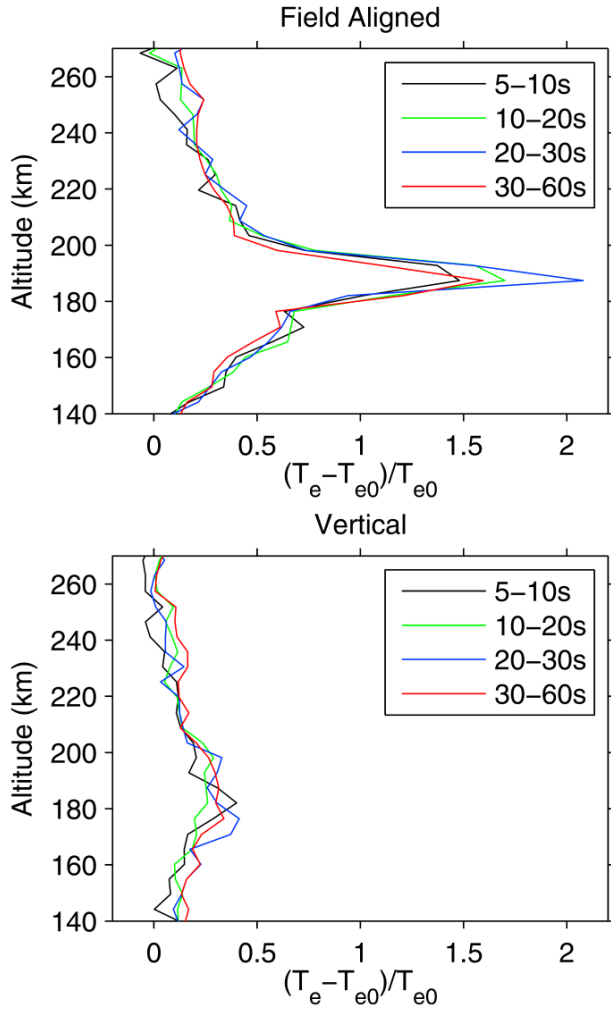


FIGURE 1.15: Electron temperature enhancement variation with time as reported by [Honary et al., 2011] for an O-mode heating experiment performed at EISCAT on 27 September 2007. For the results shown in the upper panel, the heater pump wave was directed along the local geomagnetic field direction; for the results in the lower panel, it was directed vertically along the electron density gradient. The large variation in perturbed temperature with heater direction demonstrates the *Magnetic Zenith Effect*.

Image credit: [Honary et al., 2011]

“large-scale” in this context corresponds to structures with a scale-size of $\sim 10\text{ km}$ or greater perpendicular to the geomagnetic field direction (on the so-called *thermal* scale). As plasma transport processes are more efficient parallel to the field, these features commonly exhibit parallel spatial proportions many times larger than their perpendicular extent. Large-scale plasma modifications commonly observed include significant enhancement of the electron temperature in the heated region, as reported by [Gordon and Carlson, 1974, Meltz et al., 1974, Djuth et al., 1987, Stocker et al., 1992, Honary

et al., 1993] and others. Contributing mechanisms behind this enhanced temperature could include collisional dissipation of the high-amplitude pump standing wave, and “anomalous” absorption of plasma waves excited via one or more of the instabilities described below. The ponderomotive force is enhanced close to the pump wave reflection height due to the high-amplitude standing wave, and can also contribute to large-scale, nonlinear modification of the plasma in the heated volume. Heating experiments at EISCAT frequently observe electron temperature increases in the range $\sim 2 - 3$ times the undisturbed temperature or greater, as shown by Figure 1.15 (reproduced here from [Honary et al., 2011]). Large-scale temperature enhancement has been observed to depend strongly on the inclination angle of the incident EM pump wave relative to both the direction of electron density variation and the geomagnetic field direction [Honary et al., 2011, Kosch et al., 2000, Pedersen et al., 2003]; electron temperatures observed during geomagnetic field-aligned heating have been observed to be a factor of 2 or greater than those observed during vertically-aligned heating under similar conditions [Rietveld et al., 2003, Dhillon and Robinson, 2005, Honary et al., 2011], as shown by the comparison in Figure 1.15. This angular dependence is a defining characteristic of the *Magnetic Zenith Effect*, which will be investigated in more detail through numerical simulation in Chapter 4.

Substantial changes to the electron density have also been commonly observed on a diverse hierarchy of spatial scales, from large-scale density depletions in the heated region [Gurevich et al., 2002] to small-scale irregularities aligned with the geomagnetic field and having perpendicular scale sizes ranging from a few metres down to a few centimetres, as detected by rockets and VHF-UHF backscattering [Kelley et al., 1995]. Field-aligned irregularities of this nature play an important role in the thermal resonance instability described below and may cause *anomalous absorption* of the pump wave as described in detail in [Robinson, 1989]; close to the O-mode reflection height this anomalous absorption may dominate over collision-based absorption.

1.6.4 Parametric Instabilities

Illumination of the ionosphere using high-power EM waves can result in the excitation of a wide variety of plasma instabilities, many of which can lead to significant modification of the plasma medium. One of the most important and commonly identified instabilities is the class of nonlinear wave-wave interactions known as *parametric instabilities*, named after their theoretical similarities to the coupled-oscillator parametric amplifiers used in electrical engineering. Detailed analysis of parametric processes in the ionosphere can be found in, for example, [Fejer, 1979] or [Thidé, 1990]. In a parametric process, an initial “parent” or “pump” wave with parameters (ω_0, \mathbf{k}_0) decays into two or more daughter waves:

$$(\omega_0, \mathbf{k}_0) \rightarrow (\omega_1, \mathbf{k}_1) + (\omega_2, \mathbf{k}_2) + \dots \quad (1.114)$$

In the ionospheric-heating context the parent wave is often the initially-transmitted EM pump wave, however it could also be a high-frequency plasma wave excited by a previous interaction. In a parametric decay interaction, the following frequency and wave matching conditions must be met for the process to be viable:

$$\omega_0 = \omega_1 \pm \omega_2 \pm \dots \quad \mathbf{k}_0 = \mathbf{k}_1 \pm \mathbf{k}_2 \pm \dots \quad (1.115)$$

Examples of several parametric decay processes are shown schematically in $\omega - k$ space in Figure 1.16.

Due to the diverse range of plasma waves that may exist in the F-region, there are often several combinations of waves that allow the matching conditions (1.115) to be satisfied; one of the combinations most frequently identified during heating experiments is referred to as the *parametric decay instability* (PDI). The PDI involves decay of an incident electromagnetic pump wave to a high-frequency Langmuir electron plasma wave and an ion acoustic wave, as depicted by Figure 1.16 (B). Physically, the electron oscillations generated by the EM pump wave field couple with an acoustic disturbance in the ion density to produce an electric field (induced by the charge difference between the fast displaced electrons and the slow ions). This plasma wave field beats with the

This image has been removed by the author
for copyright reasons.

For the original image, please see [Chen,
1984], Figure 8-14.

FIGURE 1.16: Parametric wave-matching conditions for the following instabilities: (A) decay of a Langmuir electron plasma wave to an ion-acoustic wave plus a frequency-downshifted Langmuir wave (EDI / LDI); (B) decay of an EM pump wave to a Langmuir wave and an ion-acoustic wave (PDI); (C) decay of an EM pump wave to a frequency-downshifted EM wave plus an ion-acoustic wave (SBS); (D) decay of an EM pump wave to a pair of plasma waves propagating in opposite directions (TPD).

Image credit: [Chen, 1984]

ion density variation, leading to a non-uniform distribution of the E-field amplitude that enhances the ion irregularity via the ponderomotive force. Under the correct conditions, this feedback loop leads to an instability via which the EM pump wave is efficiently converted to an electron plasma wave and a travelling ion density disturbance (ion-acoustic wave). As the ion-acoustic frequency is small compared to the electron plasma frequency, the daughter Langmuir wave is only slightly downshifted in frequency with respect to the parent wave; as such this process occurs most favourably close to the O-mode reflection height, where the pump wave frequency comes close to matching the local electron frequency. In the F-region of the ionosphere, the threshold for this instability is around $\sim 0.1 \text{ V/m}$ [Stubbe and Kopka, 1981] and can be easily exceeded in the swollen-amplitude region below the O-mode reflection height. The timescale over which the instability develops is of the order $\sim 10^{-3} \text{ s}$ in this region. The Langmuir wave dissipates its energy into the local plasma with an attenuation distance ~ 1000 times

shorter than that for an O-mode pump wave in the F-region [Rietveld et al., 1993], hence the plasma wave decay component from the PDI process can be completely absorbed in a very localised region of the heated volume; this form of plasma-wave-driven anomalous absorption is understood to be one of the primary drivers of the large-scale electron temperature enhancements observed in O-mode heating experiments and is an effective mechanism for transferring the EM pump wave energy to the plasma.

Further parametric decay of the Langmuir plasma wave can occur via the *electron/Langmuir decay instability* (EDI / LDI) illustrated in Figure 1.16 (A), in which the initial pump Langmuir wave decays to an acoustic wave and a daughter Langmuir wave with a frequency slightly downshifted with respect to the parent wave (by a factor of the acoustic wave frequency). This process can occur multiple times in succession resulting in a cascade of excited plasma waves with frequencies offset from the initial heater frequency by multiples of the acoustic frequency and the formation of a *weak Langmuir turbulence* region.

A variation of the PDI process in which the low-frequency decay product is a non-propagating periodic ion density variation rather than the travelling ion-acoustic wave is known as the *oscillating two-stream instability* (OTSI). Under F-region conditions the OTSI has a higher threshold than the PDI by a factor of ~ 2 , however this is still sufficiently low that the instability is frequently observed close to the O-mode reflection region during heating experiments.

Analysis of stimulated electromagnetic emission spectra has been used to infer the existence of several other parametric decay processes, in which excited plasma wave modes decay to low frequency components plus EM radiation that can be detected by ground-based spectral analysers. For example, the downshifted maximum (DM) sideband is attributed to the decay of an upper-hybrid mode to an O-mode wave and a lower-hybrid mode [Stubbe et al., 1994], while the broad upshifted maximum (BUM) feature is thought to be the result of the four-body decay of the second harmonic of either the EM pump or upper-hybrid mode to a daughter mode close to an electron gyroharmonic frequency (either an upper-hybrid or electron Bernstein mode) and an O-mode

EM wave [Leyser et al., 1989].

Further parametric instabilities may include: decay of the EM pump wave to a high-frequency upper-hybrid or electron Bernstein wave and a low frequency acoustic or lower-hybrid wave; the *stimulated Brillouin scattering instability* (SBS), by which an EM wave decays to a frequency-downshifted EM wave plus an acoustic wave as shown in Figure 1.16 (C); and the *two-plasmon decay* (TPD) process by which an EM wave decays to two daughter plasma waves, as shown in Figure 1.16 (D).

1.6.5 Thermal Resonance Instabilities

One of the main sources of anomalous absorption of the heater pump wave is understood to be the *thermal resonance instability*. This instability is connected with the growth of small-scale field aligned irregularities around the upper-hybrid resonance (UHR) region where the frequency of the incident pump wave is close to the local upper-hybrid wave frequency (this occurs at $X = 1 - Y^2$). In this region, upper-hybrid waves propagating in a direction perpendicular to the geomagnetic field are readily excited [Wong et al., 1981, Dysthe et al., 1982, Antani et al., 1996]. ES waves of this nature induce the formation of striations in the electron density profile, elongated along the magnetic field direction and with a comparatively small transverse scale size. Explosive heating of electron plasma local to the striations then proceeds via the nonlinear resonance instability [Gurevich et al., 2001, Gondarenko et al., 2005], as incident pump wave electric field becomes trapped in the density depletions and amplified through efficient excitation of further UH modes. Collisional damping of the trapped waves is highly efficient within the striations and leads to an increase in the local plasma temperature, and consequently to a decrease in the electron density within the irregularities. As the striations deepen, the efficiency of trapping increases, and leads to a rapid, nonlinear increase in the electron temperature around the UH resonance height. This process allows the energy of the EM pump wave to be very efficiently dissipated in the plasma around the UHR region. The timescale required for thermal instabilities of this type to develop is $\sim 1 - 10\text{ s}$. Onset of this instability requires pre-existing field-aligned density irregularities to be present in

the resonance region; these could either be naturally occurring ionospheric “noise” or produced via a prior heating-induced process such as that described by [Das and Fejer, 1979].

1.6.6 Self-Focusing Instabilities

A further instability associated with the formation of field-aligned density structures is the thermal *self-focusing instability* (SFI). Initially-small-scale density irregularities generated around the upper-hybrid resonance region reduce the local electron plasma density and have a refractive, lensing effect on the incident EM wave. This focuses the pump wave and leads to enhancement of the E-field amplitude in this region [Gurevich et al., 2001, Gondarenko et al., 2003]. Self-focusing of this nature results in further nonlinear enhancement of the electron temperature and causes the evolution of a hierarchy of density-depleted structures around the O-mode reflection height, from the small-transverse-scale (1-10s of metres) striations associated with the thermal resonance instability to self-organised bunches of striations forming soliton-like density depleted structures spanning several kilometres in transverse scale [Gurevich et al., 1998]. This increased growth of density-depleted structures further reduces the net electron density in the region and enhances the focusing effect, providing a feedback loop that powers nonlinear growth of the electron temperature around the upper-hybrid region. The timescale for this process to manifest is of order $\sim 1 \text{ min}$, making the SFI relatively slow compared to the PDI or thermal resonance processes.

Chapter 2

Introduction: Numerical Simulation

The wide and varied discipline of *computational physics* refers to any situation where a series of coupled quantitative equations are implemented in a numerical computational domain. A computational treatment can allow complex, nonlinear systems for which no analytical solution is possible to be accurately evaluated. Often it is useful to augment experimental observations with numerical simulations which allow the underlying physical mechanics to be studied at higher resolution than in a real-world experiment, allowing fine-detail investigation of dynamical behaviour. In a simulation study, the initial conditions can be precisely set, tuned and varied; background conditions are not subject to natural variation or physical noise. The myriad of complicated collective interactions which may occur in a plasma can be infeasibly difficult to describe accurately through analytical techniques, but are far more amenable to a numerical treatment. This thesis focuses on the simulation of plasma interactions and instabilities which may occur during an ionospheric modification experiment, with the aim of using computational techniques to identify and investigate the underlying physical mechanisms behind several observed phenomena.

In this Chapter, the computational foundations fundamental to these simulations are introduced. The formulation of an electromagnetic Finite-Difference Time-Domain (FDTD)

scheme, which will form the basis of the plasma simulation code described in Chapter 3 is outlined, and the factors which determine the stability, accuracy and performance of such a scheme are discussed. The introduction below draws from a number of source textbooks, primarily those by [Taflove and Hagness, 2000] and [Schneider, 2010], as well as the classic FDTD paper by [Yee, 1966]. The class of FDTD algorithm described here follows the original Yee scheme and represents the most abundantly-utilised formulation, however alternative time-stepping algorithms and gridding schemes can be used; for more details, see the textbooks listed above.

2.1 The Finite-Difference Time-Domain Method

As high-performance computing technology has evolved, rapidly gaining in potency, the Finite-Difference Time-Domain method has become an increasingly popular and powerful technique for modelling the propagation of electromagnetic waves through a variety of media. For almost 150 years following the formulation of James Clerk Maxwell's famous equations of electromagnetism, evaluation of these equations to describe the interaction of an EM wave with dispersive matter has been performed most commonly under steady-state conditions, yielding frequency-domain solutions. Such solutions are limited in application - they tend only to be relevant to specific, simple geometries, often require tedious and computationally-demanding linear algebra operations to compute, and experience difficulties modelling non-linear interactions. From around 1990, interest in finding time-domain solutions to Maxwell's equations using computational techniques began to expand rapidly. The Finite-Difference Time-Domain method is one such approach. Using a methodology first proposed by [Yee, 1966], an FDTD model simulates the fundamental EM wave interactions at a spatially discrete series of nodes in computational space, and advances the field magnitude at each node in quantised time steps, most commonly by using a "leapfrog"-style update algorithm and approximate expressions for the fundamental governing equations. FDTD has an advantage over many other simulation techniques as it deals with complex, nonlinear and impulsive interactions in a time-explicit and natural manner, avoiding complex and computationally-intense

linear-algebra calculations. The mesh-based structure allows material properties to be defined separately at each point; consequently, variations in medium properties such as composition, density, temperature and distribution can be accurately represented.

2.1.1 Discretisation and the Yee Cell

Yee's FDTD scheme replaces the temporal and spatial partial derivatives in Maxwell's time-dependent field equations (2.1) and (2.2) (shown here without currents) with second-order finite-difference approximations as described in Section 2.1.2 below.

$$\mu_0 \frac{\partial \mathbf{H}}{\partial t} = -\nabla \times \mathbf{E} \quad (2.1)$$

$$\varepsilon_0 \frac{\partial \mathbf{E}}{\partial t} = \nabla \times \mathbf{H} \quad (2.2)$$

These approximated field equations are applied to a discretised computational model of space (referred to below as the “computational domain” or “computational grid”) where electric and magnetic fields are described by a discrete grid of field nodes separated in space by quantised spatial steps and where field values are only known at quantised time steps. The nodes are offset in space and time such that fields can be sequentially updated in a leapfrog manner as the simulation steps forward in time, using the approximated fully-explicit “update” equations. For example, the update equations can be used to find E-field node values at a certain time-step using previously stored H-field values. The simulation is then advanced slightly in time, meaning that the calculated E-field values are now in the past with respect to the simulation time. These “past” values can be used by the update equations to calculate new values for all H-field components. This constitutes one full time step of the simulation. This simple cycle is repeated as the model steps forward in time, sequentially updating the field components using only “past” or “present” values of previously-updated fields stored within the computer memory to find “future” values. Yee's scheme consisted of E- and H-field nodes only; to allow the simulation of EM wave propagation through plasma, however, the model must be extended to include plasma fluid velocity, fluid temperature and density nodes also, as described in Chapter 3.

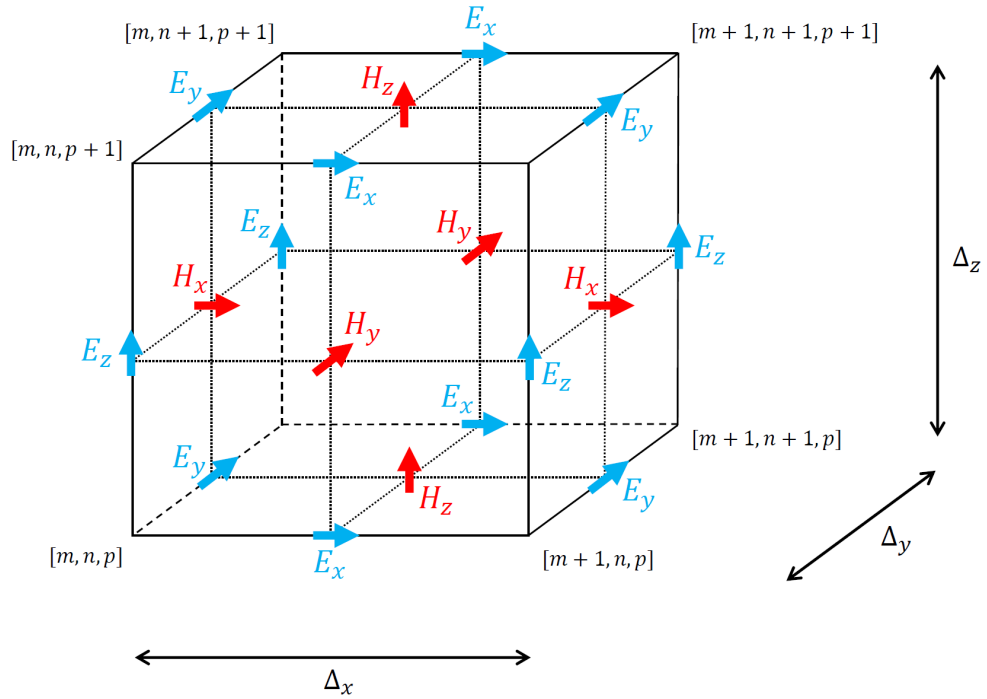


FIGURE 2.1: Schematic diagram of the fundamental Yee cell [Yee, 1966]. E-field and H-field component nodes are offset in both space and time, enabling the simulation to be advanced in time using a leapfrog-style update algorithm.

The basic unit of an FDTD scheme is the *Yee cell* [Yee, 1966] - the fundamental building block that defines the relative positions of all field nodes. The computational grid can be thought of as a repeating lattice of identical Yee cells. A schematic diagram of the basic Yee cell for EM fields is shown in Figure 2.1.

A Yee cell has dimensions Δ_x , Δ_y and Δ_z , which represent the discrete spatial steps in each Cartesian direction. These steps need not be equal, but for the purposes of this introduction uniform spatial discretisation is assumed, such that $\Delta_x = \Delta_y = \Delta_z = \Delta$. The discrete time step representing one complete cycle of field updates is represented by Δ_t . The position of a discretised field node in time and space within the computational domain can be described by integer multiples of the spatial and temporal steps. For example, the continuous-world field $E^t(x, y, z)$ describing the E-field at position (x, y, z) and time t can be expressed within the computational domain as $E^{q\Delta_t}(m\Delta_x, n\Delta_y, p\Delta_z)$, where m , n , p and q are integers. This notation is abbreviated to $E^q[m, n, p]$ for convenience. The discrete EM field node positions in the basic Yee cell, offset in both

space and time, are given by:

$$\begin{aligned} & E_x^q[m + \frac{1}{2}, n, p], E_y^q[m, n + \frac{1}{2}, p], E_z^q[m, n, p + \frac{1}{2}] \\ & H_x^{q+\frac{1}{2}}[m, n + \frac{1}{2}, p + \frac{1}{2}], H_y^{q+\frac{1}{2}}[m + \frac{1}{2}, n, p + \frac{1}{2}], H_z^{q+\frac{1}{2}}[m + \frac{1}{2}, n + \frac{1}{2}, p] \end{aligned}$$

2.1.2 Finite-Difference Approximation

The equations governing the propagation of an electromagnetic wave in a dispersive medium such as a plasma contain several coupled partial differential equations. These can prove to be difficult if not impossible to solve analytically and often require a harsh regime of assumptions to be implemented before a solution can be achieved. The FDTD method makes no attempt to solve these equations exactly; instead the spatial and temporal partial derivatives describing continuous fields are approximated to linear equations describing discrete field nodes using a centralised *finite-difference* approximation technique. The FDTD simulation then uses the approximated expressions to directly obtain numerical values for the partial derivatives, as described in Section 2.1.3 below.

To demonstrate the finite-difference approximation, consider a continuously-varying spatial function $f(x)$. Expanding $f(x)$ in a Taylor Series about the points $x_0 + \frac{\Delta}{2}$ and $x_0 - \frac{\Delta}{2}$ yields:

$$f(x_0 + \frac{\Delta}{2}) = f(x_0) + \frac{\Delta}{2} f'(x_0) + \frac{1}{2!} (\frac{\Delta}{2})^2 f''(x_0) + \frac{1}{3!} (\frac{\Delta}{2})^3 f'''(x_0) + \dots \quad (2.3)$$

$$f(x_0 - \frac{\Delta}{2}) = f(x_0) - \frac{\Delta}{2} f'(x_0) + \frac{1}{2!} (\frac{\Delta}{2})^2 f''(x_0) - \frac{1}{3!} (\frac{\Delta}{2})^3 f'''(x_0) + \dots \quad (2.4)$$

Subtracting (2.3) from (2.4) to find an expression for the first derivative $f'(x_0)$ gives:

$$f(x_0 + \frac{\Delta}{2}) - f(x_0 - \frac{\Delta}{2}) = \Delta f'(x_0) + O(\Delta^3) \quad (2.5)$$

Thus for small values of Δ , the first spatial derivative of $f(x)$ at point x_0 can be expressed as:

$$f'(x_0) \simeq \frac{f(x_0 + \frac{\Delta}{2}) - f(x_0 - \frac{\Delta}{2})}{\Delta} \quad (2.6)$$

Note that this expression does not depend on the value of $f(x)$ at point x_0 itself, but on the values of the function evaluated at nearby points $x_0 + \frac{\Delta}{2}$ and $x_0 - \frac{\Delta}{2}$. This property makes the finite-difference approximation particularly useful in a discretised spatial environment as it allows spatial partial derivatives to be expressed in terms of nearest-neighbour field nodes, where quantity Δ represents one discrete spatial step separating grid nodes. A similar method can be used to extend this technique to approximate temporal partial derivatives.

Expression (2.6) is accurate up to and including second order terms in Δ , and is thus commonly referred to as a *second-order* finite-difference approximation. Higher-order schemes with enhanced accuracy can be obtained by retaining higher-order Δ terms. For example, a fourth-order- accurate scheme can be formulated by considering the Taylor expansions of $f(x_0 + \frac{3\Delta}{2})$ and $f(x_0 - \frac{3\Delta}{2})$ and combining these in linear combinations with (2.3) from (2.4) to eliminate all f'' , f''' and f'''' terms. This leaves an expression for $f'(x_0)$ retaining all terms up to and including fourth-order in Δ [Schneider, 2010]:

$$f'(x_0) = \frac{9}{8} \frac{f(x_0 + \frac{\Delta}{2}) - f(x_0 - \frac{\Delta}{2})}{\Delta} - \frac{1}{24} \frac{f(x_0 + \frac{3\Delta}{2}) - f(x_0 - \frac{3\Delta}{2})}{\Delta} + O(\Delta^5) \quad (2.7)$$

Schemes of sixth-order accuracy or higher can be formulated in a similar manner.

In the work described here, finite-difference schemes of second-order accuracy were employed. The main motivation for this was computational efficiency; the fourth-order scheme described by (2.7) above requires the values of four field nodes to perform the calculation, as opposed to two nodes in the second-order case. Not only is the calculation larger and thus more time-consuming, it requires twice the number of memory-fetches, significantly increasing runtime and reducing performance. A fourth-order temporal derivative will require the storage of several tiers of field time-history that are not required in the second-order case. Further, the greater grid “footprint” of the higher-order finite-difference operators can lead to difficulties around the computational domain boundaries, such as when some nodes required for the calculation lie within a termination region and some in the simulation space.

2.1.3 Update Equations for Electromagnetic Waves

The classic Yee Cell shown in Figure 2.1 arranges each H-field component such that it is surrounded by a circulating pattern of E-field components and *vice versa*. This formulation allows the coupled curl equations (2.1) and (2.2) to be expressed in a 3D discretised form without the need to perform temporal or spatial averaging of nodes. To form update equations for the **H** components, the partial differentials of (2.1) are evaluated as second-order finite-difference approximations at integer timestep q about the Yee cell points $(m, n + \frac{1}{2}, p + \frac{1}{2})$, $(m + \frac{1}{2}, n, p + \frac{1}{2})$ and $(m + \frac{1}{2}, n + \frac{1}{2}, p)$ to form independent equations for H_x , H_y and H_z respectively (see, for example, [Taflove and Hagness, 2000] for more details). These can then be rearranged to form update equations for the **H** components: equations that express $H_{xyz}^{q+\frac{1}{2}}$ node values as a function of quantities at stored timesteps q and $q - \frac{1}{2}$ are shown in (2.8) below. Note that these equations, and all others that follow, assume uniform spatial grid spacing in all dimensions, such that $\Delta_x = \Delta_y = \Delta_z$.

$$\begin{aligned} \left\{ \begin{array}{l} H_x^{q+1/2}[m, n + \frac{1}{2}, p + \frac{1}{2}] \\ H_y^{q+1/2}[m + \frac{1}{2}, n, p + \frac{1}{2}] \\ H_z^{q+1/2}[m + \frac{1}{2}, n + \frac{1}{2}, p] \end{array} \right\} &= \left\{ \begin{array}{l} H_x^{q-1/2}[m, n + \frac{1}{2}, p + \frac{1}{2}] \\ H_y^{q-1/2}[m + \frac{1}{2}, n, p + \frac{1}{2}] \\ H_z^{q-1/2}[m + \frac{1}{2}, n + \frac{1}{2}, p] \end{array} \right\} \dots \\ \dots - \frac{\Delta_t}{\mu_0 \Delta_x} \left\{ \begin{array}{l} E_z^q[m, n + 1, p + \frac{1}{2}] - E_z^q[m, n, p + \frac{1}{2}] - E_y^q[m, n + \frac{1}{2}, p + 1] + E_y^q[m, n + \frac{1}{2}, p] \\ E_x^q[m + \frac{1}{2}, n, p + 1] - E_x^q[m + \frac{1}{2}, n, p] - E_z^q[m + 1, n, p + \frac{1}{2}] + E_z^q[m, n, p + \frac{1}{2}] \\ E_y^q[m + 1, n + \frac{1}{2}, p] - E_z^q[m, n + \frac{1}{2}, p] - E_x^q[m + \frac{1}{2}, n + 1, p] + E_x^q[m + \frac{1}{2}, n, p] \end{array} \right\} \end{aligned} \quad (2.8)$$

In a similar manner, the partial differentials of (2.2) are evaluated at half-integer timestep $q + \frac{1}{2}$ about Yee cell points $(m + \frac{1}{2}, n, p)$, $(m, n + \frac{1}{2}, p)$ and $(m, n, p + \frac{1}{2})$ to form update equations for E_x , E_y and E_z respectively, as shown in (2.9) below:

$$\begin{aligned} \begin{Bmatrix} E_x^{q+1}[m+\frac{1}{2}, n, p] \\ E_y^{q+1}[m, n+\frac{1}{2}, p] \\ E_z^{q+1}[m, n, p+\frac{1}{2}] \end{Bmatrix} &= \begin{Bmatrix} E_x^q[m+\frac{1}{2}, n, p] \\ E_y^q[m, n+\frac{1}{2}, p] \\ E_z^q[m, n, p+\frac{1}{2}] \end{Bmatrix} + \frac{\Delta t}{\varepsilon_0 \Delta x} \begin{Bmatrix} H_z^{q+1/2}[m+\frac{1}{2}, n+\frac{1}{2}, p] \dots \\ H_x^{q+1/2}[m, n+\frac{1}{2}, p+\frac{1}{2}] \dots \\ H_y^{q+1/2}[m+\frac{1}{2}, n, p+\frac{1}{2}] \dots \\ \dots - H_z^{q+1/2}[m+\frac{1}{2}, n-\frac{1}{2}, p] - H_y^{q+1/2}[m+\frac{1}{2}, n, p+\frac{1}{2}] + H_y^{q+1/2}[m+\frac{1}{2}, n, p-\frac{1}{2}] \\ \dots - H_x^{q+1/2}[m, n+\frac{1}{2}, p-\frac{1}{2}] - H_z^{q+1/2}[m+\frac{1}{2}, n+\frac{1}{2}, p] + H_z^{q+1/2}[m-\frac{1}{2}, n+\frac{1}{2}, p] \\ \dots - H_y^{q+1/2}[m-\frac{1}{2}, n, p+\frac{1}{2}] - H_x^{q+1/2}[m, n+\frac{1}{2}, p+\frac{1}{2}] + H_x^{q+1/2}[m, n-\frac{1}{2}, p+\frac{1}{2}] \end{Bmatrix} \quad (2.9) \end{aligned}$$

Equations (2.8) and (2.9), when combined with an appropriate boundary condition (see Section 2.3 for more details), form a consistent time-stepping update scheme to describe an electromagnetic wave propagating in three-dimensional free space. A two-dimensional scheme can be formed by assuming that the structure under simulation extends infinitely in one dimension transverse to the plane of wave propagation, meaning that all field or material gradients along this direction tend to zero. For problems with essentially 2D geometry (for example the ionospheric heating simulations described in Chapters 4–6 of this thesis) this allows the scale of the simulation to be greatly reduced, vastly diminishing memory and processing requirements. Although this formulation restricts wave propagation to two dimensions, all three Cartesian field components are retained, meaning that wave properties such as polarisation can still be accurately simulated. A 2D formulation for the case of xz -plane propagation and $\partial/\partial y \rightarrow 0$ is given by (2.10) and (2.11) below.

$$\begin{aligned} \begin{Bmatrix} H_x^{q+1/2}[m, p+\frac{1}{2}] \\ H_y^{q+1/2}[m+\frac{1}{2}, p+\frac{1}{2}] \\ H_z^{q+1/2}[m+\frac{1}{2}, p] \end{Bmatrix} &= \begin{Bmatrix} H_x^{q-1/2}[m, p+\frac{1}{2}] \\ H_y^{q-1/2}[m+\frac{1}{2}, p+\frac{1}{2}] \\ H_z^{q-1/2}[m+\frac{1}{2}, p] \end{Bmatrix} \dots \\ &\dots - \frac{\Delta t}{\mu_0 \Delta x} \begin{Bmatrix} E_y^q[m, p] - E_y^q[m, p+1] \\ E_x^q[m+\frac{1}{2}, p+1] - E_x^q[m+\frac{1}{2}, p] - E_z^q[m+1, p+\frac{1}{2}] + E_y^q[m, p+\frac{1}{2}] \\ E_y^q[m+1, p] - E_y^q[m, p] \end{Bmatrix} \quad (2.10) \end{aligned}$$

$$\begin{aligned} \left\{ \begin{array}{l} E_x^{q+1}[m+\frac{1}{2}, p] \\ E_y^{q+1}[m, p] \\ E_z^{q+1}[m, p+\frac{1}{2}] \end{array} \right\} &= \left\{ \begin{array}{l} E_x^q[m+\frac{1}{2}, p] \\ E_y^q[m, p] \\ E_z^q[m, p+\frac{1}{2}] \end{array} \right\} \dots \\ &\dots + \frac{\Delta_t}{\varepsilon_0 \Delta_x} \left\{ \begin{array}{l} H_y^{q+1/2}[m+\frac{1}{2}, p-\frac{1}{2}] - H_y^{q+1/2}[m+\frac{1}{2}, p+\frac{1}{2}] \\ H_x^{q+1/2}[m, p+\frac{1}{2}] - H_x^{q+1/2}[m, p-\frac{1}{2}] - H_z^{q+1/2}[m+\frac{1}{2}, p] + H_z^{q+1/2}[m-\frac{1}{2}, p] \\ H_y^{q+1/2}[m+\frac{1}{2}, n, p+\frac{1}{2}] - H_y^{q+1/2}[m-\frac{1}{2}, n, p+\frac{1}{2}] \end{array} \right\} \end{aligned} \quad (2.11)$$

Propagation through conductive and/or dielectric media requires additional terms to be included in the FDTD formulation. For the case of scalar, frequency-independent, steady-state conduction and dielectric constants, this can be introduced to the FDTD scheme by defining the electrical and magnetic conductivities, the relative permittivity, and the relative permeability at each component grid-point. These values can be pre-calculated and stored in memory at simulation initialisation. As the medium parameters are set independently at each grid node, background structures with complicated geometries or distributions can easily be modelled. To describe wave propagation in media of this type, Maxwell's Equations are modified to include the electrical and magnetic conduction currents ($\sigma_E \mathbf{E}$ and $\sigma_M \mathbf{H}$, where $\sigma_{E,M}$ are the electrical and magnetic conductivities), with the free-space permittivities and permeabilities replaced by the total values ($\varepsilon_0 \rightarrow \varepsilon$; $\mu_0 \rightarrow \mu$) to yield (2.12) and (2.13).

$$\mu \frac{\partial \mathbf{H}}{\partial t} = -\nabla \times \mathbf{E} - \sigma_M \mathbf{H} \quad (2.12)$$

$$\varepsilon \frac{\partial \mathbf{E}}{\partial t} = \nabla \times \mathbf{H} - \sigma_E \mathbf{E} \quad (2.13)$$

In the derivation of update equation (2.9) for \mathbf{E} above, the equation is evaluated at time-step $q + 1/2$. As an undifferentiated \mathbf{E} -term now also appears as part of the conduction current but is not known exactly at this time-step, it must be approximated via a semi-implicit average using stored E-field values to maintain consistency:

$$\mathbf{E}^{q+1/2} = \frac{\mathbf{E}^{q+1} + \mathbf{E}^q}{2} \quad (2.14)$$

This technique can be used to find a temporal or spatial average at grid points where a field value is required but not explicitly stored. In Chapter 3, spatial averages employing stencils of four or more nearby grid nodes are required to form a consistent plasma-fluid FDTD scheme.

With the inclusion of real, constant, scalar electrical conduction and permittivity, the finite-difference treatment employed to derive the free-space FDTD equations can be applied to (2.12) and (2.13) (see, for example, [Schneider, 2010]). Using the E_x component of (2.13) as an example, this gives:

$$\varepsilon[m + \frac{1}{2}, n, p] \left(\frac{E_x^{q+1}[m + \frac{1}{2}, n, p] \dots - E_x^q[m + \frac{1}{2}, n, p]}{\Delta_t} \right) = \sigma_E[m + \frac{1}{2}, n, p] \left(\frac{E_x^{q+1}[m + \frac{1}{2}, n, p] \dots + E_x^q[m + \frac{1}{2}, n, p]}{2} \right) \dots \\ \dots + \left(\frac{H_z^{q+1/2}[m + \frac{1}{2}, n + \frac{1}{2}, p] - H_z^{q+1/2}[m + \frac{1}{2}, n - \frac{1}{2}, p] \dots - H_y^{q+1/2}[m + \frac{1}{2}, n, p + \frac{1}{2}] + H_y^{q+1/2}[m + \frac{1}{2}, n, p - \frac{1}{2}]}{\Delta_x} \right) \quad (2.15)$$

Rearranging this to give an expression for E_x^{q+1} yields a consistent update equation incorporating the effects of conduction and dielectric permittivity:

$$E_x^{q+1}[m + \frac{1}{2}, n, p] = \left(\frac{1 - \frac{\Delta_t \sigma_E[m + \frac{1}{2}, n, p]}{2\varepsilon[m + \frac{1}{2}, n, p]}}{1 + \frac{\Delta_t \sigma_E[m + \frac{1}{2}, n, p]}{2\varepsilon[m + \frac{1}{2}, n, p]}} \right) \left(\frac{E_x^{q+1}[m + \frac{1}{2}, n, p] \dots + E_x^q[m + \frac{1}{2}, n, p]}{2} \right) \dots \\ \dots + \left(\frac{\frac{\Delta_t}{\varepsilon[m + \frac{1}{2}, n, p]}}{\frac{1 + \Delta_t \sigma_E[m + \frac{1}{2}, n, p]}{2\varepsilon[m + \frac{1}{2}, n, p]}} \right) \left(\frac{H_z^{q+1/2}[m + \frac{1}{2}, n + \frac{1}{2}, p] - H_z^{q+1/2}[m + \frac{1}{2}, n - \frac{1}{2}, p] \dots - H_y^{q+1/2}[m + \frac{1}{2}, n, p + \frac{1}{2}] + H_y^{q+1/2}[m + \frac{1}{2}, n, p - \frac{1}{2}]}{\Delta_x} \right) \quad (2.16)$$

Similar expressions can be found for the remaining **E** and **B** components by an equivalent process. The coefficients containing the ε , μ and σ terms can be pre-calculated and stored in memory (which may require some spatial averaging on calculation at inter-cell nodes), or indexed by media type to further save memory.

2.2 Dispersion and Stability

2.2.1 Dispersion in the FDTD Domain

In the real, continuous (i.e. non-computational, un-discretised) world, a dispersion equation defines in essence the relationship between the frequency of a plane wave and the speed at which that wave propagates through a medium. This can be described entirely using the properties of the wave and of the dispersive medium only. Due to the discretised nature of the FDTD computational domain, simulated waves do not obey the standard continuous-world dispersion relationships exactly; instead they follow computational-world equivalents which must be described not only in terms of the medium parameters, but also in terms of the domain-specific discretisation parameters. The exact forms of the computational dispersion relations are dictated by the nodal arrangement of the Yee cell and the structure of the time-advancement algorithm. The review of numerical dispersion below was drawn primarily from the discussions in [Taflove and Hagness, 2000] and [Schneider, 2010]; more details can be found in these or other textbooks.

To derive computational-world dispersion equations for the simple case of the FDTD update equations (2.8) and (2.9) for plane EM waves in a vacuum, the shift-operator methodology of [Schneider, 2010] is used below. The case of a 1D simulation with propagation in the x -direction only is used here; the treatment can be easily extended to higher dimensions. Spatial and temporal shift operators $A_x^{\pm\frac{1}{2}}$ and $A_t^{\pm\frac{1}{2}}$, acting to move a computational-domain field forwards or backwards by a discrete half-step, can be defined as:

$$A_x^{\pm\frac{1}{2}} E^q[m] = E^q[m \pm \frac{1}{2}] \quad A_t^{\pm\frac{1}{2}} E^q[m] = E^{q\pm\frac{1}{2}}[m] \quad (2.17)$$

From these, discrete finite-difference operators F_x and F_t can be defined:

$$F_x E^q[m] = \left[\frac{A_x^{+\frac{1}{2}} - A_x^{-\frac{1}{2}}}{\Delta_x} \right] E^q[m] = \frac{E^q[m + \frac{1}{2}] - E^q[m - \frac{1}{2}]}{\Delta_x} \quad (2.18)$$

$$F_t E^q[m] = \left[\frac{A_t^{+\frac{1}{2}} - A_t^{-\frac{1}{2}}}{\Delta_t} \right] E^q[m] = \frac{E^{q+\frac{1}{2}}[m] - E^{q-\frac{1}{2}}[m]}{\Delta_t} \quad (2.19)$$

Under the assumption that all EM fields in the FDTD grid can be described by numerical plane waves, all computational-domain solutions of the basic form $e^{i[\omega q\Delta_t - \tilde{\mathbf{k}} \cdot \tilde{\mathbf{x}}\Delta_x]}$, where $\tilde{\mathbf{x}} = (m, n, p)$ and $\tilde{\mathbf{k}}$ is the numerical wavenumber, will be eigenfunctions of the shift operators. This can be demonstrated for the 1D spatial shift operation:

$$\begin{aligned} A_x^{\pm\frac{1}{2}} E^q[m] &= A_x^{\pm\frac{1}{2}} E_0 e^{i(\omega q\Delta_t - \tilde{k}_x m \Delta_x)} & A_t^{\pm\frac{1}{2}} E^q[m] &= A_t^{\pm\frac{1}{2}} E_0 e^{i(\omega q\Delta_t - \tilde{k}_x m \Delta_x)} \\ &= E_0 e^{i(\omega q\Delta_t - \tilde{k}_x [m \pm \frac{1}{2}] \Delta_x)} & &= E_0 e^{i(\omega [q \pm \frac{1}{2}] \Delta_t - \tilde{k}_x m \Delta_x)} \\ &= E_0 e^{i(\omega q\Delta_t - \tilde{k}_x m \Delta_x)} e^{\mp i \tilde{k}_x \Delta_x / 2} & &= E_0 e^{i(\omega q\Delta_t - \tilde{k}_x m \Delta_x)} e^{\pm i \omega \Delta_t / 2} \\ &= e^{\mp i \tilde{k}_x \Delta_x / 2} E^q[m] & &= e^{\pm i \omega \Delta_t / 2} E^q[m] \end{aligned} \quad (2.20) \quad (2.21)$$

Using (2.20) and (2.21), the finite-difference operators can be re-written in terms of eigenvalues of the discrete shift operators:

$$\begin{aligned} F_x E^q[m] &= \left(\frac{A_x^{+\frac{1}{2}} - A_x^{-\frac{1}{2}}}{\Delta_x} \right) E^q[m] & F_t E^q[m] &= \left(\frac{A_t^{+\frac{1}{2}} - A_t^{-\frac{1}{2}}}{\Delta_t} \right) E^q[m] \\ &= \left(\frac{e^{-i \tilde{k}_x \Delta_x / 2} - e^{-i \tilde{k}_x \Delta_x / 2}}{\Delta_x} \right) E^q[m] & &= \left(\frac{e^{-i \omega \Delta_t / 2} - e^{-i \omega \Delta_t / 2}}{\Delta_t} \right) E^q[m] \\ &= -\frac{2i}{\Delta_x} \sin \left(\frac{\tilde{k}_x \Delta_x}{2} \right) E^q[m] & &= \frac{2i}{\Delta_t} \sin \left(\frac{\omega \Delta_t}{2} \right) E^q[m] \\ &= -i K_x E^q[m] & &= i \Omega E^q[m] \end{aligned} \quad (2.22) \quad (2.23)$$

Similar treatment can be applied for F_y or F_z in the higher-dimension case. Thus the finite-difference operators $F_{x,y,z}$ and F_t can be replaced in the harmonic approximation by eigenvalues which are dependent on the discrete gird parameters only:

$$F_{x,y,z} \rightarrow -i K_{x,y,z} = -\frac{2i}{\Delta_x} \sin \left(\frac{\tilde{k}_{x,y,z} \Delta_x}{2} \right) \quad (2.24)$$

$$F_t \rightarrow i \Omega = \frac{2i}{\Delta_t} \sin \left(\frac{\omega \Delta_t}{2} \right) \quad (2.25)$$

Equivalent spatial step sizes in all directions has been assumed ($\Delta_x = \Delta_y = \Delta_z$). It can be seen that as the simulation resolution is made finer and discrete step sizes are reduced, the K and Ω parameters converge on their continuous-world analogues (taking

into account that $\tilde{k} \rightarrow k$ as $\Delta_x \rightarrow 0$ [Taflove and Hagness, 2000]):

$$\lim_{\Delta_x \rightarrow 0} \left\{ K_{x,y,z} = \frac{2}{\Delta_x} \sin \left(\frac{\tilde{k}_{x,y,z} \Delta_x}{2} \right) \right\} \rightarrow k_{x,y,z} \quad (2.26)$$

$$\lim_{\Delta_t \rightarrow 0} \left\{ \Omega = \frac{2}{\Delta_t} \sin \left(\frac{\omega \Delta_t}{2} \right) \right\} \rightarrow \omega \quad (2.27)$$

Following the same procedure as in Section 1.4.1 and references therein, a dispersion relation for plane waves in a vacuum can be constructed for the numerical grid. Using the numerical harmonic approximations (2.24) and (2.25), Maxwell's vacuum EM equations (2.1) and (2.2) become:

$$i\mu_0 \Omega \hat{\mathbf{H}} = -i\mathbf{K} \times \hat{\mathbf{E}} \quad (2.28)$$

$$i\varepsilon_0 \Omega \hat{\mathbf{E}} = i\mathbf{K} \times \hat{\mathbf{H}} \quad (2.29)$$

Taking the curl of (2.29) (still in the numerical-harmonic domain) and taking advantage of Gauss' Law in free space, $-i\mathbf{K} \cdot \hat{\mathbf{E}} = 0$:

$$\begin{aligned} \mu_0 \Omega \mathbf{K} \times \hat{\mathbf{H}} &= -\mathbf{K} \times \mathbf{K} \times \hat{\mathbf{E}} \\ \mu_0 \Omega \left[\varepsilon_0 \Omega \hat{\mathbf{E}} \right] &= - \left[\mathbf{K}(\mathbf{K} \cdot \hat{\mathbf{E}}) - K^2 \hat{\mathbf{E}} \right] \\ \Omega^2 &= \frac{1}{\mu_0 \varepsilon_0} [K_x^2 + K_y^2 + K_z^2] \\ \Rightarrow \left(\frac{2}{\Delta_t} \right)^2 \sin^2 \left(\frac{\omega \Delta_t}{2} \right) &= \sum_{j=x,y,z} \left(\frac{2c}{\Delta_j} \right)^2 \sin^2 \left(\frac{\tilde{k}_j \Delta_j}{2} \right) \end{aligned} \quad (2.30)$$

As discretisation parameters tend to zero, this approaches the continuous-world free space dispersion relationship for plane waves derived in Section 1.4:

$$\lim_{\Delta_x, \Delta_t \rightarrow 0} \left\{ \Omega^2 = c^2 K^2 \right\} \rightarrow \omega^2 = c^2 k^2 \quad (2.31)$$

The discrete nature of the FDTD grid affects the propagation of simulated waves within the computational domain, independent of the background context. Effects such as numerical dispersion, dissipation and anisotropy arise naturally as a direct consequence of the discontinuous staggered-node scheme and the approximations incurred through finite-difference treatment of differentials; the accuracy of a FDTD scheme depends

strongly on the choice of discrete step parameters. To demonstrate this, the numerical phase velocity of a plane wave travelling in the FDTD domain can be expressed from (2.30) as:

$$\tilde{c}_p = \frac{\omega}{|\tilde{\mathbf{k}}|} = \frac{2}{|\tilde{\mathbf{k}}|\Delta_t} \arcsin \left\{ \frac{c\Delta_t}{\Delta_x} \left[\sin^2 \left(\frac{\tilde{k} \cos(\theta)\Delta_x}{2} \right) + \sin^2 \left(\frac{\tilde{k} \sin(\theta)\Delta_x}{2} \right) \right]^{\frac{1}{2}} \right\} \quad (2.32)$$

Here wave propagation has been limited to the xz -plane for simplicity, with the angle between $\tilde{\mathbf{k}}$ and the z -axis given by θ . From this equation, it can be seen that the phase speed of a plane wave in the FDTD domain is not identically-equal to the continuous-world speed of light due to the effects of the numerical grid. The error in numerical phase velocity, calculated using (2.33) is strongly influenced by the choice of grid parameters.

$$\text{error}(\tilde{c}_p) = \frac{\tilde{c}_p - c}{c} \quad (2.33)$$

The effects of numerical dispersion (in the free-space scenario described here) are not dependent on the exact choice of plane-wave frequency and wavelength, but instead on the ratios between wave parameters and grid parameters; dimensionless quantities such as $f_0\Delta_t$ and λ_0/Δ_x govern the impact of grid-based dispersion of wave propagation. The ratio between the temporal and spatial discrete step sizes themselves, expressed below as the dimensionless *Courant number* (2.34) [Taflove and Hagness, 2000], also has a significant effect on both the dispersive and anisotropic properties of the grid.

$$S_c = \frac{c\Delta_t}{\Delta_x} \quad (2.34)$$

Figure 2.2 shows how the numerical phase velocity varies with the number of grid cells per wavelength (λ_0/Δ_x) for the case of a wave propagating along one of the principle grid axes ($\theta = 0^\circ$, $\pm 90^\circ$, or $\pm 180^\circ$) for a range of S_c ratios. The $S_c = 1$ curve in this example represents the ideal case, with no deviation from the continuous-world phase velocity regardless of the discrete resolution. From (2.34) it can be seen that this corresponds to the case that a wave propagating at the speed of light will travel a distance of precisely Δ_x in a single time-step; thus a wave travelling along one of the grid axes can be sampled

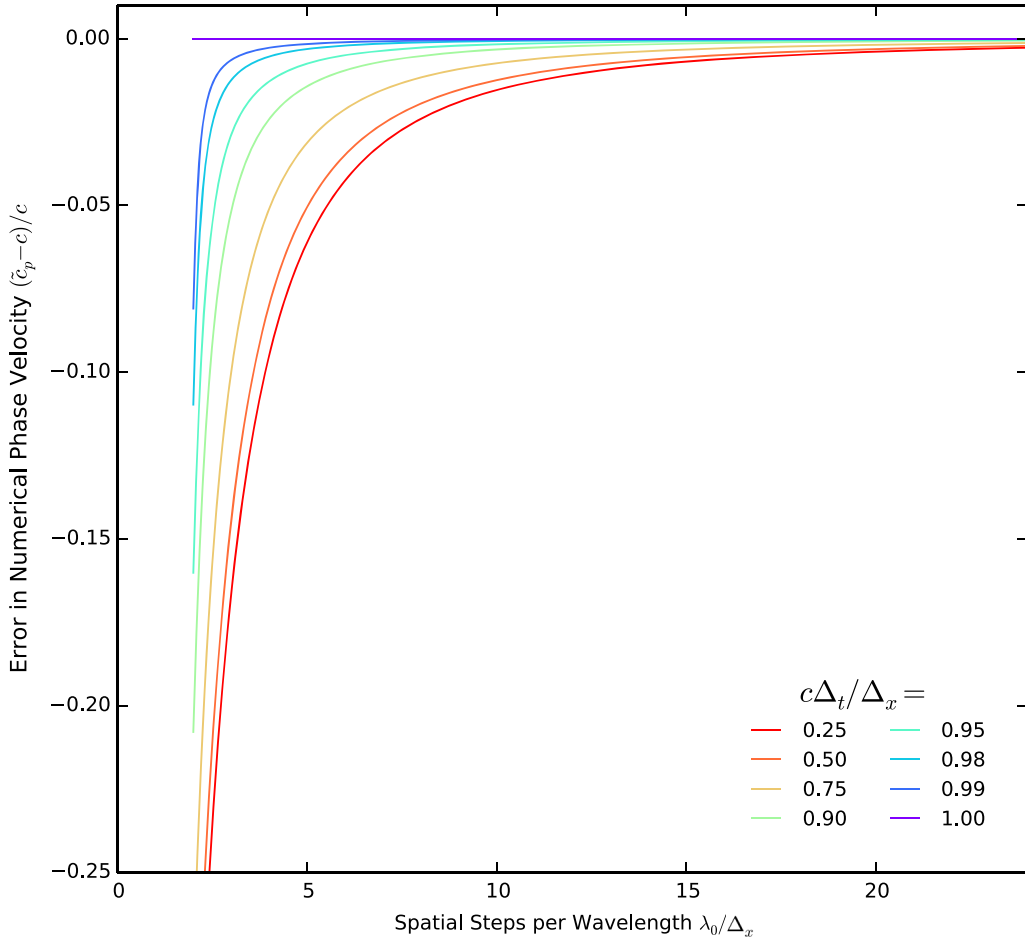


FIGURE 2.2: Variation of numerical phase velocity \tilde{c}_p with the number of grid cells per wavelength λ_0/Δ_x for the case of a plane wave propagating along one of the principle gird axes. As the Courant number is reduced, the magnitude of the numerical dispersion error can be seen to increase, particularly at low resolutions.

at any resolution above the Nyquist limit without incurring any numerical dispersion error. As the Courant number is reduced, the numerical error can be seen to increase, particularly at low resolutions. As the number of spatial steps per wavelength increases, the phase velocity in the FDTD domain converges on the continuous-world value.

In addition to a dependence on grid parameters, the numerical phase velocity (2.32) is clearly dependent on the direction of wave propagation θ : the numerical domain is thus an anisotropic environment. This is demonstrated in Figure 2.3 which shows how the numerical phase velocity error varies with wave propagation angle, for a range of grid resolutions. In this case the Courant ratio was fixed at $S_c = 0.5$. The ideal case of $\tilde{c}_p = c$ is indicated by a dotted line. From this it can be seen that for all resolutions, the phase

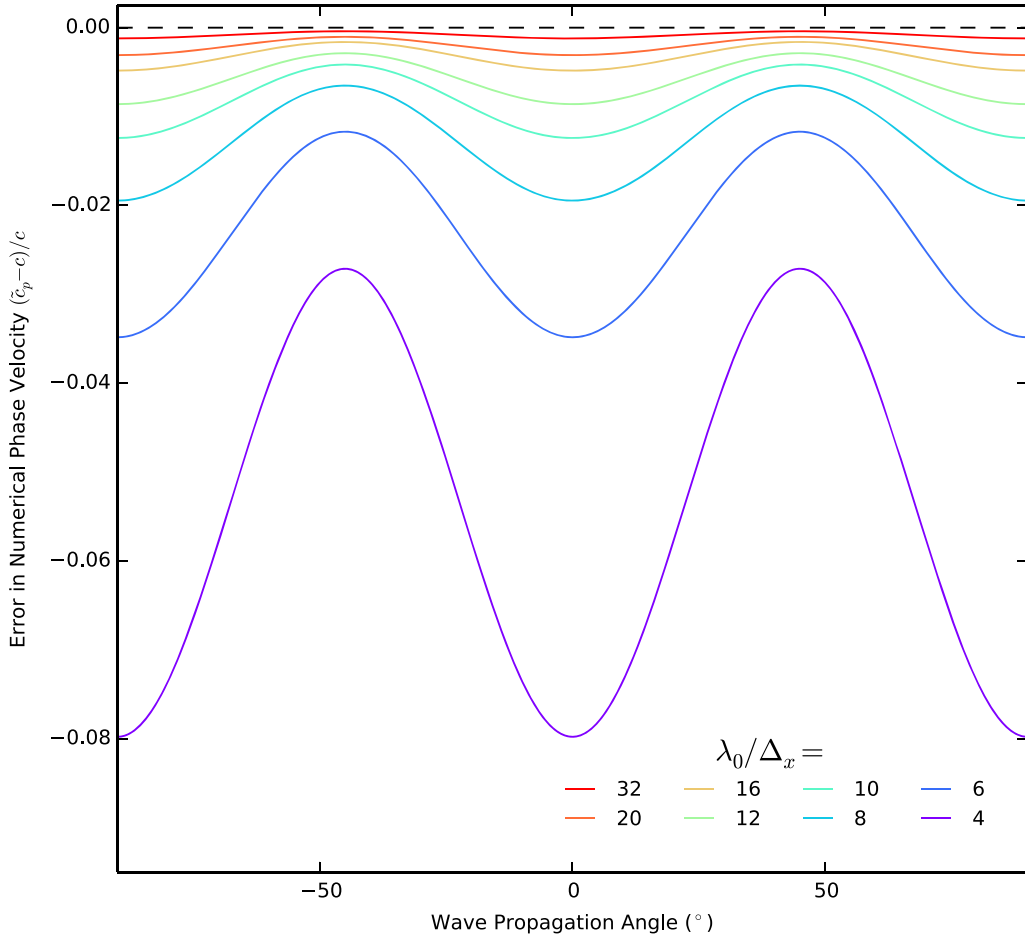


FIGURE 2.3: Variation in numerical phase velocity error with wave propagation angle, for a range of grid resolutions. The Courant ratio was fixed at $S_c = 0.5$. The ideal case of $\tilde{c}_p = c$ is indicated by a dotted line.

velocity is greatest for propagation at $\pm 45^\circ$ and least along the principle grid axes (0° , $\pm 90^\circ$). As the number of grid points per wavelength is decreased, the error in phase velocity due to numerical effects deviates further from the ideal case. The magnitude of anisotropy is also affected by grid parameters: the variation between the maximum \tilde{c}_p (at 45°) and minimum \tilde{c}_p (at 0°) is greater at coarser resolutions.

The effect of numerical anisotropy also makes the choice of Courant ratio crucial to maintaining simulation stability. Figure 2.4 again shows the variation in numerical phase velocity error with propagation direction, this time for a range of Courant ratios while the resolution is kept constant at $\Delta_x = \lambda_0/16$ (chosen as a typical example of the resolution used in the scientific simulations described in Chapters 3-6 below). The ideal case of $\tilde{c}_p = c$ is indicated by a dotted line. As expected from the discussion above, the

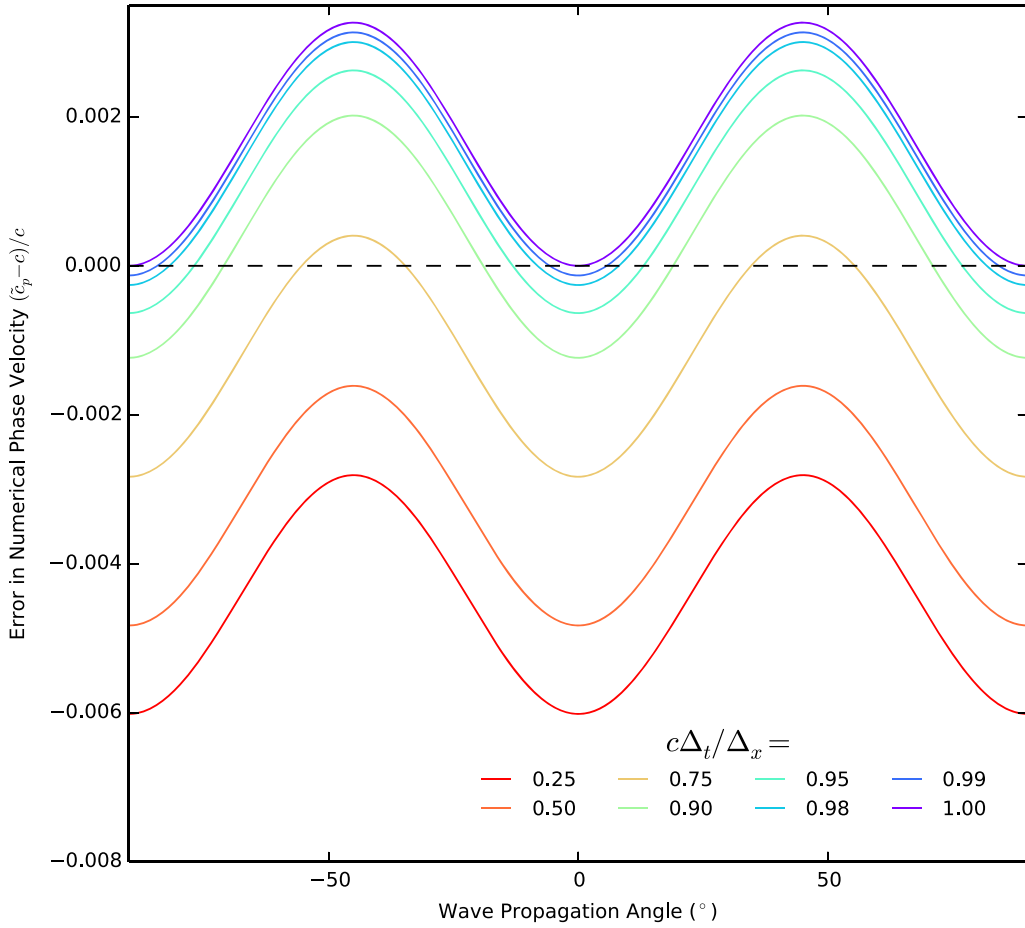


FIGURE 2.4: Variation in numerical phase velocity error with wave propagation angle, for a range of Courant ratios. The resolution was fixed at $\Delta_x = \lambda_0/16$. The ideal case of $\tilde{c}_p = c$ is indicated by a dotted line. For cases where $S_c > 1/\sqrt{2}$, the numerical phase velocity is superluminal at some or all propagation angles.

deviation from the ideal case increases as S_c is reduced. Troublingly, it can be seen that for the instances where $S_c > 1/\sqrt{2}$ the numerical phase velocity is superluminal at some or all propagation angles and is clearly not physical. This implies that under certain conditions wave energy can travel through more than one grid cell per time step, leading to numerical instabilities that may severely disrupt a simulation.

The above analysis demonstrates that, regardless of the simulated background medium, the numerical grid itself is a dispersive and anisotropic environment where wave propagation will be affected by the choice of discretisation parameters. Simulation accuracy can be improved by reducing the step sizes in relation to the wave period and wavelength, and increasing the Courant ratio such that $c\Delta_t/\Delta_x \rightarrow 1$. The latter must be done with

care as it may lead to superluminal phase velocities within the numerical domain, and, consequently to an unstable simulation. The situation becomes more complicated for the case of a collisional, magnetised plasma background, however the basic premise of grid-based numerical dispersion and anisotropy remains. The effect of numerical dispersion on simulation accuracy for the case of a magnetised plasma-fluid scheme is investigated further in Chapter 3.

2.2.2 Stability Criteria and the Courant-Friedrichs-Lowy Condition

An important consideration in any FDTD scheme is the stability of the simulation. Above it has been shown that the choice of discrete parameters Δ_x and Δ_t can influence the propagation of waves in the FDTD domain and hence the numerical error inherent in the simulation. If the grid parameters are not chosen carefully, some or all simulated frequency components can have solutions which are unstable and may grow with time, significantly reducing the accuracy of the simulation and potentially obscuring the intended signal entirely. The review of FDTD stability below was drawn primarily from the discussions in [Taflove and Hagness, 2000]; more details can be found in this or other textbooks.

From the numerical dispersion relation for a 3D domain (2.30), the complex-valued angular frequency can be defined as:

$$\begin{aligned}\tilde{\omega} &= \frac{2}{\Delta_t} \arcsin \left\{ \frac{c\Delta_t}{\Delta_x} \left[\sin^2 \left(\frac{\tilde{k}_x \Delta_x}{2} \right) + \sin^2 \left(\frac{\tilde{k}_y \Delta_x}{2} \right) + \sin^2 \left(\frac{\tilde{k}_z \Delta_x}{2} \right) \right]^{\frac{1}{2}} \right\} \\ \Rightarrow \tilde{\omega} &= \frac{2}{\Delta_t} \arcsin \left\{ \frac{\Omega \Delta_t}{2} \right\}\end{aligned}\quad (2.35)$$

It is clear that under certain conditions, the $\Omega \Delta_t / 2$ term in the $\arcsin()$ can have a value > 1 ; this leads to the superluminal phase velocities seen in Figure 2.4 and a complex value of the numerical frequency. When a complex numerical frequency is introduced to the plane wave expression (2.36) it can be seen that positive-imaginary frequencies lead to an evanescent attenuation of the wave signal with simulation time and thus a numerical dissipation of wave energy, whereas negative-imaginary frequencies lead to an

exponential growth of wave amplitude with simulated time and thus a state of numerical instability [Taflove and Hagness, 2000]:

$$\mathbf{E}_0 e^{i(\tilde{\omega} q \Delta_t - \tilde{\mathbf{k}} \cdot \tilde{\mathbf{x}})} = \mathbf{E}_0 e^{i([\tilde{\omega}_{real} + i\tilde{\omega}_{imag}]q \Delta_t - \tilde{\mathbf{k}} \cdot \tilde{\mathbf{x}})} = \mathbf{E}_0 e^{-\tilde{\omega}_{imag} q \Delta_t} e^{i(\tilde{\omega}_{real} q \Delta_t - \tilde{\mathbf{k}} \cdot \tilde{\mathbf{x}})} \quad (2.36)$$

Using the identity $\arcsin(z) = i \ln(i z + \sqrt{1 - z^2})$ in (2.35) allows an expression for $\tilde{\omega}_{imag}$ to be calculated:

$$\begin{aligned} \tilde{\omega} &= \frac{2i}{\Delta_t} \ln \left(i \frac{\Omega \Delta_t}{2} + \sqrt{1 - \left[\frac{\Omega \Delta_t}{2} \right]^2} \right) \\ \tilde{\omega}_{real} + i\tilde{\omega}_{imag} &= \frac{2i}{\Delta_t} \ln \left(e^{+i\frac{\pi}{2}} \left[\frac{\Omega \Delta_t}{2} + \sqrt{\left[\frac{\Omega \Delta_t}{2} \right]^2 - 1} \right] \right) \\ \tilde{\omega}_{real} + i\tilde{\omega}_{imag} &= \frac{\pi}{\Delta_t} - \frac{2i}{\Delta_t} \ln \left(\frac{\Omega \Delta_t}{2} + \sqrt{\left[\frac{\Omega \Delta_t}{2} \right]^2 - 1} \right) \\ \Rightarrow \tilde{\omega}_{imag} &= -\frac{2}{\Delta_t} \ln \left(\frac{\Omega \Delta_t}{2} + \sqrt{\left[\frac{\Omega \Delta_t}{2} \right]^2 - 1} \right) \end{aligned} \quad (2.37)$$

Substituting this into the numerical plane wave equation:

$$\begin{aligned} \mathbf{E}^q(\tilde{\mathbf{x}}) &= \mathbf{E}_0 e^{2q \ln\left(\Omega \Delta_t / 2 + \sqrt{[\Omega \Delta_t / 2]^2 - 1}\right)} e^{i(\tilde{\omega}_{real} q \Delta_t - \tilde{\mathbf{k}} \cdot \tilde{\mathbf{x}})} \\ &= \mathbf{E}_0 \left(\frac{\Omega \Delta_t}{2} + \sqrt{\left[\frac{\Omega \Delta_t}{2} \right]^2 - 1} \right)^{2q} e^{i(\tilde{\omega}_{real} q \Delta_t - \tilde{\mathbf{k}} \cdot \tilde{\mathbf{x}})} \end{aligned} \quad (2.38)$$

Thus, since for all $\Omega \Delta_t / 2 > 1$ the coefficient $\left(\Omega \Delta_t / 2 + \sqrt{[\Omega \Delta_t / 2]^2 - 1} \right)^{2q}$ is greater than zero, a negative-imaginary numerical frequency component leads to an unbounded amplification of the simulated wave signal which grows rapidly with time.

From this, restrictions can be placed on the choice of grid discretisation parameters that ensure stability. From (2.30), the maximum possible value of $\Omega \Delta_t / 2$ will occur when $\tilde{\mathbf{k}} = (\pm\pi/\Delta_x, \pm\pi/\Delta_x, \pm\pi/\Delta_x)$:

$$\begin{aligned} \frac{\Omega \Delta_t}{2} &\leq c \Delta_t \sqrt{\left(\frac{1}{\Delta_x} \right)^2 + \left(\frac{1}{\Delta_x} \right)^2 + \left(\frac{1}{\Delta_x} \right)^2} \\ \Rightarrow \frac{\Omega \Delta_t}{2} &\leq \frac{c \Delta_t}{\Delta_x} \sqrt{3} \end{aligned} \quad (2.39)$$

To ensure stability, the condition $\Omega\Delta_t/2 \leq 1$ must be enforced, allowing the *Courant-Friedrichs-Lowy* (CFL) criterion for stability [Courant et al., 1967] to be defined as:

$$\Rightarrow S_c \equiv \frac{c\Delta_t}{\Delta_x} \leq \frac{1}{\sqrt{3}} \quad (2.40)$$

where S_c is the Courant ratio defined in Section 2.2.1 above. In general terms, for equal spatial step sizes in all directions, the criteria for stability is:

$$S_c \equiv \frac{c\Delta_t}{\Delta_x} \leq \frac{1}{\sqrt{N_{dims}}} \quad (2.41)$$

where N_{dims} is the number of grid dimensions. In essence, this condition ensures that wave energy in the FDTD grid cannot propagate faster than light speed and cannot cross more than one grid cell per time-step. As with the dispersion equations described above, this picture becomes more complicated when a physically-dispersive background medium is included in the FDTD scheme; this effect explored in more detail for the case of a magneto-ionic plasma in Chapter 3.

2.2.3 Choosing Simulation Parameters

The choice of parameters to be used in an FDTD model is a delicate balance; one which depends largely on the nature of the features one wishes to observe, and the accuracy of results one desires. As the above analysis has shown, no parameters can be varied arbitrarily or independently: all are intrinsically coupled to the performance of the model. The computational-space discretisation step sizes must be carefully chosen around these pre-defined physical values in order to preserve the stability and accuracy of the model. The CFL condition places hard limits on the step sizes in all model conditions; exceeding this limit invariably results in unphysical numerical fields which grow rapidly to infinity. Below this limit, care must be taken to tailor the step sizes to the spatial scale, wavelength and frequency spectrum of the features one wishes to observe: over- or under-sampling a particular wave will likely result in inaccurate or unphysical results. After base-line stability, the ability of the model to perform the

intended experiment and record results adequately should be of prime concern. The fine-tuning of the step-size parameters must be based around a trade-off between simulation accuracy and computational efficiency; intuitively, and as shown in the analysis above, reducing the step sizes will increase the accuracy of the model, but will potentially result in far greater computing run-times and memory requirements, particularly when long wavelength signals are to be considered.

2.3 Boundary Conditions

One of the most critical elements of an FDTD model is the manner in which the computational domain is terminated. The size of the domain - in this context “size” refers to the number of cells contained in the model, not the physical scales under simulation - is limited by the computer processing power and memory available: the larger the domain, the more computationally-intensive the model becomes. The FDTD scheme described in this thesis was designed to study the interaction between ground-launched radio waves and ionospheric plasma located at an altitude of 200 *km* or higher, however the physical scale of this complete system is many orders of magnitude larger than the wavelengths of plasma and EM waves under investigation. It is thus infeasible to construct a computational domain containing the entire system; instead, a smaller computational domain is assembled containing only the region of interest, terminated with boundary conditions designed to make it appear that the domain is a small part of a much larger system. The intended purpose of these boundaries is to absorb any outgoing waves, creating the impression that they have continued to propagate away from the region of interest as part of an effectively-infinite continuous system. An ideal FDTD boundary will completely absorb any outgoing wave components - periodic or evanescent - leaving the computational domain without introducing any numerical reflection artefacts. It is realistically impossible to completely avoid small numerical reflections at the domain boundaries, however very efficient boundary condition formulations exist which result in a reflected field of negligibly-small amplitudes under most conditions.

2.3.1 Mur Absorbing Boundary Conditions

An *absorbing boundary condition* (ABC) attempts to fully absorb any wave component incident on the computational domain boundary with minimal spurious numerical reflection. This section describes a class of analytical ABC first proposed by Engquist and Majda [Engquist and Majda, 1977] and using the discretisation scheme of Mur [Mur, 1981], following the formulation described in [Schneider, 2010]. The Mur ABC uses the advective wave equation for EM waves to form an update equation for the outer nodes of the FDTD grid. Nodes on the very outer surface of the computational domain cannot update using the normal update equations, as these will try to make reference to non-existent field nodes outside of the grid. Instead, this ABC updates these nodes in a manner that assumes that all fields immediately inside the boundary will tend to propagate directly out of the domain as a travelling plane wave described by:

$$\left(\nabla^2 - \mu_0 \epsilon_0 \frac{\partial^2}{\partial t^2} \right) \mathbf{E} = 0 \quad (2.42)$$

As an example, consider the z -component of the E-field travelling in the x -direction. ABC equations are necessary for this combination case because E_z nodes appear on the x -boundaries of the computational domain (due to the structure of the Yee cell, see Figure 2.1). Indeed, ABC equations are required for all field components tangential to a domain boundary. For this example, (2.42) can be split into a pair of first-order advective equations describing waves travelling in the $\pm x$ -directions:

$$\begin{aligned} \left(\frac{\partial}{\partial x} - \sqrt{\mu_0 \epsilon_0} \frac{\partial}{\partial t} \right) \left(\frac{\partial}{\partial x} + \sqrt{\mu_0 \epsilon_0} \frac{\partial}{\partial t} \right) E_z &= 0 \\ \Rightarrow \frac{\partial E_z}{\partial x} &= \pm \frac{1}{c} \frac{\partial E_z}{\partial t} \end{aligned} \quad (2.43)$$

Considering the equation for the wave travelling in the negative x -direction, an ABC update equation for the boundary nodes at the $x = 0$ edge can be found first by expanding the partial derivatives in finite-difference approximations about time step $q + \frac{1}{2}$ and the point half a spatial step inside the computational domain from the $x = 0$ boundary,

$[\frac{1}{2}, n, p + \frac{1}{2}]$, then by rearranging to yield an expression for E_z^{q+1} on the boundary (2.44):

$$\begin{aligned} & \frac{\frac{1}{2} \left(E_z^{q+1}[1, n, p + \frac{1}{2}] + E_z^q[1, n, p + \frac{1}{2}] \right) - \frac{1}{2} \left(E_z^{q+1}[0, n, p + \frac{1}{2}] + E_z^q[0, n, p + \frac{1}{2}] \right)}{\Delta_x} \dots \\ & \dots = \left(\frac{1}{c} \right) \frac{\frac{1}{2} \left(E_z^{q+1}[1, n, p + \frac{1}{2}] + E_z^{q+1}[0, n, p + \frac{1}{2}] \right) - \frac{1}{2} \left(E_z^q[1, n, p + \frac{1}{2}] + E_z^q[0, n, p + \frac{1}{2}] \right)}{\Delta_t} \\ & \Rightarrow E_z^{q+1}[0, n, p + \frac{1}{2}] = E_z^q[1, n, p + \frac{1}{2}] - \frac{1 - S_c}{1 + S_c} \left(E_z^{q+1}[1, n, p + \frac{1}{2}] - E_z^q[0, n, p + \frac{1}{2}] \right) \quad (2.44) \end{aligned}$$

Note that this derivation uses the semi-implicit averaging technique described in Section 2.1.3 to evaluate E_z at half-integer time-steps and x -coordinates. Similar equations can be formulated for other field components and at the other grid boundaries. As the H-field has no components tangential to the edge of the Yee cell, no ABC update equations are required for the magnetic field in this scheme. The 1st order Mur ABC provides a simple and computationally-efficient method of boundary termination; the $(1 - S_c)/(1 + S_c)$ coefficient is constant and can be pre-calculated, and for each boundary field node only one additional value must be stored in the computer memory ($E_z^q[1, n, p + \frac{1}{2}]$). This ABC is effective at absorbing any wave propagating at normal incidence towards the boundary, however, as the angle of incidence reduces, the success of this boundary condition also reduces. The ABC's assumption that all fields in the outermost-but-one nodes will be propagating directly out of the domain causes a leeching effect close to the boundary, degrading the tangential component of a simulated field as well as absorbing the normally-incident component. Further, this class of ABC is known to be unstable at late times under certain circumstances (see, for example, [Yusheng and Wenbing, 1996]). To achieve greater accuracy and more complete absorption, higher-order implementations of this ABC can be formulated, as described in [Taflove and Hagness, 2000]. In essence, the 1st-order ABC (2.44) is formed by a single application of the advective operator $[\frac{\partial}{\partial x} + \sqrt{\mu_0 \epsilon_0} \frac{\partial}{\partial t}]$; multiple-order versions can be formed by multiple application of this operator. For example the 2nd-order equivalent of (2.44)

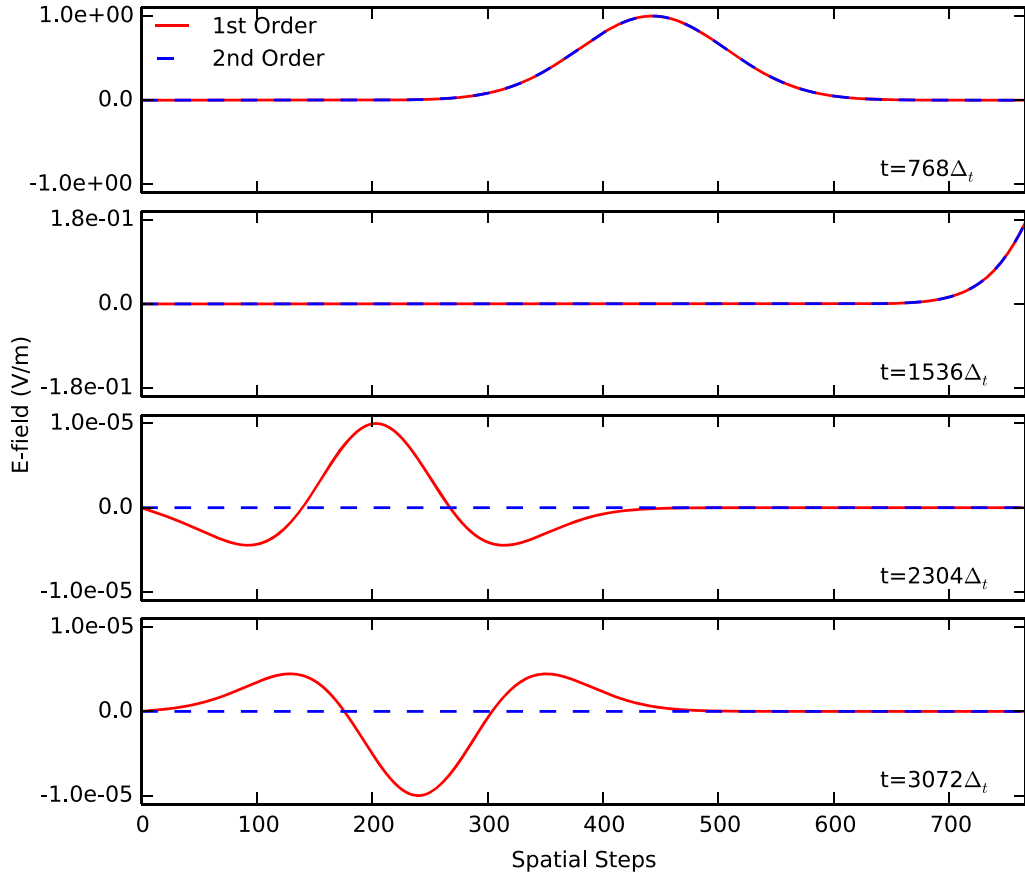


FIGURE 2.5: Comparison between 1st-order (red) and 2nd-order (blue) Mur-style ABCs when a Gaussian pulse signal is incident from the left, for the case of $S_c = 1/\sqrt{3}$.

[Taflove and Hagness, 2000] is given by:

$$\begin{aligned}
 E_z^{q+1}[0, n, p + \frac{1}{2}] &= \frac{-S_c^2 + 2S_c - 1}{S_c^2 + 2S_c + 1} \left(E_z^{q+1}[2, n, p + \frac{1}{2}] + E_z^{q-1}[0, n, p + \frac{1}{2}] \right) \dots \\
 \dots + \frac{-2S_c^2 + 2}{S_c^2 + 2S_c + 1} \left(E_z^q[0, n, p + \frac{1}{2}] + E_z^q[2, n, p + \frac{1}{2}] - E_z^{q+1}[1, n, p + \frac{1}{2}] - E_z^{q-1}[1, n, p + \frac{1}{2}] \right) \dots \\
 \dots + \frac{4S_c^2 + 4}{S_c^2 + 2S_c + 1} \left(E_z^q[1, n, p + \frac{1}{2}] \right) - E_z^{q-1}[2, n, p + \frac{1}{2}]
 \end{aligned} \tag{2.45}$$

The effect of 1st- and 2nd-order Mur ABCs on a Gaussian pulse signal is shown in Figure 2.5 for the case of $S_c = 1/\sqrt{3}$. The higher-order Mur ABC can be seen to be significantly more effective at absorbing the pulse signal incident on the boundary than the 1st-order implementation, with the amplitude of spurious reflected signal smaller in the 2nd-order case by a factor of $\sim 10^{-5}$. The 2nd-order implementation however requires a longer

calculation and three extra node values to be held in memory per boundary cell (as opposed to one in the 1st-order case). It also suffers from the same drawbacks as all Mur-style ABCs: poor performance when waves are obliquely-incident, and numerical instability at later times.

2.3.2 Perfectly-Matched Layer

The analytical Mur ABC formulation described above will provide adequate termination of the FDTD computational domain under most conditions, however, it will invariably yield a small-amplitude numerical reflection error at the boundary, particularly in the case of oblique wave propagation. This reflection can lead to late-time instability in the simulation and signal-to-noise issues when attempting to measure low-amplitude fields. A popular alternative method of boundary termination is the *perfectly-matched layer* (PML), which is commonly thought of as the “state-of-the-art” method of terminating the FDTD grid. First proposed by [Berenger, 1994], the PML acts as a non-physical, artificial “lossy” layer at the edges of the FDTD domain, which will reduce the amplitude of any waves propagating towards the domain boundaries. An ideal PML will fully absorb any wave trying to leave the domain with no numerical reflection, whilst leaving waves propagating in a direction tangential to the domain boundary unaffected. In practice, all PML layers still incur a measure of spurious numerical reflection at the PML-nonPML interface, however it is usually possible to achieve significantly smaller amplitudes of unwanted reflection using a PML than by using a differential ABC. In Berenger’s original formulation, the **E** and **H** wave fields are expressed as a linear combination of separate unphysical tangential and perpendicular components, on each of which the PML acts differently; this is the “split-field” PML formulation. This splitting introduces an anisotropy to the system necessary to allow the PML to imitate an unphysical material with the exact phase and conductivity properties required to eliminate reflections at the PML-nonPML interface while providing wave absorption in the outwards propagation direction only. The split-field method, while effective, is unable to absorb evanescent waves [Berenger, 2002], meaning that any model using the split-field PML must be sufficiently large such that all evanescent waves have decayed to insignificant

amplitudes by the time they encounter the PML. The split field PML is also relatively computationally demanding, as it requires multiple time levels of each “split” field to be stored simultaneously. This form of PML has been since replaced by more effective and less computationally-heavy PML techniques. One such is the convolutional-PML (CPML) or Complex Frequency Shifted-PML (CFS-PML) formulation, first described by [Kuzuoglu and Mittra, 1996], which involves shifting the frequency-dependent pole of the unphysical lossy layer’s anisotropic relative permittivity into the imaginary plane, eliminating the need for the splitting and resulting in a well-matched boundary layer capable of dealing with both travelling and evanescent waves. The CPML derivation below follows the methodology of [Schneider, 2010] and describes the formulation of the boundary termination scheme used in subsequent chapters.

The basis of the PML is an artificially-conductive lossy region, in which a propagating wave will lose amplitude as it travels. As such, the formulation of a PML begins with the introduction of arbitrary electrical and magnetic conduction current terms to Maxwell’s curl equations to form the expressions (2.12) and (2.13) encountered above. These conduction current terms will cause the loss in amplitude required to absorb waves entering the PML layer. To suppress reflection at the PML-nonPML interface [Berenger, 1994], the *perfectly-matched* condition must be enforced:

$$\frac{\sigma_E}{\varepsilon} = \frac{\sigma_M}{\mu} \quad (2.46)$$

For ease of notation, the relative permittivity and permeability will be absorbed into the conductivity constants such that $\frac{\sigma_E}{\varepsilon} \rightarrow \frac{\sigma'_E}{\varepsilon_0}$ and $\frac{\sigma_M}{\mu} \rightarrow \frac{\sigma'_M}{\mu_0}$. Assuming plane wave solutions for \mathbf{E} and \mathbf{H} , the Fourier transform $\frac{\partial}{\partial t} \rightarrow i\omega$ can be used to rewrite equations (2.12) and (2.13) in the frequency-domain:

$$\nabla \times \mathbf{E} = -i\omega\mu\mathbf{H} - \sigma_M\mathbf{H} = -i\omega\mu \left(1 + \frac{\sigma_M}{i\omega\mu} \right) \mathbf{H} = -i\omega\mu S_M \mathbf{H} \quad (2.47)$$

$$\nabla \times \mathbf{H} = i\omega\varepsilon\mathbf{E} + \sigma_E\mathbf{E} = i\omega\varepsilon \left(1 + \frac{\sigma_E}{i\omega\varepsilon} \right) \mathbf{E} = i\omega\varepsilon S_E \mathbf{E} \quad (2.48)$$

All behaviour of the PML is contained in the S -factors. Making use of the perfectly-matched condition (2.46):

$$\begin{aligned} S_E &= 1 + \frac{\sigma'_E}{i\omega\varepsilon_0} = 1 + \frac{\sigma'_M}{i\omega\mu_0} = S_M \\ \Rightarrow S_E &= S_M = S = 1 + \frac{\sigma'}{i\omega\varepsilon_0} \end{aligned} \quad (2.49)$$

This expression encounters an infinity as $\omega \rightarrow 0$. As the PML is an inherently unphysical construction, the expression can be modified in such a way that this singularity is removed while remaining consistent:

$$S \rightarrow b + \frac{\sigma'}{a + i\omega\varepsilon_0} \quad (2.50)$$

where a and b are real constants with values greater than zero. This redefinition has the effect of moving the frequency pole of the PML relative permittivity from the real axis to the complex plane, and allows an effective PML to be formulated without the need for field splitting [Schneider, 2010].

To provide the required anisotropy such that the PML absorbs outgoing waves and leaves others unaffected, it is necessary to have an independent S -factor for each spatial direction:

$$S_j = b_j + \frac{\sigma'_j}{a_j + i\omega\varepsilon_0} \quad j = x, y, z \quad (2.51)$$

By redefining the ∇ operator, the original curl form of equations (2.47) and (2.48) can be recovered; this formulation is often referred to as a “stretched-coordinate” PML as each Cartesian direction is effectively scaled by a complex S -factor.

$$\nabla \rightarrow \tilde{\nabla} = \hat{\mathbf{x}} \left(\frac{1}{S_x} \right) \frac{\partial}{\partial x} + \hat{\mathbf{y}} \left(\frac{1}{S_y} \right) \frac{\partial}{\partial y} + \hat{\mathbf{z}} \left(\frac{1}{S_z} \right) \frac{\partial}{\partial z} \quad (2.52)$$

$$-i\omega\mu\mathbf{H} = \left(\frac{1}{S} \right) \nabla \times \mathbf{E} = \tilde{\nabla} \times \mathbf{E} \quad (2.53)$$

$$i\omega\varepsilon\mathbf{E} = \left(\frac{1}{S} \right) \nabla \times \mathbf{H} = \tilde{\nabla} \times \mathbf{H} \quad (2.54)$$

Equations (2.53) and (2.53) can be used to derive update equations for fields propagating within the PML region. Taking the E_x component of equation (2.54) as an example:

$$i\omega\epsilon E_x = \left(\frac{1}{S_y}\right) \frac{\partial H_z}{\partial y} - \left(\frac{1}{S_z}\right) \frac{\partial H_y}{\partial z} \quad (2.55)$$

Converting frequency domain equation (2.55) back into the time domain gives:

$$\epsilon \frac{\partial E_x}{\partial t} = \bar{S}_y \otimes \frac{\partial H_z}{\partial y} - \bar{S}_z \otimes \frac{\partial H_y}{\partial z} \quad (2.56)$$

where the \bar{S} -factors are defined as the inverse Fourier transform of the reciprocal S -factors:

$$\bar{S}_j = \mathcal{F}^{-1} \left[\frac{1}{S_j} \right] \quad (2.57)$$

From the definition of S_j given in (2.51), its reciprocal can be written as:

$$\frac{1}{S_j} = \frac{1}{b_j} + \frac{\frac{a_j}{a_j b_j + \sigma'_j} - \frac{1}{b_j}}{1 + i\omega \left(\frac{\epsilon_0 b_j}{a_j b_j + \sigma'_j} \right)} \quad (2.58)$$

Using (2.58) and Fourier transform pairs $1 \longleftrightarrow \delta(t)$ and $1/(1 + i\omega\tau) \longleftrightarrow (1/\tau) e^{-t/\tau} U(t)$, where $U(t)$ is the unit step function, the inverse Fourier transform of (2.57) becomes:

$$\begin{aligned} \bar{S}_j &= \frac{1}{b_j} \delta(t) + \frac{\sigma'_j}{b_j^2 \epsilon_0} \exp \left[-t \left(\frac{a_j}{\epsilon_0} + \frac{\sigma'_j}{b_j \epsilon_0} \right) \right] U(t) \\ &= \frac{1}{b_j} \delta(t) + X_j(t) \end{aligned} \quad (2.59)$$

This allows the time-domain governing equation (2.55) to be rewritten as:

$$\epsilon \frac{\partial E_x}{\partial t} = \left(\frac{1}{b_y}\right) \frac{\partial H_z}{\partial y} - \left(\frac{1}{b_z}\right) \frac{\partial H_y}{\partial z} + X_y(t) \otimes \frac{\partial H_z}{\partial y} - X_z(t) \otimes \frac{\partial H_y}{\partial z} \quad (2.60)$$

Evaluating at time $q\Delta_t$, the convolution terms in (2.60) can be written as:

$$\phi_{E_{xy}}^q = X_y(t) \otimes \frac{\partial H_z}{\partial y} |_{t=q\Delta_t} = \int_{\tau=0}^{q\Delta_t} X_y(\tau) \frac{\partial H_z(q\Delta_t - \tau)}{\partial y} d\tau$$

or more generally:

$$\phi_{E_{ij}}^q = \int_{\tau=0}^{q\Delta t} X_j(\tau) \frac{\partial H_k(q\Delta t - \tau)}{\partial j} d\tau \quad (2.61)$$

where indices $[i, j, k]$ correspond to $[x, y, z]$, $[y, z, x]$ or $[z, x, y]$. Following the procedure outlined in [Schneider, 2010], convolution term $\phi_{E_{ij}}^q$ can be expressed in recursive form:

$$\phi_{E_{ij}}^q = A_j \frac{\partial H_k^q}{\partial j} + B_j \phi_{E_{ij}}^{q-1} \quad (2.62)$$

where:

$$B_j = \exp \left[- \left(\frac{a_j}{\varepsilon_0} + \frac{\sigma'_j}{b_j \varepsilon_0} \right) \Delta_t \right] \quad (2.63)$$

$$A_j = \frac{\sigma'_j}{a_j b_j^2 + \sigma'_j b_j} (B_j - 1) \quad (2.64)$$

The value of $\phi_{E_{ij}}^q$ at each node in the PML region can be updated every time step as part of the standard update algorithm, and applied as an additive constant to any fields propagating in the PML regions. This form of the convolution term requires only one time level of the constituent fields to be stored at any one time, and is non-zero only in the PML boundary regions, meaning that relatively little extra memory is needed for implementation. From (2.60), the general update equation for the electric field within the CPML region is given by:

$$\varepsilon_0 \frac{\partial E_i}{\partial t} \Big|_{q+\frac{1}{2}} = \left(\frac{1}{b_j} \right) \frac{\partial H_k^{q+\frac{1}{2}}}{\partial j} - \left(\frac{1}{b_k} \right) \frac{\partial H_j^{q+\frac{1}{2}}}{\partial k} + \phi_{E_{ij}}^{q+\frac{1}{2}} - \phi_{E_{ik}}^{q+\frac{1}{2}} \quad (2.65)$$

A similar generalised expression can be found for the magnetic field:

$$\mu_0 \frac{\partial H_i}{\partial t} \Big|_q = \left(\frac{1}{b_k} \right) \frac{\partial E_j^q}{\partial k} - \left(\frac{1}{b_j} \right) \frac{\partial E_k^q}{\partial j} + \phi_{H_{ik}}^q - \phi_{H_{ij}}^q \quad (2.66)$$

2.4 FDTD Advantages and Limitations

From the early 1990s and the explosion of interest in computational physics, the popularity of the FDTD method has expanded considerably; growing with the advancement of computing technology and brute-force processing capability, growing further still as researchers come to appreciate the power and sheer scope of this technique. As part of the introduction to their textbook on the subject, Taflove and Hagness [Taflove and Hagness, 2000] listed seven primary reasons why FDTD has become such a popular numerical simulation technique:

1. *FDTD uses no linear algebra.*
2. *FDTD is accurate and robust.*
3. *FDTD treats impulsive behaviour naturally.*
4. *FDTD treats nonlinear behaviour naturally.*
5. *FDTD is a systematic approach.*
6. *FDTD scales with high efficiency on parallel-processing computers.*
7. *FDTD can take advantage of recent developments in computer visualisation.*

These strengths, still starkly relevant today, make the FDTD method an ideal basis for the code described in this thesis. As a tool to model electromagnetic wave propagation in space plasmas, the FDTD method has many advantages over other techniques; perhaps the most important of these is that a FDTD simulation produces solutions to the relevant governing equations that are fully explicit in time, unlike many other techniques which will only output frequency-domain steady-state sinusoidal solutions. This is particularly useful when treating complex non-linear behaviour such as ionospheric wave interactions. The time-domain nature of FDTD also leads to a greater flexibility than that found in many frequency-explicit methods, as it allows an FDTD model both to process broadband input signals and to output a wide range of frequency components in a single simulation run. The dynamic range of the sampled frequency spectrum is limited only

by the minimum time-step size and duration of simulation (or by the spatial-step size and domain dimensions for the case of spatial frequency).

Many alternative methods such as the Finite Element Method involve vast matrices of coefficients and require extensive linear algebra calculations to be performed, leading to long computing times and necessitating substantial computer memory. The FDTD method is far less computationally-intensive and thus is far less limited in its applications. The particular FDTD formulation presented in Chapter 3 of this thesis requires that field component values must only be stored in the computer memory for one time step, unlike many other similar direct-integration formulations which require multiple time steps to be stored simultaneously. Further, FDTD schemes are naturally amenable to parallelisation; each field node can be updated independently over the course of a time-step, allowing for almost 100% parallelisation during calculation, a property which was exploited to significantly accelerate the code described in this thesis using GPU technology (see Chapter 3, Section 3.3).

FDTD is ideal for modelling situations with complex geometries or media where the domain parameters vary in space as all medium parameters are specified independently at each point in the computational grid. For ionospheric simulations, the ability to set an inhomogeneous plasma background is critical. Time-varying medium parameters can easily be incorporated into the FDTD time-stepping algorithm to allow the simulation of dynamical systems such as those often found in space physics. In Chapter 3 this property is used to incorporate the time-dependent evolution of the plasma temperature and density into the FDTD time-advancement algorithm. The time-explicit coupling between the plasma medium and EM fields enabled the development of non-linear plasma waves and instabilities to proceed naturally in the simulation.

From the perspective of a researcher, the FDTD technique is intuitive and user-friendly; it is usually straightforward for a user to predict and interpret the output of a FDTD simulation, and the accuracy and sources error found in these results are well documented and understood. The time-domain nature of the model means that some data processing (for example: on-the-hoof FFT calculation) can be performed simultaneously with the

simulation, and the fact that field is known at all points in the domain lends itself to modern techniques in computer visualisation for the output of results.

Limitations of the general FDTD scheme are largely connected with the coarseness or otherwise of the grid discretisation, and by extension, to the gross capacity and brute-force power of accessible processing hardware. The applicability of a FDTD scheme to a given simulation scenario is a compromise between the raw physical properties one wishes to model and the computational resources available. The size of the computational grid must be chosen such that the longest EM wavelength and largest geometric feature can be contained within the grid boundaries. This may lead to prohibitively large domain sizes, correspondingly draining memory while increasing runtime. Likewise, the discretisation must be fine enough such that the shortest EM wavelength and smallest geometrical features present can be sampled accurately (Nyquist's theorem: at least 2 samples per oscillation period are required to sample a signal without aliasing). For example, if one wishes to study the low-frequency acoustic waves caused by the action of a high-frequency EM pulse on plasma, one must design a FDTD domain with a spatial extent sufficiently large to sample the acoustic wavelength but also with a minimum discretisation fine enough to accurately simulate the short-wavelength EM wave in both time and space. These restrictions lead to certain scenarios (for example: the modelling very long, very thin wires) being particularly difficult to simulate efficiently using FDTD, to the point that it becomes computationally infeasible.

Likewise, the CFL conditions described in Section 2.2.2 can place somewhat restrictive demands on domain parameter choice, as these dictate that discrete step sizes cannot be adjusted arbitrarily without compromising stability. A consequence of selecting an appropriately small time-step to meet the problem specifications is that this must proportionately enforce an upper limit on space-step size if the CFL criteria are to be fulfilled. These discrete parameter conditions are often difficult to meet without the use of extensive computing power, and limit the applicability of a particular FDTD scheme to situations for which the stability requirements can be met within the hardware constraints.

A further disadvantage of FDTD is that the staggered field nodes may mean that it is impossible to have a smooth or “knife-edge” boundary between media in the model, and it is often necessary to average fields or parameters at such interfaces. This may lead to small inaccuracies or numerical artefacts at these boundaries, and an unphysical distribution of parameters may be required to circumvent this issue.

In the context of simulating the propagation and interaction of radio-frequency EM waves in an ionospheric plasma, the advantages of using FDTD techniques far outweigh the detriments. Any inadequacies can in principle be solved by throwing more computing at the problem; if it is impossible, in practice, to overcome these issues completely, they can at least be suppressed such that they merely a well-understood background to a stable and accurate simulation.

Chapter 3

Development of a GPU-Accelerated FDTD Scheme for Electromagnetic Wave Interaction with Plasma

The work presented in this Chapter has been published as part of:

[Cannon and Honary, 2015] P. D. Cannon, F. Honary, 2015, *A GPU-Accelerated Finite-Difference Time-Domain Scheme for Electromagnetic Wave Interaction with Plasma*, IEEE Transactions on Antennas and Propagation, 63 (7), 3042-3054,
doi:10.1109/TAP.2015.2423710 © 2015 IEEE.

3.1 Introduction

In the previous Chapter, the *Finite-Difference Time-Domain* method was introduced as a popular and powerful technique for modelling the propagation of electromagnetic waves through a variety of media. One of the most appealing applications of the FDTD method is the study of the interaction of EM waves with plasmas, and the wide range of

instabilities and non-linear phenomena that may result; many of these processes are not fully understood and would benefit from detailed study via numerical simulation. As FDTD is well suited to the computational modelling of these scenarios, the original Yee FDTD scheme [Yee, 1966] has often been adapted to describe the propagation of EM waves through dispersive media or simple plasmas using a variety of discretisation and time-integration schemes [Joseph et al., 1991, Luebbers et al., 1991, Luebbers and Hunsberger, 1992, Hawkins and Kallman, 1993, Young and Brueckner, 1994, Chen et al., 1998]. A detailed review of plasma-fluid FDTD techniques with emphasis on the computational cost of each can be found in [Cummer, 1997]. These FDTD schemes have often been extended further to incorporate the anisotropic effect of a magnetic field on a plasma fluid. This includes, for example, the 3-dimensional scheme described by [Young, 1994], which co-locates plasma fluid velocity vector nodes with the E-field vector nodes in the computational grid for ease of coupling between the EM wave equations and the Lorentz equation of motion. This implementation includes a scalar pressure node located at the corner of each basic computational unit cell (known as the *Yee cell*; see Section 2.1.1 above) to allow a warm plasma medium to be modelled. [Lee and Kalluri, 1999] locate the plasma current nodes in the centre of the Yee cell to avoid spatial averaging between nodes and introduce a dynamic plasma medium through inclusion of a time-dependent plasma frequency that is updated between simulation steps. [Yu and Simpson, 2010] co-locate the plasma current nodes with the E-field nodes and include individual coupled equations to describe the current due to electrons and both positive and negative ion species. This scheme has been used to develop a 3D global Earth-ionosphere FDTD model which has been used to study low-frequency wave propagation [Yu and Simpson, 2012], and has the potential to be coupled to other atmospheric models as part of a multiphysics simulator. Numerical simulation of the time-dependent behaviour of the plasma medium in response to interaction with an EM wave has been performed by [Gondarenko et al., 2003] who use a 1D or 2D alternating direction implicit (ADI) finite-difference algorithm to simulate linear mode conversion processes due to a radio-frequency (RF) pump wave incident on an idealized ionospheric plasma. The numerical scheme considers “slow” timescales that are comparable to that of the plasma density evolution. This formulation is extended in [Gondarenko et al., 2005] to include updates

to the plasma temperature and density as part of the simulation algorithm to study the growth of density structures.

This Chapter presents the formulation and implementation of a 3D FDTD model which has been developed for use in modelling the propagation of high-power radio waves through a dynamic, magnetised and collisional plasma; the resulting high-performance numerical code can be used as a virtual laboratory in which many of the varied wave and plasma interactions and instabilities that may occur during an artificial ionospheric modification experiment can be investigated in detail. This formulation extends previously-established schemes with new finite-difference equations for the variation of plasma temperature and density with time, which are incorporated into the simulation update algorithm and as such allow the investigation of non-linear perturbations of the plasma medium. This FDTD scheme has been developed to study the interaction between ionospheric plasmas and radio-frequency EM waves, however the formulation is equally applicable to waves of any frequency interacting with lab-based plasma, astrophysical plasma, or any medium where a fluid plasma description holds, provided sufficient computing resources are available and that stability criteria can be met. Results of scientific investigations into ionospheric plasma processes performed using the FDTD code described in this Chapter are presented in Chapters 4, 5 and 6 below.

This Chapter is organised as follows: in Section 3.2, formation of the model's update algorithm is described, and factors contributing to the stability and accuracy of the scheme are discussed. In Section 3.3, the possibility of accelerating the FDTD code using GPU technology is explored, and found to be of great benefit to code performance. Section 3.4 presents a series of numerical tests performed to validate the performance of the FDTD scheme, in which simulation results are compared to the predictions of plasma theory and benchmarked against results provided by the VORPAL 4.2.2 software [Nieter and Cary, 2004].

3.2 Methodology

3.2.1 Governing Equations

The formation of the FDTD algorithm assumes a multi-fluid description of a dynamic, anisotropic, collisional plasma, in which electron or charged ion species are treated as individual fluids of continuous mass and charge, as introduced in Section 1.3.2 above. The effect on wave propagation due to the presence of plasma is introduced through the coupling of Maxwell's wave equations with the Lorentz equations of motion for each constituent plasma species, with anisotropy introduced through inclusion of a static externally-applied magnetic field. The time-dependent variation of plasma temperature and density are treated by the inclusion of expressions for the dynamic behaviors of small perturbations of the plasma fluid temperature and density [Gurevich, 1978, Robinson, 1989]. Together, these form a set of coupled first-order partial differential equations which govern the time dependent behavior of the EM wave and plasma medium, as given in Section 1.3.2 previously:

$$\nabla \times \mathbf{E} = -\mu_0 \frac{\partial \mathbf{H}}{\partial t} \quad (3.1)$$

$$\nabla \times \mathbf{H} - \sum_a N_a e_a \mathbf{U}_a = \epsilon_0 \frac{\partial \mathbf{E}}{\partial t} \quad (3.2)$$

$$N_a m_a \frac{\partial \mathbf{U}_a}{\partial t} = N_a e_a (\mathbf{E} + \mathbf{U}_a \times \mathbf{B}) - N_a m_a \nu_a \mathbf{U}_a - \nabla (k_B N_a T_a) \quad (3.3)$$

$$\frac{\partial N_a}{\partial t} + \nabla \cdot (N_a \mathbf{U}_a) = 0 \quad (3.4)$$

$$\frac{3}{2} k_B \frac{\partial}{\partial t} (N_a T_a) + \nabla \cdot \mathbf{Q}_a - N_a e_a \mathbf{E} \cdot \mathbf{U}_a - \Delta \epsilon_a = 0 \quad (3.5)$$

In these expressions, subscript a refers to plasma component species. \mathbf{U} is the time-varying fluid bulk velocity vector, $\mathbf{B} = B \hat{\mathbf{b}}$ is the static background magnetic flux density, T and N are the plasma temperature and number density, ν is the effective collision frequency, $\nabla \cdot \mathbf{Q}$ describes the heat flux transport and $\Delta \epsilon$ is a collisional heating term. These expressions reduce to that of an unmagnetised plasma on removal of the \mathbf{B} term, or a collisionless plasma on removal of the ν term.

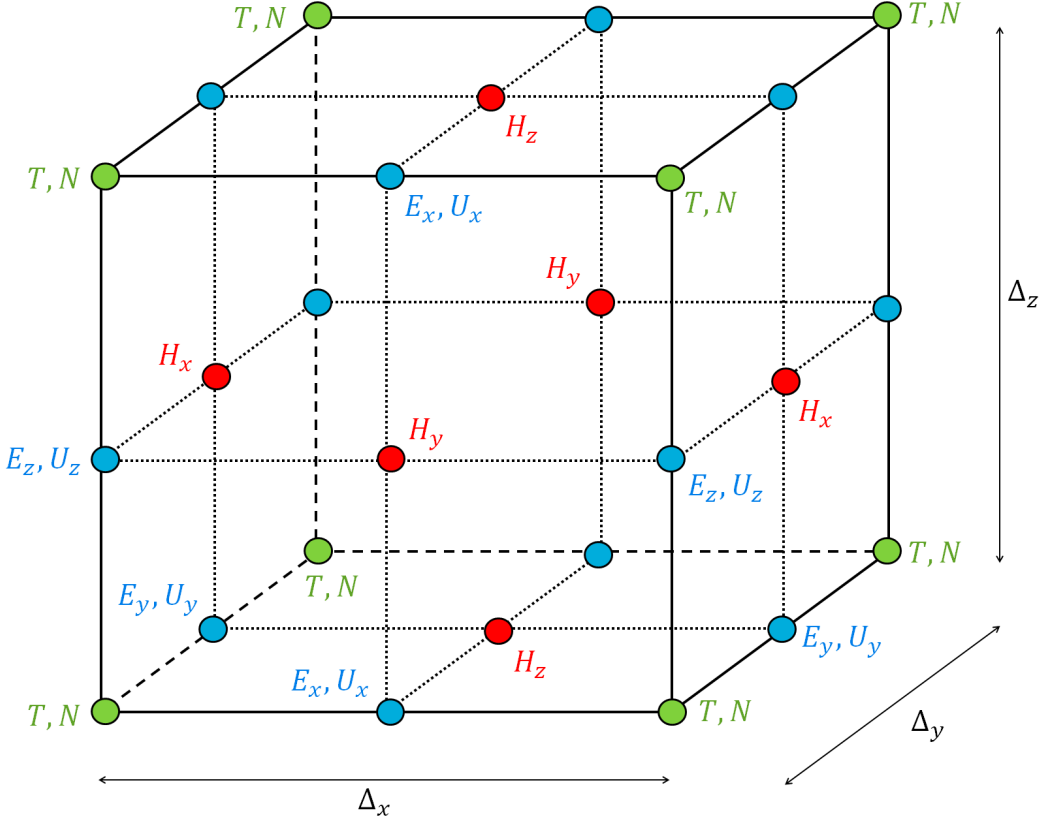


FIGURE 3.1: The basic computational grid unit cell, with the positions of field nodes indicated. *Image reproduced from [Cannon and Honary, 2015] © 2015 IEEE.*

3.2.2 Discretisation Scheme

The set of governing equations (3.1-3.5) is amenable to a full finite-difference treatment. The discretisation scheme used in this model is shown in Figure 3.1, which shows the spatial location of the electric field, magnetic field and fluid velocity vector components, along with the temperature and density scalar nodes, in a grid unit cell; this is similar to the original Yee cell shown in Figure 2.1, but with the addition of extra nodes related to the plasma. The **E** and **U** component nodes are taken to lie on the same points of the grid to facilitate efficient coupling between the electric field and the plasma, with E_x and U_x located at $(m + \frac{1}{2}, n, p)$, E_y and U_y located at $(m, n + \frac{1}{2}, p)$ and E_z and U_z located at $(m, n, p + \frac{1}{2})$, where m , n and p are integer coordinates describing the x , y and z Cartesian position of a node in the computational grid in units of the discrete special steps Δ_x , Δ_y and Δ_z respectively. To provide a finite differencing scheme consistent with the curl operators in Maxwell's equations (3.1) and (3.2), the **H** nodes are spatially offset

from the **E** nodes, with H_x located at $(m, n + \frac{1}{2}, p + \frac{1}{2})$, H_y located at $(m + \frac{1}{2}, n, p + \frac{1}{2})$ and H_z located at $(m + \frac{1}{2}, n + \frac{1}{2}, p)$. Temperature and density nodes are located at (m, n, p) in each cell to allow accurate finite-difference evaluation of the grad and div operations in (3.3) - (3.5). To facilitate consistent evaluation of the temporal partial derivatives, the **E**, **T** and **N** nodes are calculated at integer values of discrete time step $q\Delta_t$ (where q is an integer) while the **H** and **U** nodes are calculated at half-integer time steps $(q + \frac{1}{2})\Delta_t$.

3.2.2.1 Update Equation for Magnetic Field

The formation of the FDTD update equations for the magnetic field is well established and proceeds as described in Section 2.1.3. For the calculations below, equal spatial step sizes will be assumed in all grid directions ($\Delta_x = \Delta_y = \Delta_z$). Independent update equations for the H_x , H_y and H_z components are shown in (3.6), where the notation $H_x^{q+\frac{1}{2}}[m, n + \frac{1}{2}, p + \frac{1}{2}]$ represents the value of H_x that exists at point $(m, n + \frac{1}{2}, p + \frac{1}{2})$ in the FDTD grid at time step $q + \frac{1}{2}$.

3.2.2.2 Update Equation for Electric Field

The classic Yee method outlined in Section 2.1.3 is likewise followed to form update equations for the E nodes. The location of the $E_{x,y,z}$ and $U_{x,y,z}$ nodes at the same point of the fundamental grid cell allows the Yee formulation to be easily extended to include the term coupling the E-field to the particle velocity in a similar method to [Yu and Simpson, 2012] with no loss of accuracy due to spatial or temporal averaging. The complete **E** node update equations are shown in (3.7).

3.2.2.3 Update Equation for Fluid Velocity

FDTD treatment of plasma fluid velocity is well established and proceeds here following the methods similar to that of [Young, 1994]. The temporal partial differential in (3.3) is expanded as a finite-difference approximation about integer time step q . As the **U**

$$\begin{aligned}
& \left\{ \begin{array}{l} H_x^{q+1/2}[m, n + \frac{1}{2}, p + \frac{1}{2}] \\ H_y^{q+1/2}[m + \frac{1}{2}, n, p + \frac{1}{2}] \\ H_z^{q+1/2}[m + \frac{1}{2}, n + \frac{1}{2}, p] \end{array} \right\} = \left\{ \begin{array}{l} H_x^{q-1/2}[m, n + \frac{1}{2}, p + \frac{1}{2}] \\ H_y^{q-1/2}[m + \frac{1}{2}, n, p + \frac{1}{2}] \\ H_z^{q-1/2}[m + \frac{1}{2}, n + \frac{1}{2}, p] \end{array} \right\} \dots \\
& \dots - \frac{\Delta_t}{\mu_0 \Delta x} \left\{ \begin{array}{l} E_z^q[m, n + 1, p + \frac{1}{2}] - E_z^q[m, n, p + \frac{1}{2}] - E_y^q[m, n + \frac{1}{2}, p + 1] + E_y^q[m, n + \frac{1}{2}, p] \\ E_x^q[m + \frac{1}{2}, n, p + 1] - E_x^q[m + \frac{1}{2}, n, p] - E_z^q[m + 1, n, p + \frac{1}{2}] + E_y^q[m, n, p + \frac{1}{2}] \\ E_y^q[m + 1, n + \frac{1}{2}, p] - E_y^q[m, n + \frac{1}{2}, p] - E_x^q[m + \frac{1}{2}, n + 1, p] + E_x^q[m + \frac{1}{2}, n, p] \end{array} \right\} \quad (3.6) \\
& \left\{ \begin{array}{l} E_x^{q+1}[m + \frac{1}{2}, n, p] \\ E_y^{q+1}[m, n + \frac{1}{2}, p] \\ E_z^{q+1}[m, n, p + \frac{1}{2}] \end{array} \right\} = \left\{ \begin{array}{l} E_x^q[m + \frac{1}{2}, n, p] \\ E_y^q[m, n + \frac{1}{2}, p] \\ E_z^q[m, n, p + \frac{1}{2}] \end{array} \right\} - \left(\frac{e_a \Delta t}{\varepsilon_0} \right) \sum_a \left\{ \begin{array}{l} N_a^{q+1/2}[m + \frac{1}{2}, n, p] \cdot U_{x,a}^{q+1/2}[m + \frac{1}{2}, n, p] \\ N_a^{q+1/2}[m, n + \frac{1}{2}, p] \cdot U_{y,a}^{q+1/2}[m, n + \frac{1}{2}, p] \\ N_a^{q+1/2}[m, n, p + \frac{1}{2}] \end{array} \right\} \dots \\
& \dots + \frac{\Delta_t}{\varepsilon_0 \Delta x} \left\{ \begin{array}{l} H_z^{q+1/2}[m + \frac{1}{2}, n + \frac{1}{2}, p] - H_z^{q+1/2}[m + \frac{1}{2}, n, p + \frac{1}{2}] - H_y^{q+1/2}[m + \frac{1}{2}, n, p - \frac{1}{2}] + H_y^{q+1/2}[m + \frac{1}{2}, n, p - \frac{1}{2}] \\ H_x^{q+1/2}[m, n + \frac{1}{2}, p + \frac{1}{2}] - H_x^{q+1/2}[m, n + \frac{1}{2}, p - \frac{1}{2}] - H_z^{q+1/2}[m + \frac{1}{2}, n + \frac{1}{2}, p] + H_z^{q+1/2}[m - \frac{1}{2}, n + \frac{1}{2}, p] \\ H_y^{q+1/2}[m + \frac{1}{2}, n, p + \frac{1}{2}] - H_y^{q+1/2}[m - \frac{1}{2}, n, p + \frac{1}{2}] - H_x^{q+1/2}[m, n + \frac{1}{2}, p + \frac{1}{2}] + H_x^{q+1/2}[m, n - \frac{1}{2}, p + \frac{1}{2}] \end{array} \right\} \quad (3.7)
\end{aligned}$$

nodes are only known at half-integer time steps, the undifferentiated \mathbf{U} terms on the right-hand side of (3.3) must be temporally averaged around q as shown by (3.8):

$$\mathbf{U}^q = \frac{\mathbf{U}^{q+\frac{1}{2}} + \mathbf{U}^{q-\frac{1}{2}}}{2} \quad (3.8)$$

Semi-implicit averaging of this nature has been encountered in Section 2.1.3 of the previous Chapter. The $\mathbf{U} \times \mathbf{B}$ cross product in (3.3) introduces coupling between \mathbf{U} components, thus to maintain consistency the equation must be rearranged using matrices \mathbf{S} (3.10) and \mathbf{R} (3.11) to give an update equation for $\mathbf{U}^{q+\frac{1}{2}}$ in terms of past values \mathbf{U}^q , shown in (3.9). In this expression, ω_{ca} refers to the cyclotron frequency of plasma species a .

Four-node spatial averaging is required when no node of a particular type exists at the desired location of the Yee cell. For example, the $E_x[m, n + \frac{1}{2}, p]$ value required in (3.9) does not exist as a predefined node, but can be formed by spatial averaging of the four surrounding E_x nodes equidistant from the desired reference point, as shown in (3.13):

$$E_x[m, n + \frac{1}{2}, p] = \frac{1}{4} \left(E_x[m + \frac{1}{2}, n, p] + E_x[m + \frac{1}{2}, n + 1, p] \dots \right. \\ \left. \dots + E_x[m - \frac{1}{2}, n, p] + E_x[m - \frac{1}{2}, n + 1, p] \right) \quad (3.13)$$

This treatment is applied to all cases where the value of a variable is required at a grid position where no update node exists. Collisions are treated using an effective collision frequency term $\nu_a = \nu_{an} + \sum_b \nu_{ab}$ for each species, which can be set independently at each node. This expression encompasses collisions with neutral particles through ν_{an} and collisions with the other plasma species present in the simulation through the ν_{ab} terms. In reality the effective collision frequency will vary with time due to changes in particle temperature and density, however for the purposes of this Chapter it is kept constant after initialisation. In future Chapters, the collision frequency is calculated each time step using the simulated density and temperature values (see Chapter 4, Section 4.2, below for more details). The grad term coupling the particle fluid velocity to the temperature and density $\nabla(k_B N_a T_a)$ in (3.3) is evaluated by finite difference

$$\mathbf{U}_a^{q+1/2} = \mathbf{R}_a \cdot \mathbf{U}_a^{q-1/2} + \left(\frac{e_a \Delta t}{m_a} \right) \mathbf{S}_a^{-1} \cdot \mathbf{E}^q + \left(\frac{k_B \Delta t}{m_a N_a^q} \right) \mathbf{S}_a^{-1} \cdot (\nabla N_a^q T_a^q) \quad (3.9)$$

$$\mathbf{S}_a = \left\{ \mathbf{I} - \frac{1}{2} \Delta_t \begin{pmatrix} -\nu_a & -\omega_{ca} b_z & \omega_{ca} b_y \\ \omega_{ca} b_z & -\nu_a & -\omega_{ca} b_x \\ -\omega_{ca} b_y & \omega_{ca} b_x & -\nu_a \end{pmatrix} \right\} \quad (3.10)$$

$$\begin{cases} U_x^{q+\frac{1}{2}} [m + \frac{1}{2}, n, p] \\ U_y^{q+\frac{1}{2}} [m, n + \frac{1}{2}, p] \\ U_z^{q+\frac{1}{2}} [m, n, p + \frac{1}{2}] \end{cases} = \begin{cases} [R_a]^{00} U_x^{q-\frac{1}{2}} [m + \frac{1}{2}, n, p] + [R_a]^{01} U_y^{q-\frac{1}{2}} [m + \frac{1}{2}, n, p] + [R_a]^{02} U_z^{q-\frac{1}{2}} [m + \frac{1}{2}, n, p] \\ [R_a]^{10} U_x^{q-\frac{1}{2}} [m, n + \frac{1}{2}, p] + [R_a]^{11} U_y^{q-\frac{1}{2}} [m, n + \frac{1}{2}, p] + [R_a]^{12} U_z^{q-\frac{1}{2}} [m, n + \frac{1}{2}, p] \\ [R_a]^{20} U_x^{q-\frac{1}{2}} [m, n, p + \frac{1}{2}] + [R_a]^{21} U_y^{q-\frac{1}{2}} [m, n, p + \frac{1}{2}] + [R_a]^{22} U_z^{q-\frac{1}{2}} [m, n, p + \frac{1}{2}] \end{cases} \dots$$

$$\dots + \left(\frac{k_B \Delta t}{m_a \Delta x} \right) \begin{bmatrix} [S_a^{-1}]^{00} (T_a^q [m + 1, n, p] - T_a^q [m, n, p]) + [S_a^{-1}]^{01} (T_a^q [m, n + \frac{1}{2}, p] - T_a^q [m, n - \frac{1}{2}, p]) + [S_a^{-1}]^{02} (T_a^q [m, n, p + \frac{1}{2}] - T_a^q [m, n, p - \frac{1}{2}]) \\ [S_a^{-1}]^{10} (T_a^q [m + \frac{1}{2}, n, p] - T_a^q [m - \frac{1}{2}, n, p]) + [S_a^{-1}]^{11} (T_a^q [m, n + 1, p] - T_a^q [m, n, p]) + [S_a^{-1}]^{12} (T_a^q [m, n, p + \frac{1}{2}] - T_a^q [m, n, p - \frac{1}{2}]) \\ [S_a^{-1}]^{20} (T_a^q [m + \frac{1}{2}, n, p] - T_a^q [m - \frac{1}{2}, n, p]) + [S_a^{-1}]^{21} (T_a^q [m, n + \frac{1}{2}, p] - T_a^q [m, n, p + \frac{1}{2}]) + [S_a^{-1}]^{22} (T_a^q [m, n, p + 1] - T_a^q [m, n, p]) \end{bmatrix}$$

$$\dots + \left(\frac{e_a \Delta t}{m_a} \right)^T \begin{bmatrix} N_a^q [m + \frac{1}{2}, n, p] \\ N_a^q [m + \frac{1}{2}, n, p] \\ T_a^q [m, n + \frac{1}{2}, p] \\ N_a^q [m, n + \frac{1}{2}, p] \\ T_a^q [m, n, p + \frac{1}{2}] \\ N_a^q [m, n, p + \frac{1}{2}] \end{bmatrix} \cdot \begin{cases} [S_a^{-1}]^{00} (N_a^q [m + 1, n, p] - N_a^q [m, n, p]) + [S_a^{-1}]^{01} (N_a^q [m, n + \frac{1}{2}, p] - N_a^q [m, n, p + \frac{1}{2}]) \\ [S_a^{-1}]^{10} (N_a^q [m + \frac{1}{2}, n, p] - N_a^q [m - \frac{1}{2}, n, p]) + [S_a^{-1}]^{11} (N_a^q [m, n + 1, p] - N_a^q [m, n, p]) + [S_a^{-1}]^{12} (N_a^q [m, n, p + \frac{1}{2}] - N_a^q [m, n, p - \frac{1}{2}]) \\ [S_a^{-1}]^{20} (N_a^q [m + \frac{1}{2}, n, p] - N_a^q [m - \frac{1}{2}, n, p]) + [S_a^{-1}]^{21} (N_a^q [m, n + \frac{1}{2}, p] - N_a^q [m, n, p - \frac{1}{2}]) + [S_a^{-1}]^{22} (N_a^q [m, n, p + 1] - N_a^q [m, n, p]) \end{cases} \dots$$

$$\dots + \left(\frac{e_a \Delta t}{m} \right) \begin{cases} [S_a^{-1}]^{00} E_x^q [m + \frac{1}{2}, n, p] + [S_a^{-1}]^{01} E_y^q [m + \frac{1}{2}, n, p] + [S_a^{-1}]^{02} E_z^q [m + \frac{1}{2}, n, p] \\ [S_a^{-1}]^{10} E_x^q [m, n + \frac{1}{2}, p] + [S_a^{-1}]^{11} E_y^q [m, n + \frac{1}{2}, p] + [S_a^{-1}]^{12} E_z^q [m, n + \frac{1}{2}, p] \\ [S_a^{-1}]^{20} E_x^q [m, n, p + \frac{1}{2}] + [S_a^{-1}]^{21} E_y^q [m, n, p + \frac{1}{2}] + [S_a^{-1}]^{22} E_z^q [m, n, p + \frac{1}{2}] \end{cases} \quad (3.12)$$

approximation about the points $(m + \frac{1}{2}, n, p)$, $(m, n + \frac{1}{2}, p)$ and $(m, n, p + \frac{1}{2})$ for the U_x , U_y and U_z update equations respectively. Further spatial averaging is required to perform this operation. The complete \mathbf{U} node update equations are shown in (3.12). In this expression, the notation $[R]^{ij}$ refers to the value located at the i^{th} row and j^{th} column of matrix \mathbf{R} .

3.2.2.4 Update Equation for Plasma Density and Temperature

Development of this code was motivated by the need for a numerical scheme capable of performing detailed simulations of ionospheric heating experiments; as such, it was important for the scheme to be able to simulate the response of the ionospheric plasma medium to an incident EM wave. To accomplish this, the FDTD techniques described in Section 3.2.2.1 - Section 3.2.2.3 above were augmented with new time-explicit update equations to simulate changes to the plasma density and temperature. Including on-grid updates for perturbations to the plasma medium in the time-stepping algorithm allows non-linear plasma processes such as the self-focusing instability to be simulated. A standard first-order linearisation technique such as that described in [Inan and Golkowski, 2011] was used to express N and T as combinations of a constant background part and a small time-dependent perturbation part such that $N(t) = N_0 + \tilde{N}(t)$ and $T(t) = T_0 + \tilde{T}(t)$. Equations (3.4) and (3.5) are reformed using the linearised fields such that they become expressions describing the time-dependent behaviour of the perturbed parts only. Update equation formation then proceeds via finite difference approximation about time step $q + \frac{1}{2}$ and point (m, n, p) . Averaging between nodes is required to ensure consistent evaluation of the grad and div terms in each expression.

A variety of forms can be used for the heat flux transport $\nabla \cdot \mathbf{Q}_a$ and collisional heating $\Delta\epsilon_a$ terms in (3.5), however care must be taken as not all valid expressions are amenable to the finite-differencing scheme used here. As this model has been developed for use in simulation of wave-plasma interactions in the ionosphere an elastic expression [Robinson, 1989] is used for the collisional term, with $\Delta\epsilon_a = -\frac{N_a m_a \nu_a}{m_a + m_0} [3(T_0 - T_a) + m_0 U_a^2]$, where m_0 and T_0 represent the mass and temperature of background species. A further term taking

$$\tilde{N}_a^{q+1}[m, n, p] = \left(\frac{1 - \frac{\Delta t}{2} \nabla \cdot \mathbf{U}_a^{q+1/2}}{1 + \frac{\Delta t}{2} \nabla \cdot \mathbf{U}_a^{q+1/2}} \right) \tilde{N}_a^q[m, n, p] - \frac{\Delta t}{1 + \frac{\Delta t}{2} \nabla \cdot \mathbf{U}_a^{q+1/2}} \left(N_{a0}[m, n, p] \nabla \cdot \mathbf{U}_a^{q+1/2} + \mathbf{U}_a^{q+1/2} \cdot \nabla (N_{a0}) - \Delta N_a \right) \quad (3.14)$$

where:

$$\nabla \cdot \mathbf{U}_a^{q+1/2} = \frac{1}{\Delta x} \left(U_x^{q+1/2} [m + \frac{1}{2}, n, p] - U_x^{q+1/2} [m - \frac{1}{2}, n, p] + U_y^{q+1/2} [m, n + \frac{1}{2}, p] - U_y^{q+1/2} [m, n - \frac{1}{2}, p] + U_z^{q+1/2} [m, n, p + \frac{1}{2}] - U_z^{q+1/2} [m, n, p - \frac{1}{2}] \right)$$

$$\begin{aligned} \mathbf{U}_a^{q+1/2} \cdot \nabla (N_{a0}) &= \frac{1}{2 \Delta x} \left\{ U_x^{q+1/2} [m, n, p] (N_{a0}[m + 1, n, p] - N_{a0}[m - 1, n, p]) \dots \right. \\ &\quad \dots + U_y^{q+1/2} [m, n, p] (N_{a0}[m, n + 1, p] - N_{a0}[m, n - 1, p]) + U_z^{q+1/2} [m, n, p] (N_{a0}[m, n, p + 1] - N_{a0}[m, n, p - 1]) \left. \right\} \end{aligned}$$

$$\tilde{T}_a^{q+1}[m, n, p] = \frac{1}{1 - A/2} \left\{ (1 + A/2) \tilde{T}_a^q[m, n, p] + AT_{a0}[m, n, p] + \frac{2 \Delta t}{3k_B} \left(e_a \mathbf{E}^{q+1/2} \cdot \mathbf{U}_a^{q+1/2} + \frac{\Delta \varepsilon_a^{q+1/2} - \nabla \cdot \mathbf{Q}_a^{q+1/2}}{N_{a0}[m, n, p] + \tilde{N}_a^{q+1/2}[m, n, p]} \right) \right\} \quad (3.15)$$

where:

$$A = \Delta t \nabla \cdot \mathbf{U}_a^{q+1/2} + \Delta t \left\{ \frac{\mathbf{U}_a^{q+1/2} \cdot \nabla (N_{a0} + \tilde{N}_a^{q+1/2}) - \Delta N_a}{N_{a0}[m, n, p] + \tilde{N}_a^{q+1/2}[m, n, p]} \right\}$$

$$\mathbf{E}^{q+1/2} \cdot \mathbf{U}_a^{q+1/2} = E_x^{q+1/2} [m, n, p] \cdot U_x^{q+1/2} [m, n, p] + E_y^{q+1/2} [m, n, p] \cdot U_y^{q+1/2} [m, n, p] + E_z^{q+1/2} [m, n, p]$$

$$\begin{aligned} \mathbf{U}_a \cdot \nabla (N_{a0} + \tilde{N}_a^{q+1/2}) &= \frac{1}{2 \Delta x} \left\{ U_x^{q+1/2} [m, n, p] (N_{a0}[m + 1, n, p] - N_{a0}[m - 1, n, p] + \tilde{N}_a^{q+1/2}[m + 1, n, p] - \tilde{N}_a^{q+1/2}[m - 1, n, p]) \dots \right. \\ &\quad \dots + U_y^{q+1/2} [m, n, p] (N_{a0}[m, n + 1, p] - N_{a0}[m, n - 1, p] + \tilde{N}_a^{q+1/2}[m, n + 1, p] - \tilde{N}_a^{q+1/2}[m, n - 1, p]) \dots \\ &\quad \dots + U_z^{q+1/2} [m, n, p] (N_{a0}[m, n, p + 1] - N_{a0}[m, n, p - 1] + \tilde{N}_a^{q+1/2}[m, n, p + 1] - \tilde{N}_a^{q+1/2}[m, n, p - 1]) \left. \right\} \quad (3.16) \end{aligned}$$

into account inelastic collisions $\frac{3}{2}N_eR(T_e - T_0)$ is included in the electron temperature update equation, where R is the heat loss per electron to the background species. A simple heat flux density expression of $\mathbf{Q}_a = \kappa_a k_B \nabla T_a$ is used, with thermal conductivity κ_a taken to be $N_a k_B T_a / m_a \nu_a$. As both collisional and heat transport terms are functions of T , these must be temporally averaged and the update equation rearranged to give an expression for T^{q+1} only.

The final form of the update equations for the density and temperature are shown by (3.14) and (3.15) respectively.

3.2.2.5 Full Update Algorithm

The complete set of update equations (3.7), (3.6), (3.12), (3.14) and (3.15) naturally lend themselves to a leapfrog time-stepping scheme, following the cyclical update pattern: $\mathbf{E}^q \rightarrow T^q \rightarrow \mathbf{H}^{q+\frac{1}{2}} \rightarrow \mathbf{U}^{q+\frac{1}{2}} \rightarrow N^{q+1} \rightarrow \mathbf{E}^{q+1} \rightarrow \dots$ Special processes such as source injectors or boundary conditions can be added into this cycle at the appropriate points to complete the update algorithm.

3.2.3 Stability and Accuracy

An important consideration in any FDTD scheme is the stability of the model. As introduced in Chapter 2, Section 2.2.2, stability in the FDTD domain is heavily dependent on the choice of computational grid parameters. In an unstable simulation, small numerical artifacts may grow rapidly with time to the extent that they may alter or obscure the simulation results. Stability is enforced by the Courant condition, which limits the ratio between the temporal and spatial discrete steps in the simulation. For a 3-dimensional grid simulating free space, this condition is given by (3.17) [Taflove and Hagness, 2000]:

$$c\Delta t \leq \frac{1}{\sqrt{\left(\frac{1}{\Delta_x}\right)^2 + \left(\frac{1}{\Delta_y}\right)^2 + \left(\frac{1}{\Delta_z}\right)^2}} \quad (3.17)$$

which can be expressed as $S_c \equiv c\Delta_t/\Delta_x \leq 1/\sqrt{3}$ for the case of equally-sized spatial steps in all directions. The Courant condition effectively ensures that energy in the simulation is not able to propagate through more than one grid cell per time step. This free-space expression for stability condition can be modified by the addition of the plasma velocity to the FDTD update scheme. It has been shown previously that in similar time-explicit calculation systems with **E** and **U** nodes located at the same spatial points on the Yee grid and **H** and **U** nodes collocated in time, that the Courant condition is dependent not only on the grid parameters but also on the plasma medium contained within the simulation domain [Young, 1994]. For an unmagnetised, collisionless plasma, the stability condition is given by equation (3.18) [Young, 1994]:

$$c\Delta_t \leq \sqrt{\frac{1 - \left(\frac{\omega_p \Delta_t}{2}\right)^2}{\left(\frac{1}{\Delta_x}\right)^2 + \left(\frac{1}{\Delta_y}\right)^2 + \left(\frac{1}{\Delta_z}\right)^2}} \quad (3.18)$$

which implies a further restriction on the discrete time step $\omega_p \Delta_t \leq 2$.

The effect of collisions or magnetically-introduced anisotropy on stability is more difficult to quantify analytically, however it has been shown by [Cummer, 1997] that direct-integration FDTD schemes are stable at the unmagnetised Courant limit for all non-zero values of $\nu_c \Delta_t$. The applicability of the non-magnetised limit to collisional and anisotropic situations has been tested numerically by [Hu and Cummer, 2006] for a time-implicit implementation, and is further verified for the time-explicit scheme presented here by the validation tests described in Section 3.4.

The FDTD technique is inherently approximate, so it is important to be able to assess the accuracy of a particular scheme. The discrete nature of the FDTD grid introduces both a numerical phase error to signals travelling through the computational domain (numerical dispersion) and an energy dissipation error (numerical dissipation) which must be accounted for. Both quantities are heavily dependent on the choice of discretisation parameters used in the FDTD grid. Numerical dispersion in the FDTD domain has been discussed for the case of free-space in Chapter 2, Section 2.2.1. The accuracy of the plasma-fluid FDTD scheme for a particular set of grid parameters can be gauged

using a dispersion analysis of the type presented in [Cummer, 1997]. This approach is equivalent to the standard dispersion calculation for an electromagnetic wave propagating through plasma in continuous space introduced in Section 1.4.1, but with the assumed plane-wave form of the constituent wave fields substituted for a numerical-world equivalent that takes into account the discrete nature of the grid:

$$e^{-i(\omega t - k_x x - k_y y - k_z z)} \rightarrow e^{-i(\omega q \Delta_t - k_x m \Delta_x - k_y n \Delta_y - k_z p \Delta_z)} \quad (3.19)$$

As described in Section 2.2.1 above, this has the effect of transforming the continuous-space partial differential operator Fourier pairs $\frac{\partial}{\partial t} \rightarrow i\omega$ and $\nabla \rightarrow -i\mathbf{k}$ into their discrete-space analogues:

$$\frac{\partial}{\partial t} \rightarrow i \left(\frac{2}{\Delta_t} \right) \sin \left(\frac{\omega \Delta_t}{2} \right) \quad (3.20)$$

$$\nabla \rightarrow -i \left(\frac{2}{\Delta_j} \right) \sin \left(\frac{k_j \Delta_j}{2} \right) \hat{\mathbf{j}} \quad \text{for } j = x, y, z \quad (3.21)$$

It can be seen from (3.20) and (3.21) that as the discrete steps approach zero, the continuous-space expressions are recovered. By applying relations (3.20) and (3.21) to (3.1) and (3.2), time-harmonic versions of Maxwell's wave equations can be formed for plane waves propagating in the numerical domain:

$$-\left(\frac{2}{\Delta_j} \right) \sin \left(\frac{k_j \Delta_j}{2} \right) \hat{\mathbf{j}} \times \mathbf{E} = -\mu_0 \left(\frac{2}{\Delta_t} \right) \sin \left(\frac{\omega \Delta_t}{2} \right) \mathbf{H} \quad (3.22)$$

$$-i \left(\frac{2}{\Delta_j} \right) \sin \left(\frac{k_j \Delta_j}{2} \right) \hat{\mathbf{j}} \times \mathbf{H} - \sum_a N_a e_a \mathbf{U}_a = i\varepsilon_0 \left(\frac{2}{\Delta_t} \right) \sin \left(\frac{\omega \Delta_t}{2} \right) \mathbf{E} \quad (3.23)$$

An expression for the frequency-dependent refractive index in the numerical domain can then be derived starting from (3.22) and (3.23), with the \mathbf{U} term in (3.23) eliminated via substitution of a numerical time-harmonic version of (3.3):

$$i \left(\frac{2}{\Delta_t} \right) \sin \left(\frac{\omega \Delta_t}{2} \right) \mathbf{U}_a = \frac{e_a}{m_a} (\mathbf{E} + \mathbf{U}_a \times \mathbf{B}) - \nu_a \mathbf{U}_a \quad (3.24)$$

Note that for this calculation a homogeneous plasma density and temperature has been assumed, as the thermal and acoustic speeds typically found in an ionospheric plasma is significantly less than the EM wave propagation velocity ($\frac{v_T}{c}, \frac{c_s}{c} \ll 1$) and thus the inclusion of finite temperature or density inhomogeneities add a negligibly small perturbation to the EM wave dispersion relation. A static magnetic field in the z -direction has been assumed, with wave propagation constrained to occur in the xz -plane. From here, the derivation follows the standard refractive index calculation for oblique plane wave propagation in a magnetised, collisional plasma introduced in Chapter 1 (see also: [Inan and Golkowski, 2011] and others) and leads to the expression shown in (3.25):

$$n^2 = \frac{c^2 K^2}{\Omega^2}$$

$$= 1 - \frac{\left(\frac{\omega_p}{\Omega}\right)^2}{1 - i\left(\frac{\nu_c}{\Omega}\right) + \frac{\omega_c^2 \sin^2 \theta}{2(\Omega^2 - \omega_p^2 - i\nu_c\Omega)} \pm \left[\left\{ \frac{\omega_c^2 \sin^2 \theta}{2(\Omega^2 - \omega_p^2 - i\nu_c\Omega)} \right\}^2 + \left(\frac{\omega_p}{\Omega}\right)^2 \cos^2 \theta \right]^{\frac{1}{2}}}$$
(3.25)

This is similar to the familiar Appelton-Hartree equation [Ginzburg, 1970] for oblique wave propagation, but with the continuous-space frequency replaced by the numerical equivalent Ω , given in (3.26):

$$\Omega = \frac{2}{\Delta t} \sin\left(\frac{\omega \Delta t}{2}\right) \quad (3.26)$$

In this expression ω_p represents the fundamental plasma frequency, ω_c is the cyclotron frequency and θ is the angle between the external B-field and the direction of wave propagation. In the unmagnetised, collisionless limit, dispersion relation (3.25) can be used to derive stability criterion (3.18).

To assess the accuracy of the FDTD scheme, the frequency dependence of the discrete-space refractive index was calculated for a range of discretisation regimes. Medium parameters were fixed such that $\omega_p = 1.78 \times 10^7 \text{ rad s}^{-1}$, $\omega_c = 8.18 \times 10^6 \text{ rad s}^{-1}$ and $\nu_c = 500 \text{ s}^{-1}$ for an electron-only plasma. These were chosen to be typical of the ionospheric F-region conditions that this code was developed to investigate. The magnetic field direction was set to be $\theta = \frac{\pi}{4}$ from the z -axis in the xz -plane, with wave propagation

taken to be along the z -direction. The Courant number was chosen to be $S_c = \frac{c\Delta t}{\Delta_x} = 0.5$ to ensure stability, with spatial step sizes set to be equal in each grid direction ($\Delta_x = \Delta_y = \Delta_z$). Discretisation was varied by changing the size of discrete time step Δ_t (changing this parameter also scaled the discrete spatial step size through the relationship with fixed S_c). The equivalent refractive index for non-discrete continuous space was calculated from (3.25) and (3.26) in the limit $\Delta_t, \Delta_{x,y,z} \rightarrow 0$. In this limit, $\Omega \rightarrow \omega$ and (3.25) reverts to the familiar non-numerical Appelton-Hartree equation. The error between the numerical refractive index curve and its continuous-space counterpart is then calculated using (3.27).

$$\text{error}(\omega) = \left| \frac{n_{\text{continuous}}(\omega) - n_{\text{numerical}}(\omega)}{n_{\text{continuous}}(\omega)} \right| \quad (3.27)$$

By considering the real part of the refractive index, the numerical dispersion error introduced by the discrete nature of the grid could be evaluated. Likewise, considering the imaginary part allowed the energy dissipation error to be evaluated. Figure 3.2 shows the continuous-space dispersion curves for the ordinary-mode (O-mode; left panels) and extraordinary-mode (X-mode; right panels) branches of dispersion relation (3.25) compared to curves calculated for different values of dimensionless parameter $\omega_p \Delta_t$. The lower panels show the relative errors calculated using (3.27). Figure 3.3 shows the equivalent dissipation curves. As would be expected, deviation from the continuous-space case decreases as the discrete step sizes are reduced. The greatest source of error in all cases is in the frequency at which cutoffs and resonances occur, which shift to higher frequencies as the discretisation becomes more coarse. As $\omega_p \Delta_t$ is increased to 2, the numerical dispersion and dissipation relationships break down completely and bear very little resemblance to the desired curves, as predicted by the stability requirement $\omega_p \Delta_t < 2$ introduced above.

Grid parameter choice for this FDTD scheme is ultimately constrained by the need for stability and the requirement for a simulation to sample features of a desired spatial or temporal resolution. Beyond this, discrete step size choice must be a compromise between the accuracy needs of a given simulation and the computational resource required

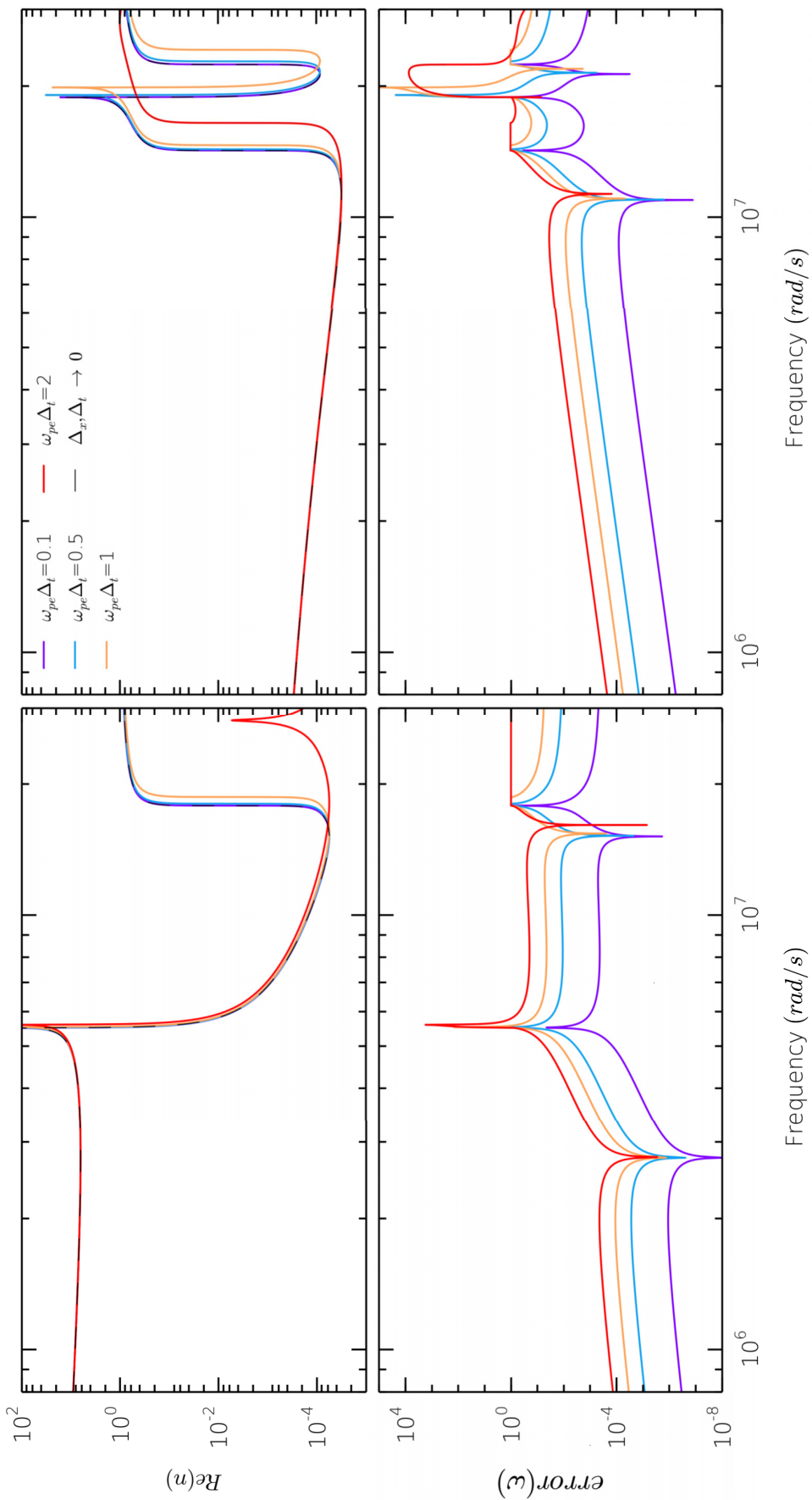


FIGURE 3.2: Dispersion curves (upper) and relative errors when compared to the continuous-world regime (lower) for a range of dimensionless parameter $\omega_p \Delta_t$ shown for the ordinary mode (left) and extraordinary mode (right) branches of (3.25). Positive root shown only.

Image reproduced from [Cannon and Honary, 2015] © 2015 IEEE.

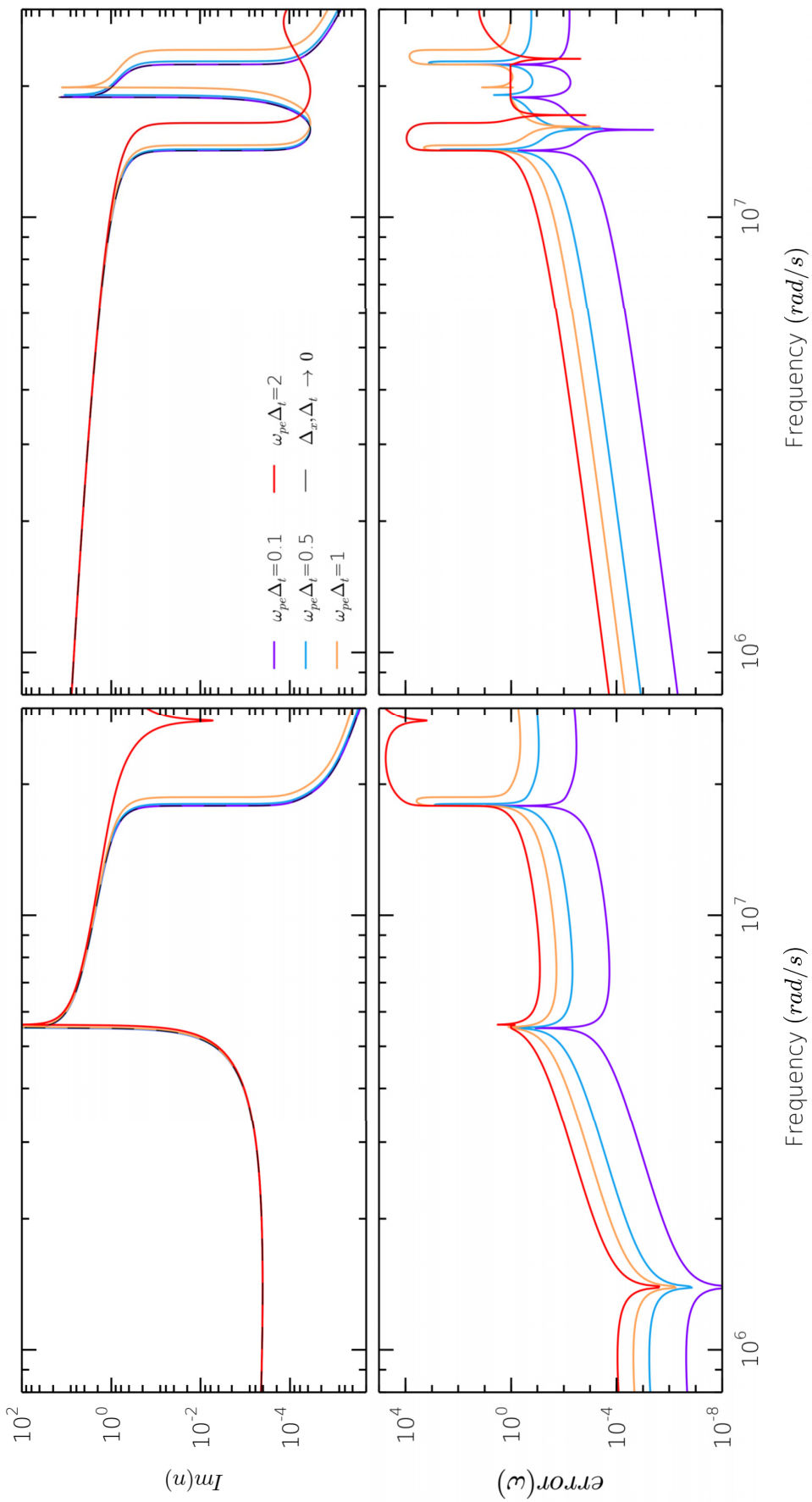


FIGURE 3.3: Dissipation curves (upper) and relative errors when compared to the continuous-world regime (lower) for a range of dimensionless parameter $\omega_p \Delta_t$ shown for the ordinary mode (left) and extraordinary mode (right) branches of (3.25). Positive root shown only.

Image reproduced from [Cannon and Honary, 2015] © 2015 IEEE.

to run it, which would be expected to increase drastically with accuracy. For example, the simulation of an RF wave interaction with a kilometre-scale plasma feature requires the simulation time step to be sufficiently small (of order 10^{-8} s) such that the wave period can be well resolved, however this automatically scales the spatial step size to be small (of order 10 m) to maintain stability, meaning a large computational grid is required to model the desired feature. A larger grid necessarily means more memory is required and more calculations must be performed, thus increasing run-time.

3.3 Computational Performance

Among the prime considerations when developing the FDTD code was that simulation runtimes be kept to a minimum. As has been explored by [Cummer, 1997], the direct integration method of FDTD used here is under most circumstances the most computationally efficient of finite-difference schemes, with smaller equivalent-simulation runtimes than the recursive convolution and exponential fitting methods it was tested against.

As the FDTD method scales particularly well with the *Single-Instruction Multiple-Data* (SIMD) concept of parallel processing, huge benefits in performance (often several orders of magnitude) were encountered when the code was accelerated using *Graphical Processing Unit* (GPU) technology, as has been reported previously by [Sypekand et al., 2009]. The multi-processor architecture of the GPU allows similar-type nodes to be updated simultaneously whilst still following the overall update algorithm described in Section 3.2, vastly reducing processing time when compared to a serial implementation. A major advantage of the use of GPU technology was that almost all calculations and memory operations occur “on-chip”, with the only (comparatively slow) communication with the host machine occurring at initialisation when memory arrays and input data were loaded onto the chip, and at the points where the code performed a data dump.

The FDTD code was written using the *OpenCL* parallel processing language, allowing it to be easily ported between heterogeneous devices of different hardware configurations. In the OpenCL implementation, the GPU receives computation instructions from the host CPU in the form of pre-compiled *kernel* functions. Before execution of a kernel,

the computational grid is divided into *work items* (equivalent to CUDA *threads*), with each work item handling the update of an individual node in the grid. Due to the data-parallel properties of OpenCL, each work item can simultaneously execute the same arithmetic instruction on different parts of the data stored in the GPU memory. The grid can be also subdivided into discrete blocks of work items with user-defined dimensions, known as *work groups*. On kernel execution, work groups to be processed are distributed amongst the available device *compute units* by an on-chip *instruction unit*. Each compute unit is a multicore processor made up of many discrete *processing elements* capable of performing simple arithmetic operations. Once a work group has been assigned to a compute unit, the processing elements simultaneously execute the same kernel instruction on *wavefronts* of 32 consecutively-indexed work items. For the FDTD code described here, synchronous kernel execution was used to maintain consistency between nodes, meaning that all compute units on the device must finish executing a particular kernel before moving on to the next set of kernel instructions in the queue.

The choice of work group dimensions is therefore of critical importance to code performance; after division of the grid, there must be a sufficient number of work groups to fully occupy all compute units, and each must be large enough to ensure that all processing elements are in operation as close to 100% of the time as possible. Wavefronts are executed concurrently, and thus a high number of active wavefronts are required to mask delays due to thread stalling or memory latency. Additionally, members of a work group have shared access to the fast-access scratch memory (OpenCL *local* memory) available on the GPU chip, which can significantly reduce memory transaction times and thus speed up performance, but is limited in size compared to chip *global* memory.

To test the impact of changing the number of work groups on FDTD code performance, a simple simulation was repeated for varying ratio of the total number of work groups to device compute units, with work group size kept constant. The tests were performed on a Nvidia Tesla M2075 GPU containing a total of 14 compute units, with the number of FDTD grid cells fully advanced by one time step per wall-clock second used as a measure of performance. The results are shown by Figure 3.4, which demonstrates that

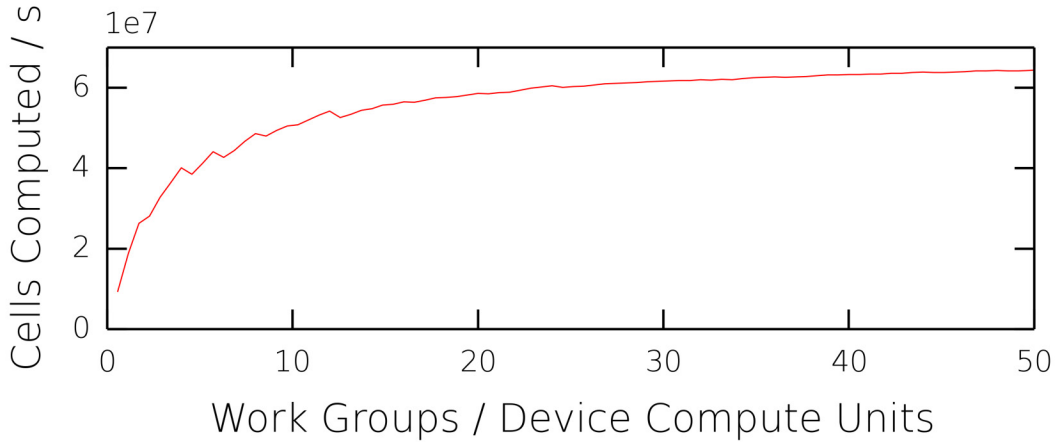


FIGURE 3.4: Variation in code performance with the number of work groups per device compute unit, for a constant work group size.

Image reproduced from [Cannon and Honary, 2015] ©2015 IEEE.

code performance increases significantly as the ratio of work groups to compute units is increased. Performance can be seen to continue to increase far beyond a ratio of one work group per compute unit due to the fact each compute unit can handle many work groups simultaneously, and increasing the workload of each compute unit ensures that the processing elements are always occupied. Saturation in this case likely occurs due to the limit on the number of active work items imposed by the limited number of private memory registers available to each compute unit.

The compute unit executes work groups in units of 32-work-item wavefronts, therefore a work group size of less than 32 will leave processing units idle and reduce performance. Likewise, a work group that is not made up of an integer number of wavefronts will reduce processing core occupancy. Figure 3.5 shows how the performance of the FDTD code varies with the number of wavefronts in a work group, for a constant total number of work groups. Performance peaks are seen at integer numbers of wavefronts per work group, as in these scenarios there are no partially-complete wavefronts. There is a general increase in performance due to increased occupancy of the compute units with greater work group sizes.

Further performance gains were achieved through use of a memory coalescence model such as that described by [Livesey et al., 2012]. In this structure, kernel execution is

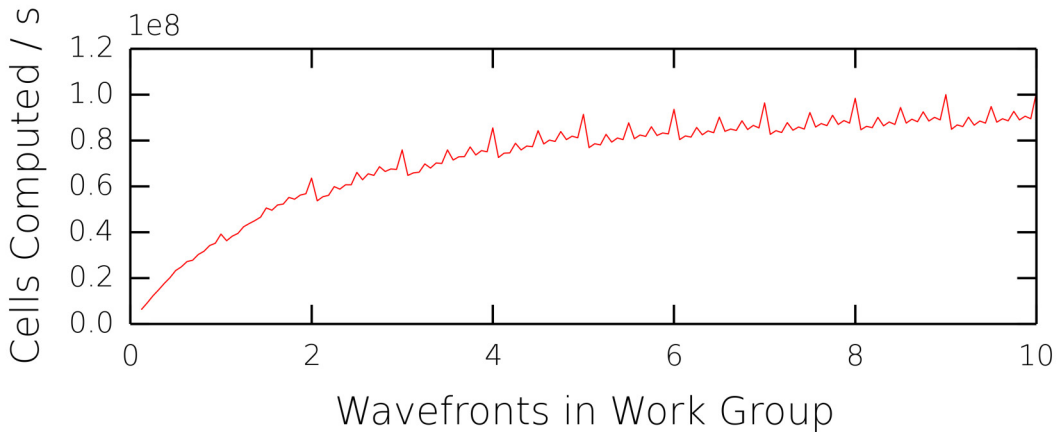


FIGURE 3.5: Variation in code performance with the number of wavefronts in a work group, for a constant total number of work groups.

Image reproduced from [Cannon and Honary, 2015] © 2015 IEEE.

organised such that all work items in a half-wavefront simultaneously access data from a contiguous block of memory, allowing the GPU to combine multiple memory calls into a single transaction and greatly reducing the net memory access time per work item. Without memory coalescence, multiple memory fetches may be required to access the same data, resulting in a significantly lower effective memory bandwidth. This is shown by Figure 3.6, which shows the FDTD code performance for varying offsets of the z -direction work item index. Adding an offset to the index causes the work item grid to be out of alignment with the data stored in page-aligned global memory, resulting in uncoalesced memory access. Increasing the offset to 32 (one whole wavefront out of alignment), brings each wavefront back into phase with the global memory and performance returns to coalesced-memory levels.

Using several GPU nodes together in a networked cluster as described by [Stefaski et al., 2012] or [Kim and Park, 2012] was found to increase performance by a factor approximately equal to the number of GPUs available, with the only major bottleneck being the communication times between nodes. In this scenario, the computational domain was split between each GPU such that each device was responsible for updating a different region of the grid and an *OpenMPI* framework used to initialise and pass commands to each GPU on separate threads. To ensure consistency, the regions of the grid updated by each GPU were set to overlap slightly, and the overlap regions passed between chips

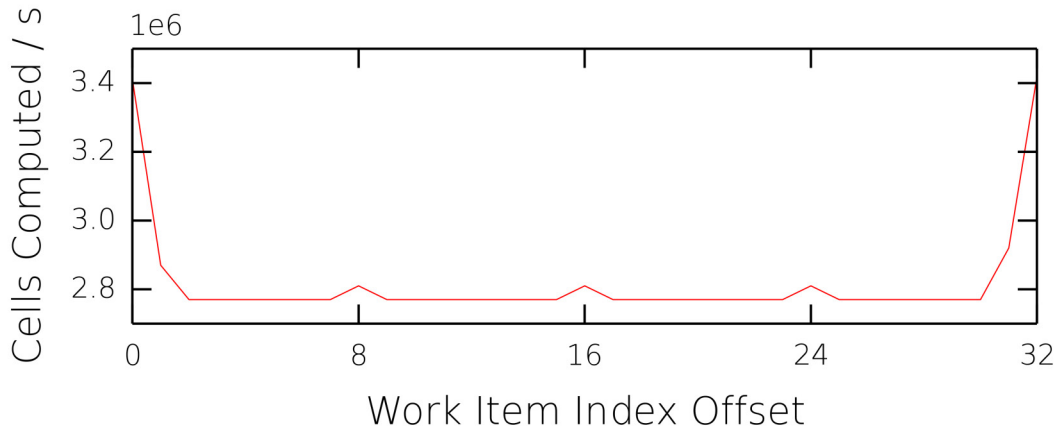


FIGURE 3.6: Code performance for varying offsets of the z-direction work item index.

Offset multiples of 32 correspond to coalesced memory access.

Image reproduced from [Cannon and Honary, 2015] © 2015 IEEE.

as boundary conditions. Increasing the size of these shared overlap regions meant that data transfer between chips did not have to occur every time step, but did introduce an additional overhead as it increased the number of redundant calculations (since the overlap regions of the grid are effectively updated twice – once by each chip that shares this region). It was found that an overlap region depth of around 32 cells produced the optimal results, however this is heavily dependent on the hardware available, and will likely vary between systems. Table 3.1 shows how the performance is increased when a serial implementation of the FDTD code running on an Intel Core i5-3750 CPU is compared to a parallel implementation running on a Nvidia Tesla M2075 GPU. The number of nodes fully advanced by one time step per wall-clock second is used as a measure of performance. Also shown is the performance of a dual-GPU implementation, which shows a gain factor of approximately 2 over the single-GPU implementation. Due to hardware limitations, an implementation using more than two GPUs could not be tested, however performance would be expected to scale approximately linearly with the number of GPUs used, with the only additional overheads arising from the transfer of overlap regions between devices.

Grid Cells	Computed nodes / second		
	CPU	Single GPU	Dual GPU
1024	1.37×10^6	2.04×10^6	1.06×10^6
4096	1.64×10^6	8.38×10^6	4.21×10^6
16384	2.00×10^6	3.34×10^7	1.72×10^7
65536	1.63×10^6	6.62×10^7	6.83×10^7
102400	1.80×10^6	8.00×10^7	1.00×10^8
262144	2.13×10^6	7.99×10^7	1.27×10^8
589824	2.36×10^6	9.29×10^7	1.40×10^8
1048576	2.38×10^6	8.19×10^7	1.59×10^8

TABLE 3.1: Table comparing the performance of a serial implementation of the FDTD code running on a single CPU with parallel implementations running on a single GPU and on two networked GPUs.

Table reproduced from [Cannon and Honary, 2015] © 2015 IEEE.

3.4 Validation

3.4.1 Wave Propagation Through Homogeneous Plasma

To test the validity of the FDTD algorithm, the model was used to simulate the propagation of a plane-polarised electromagnetic wave through a homogeneous block of plasma, in a similar manner to the numerical experiments used to validate the FDTD algorithm in [Yu and Simpson, 2012]. Several test cases involving different homogeneous plasma regimes were considered. In each case the results were benchmarked against those obtained using Tech-X’s VORPAL 4.2.2 software package [Nieter and Cary, 2004] and the predictions of plasma theory. Fractional errors between the FDTD E-field signal and the benchmark E-field signals were calculated using:

$$\text{error}(t) = \left| \frac{E_{\text{Benchmark}}(t) - E_{\text{FDTD}}(t)}{E_{\text{Benchmark}}(t)} \right| \quad (3.28)$$

The grid was initialised with discrete spatial steps of $\Delta_x = \Delta_y = \Delta_z = 11.626\text{ m}$ and a discrete step size of $\Delta_t = 1.939 \times 10^{-8}\text{ s}$ chosen to give a Courant number of 0.5, ensuring stability. Discretisation parameters were chosen to represent those used in a typical ionospheric simulation, with accuracy balanced by a need for computational efficiency. The simulation boundaries were terminated using 2nd-order absorbing boundary conditions of the type described by Mur [Mur, 1981] and introduced in Section 2.3.1 above, which allowed outgoing waves to be absorbed with minimal numerical reflection. The boundaries of the VORPAL comparison simulation were terminated using absorbing boundary conditions, and a particle-in-cell (PIC) approach implementing a Boris push update to particle velocities [Boris, 1970] used to mediate any interaction between the simulated EM field and plasma. A linearly-polarised input pulse in the form of a twice-differentiated Gaussian described by (3.29) was introduced into the computational domain from the lower z boundary, and allowed to propagate through the domain in the positive z -direction.

$$E_x(q) = \left[1 - \frac{1}{2} (\omega_{peak} q \Delta_t - 1)^2 \right] \exp \left[- \left(\frac{\omega_{peak} q \Delta_t}{2\pi} - 1 \right)^2 \right] \quad (3.29)$$

This form of pulse was particularly suitable as the frequency of peak amplitude could be set easily using the w_{peak} parameter, and it avoided the DC frequency component found in undifferentiated Gaussian signals. For the following tests, the peak frequency of the input pulse was set to be $\omega_{peak} = 4.55 \times 10^6 \text{ rad s}^{-1}$, corresponding to a wavelength of 36 cells. The free space time-domain and frequency-domain signals from this pulse measured at a point 128 cells from the source plane are shown in Figure 3.7. In this simple free-space example the FDTD model was in almost perfect agreement with the benchmark, with the greatest error between signals of order 10^{-4} V/m (calculated using (3.28)).

The pulse was then introduced into a spatially-homogeneous unmagnetised electron-only plasma medium, of electron number density $2 \times 10^9 \text{ m}^{-3}$. Figures 3.8 and 3.9 show the time- and frequency-domain signals respectively, again recorded at a point 128 cells from the source plane. Signals from both the FDTD code and VORPAL are shown, alongside

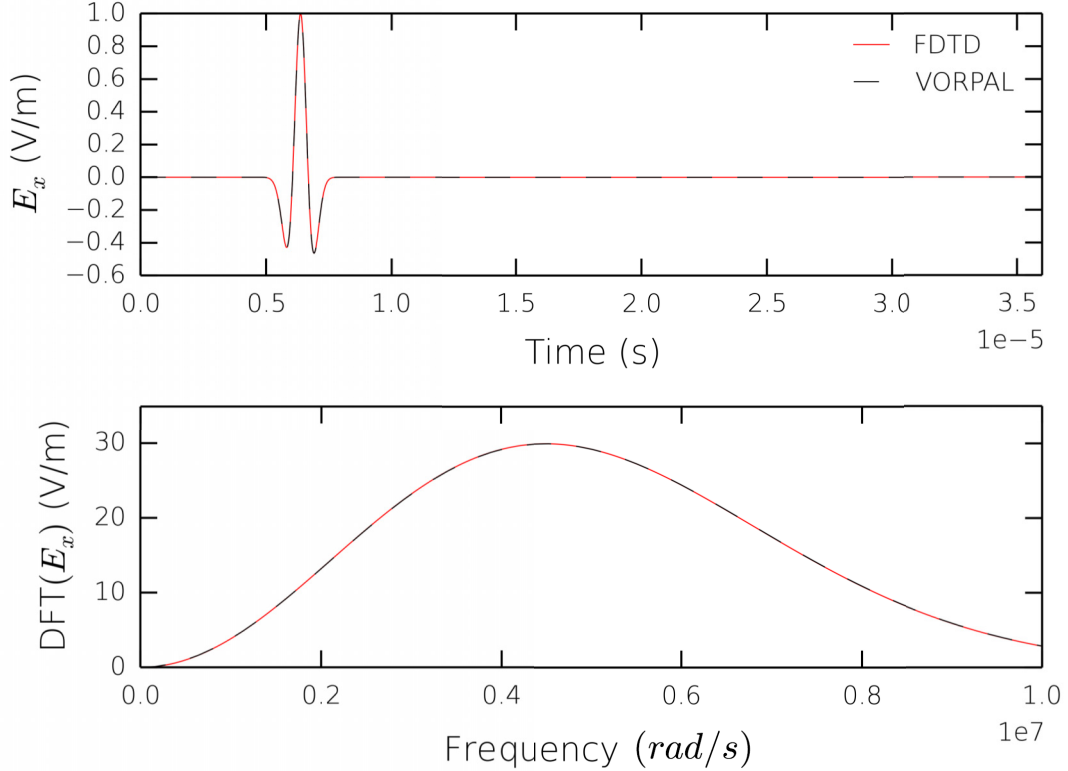


FIGURE 3.7: E_x signal for an EM pulse of form (3.29) propagating through a free-space simulation, recorded at a point 128 cells from the $z = 0$ launch plane. Upper panel shows time domain comparison of signals measured using the FDTD algorithm described in this work (red) and an equivalent VORPAL simulation (black). Lower panel shows the frequency domain form of the signals, which peak at $\omega_{peak} = 4.55 \times 10^6 \text{ rad s}^{-1}$. Computational grid parameters of $\Delta_t = 1.939 \times 10^{-8} \text{ s}$ and $\Delta_x = 11.626 \text{ m}$ were used in these simulations. *Image reproduced from [Cannon and Honary, 2015] © 2015 IEEE.*

the expected result from plasma theory. The time-domain waveform shows a distorted pulse with a long tail oscillating at the electron plasma frequency. This agrees with expected behaviour, as in a dispersive plasma different frequency components should propagate through the plasma at different velocities, causing the observed distortion. The slow tail is caused by frequency components on or close to the electron plasma frequency which propagate with very low group velocities. The large spikes in error were likely due to small phase differences between the signals under comparison. The error calculation involved dividing by the benchmark signal; when this signal was very close to zero, a large instantaneous fractional error could be produced. Aside from this, the FDTD algorithm results demonstrate good agreement with both the benchmark and theory, with substantial error between the FDTD and benchmark signals only creeping

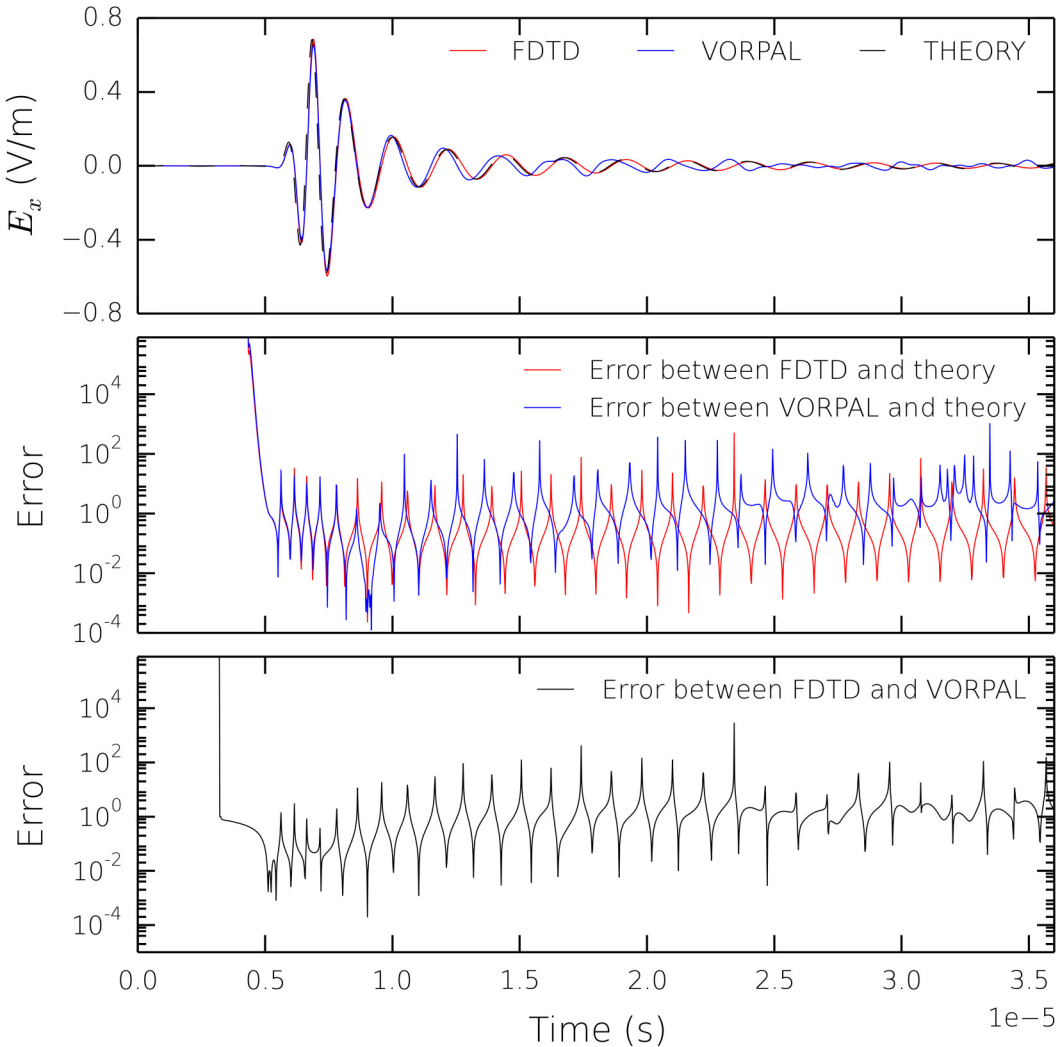


FIGURE 3.8: Time domain E_x signal for pulse propagating through an unmagnetised plasma simulation. Upper panel shows FDTD signal (red), VORPAL signal (blue) and the expected result from plasma theory (black). Central panel shows the error between the simulated signals and the predictions of plasma theory. Lower panel shows the error between FDTD and VORPAL signals. Computational grid parameters of $\Delta_t = 1.939 \times 10^{-8} s$ and $\Delta_x = 11.626 m$ were used in these simulations.

Image reproduced from [Cannon and Honary, 2015] © 2015 IEEE.

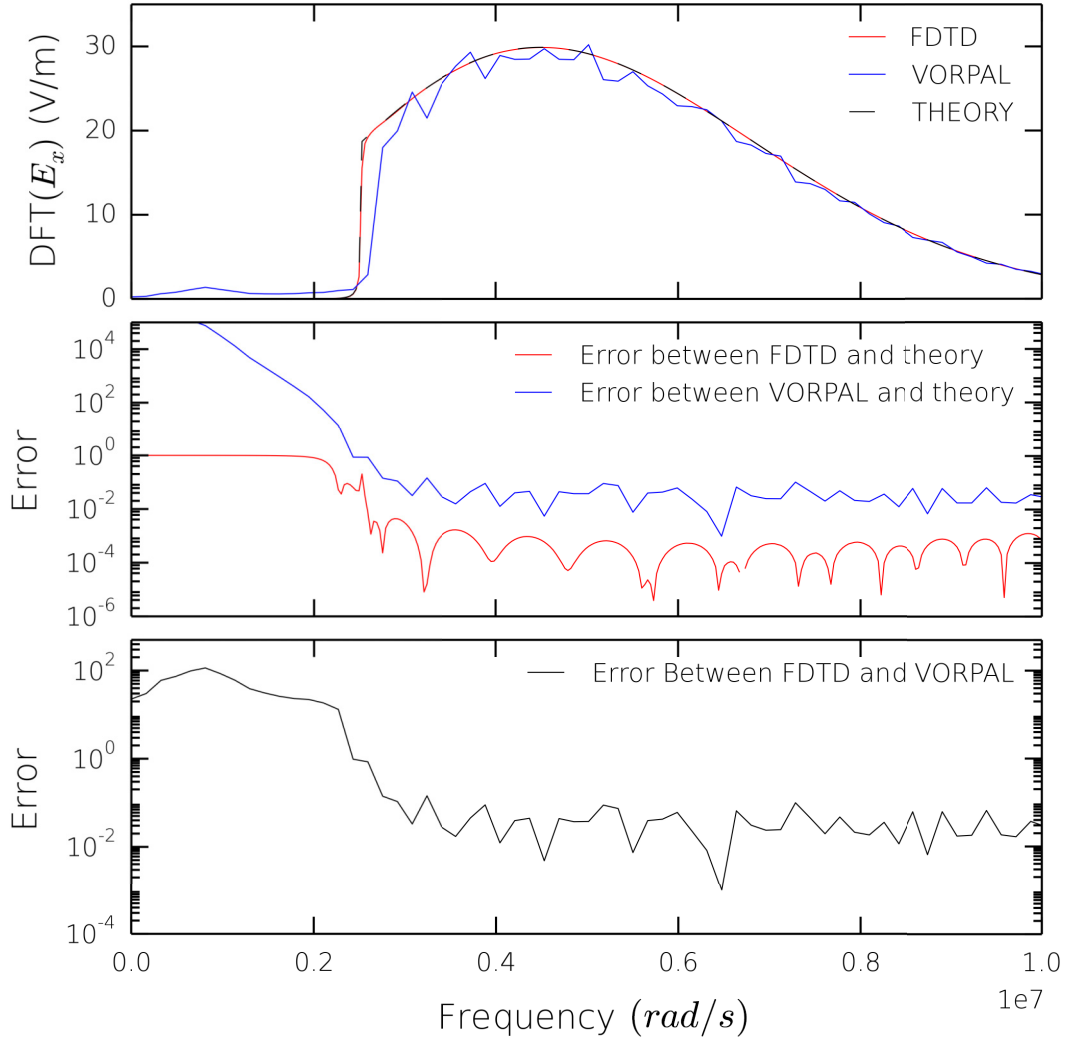


FIGURE 3.9: Frequency domain E_x signal for pulse propagating through an unmagnetised plasma simulation. Upper panel shows discrete Fourier transform of FDTD signal (red), VORPAL signal (blue) and the expected result from plasma theory (black). A clear cutoff can be seen at simulation plasma frequency $\omega_p = 2.5 \times 10^6 \text{ rad s}^{-1}$. Central panel shows the error between the simulated signals and the predictions of plasma theory. Lower panel shows the error between FDTD and VORPAL signals. Computational grid parameters of $\Delta_t = 1.939 \times 10^{-8} \text{ s}$ and $\Delta_x = 11.626 \text{ m}$ were used in these simulations. *Image reproduced from [Cannon and Honary, 2015] © 2015 IEEE.*

into the trace during later-time tail. This difference is likely due to the different levels of numerical dispersion present in each simulation. The FDTD result was found to match very closely to the theoretical prediction at all times sampled. The frequency-domain waveform shown in the upper panel of Figure 3.9 clearly demonstrates a cut-off at the electron plasma frequency $\omega_p = 2.52 \times 10^6 \text{ rad s}^{-1}$. This agrees well with expectations, as no frequency components below the fundamental plasma frequency should be able to propagate through a plasma of this type. Note that this frequency is the numerical plasma frequency, calculated using the methods of Section 3.2.3 above, and depends not only on the plasma density but the choice of grid discretisation parameters. As shown in Figures 3.2 and 3.3, and discussed in detail in [Cummer, 1997], a consequence of the temporal and spatial grid discretisation is a numerical modification of the plasma cut-off frequencies; the numerical-world electron plasma frequency, for example, can be related to its continuous-world counterpart by:

$$\tilde{\omega}_{pe} = \frac{2}{\Delta_t} \arcsin \left(\frac{\omega_{pe} \Delta t}{2} \right) \quad (3.30)$$

Here, ω_{pe} is the continuous-world plasma frequency, as calculated from cold-plasma theory, and $\tilde{\omega}_{pe}$ is the numerical-world value of the plasma frequency, as measured in the computational domain.

A static magnetic field of magnitude $\mathbf{B} = 10\hat{\mathbf{z}}\mu T$ was then applied to the medium, fixing the electron cyclotron frequency in the simulation to be $\omega_c = 1.76 \times 10^6 \text{ rad s}^{-1}$. The magnetic field was directed parallel to the direction of pulse propagation. In this situation, the initially linearly-polarised pulse should decompose into left-handed and right-handed circularly-polarised components as it propagates through the magnetised plasma. The left- and right-handed components propagate at different phase velocities and experience different cut-off frequencies below which they will not propagate, given by (3.31) and (3.32):

$$\omega_{LHC} = \frac{1}{2} \left([\omega_c^2 + 4\omega_p^2]^{\frac{1}{2}} - \omega_c \right) = 1.79 \times 10^6 \text{ rad s}^{-1} \quad (3.31)$$

$$\omega_{RHC} = \frac{1}{2} \left([\omega_c^2 + 4\omega_p^2]^{\frac{1}{2}} + \omega_c \right) = 3.55 \times 10^6 \text{ rad s}^{-1} \quad (3.32)$$

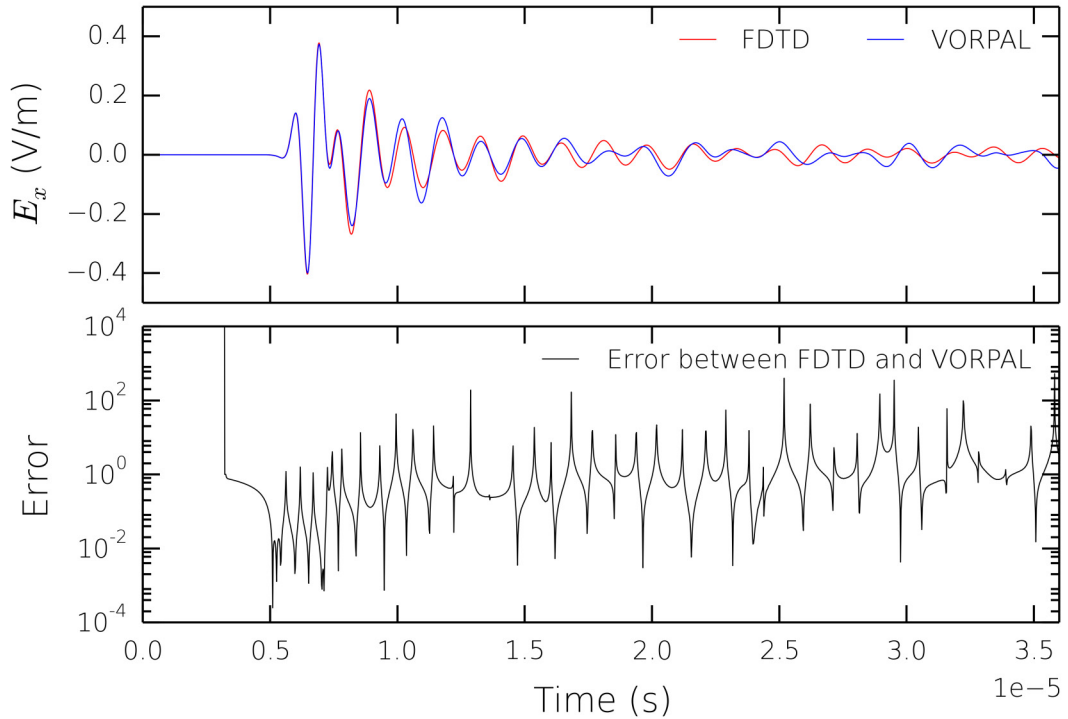


FIGURE 3.10: Time domain E_x signal for pulse propagating through a magnetised plasma simulation. Upper panel shows FDTD signal (red) and VORPAL signal (blue). Lower panel shows the error between FDTD and VORPAL signals. Computational grid parameters of $\Delta_t = 1.939 \times 10^{-8} \text{ s}$ and $\Delta_x = 11.626 \text{ m}$ were used in these simulations.

Image reproduced from [Cannon and Honary, 2015] © 2015 IEEE.

The time- and frequency-domain signals for this case are shown in Figures 3.10 and 3.11. The time domain signal agrees well with the benchmark until, as encountered in the previous case, a small error creeps into the low-amplitude tail. Again, this is likely due to the different numerical dispersion regimes. The predicted cut-offs can clearly be seen in the frequency-domain signal. There are substantial discrepancies between the FDTD and VORPAL signals at lower frequencies below ω_{RHC} , which can most likely be attributed to the very different methods of simulating plasma behaviour employed by each code, and the restrictive computational parameters selected for the comparison. In the FDTD code, plasma velocities, temperatures and densities are calculated at strictly-defined grid locations, as described in section 3.2 above. By contrast, the particle-in-cell (PIC) approach used by VORPAL simulates the motion of discrete macroparticles (simulated plasma super-particles representing many thousands of actual particles) which are not tied to the grid and are able to possess individual positions and velocities within

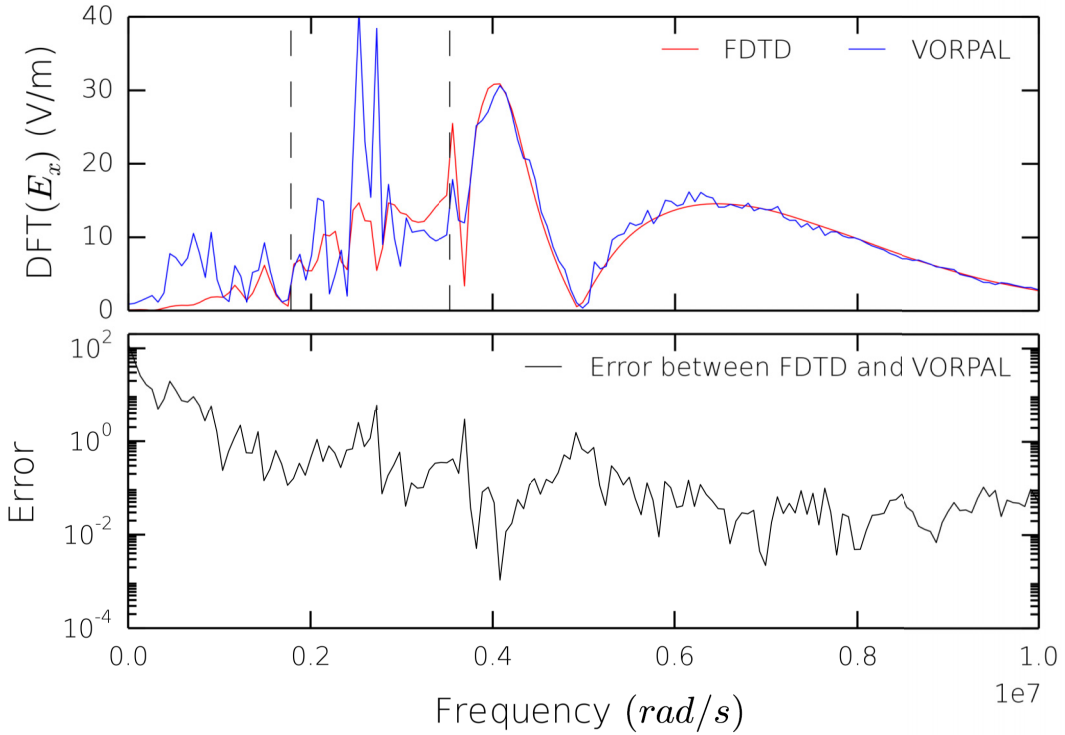


FIGURE 3.11: Frequency domain E_x signal for pulse propagating through a magnetised plasma simulation. Upper panel shows discrete Fourier transform of FDTD signal (red) and VORPAL signal (blue). Clear cutoffs can be seen due to the different propagation characteristics of the right- and left-hand circularly polarised components. The expected positions of the cutoffs are indicated in black. Lower panel shows the error between FDTD and VORPAL signals. Computational grid parameters $\Delta_t = 1.939 \times 10^{-8} s$ and $\Delta_x = 11.626 m$ were used in these simulations.

Image reproduced from [Cannon and Honary, 2015] © 2015 IEEE.

the computational domain; the plasma properties at each grid node are then calculated at each time step by considering the distribution and velocities of nearby macroparticles (for more details on the PIC method, see [Birdsall and Langdon, 1985]). Increasing the spatial and temporal resolution would be expected to increase the accuracy of both codes, reducing the difference between signals as they both converge on the theoretical solution (the accuracy of the PIC method could also have been significantly improved by increasing the number of macroparticles present in the simulation, however this would incur far greater simulation runtimes). At the coarse resolution used here, however, the different methods may be expected to yield sufficiently different results to cause the discrepancies observed between signals. This resolution were chosen to favour computational efficiency over accuracy, and was typical of that required to ensure realistic

simulation runtimes during the ionospheric modification simulations described in later Chapters. In all the above tests, the FDTD code was found to complete the simulation considerably more quickly than the benchmark software, with the single-core CPU version of VORPAL found to perform on average 4.7×10^5 node updates per second compared to a rate of 2.4×10^6 node updates per second achieved by the FDTD code on the same hardware. The GPU accelerated version of the FDTD code was able to run the simulations almost 2 orders of magnitude faster than this with a node update rate of $1.1 \times 10^8 \text{ nodes s}^{-1}$ achieved using a single-GPU implementation. A GPU enabled version of VORPAL was not available for comparison.

3.4.2 Wave Propagation Through Inhomogeneous Plasma

This Section describes further validation tests that were more representative of the intended end-use of the model, and relevant to the scientific simulation studies presented in later Chapters. Simple numerical experiments were performed demonstrating the ability of the FDTD algorithm to replicate some of the key features that are required for realistic simulation of RF wave propagation in the ionosphere. The model was set up to simulate a simple ionospheric heating experiment, with a continuous harmonic input wave at a frequency of $\omega_0 = 2.7 \times 10^7 \text{ rad s}^{-1}$ introduced into a domain containing a linear electron density profile given by (3.33):

$$N_0(z) = N_{crit} \left(1 + \frac{z - z_{crit}}{L_z} \right) \quad (3.33)$$

where N_{crit} is the critical density at which the plasma frequency equals the frequency of the incident wave, z_{crit} is the height at which this density occurs and L_z is the scale size of the gradient. The variable z refers to the distance from the lower edge of the simulation domain. For these tests, z_{crit} was set to be at 29.8 km from the lower edge of the simulation and L_z set to be 60 km .

The simulation was initialised using the discretisation parameters used in Section 3.4.1 above and run in a 2-dimensional configuration in which all y -direction gradients were assumed to be zero. A static background magnetic field of magnitude $4.65 \times 10^{-5} \text{ T}$

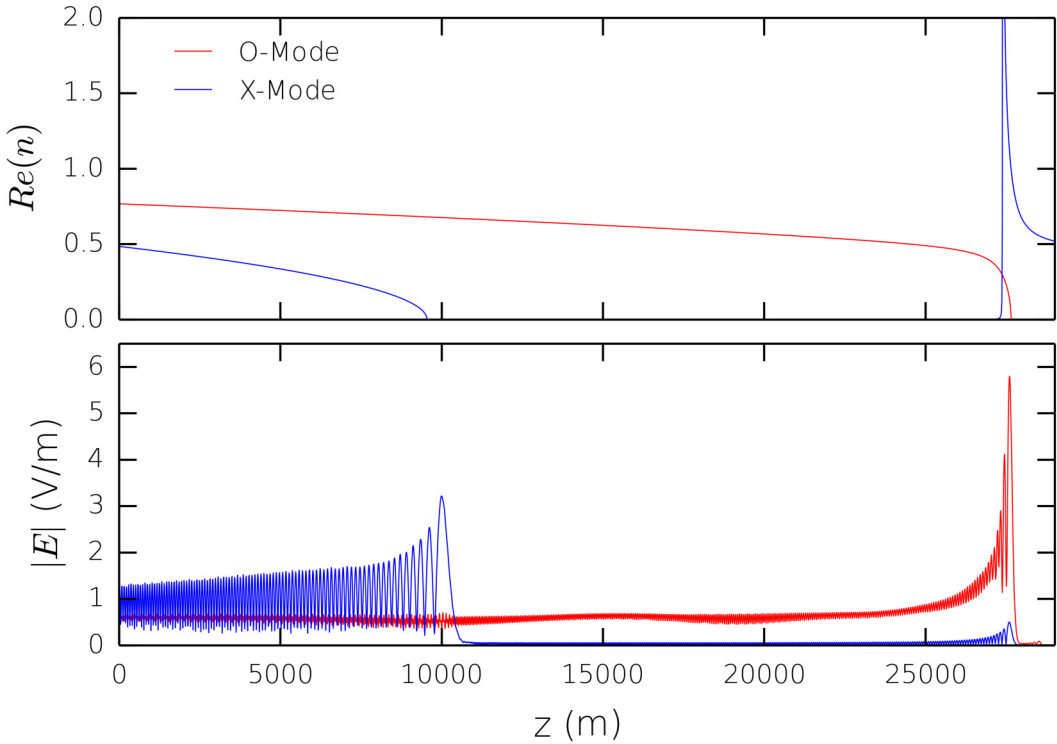


FIGURE 3.12: Upper panel shows the numerical refractive index curves for a magnetised plasma of density profile (3.33). Lower panel shows a comparison of the time averaged O- and X-mode E-field amplitudes measured along the central axis of the computational domain. Computational grid parameters $\Delta_t = 1.939 \times 10^{-8} s$ and $\Delta_x = 11.626 m$ were used in the O-mode and X-mode propagation simulations.

Image reproduced from [Cannon and Honary, 2015] © 2015 IEEE.

at an angle of 12° to the z -axis was applied to mimic the geomagnetic field. Background electron temperature was set to $1500 K$ and electron-neutral collision frequency to $500 s^{-1}$. Domain boundaries were terminated by a 64-cell complex-frequency-shifted perfectly matched layer [Berenger, 1994], which allowed outgoing waves at a range of oblique angles to be absorbed effectively with minimal numerical reflection. The derivation of the PML configuration used by this code was discussed in Section 2.3.2 above. The input wave was given an angular spread to appear as if it originated from a point located $220 km$ below the $z = 0$ launch edge. The polarisation of the wave could be set at launch to represent either the O-mode or X-mode using the polarisation relations given in [Budden, 1961] for a cold, collisional, magnetised plasma. The FDTD model was used to check that the propagation of these modes proceeded in the expected manner.

The upper panel of Figure 3.12 shows how the refractive index for O- and X-mode waves

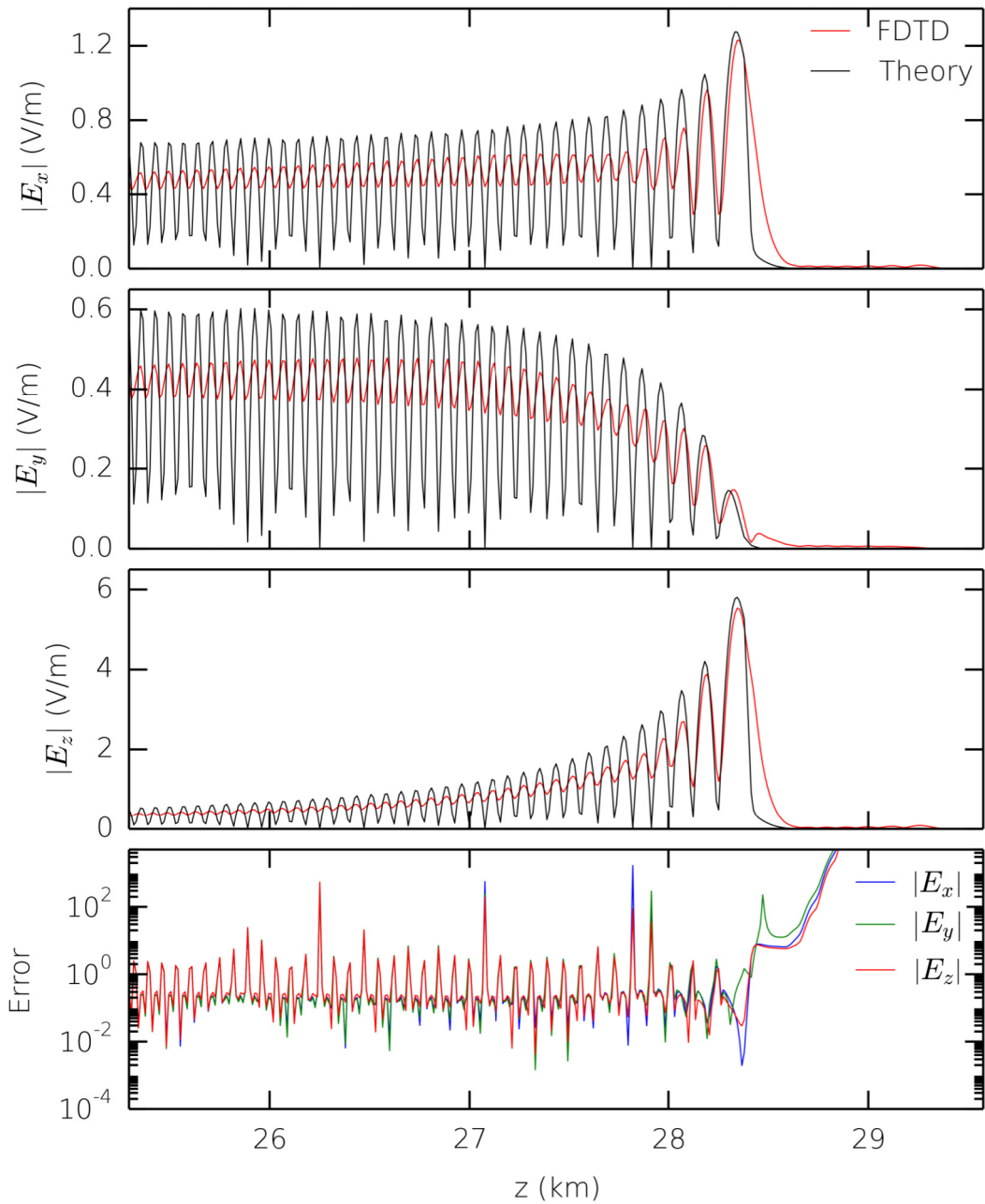


FIGURE 3.13: Comparison between standing wave pattern developed in FDTD simulation and theoretical calculation following the method of [Lundborg and Thidé, 1986]. Computational grid parameters $\Delta_t = 1.939 \times 10^{-8} \text{ s}$ and $\Delta_x = 11.626 \text{ m}$ were used in the simulation of the O-mode E-field standing wave pattern.

Image reproduced from [Cannon and Honary, 2015] © 2015 IEEE.

in this simulation varies with altitude. The curves shown are the numerical forms of the refractive index curves specific to the chosen discretisation parameters, calculated as described in Section 3.2.3. The traces in the lower panel of Figure 3.12 show the time-averaged electric field amplitude measured along the central axis of the computational domain after 2×10^6 time steps for both the O- and X-mode input waves. The results demonstrate that the simulation is able to replicate the propagation characteristics of each mode successfully. The O-mode wave was able to propagate almost the whole length of the simulation domain before being reflected at z_{crit} as expected from the dispersion curve. The X-mode wave was attenuated at a distance of around 10 km from the lower edge of the simulation, the point at which the theory predicts that this wave should become evanescent. A small amount of field amplitude appears to have leaked beyond this point, possibly as an O-mode wave, and can be seen to have been slightly amplified at z_{crit} .

The Airy-like standing wave pattern that develops below the reflection height in the O-mode case is a well understood phenomenon which has been characterised by [Lundborg and Thidé, 1986], and was introduced previously in Section 1.6.1 above. As the wave approaches the O-mode reflection height, and thus propagates into regions of increasingly lower refractive index, it experiences an increase in wavelength and a corresponding increase in amplitude. This evolution of wavelength and swelling in amplitude can be modelled analytically using the WKBJ (Wentzel-Kramers-Brillouin-Jeffreys) approximation, in which the ionosphere is approximated as a vertical stack of infinitesimally-thin layers of increasing electron density, however this approach breaks down as the refractive index for O-mode waves approaches zero at the reflection layer. To fully describe the behaviour of the standing wave at and beyond this reflection height, the analytic calculation can be extended using Airy integrals as described in [Lundborg and Thidé, 1986] (which assumes that the electron profile at the reflection height is linear), or alternatively the wave pattern can be simulated using a numerical treatment such as that presented in this Chapter. Figure 3.13 shows a comparison between the standing wave pattern developed in the simulation and that predicted by theoretical calculation. Note that the numerical form of the refractive index has been used in calculating the theoretical result.

The results from the FDTD simulation are in good agreement with those from theory and successfully reproduce the expected wave pattern for all E-field components. The wave amplitudes in the simulated case are lower than the predicted values by a factor of 0.8 however this is likely due to energy leaking out of the grid through absorption at the grid boundaries. This discrepancy could also be due to the fact that the possibility of mode conversion of the O-mode wave to the Z-mode, and hence reduction of the reflected wave amplitude, was not considered in the analytical calculation but may occur in the numerical simulation.

3.5 Summary and Conclusions

This Chapter describes the formulation of a 3D FDTD scheme suitable for the simulation of radio-frequency wave propagation in a dynamic, magnetised plasma. Development of this code was motivated by the need for a numerical scheme capable of performing detailed simulations of ionospheric heating experiments. FDTD proves to be the ideal tool for geophysical modelling as the grid-based structure allows medium properties such as plasma density or temperature to be defined separately at each point. The time-explicit FDTD update algorithm enables the complicated and often non-linear fluid plasma and wave interactions to be simulated in a natural manner, while avoiding computationally-intensive linear algebra calculations. A multi-fluid description of a dynamic, anisotropic, collisional plasma was assumed. The effect on wave propagation due to the presence of plasma was introduced through the coupling of Maxwell's wave equations with the Lorentz equations of motion for each constituent plasma species, with fluid velocity component nodes co-located with the electric field component nodes in the Yee cell, but offset in time. Anisotropy was introduced through inclusion of a static externally-applied magnetic field. The scheme built on the well-established FDTD technique by extending it to include a time-explicit updates to the plasma fluid temperature and density, allowing the time-dependent response of the plasma medium to an incident EM wave to be studied. The stability criteria and accuracy of the FDTD

scheme were analysed and found to be heavily dependent on the choice of spatial and temporal discrete step parameters.

Computational efficiency is crucial for a numerical simulation of this type and it was found that accelerating the FDTD code using GPU technology yielded significantly better performance, with a dual-GPU implementation achieving a rate of node update almost two orders of magnitude faster than a serial CPU implementation. Optimisation techniques such as memory coalescence were shown to have a significant effect on code performance, and it was demonstrated that large performance gains could be achieved through careful choice of the GPU work group dimensions.

Numerical validation tests simulating EM propagation through a range of plasma regimes demonstrate that this model agrees well with both plasma theory and the results of a benchmark software package. The FDTD code was found to run the validation test simulations considerably more quickly than the benchmark software using equivalent hardware. In particular, the propagation characteristics of waves of ordinary- and extraordinary-mode polarisation in an inhomogeneous, anisotropic plasma were accurately replicated. In the case of the ordinary-mode wave, the amplitude swelling effects produced around the critical density demonstrate that the FDTD scheme is able to successfully simulate the wave-plasma interaction responsible for this phenomenon. Both these effects are crucial to work involving this model presented in Chapters 4, 5 and 6, which concern the numerical simulation of an artificial ionospheric modification experiment and the study of the resulting non-linear processes.

Chapter 4

Simulation of the Radio Window and Magnetic Zenith Effect

The work presented in this Chapter has been published as part of:

[Cannon et al., 2016] P. D. Cannon, F. Honary, N. Borisov, 20016, *Two-Dimensional Numerical Simulation of O-mode to Z-mode Conversion in the Ionosphere*, Journal of Geophysical Research: Space Physics, 121 (3), 2755-2782, doi:10.1002/2015JA022105.

4.1 Introduction

The use of high-power radio-frequency transmitters to perturb the Earth's ionosphere gives a unique opportunity to study the complex and often non-linear mechanisms that underpin the interaction between an electromagnetic wave and ionospheric plasma. The ionosphere can be treated as a vast plasma laboratory, in which experiments can be performed without the limited spatial scale-size and chamber edge effects one may encounter while performing plasma experiments in a laboratory. As introduced in Chapter 1, Section 1.6, modification ("heating") experiments in which the F-Region of the ionosphere is illuminated using radio-frequency waves polarised in the ordinary mode have resulted in the observation of a wide range of non-linear thermal phenomena associated

with the excitation of plasma waves and instabilities [Robinson, 1989, Rietveld et al., 2003]. Many of these processes can induce significant enhancements of the electron temperature around the region in which the EM wave most strongly interacts with the plasma [Gordon and Carlson, 1974, Meltz et al., 1974, Djuth et al., 1987, Stocker et al., 1992, Honary et al., 1993]. Substantial changes to the electron density have also been commonly observed on a variety of different spatial scales, from large-scale density depletions spanning several kilometres [Gurevich et al., 2002] to small-scale irregularities aligned with the geomagnetic field and having transverse scale sizes ranging from a few metres down to a few centimetres, as detected by rockets and VHF-UHF backscattering [Kelley et al., 1995].

The main processes driving the enhancement of electron temperature in ionospheric modification experiments are understood to involve the excitement of large-amplitude plasma waves close to the O-mode reflection height or upper-hybrid resonance region. Close to the reflection height, the pump wave can parametrically decay to Langmuir plasma waves via the parametric decay instability [Fejer, 1979] leading to efficient transfer of the pump wave energy to the plasma, as described in Section 1.6.4 above. Below this, near the upper-hybrid resonance region, and provided that the pump frequency is not close to an electron gyroharmonic [Rao and Kaup, 1990, Stubbe et al., 1994], electrostatic upper-hybrid waves propagating in a direction perpendicular to the geomagnetic field are readily excited via the thermal resonance instability [Wong et al., 1981, Dysthe et al., 1982, Antani et al., 1996]. As introduced in Section 1.6.5 above, upper-hybrid electrostatic waves can induce the formation of striations in the electron density profile, elongated along the magnetic field direction and with a comparatively small transverse scale size. The region of interaction is initially narrow, but broadens as the striations grow with time. In the stationary state, the vertical scale of this region is several kilometres [Borisov and Robinson, 2003]. Incident pump wave electric field becomes trapped in the density depletions and amplified through efficient excitation of further UH modes [Gurevich et al., 1995, Gurevich et al., 2001, Gondarenko et al., 2005]. Collisional damping of the trapped waves results in an increase in the local plasma temperature, and consequently to a increase in the electron density depletion within the

irregularities. This process leads to a rapid, nonlinear growth of the temperature around the upper-hybrid resonance region.

The formation of small-scale density irregularities reduces the average electron plasma density around the UH resonance region and leads to a focusing of the pump wave and thus to a further enhancement of the E-field amplitude in this region [Gurevich et al., 2001, Gondarenko et al., 2003], as described in Section 1.6.6. Self-focusing of this nature results in further nonlinear enhancement of the electron temperature and causes the evolution of a hierarchy of density-depleted structures close to the O-mode reflection height, from the small-transverse-scale (1-10s of metres) striations associated with the resonance (thermal parametric) instability to self-organised bunches of striations forming duct-like density depleted structures due to the self-focusing instability spanning up to many kilometres in transverse scale [Gurevich et al., 1998]. Close-packed duct-like structures of this nature are known to form large-scale semi-permanent density-depleted regions or duct-like channels, which may affect EM wave propagation.

Observations have revealed that the magnitude of such artificial heating-induced perturbations to the plasma density depends strongly on the inclination angle of the RF pump beam, with a greater modification to the plasma observed when the heating beam is directed away from the vertical direction towards the magnetic zenith, as reported, for example, by [Honary et al., 2011, Kosch et al., 2000, Pedersen et al., 2003] (see Figure 1.15 above, which shows a comparison between the temperature enhancement measured at EISCAT by [Honary et al., 2011] for vertical and field-aligned pump beams). This Magnetic Zenith Effect has been observed as an increase in electron temperature enhancement by a factor of 2 or greater compared to off-zenith operation [Rietveld et al., 2003, Dhillon and Robinson, 2005], and has also been seen to correspond to a greater enhancement in the characteristic ion and electron plasma lines seen in UHF incoherent scatter radar spectra and an increase in the backscatter power due to field-aligned irregularities.

To explain theoretically the unexpected electron temperature and optical emission enhancements arising due to heating directed along the magnetic zenith direction, the self-focusing instability was first suggested as the mechanism behind this effect [Gurevich et al., 2002, Gurevich et al., 2005]. The timescale for this process to manifest is known to be long (of the order of 1min). The experiments recently performed by [Honary et al., 2011] demonstrated that the rise of electron temperature occurs on a much more rapid timescale (of the order of a few seconds; comparative to the rise time of field-aligned striations). Instead, [Honary et al., 2011] proposed that this aspect-angle dependence of heating is in part due to the O-mode to Z-mode (slow branch of the extraordinary mode) conversion process that can occur in the F-region of the ionosphere for a narrow window of pump wave inclination angles. The Z-mode is able to penetrate to altitudes above the O-mode reflection height, where the conversion of EM waves trapped in field-aligned irregularities to plasma modes is more efficient. This leads to a more rapid development of the resonance instability and potentially a greater magnitude of electron temperature enhancement.

To fully understand the fundamental wave interaction process involved in the O-mode to Z-mode conversion process, it is useful to augment experimental findings with accurate numerical simulations. Similar ionospheric plasma processes have previously benefited from investigation using full-wave numerical simulation codes, for example as reported by [Gondarenko et al., 2003] who used an alternating-direction implicit (ADI) model to simulate linear mode conversion processes, [Eliasson and Stenflo, 2008] who studied the parametric decay instability and the generation of Langmuir turbulence around the interaction height using a generalized Zakharov model, or [Leyser and Nordblad, 2009, Nordblad and Leyser, 2010] who simulated the Z-mode pumping of a non-linear density ducts such as that formed via the self-focusing instability using ray tracing coupled with a Runge-Kutta scheme. In this Chapter, the GPU-accelerated FDTD code developed in Chapter 3 is used to study the O-mode to Z-mode conversion process in two spatial dimensions, allowing the variety of background density scenarios to be investigated. The time-dependent on-grid updates to the plasma density and temperature included in the FDTD algorithm meant that the impact of O- to Z-mode conversion on the growth of

thermal-scale plasma perturbations could be simulated.

The Chapter is structured as follows: in Section 4.2, the numerical simulation algorithm is briefly introduced. In Section 4.3, the simulation code is used to calculate the radio window for which conversion from O-mode to Z-mode is favourable for a simplified linear density gradient, with the results shown to be in good agreement with the theoretical predictions of [Mjølhus, 1984]. The code is then used to demonstrate how the radio window is modified by the presence of two-dimensional (2D) plasma density features of varying scale sizes, such as density-depleted ducts or striations. Section 4.4 presents the results of full-wave plasma simulations, which demonstrate that the excitation and subsequent reflection of the Z-mode wave has a strong influence on the magnitude of artificially-induced plasma perturbations, such as electron temperature enhancement, excited close to the O-mode interaction region. Simulations of plasma heating experiments for a range of pump wave launch angles show that the O-mode to Z-mode conversion process is a key mechanism contributing to the observed Magnetic Zenith Effect. In Section 4.5, the effects of adding 2D plasma irregularities are investigated, with the influence of this process on the development of artificially-induced plasma perturbations demonstrated to be heavily dependent on both pump wave inclination angle and irregularity characteristics.

4.2 Methodology

To numerically simulate an ionospheric modification experiment, this study uses the GPU-accelerated FDTD code described and validated in Chapter 3 above. The FDTD scheme assumes a multi-fluid description of a dynamic, anisotropic, collisional plasma, in which electron or charged ion species are treated as individual fluids of continuous mass and charge. The effect on wave propagation due to the presence of plasma is introduced through the coupling of Maxwell's wave equations with the Lorentz equations of motion for each constituent plasma species, with anisotropy introduced through inclusion of a static externally-applied magnetic field in a manner similar to that described by [Young, 1994] or [Yu and Simpson, 2010]. The time-dependent variation of plasma temperature and density are treated by the inclusion of expressions for the dynamic behaviours

of small perturbations of the plasma fluid temperature and density [Gurevich, 1978]. Together, these form a set of coupled first-order partial differential equations which govern the time dependent behaviour of the EM wave and plasma medium, introduced in Section 1.3.2 and repeated below:

$$\nabla \times \mathbf{E} = -\mu_0 \frac{\partial \mathbf{H}}{\partial t} \quad (4.1)$$

$$\nabla \times \mathbf{H} - \sum_a N_a e_a \mathbf{U}_a = \epsilon_0 \frac{\partial \mathbf{E}}{\partial t} \quad (4.2)$$

$$N_a m_a \frac{\partial \mathbf{U}_a}{\partial t} = N_a e_a (\mathbf{E} + \mathbf{U}_a \times \mathbf{B}) - N_a m_a \nu_a \mathbf{U}_a - \nabla (k_B N_a T_a) \quad (4.3)$$

$$\frac{\partial N_a}{\partial t} = -\nabla \cdot (N_a \mathbf{U}_a) \quad (4.4)$$

$$\frac{3}{2} k_B \frac{\partial}{\partial t} (N_a T_a) = -\nabla \cdot \mathbf{Q}_a + N_a e_a \mathbf{E} \cdot \mathbf{U}_a + \Delta \varepsilon_a \quad (4.5)$$

In these expressions, subscript a refers to plasma component species. \mathbf{U} is the time-varying fluid bulk velocity vector, $\mathbf{B} = B \hat{\mathbf{b}}$ is the static background magnetic field, T and N are the plasma temperature and number density respectively, $\nabla \cdot \mathbf{Q}$ describes the heat flux transport, $\Delta \varepsilon$ is a collisional heating term, e_a and m_a refer to particle charge and mass respectively, ϵ_0 and μ_0 are the permittivity and permeability of free space respectively, and k_B is the Boltzmann constant. The term ν represents the effective collision frequency given by Equation (4.6) [Gondarenko et al., 2005]:

$$\nu(N, T) = \nu_0 \left(\frac{N}{N_0} \right) \left(\frac{T}{T_0} \right)^{-3/2} \quad (4.6)$$

where ν_0 , N_0 and T_0 are the unperturbed effective collision frequency, number density and temperature respectively. The effective collision frequency incorporates both collisions with other plasma particles and with the neutral background species, such that $\nu_e = \nu_{ei} + \nu_{en}$ and $\nu_i = \nu_{ie} + \nu_{in}$, where ν_{ei} , ν_{ie} , ν_{en} and ν_{in} are the electron-ion, ion-electron, electron-neutral and ion-neutral collision frequencies respectively. In the simulation studies described below, the undisturbed collision frequencies ν_0 were chosen to represent typical conditions in the F-region at Tromsø, and updated every time-step via (4.6) to reflect simulated perturbations to the plasma medium.

Simulated fields are updated sequentially via a leapfrog time-stepping scheme, following the cyclical update pattern: $\mathbf{E}^q \rightarrow T^q \rightarrow \mathbf{H}^{q+\frac{1}{2}} \rightarrow \mathbf{U}^{q+\frac{1}{2}} \rightarrow N^{q+1} \rightarrow \mathbf{E}^{q+1} \rightarrow \dots$. Here \mathbf{E} , \mathbf{H} , \mathbf{U} , T and N represent the simulated electric field, magnetic field, fluid velocity, plasma temperature and density respectively. The index q refers to the simulation time step number. The inclusion in the time-stepping algorithm of on-grid updates to perturbations of the plasma medium allows non-linear plasma processes such as the resonance instability or self-focusing instability to develop naturally in the simulation volume.

No plasma particle source or loss rate terms (for example representing ionisation or recombination) were included in the equations governing density (4.4) and temperature (4.5). It was assumed that approximately steady-state background conditions would be maintained over the timescales of the simulations described below (maximum duration $\sim 1\text{ s}$) despite the influence of diffusion / transport processes driven by background density or temperature gradients. To verify this, a short test simulation was run without a source EM wave under typical conditions (equivalent to the background plasma medium and computational domain parameters used in Section 4.4 below). This indicated that the magnitude of perturbation due to diffusion alone was sufficiently small such that there was no risk of it obscuring features excited by a source wave; for example, after 1×10^6 timesteps, the average magnitude of electron density perturbation in the absence of a source wave was of order $\sim 10^{-7}N_{e0}$, compared to a typical perturbation amplitude of order $\sim 10^{-4}N_{e0}$ measured after a similar time in the presence of a source wave. However, the longer the simulation duration, the greater the chance that a breakdown of steady-state conditions due to transport processes could lead to inaccuracies in the results. To reduce this source of error, it would be desirable for future versions of this code to include plasma sources and losses to better maintain the steady-state background conditions. Ideally, these would model the local ionospheric chemistry, and would allow the impact of different neutral components and compositions on artificially-induced plasma perturbations to be investigated.

4.3 Numerical Simulation of Radio Window

A vital process in understanding the Magnetic Zenith Effect is thought to be the transition from O-mode polarised pump wave to a Z-mode (slow-branch X-mode) wave that may occur as the pump wave approaches the interaction height [Mjølhus and Flå, 1984, Mjølhus, 1990]. This process is highly dependent on the initial inclination angle of the pump wave with respect to the direction of the geomagnetic field near the O-mode reflection point. Conditions most favourable for conversion to Z-mode occur when the \mathbf{k} -vector of the incident wave is close to being parallel to the geomagnetic field direction at the height at which the transformation takes place (this corresponds to the height at which the local plasma frequency ω_{pe} matches the pump wave frequency ω_0). This effect can be seen from the EM wave dispersion curves plotted in Chapter 1, Figure 1.6, for the case of a linearly-increasing plasma density gradient. Waves capable of taking part in this conversion correspond to L-mode waves near the $k_\perp = 0$ limit of the O-mode dispersion surface; rather than being reflected at $\omega_{pe} = \omega_0$, these waves are able to continue beyond $\omega_{pe} = \omega_0$ on the Z-mode branch of the X-mode dispersion surface [Leyser and Nordblad, 2009]. The angular dependence leads to the formation of a “radio window” as described in, for example, [Mjølhus, 1984]: a range of inclination angles for which the pump wave is partially or fully transmitted beyond the O-mode reflection height as a Z-mode wave. As the direction of the incident wave \mathbf{k} -vector is governed by the refractive properties of the local plasma the wave passes through, the spatial profile of ionospheric plasma around the interaction height has a significant influence on the angular position and characteristics of the radio window, and thus potentially on the development of the Magnetic Zenith Effect.

A strength of a full-wave numerical code such as that developed in Chapter 3 is that it allows wave propagation through plasma to be accurately computed in scenarios for which analytical evaluation may be impossible without resorting to constraining regimes of approximation, for example those employed by geometric optics or similar [Budden, 1961, Ginzburg, 1970]. The FDTD scheme used here automatically incorporates linear

mode conversion processes such as the O-mode to Z-mode transition into the time-domain evolution of the simulated EM fields and the coupled on-grid updates to plasma density and temperature perturbation means that the time-dependent and nonlinear plasma response to an incident wave is directly included in any calculation. This Section presents the results of a series of simulations run using the FDTD code to investigate the effect of different plasma density profiles on the characteristics of the ionospheric radio window.

The simulation was set up as a two-dimensional scenario, with all wave propagation restricted to lie in the xz -plane, and all medium properties assumed to be homogeneous in the y -direction. A computational domain of dimensions $1280 \times 1 \times 1280$ Yee cells [Yee, 1966] was used, with the discrete spatial step size set as 5.50 m in all directions. To ensure numerical stability the Courant number [Taflove and Hagness, 2000] was chosen to be 0.5, which fixed the size of the discrete time step to be $9.17 \times 10^{-9}\text{ s}$. The simulation was terminated on all sides by a 32-cell complex-frequency-shifted perfectly-matched layer (formulated as described in Section 2.3.2) designed to ensure that any waves leaving the domain were absorbed with the minimum possible numerical reflection [Berenger, 1994]. For the plasma temperature, upper and lower edge termination was achieved using a Neumann boundary condition that set the gradient to zero along the direction of the background magnetic field. The left and right temperature boundaries, and all density boundaries were set to zero. A wave launching layer based on the principles of the total-field scattered-field implementation described in [Schneider, 2004] was used to introduce continuous electromagnetic waves of O-mode polarisation into the domain to represent the pump wave. The wave frequency was chosen to be $\omega_0 = 2\pi \times 4.54\text{ MHz}$. Background plasma parameters were chosen to represent typical F-region conditions during a heating experiment at Tromsø. Typical plasma parameters were obtained using IRI-2012 [Bilitza et al., 2014]. An idealised ionospheric plasma was represented by a one-dimensional (1D) linear vertical electron density profile of the form (4.7):

$$N_0(z) = N_{crit} \left(1 + \frac{z - z_{crit}}{L_z} \right) \quad (4.7)$$

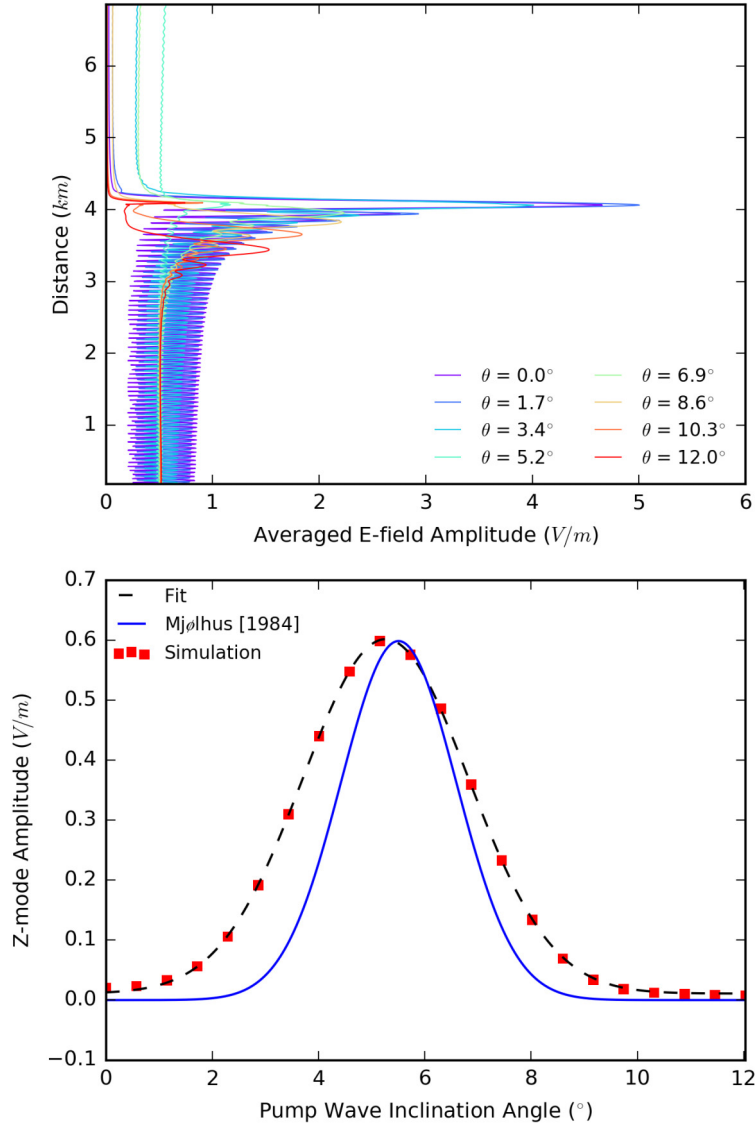


FIGURE 4.1: Angular dependence of O-mode to Z-mode conversion for linear vertical density gradient. Upper panel shows E-field amplitude averaged over $9.17 \times 10^{-4} s$ (1×10^5 time steps) for a selection of inclination angles. Penetration beyond the O-mode reflection height 4.1 km above the lower plane of the computational domain can be seen to occur most effectively for angles close to the Spitzer at 5.5° . Lower panel shows the simulated radio transmission window (red points, dashed black Gaussian fit) and the theoretical prediction from [Mjølhus, 1984] (blue). Computational grid parameters $\Delta_t = 9.17 \times 10^{-9} s$ and $\Delta_x = 5.50 m$ were used in these simulations.

In this expression, N_{crit} is the electron density at $X = \frac{\omega_{pe}^2}{\omega_0^2} = 1$, where ω_{pe} is the fundamental plasma frequency for electrons. z_{crit} is the distance above the lower edge of the simulation at which the critical density occurs, here set to be 4.11 km above the $z = 0$ plane. L_z is the scale height of the density gradient, set to be 20 km . A similar vertical profile was used for the background electron temperature, with the temperature at the critical height set to be 1800 K . A population of ions of average mass 16 AMU (representing O^+ ions) was included with a background density distribution equivalent to that of the electrons to preserve neutrality, and an initialised temperature of 900 K . The unperturbed collision frequencies for electrons and ions were set to be 500 s^{-1} and 6 s^{-1} respectively. A static magnetic field of magnitude $|\mathbf{B}| = 4.16 \times 10^{-5}\text{ T}$ was initialised in the domain at an angle of $\alpha = 12^\circ$ to the vertical. This was set to be uniform throughout the simulation domain, hence resulting in electron and ion gyrofrequencies of $\omega_{ce} = 2\pi \times 1.17\text{ MHz}$ and $\omega_{ci} = 2\pi \times 39.7\text{ Hz}$ respectively. Here and elsewhere in this thesis, the background field was held steady, and the plasma fluid velocity update equation (derived from (4.3)) linearised in \mathbf{B} . This approximation seems reasonable in the context of the ionospheric F-region, as both the spatial variation in the geomagnetic field over the distance scales simulated and the perturbation to this background field due to magnetic fields associated with the EM pump wave, and any currents associated with perturbations to the plasma would be expected to be small ($< 1\%$). Crucially, this approximation allowed several of the update coefficients involved in the simulation algorithm to be pre-calculated, saving valuable computation time. However, simulations presented below will show a modification to the electron structure, which would constitute a current and therefore a modification to the magnetic field; in future versions of the code, it would be desirable to incorporate this by including the contribution of perturbations to the magnetic field caused by both plasma modification and EM waves into the plasma velocity update step (this could be achieved by calculating $[\mathbf{B}_0 + \mu_0\mathbf{H}] \times \mathbf{U}$, where \mathbf{H} is the perturbed magnetic field, rather than simply the linearised $\mathbf{B}_0 \times \mathbf{U}$ used here) and allowing the background field profile to be set independently at each grid cell (these changes would incur an additional computational cost).

To investigate the angular characteristics of the O-mode to Z-mode conversion process,

a set of simulations were performed with the launch angle of the pump wave with respect to the vertical direction, θ , varied from $\theta = 0^\circ$ (pump wave \mathbf{k} -vector directed vertically, and in this case along the direction of the electron density gradient) to $\theta = 12^\circ$ (pump wave \mathbf{k} -vector along the direction of the simulated geomagnetic field) in $\Delta\theta = 0.01 \text{ rad}$ (0.57°) steps. The theoretical propagation paths for rays of varying inclination angle in the ionosphere can be seen, for example, in Figure 1 of [Isham et al., 2005]. The simulations were run for 1×10^5 time steps (equivalent to $9.17 \times 10^{-4} \text{ s}$), which was a sufficiently long time for a steady E-field pattern to develop, but short compared to the timescales required for electron plasma density and temperature perturbations excited due to the action of the radio wave to develop.

Each trace in the upper panel of Figure 4.1 shows the time averaged E-field amplitude measured along the original direction of propagation for a selection of simulated launch angles. In each case, a swelling effect can be seen as the pump wave approaches the $X^{num} = 1$ point at z_c where the wave is reflected (X^{num} is a numerical equivalent of variable X which takes into account the dispersive and dissipative effects of the discrete computational grid [Cummer, 1997]). At this point the O-mode pump wave is reflected downwards, leading to the generation of the large-amplitude standing waves visible in each plot around the interaction height. In most cases it can be seen that little or no wave amplitude is able to penetrate beyond the O-mode reflection point, however it is apparent that there is a window around 6° for which propagation to higher altitudes is viable. This window is the range of angles for which mode conversion from the initial ordinary wave to an extraordinary-polarised Z-mode wave is favourable, and corresponds to a set of angles for which the \mathbf{k} vector of the incident wave is close to parallel to the local geomagnetic field as the wave reaches the reflection height. The optimal angle for this process to occur in a vertically-inhomogeneous ionosphere is given by the Spitz angle (4.8) [Mjølhus, 1990] and is a function of the plasma medium parameters:

$$\theta_{Spitz} = \arcsin \left[\left(\frac{Y}{Y+1} \right)^{\frac{1}{2}} \sin(\alpha) \right] \quad (4.8)$$

where $Y = \frac{\omega_{ce}}{\omega_0}$, ω_{ce} is the electron cyclotron frequency and α is the angle between the

local geomagnetic field and the vertical. In the scenario described here, the value of the Spitz angle was calculated to be 5.5° . The average fraction of wave amplitude penetrating beyond the O-mode reflection height for each angle is indicated in the lower panel of Figure 4.1 by the red markers, and shows a Gaussian-shaped transmission window centred on 5.3° and with a full-width at half-maximum of 3.1° (Gaussian fit is indicated by the dashed black line). The theoretical window for transmission of the EM wave through the reflection barrier via O-to-Z conversion as calculated by Mjølhus [Mjølhus, 1984] for the density profile used here is indicated by the blue line.

A small E-field swelling at the reflection height is seen in the upper panel of Figure 4.1 for waves directed close to the Spitz angle despite the Z-mode conversion efficiency being close to 100%. This is due to a combination of effects: anisotropic divergence in wave direction due to numerical dispersion and the slight spread in propagation angle around the pump wave edges both lead to the reflection of a small fraction of the pump wave.

The linear density slope used in this simulation is only a simplified representation of the F-region of the ionosphere. In this 1D density gradient case, O-mode to Z-mode conversion occurs most favourably at the Spitz angle. However, in experiments performed at EISCAT, the most substantial perturbations to the plasma have often been observed when the pump wave inclination angle is greater than the Spitz. Experiments such as that reported by [Kosch et al., 2011] have observed the Magnetic Zenith Effect to manifest most strongly for inclination angles between the Spitz and field-aligned directions. [Isham et al., 2005] have also observed the maximum topside backscattered power to occur in this range, indicative of the radio window shifting towards the magnetic zenith. One mechanism that may be responsible for this shift could be the presence of a horizontal density gradient in addition to the vertical gradient, as a 2D variation in the plasma density would be expected to influence the direction of the pump wave \mathbf{k} -vector as it approached the reflection height. As mentioned in Section 4.1 above, a varied hierarchy of density structures are likely to arise when the ionosphere is illuminated by high-power radiation due to the formation of plasma irregularities of different scales. In particular, the density gradient in the horizontal direction is unlikely to be homogeneous

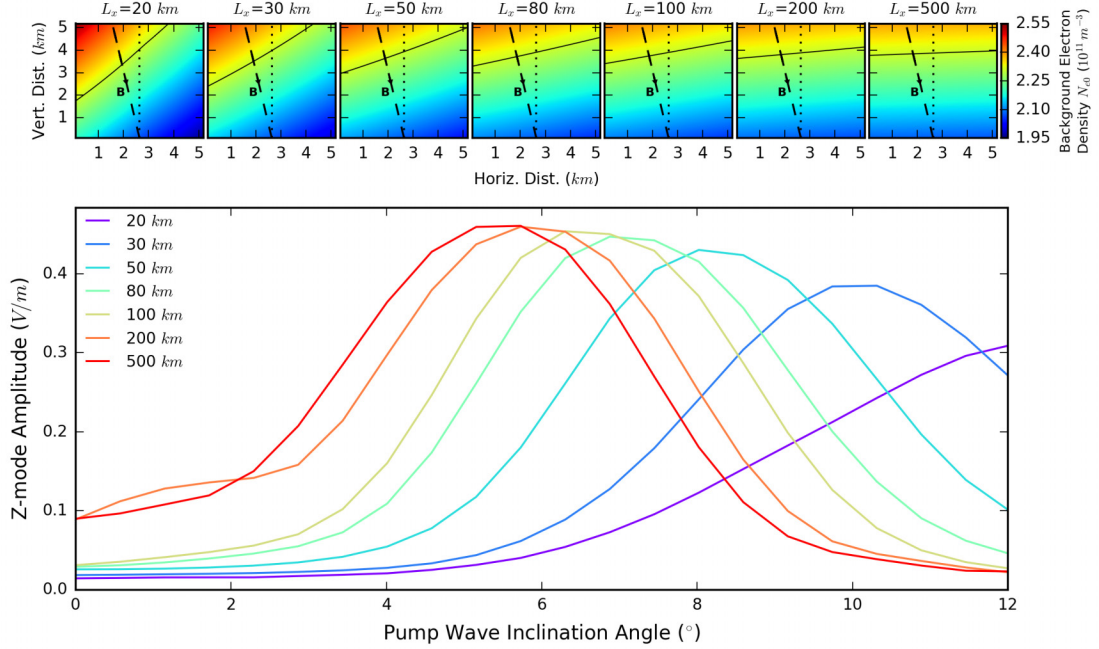


FIGURE 4.2: Simulated Z-mode window for varying horizontal slope scale size L_x when background density profile (4.9) is used as a background density profile (smaller L_x implies a steeper slope). It can be seen that increasing the steepness of the slope shifts the centre of the radio window away from the Spitz angle towards the magnetic zenith. This effect is most pronounced in the case of the 20 km curve (the steepest horizontal gradient considered here), with no radio window peak seen in the range of angles between vertical (0°) and field-aligned (12°); from the shape of the curve, it appears likely that the peak in this case occurs just beyond the zenith direction. The background plasma density, magnetic field direction (dashed line), vertical direction (dotted line) and position of the O-mode reflection height (solid black line) used for each L_x are shown in upper panels.

as was assumed in the above analysis. [Honary et al., 2011] obtained a theoretical expression for the shift in the radio window from the Spitz angle towards the magnetic zenith due to an additional horizontal density gradient, however this calculation assumed that the ionospheric inhomogeneity existed along one direction only (which in the general case can deviate from the vertical direction). The case of 2D variation of the plasma density has not been discussed before, and can only be investigated numerically.

To this end, the FDTD code was used to investigate the effect that density structures of various spatial scales have on the position of the Z-mode window. Three different inhomogeneity regimes were investigated: large-scale 2D linear gradients, single field-aligned duct-like density depletions and periodically-arranged smaller-scale field aligned irregularities.

To simulate a large-scale density-depleted patch, such as that caused by the bunching together of several non-linear density structures in the heated volume, a linear horizontal slope of scale size L_x with density increasing from left to right in the computational domain was added to the background electron density profile. Examples of the 2D background electron density profiles for a selection of L_x can be seen in the upper panels of Figure 4.2. The full form of the background density profile in this case is given by (4.9):

$$N_0(x, z) = N_{crit} \left(1 + \frac{x}{L_x}\right) \left(1 + \frac{z - z_{crit}}{L_z}\right) \quad (4.9)$$

A computational domain of dimensions $1920 \times 1 \times 1920$ was used, with the discrete step sizes set to $\Delta_t = 4.58 \times 10^{-9}$ s and $\Delta_x = 2.75$ m. All other simulation parameters were set as described above. The vertical slope scale size was kept constant at $L_z = 20$ km.

The position and width of the Z-mode window was measured for different grades of horizontal slope, changed by varying L_x , with the results shown in Figure 4.2. The introduction of a horizontal density inhomogeneity of this form was found to shift the centre of the radio window away from the Spitze direction and towards the magnetic zenith direction, with larger shifts experienced as the gradient was increased. This effect is most pronounced in the case of the 20 km curve (the steepest horizontal gradient considered here), with no radio window peak seen in the range of angles between vertical (0°) and field-aligned (12°); from the shape of the curve, it appears likely that the peak in this case occurs just beyond the zenith direction. The angular width of the window was also found to increase overall as the horizontal gradient increased, whereas the maximum transmitted E-field amplitude was found to decrease. This result supports the theory that the Z-mode window can be shifted by the presence of a horizontal density slope, and potentially explains why experiments such as [Isham et al., 2005] observed the greatest magnitude of artificially-induced plasma perturbation to be excited by pump waves directed somewhere between the Spitze and field-aligned directions. For the vertical plasma gradient used here, a peak in the Z-mode window between the Spitze and field-aligned directions (around $\theta \simeq (8-10)^\circ$) would correspond to a horizontal inhomogeneity of around $L_x \simeq 50$ km.

In the auroral ionosphere, horizontal gradients in the opposing direction (increasing from right to left in the simulation domain) may also exist. In this case, the density gradient has the effect of shifting the centre of the Z-mode window away from the Spitze and towards the vertical direction, again with a greater deviation occurring for a greater steepness of horizontal slope.

To simulate the effects of a duct-like horizontal density feature, a field-aligned density depletion of the form (4.10) was included in the background density profile.

$$N_{irreg}(x', z') = N_0(x', z') \left[1 - A_{irreg} \exp\left(-\frac{(x_0 - x')^2}{2L_{width}^2}\right) \right] \quad (4.10)$$

where x' and z' are coordinates perpendicular and parallel to the simulated geomagnetic field, A_{irreg} and L_{width} are the amplitude and width of the irregularity respectively, x_0 is a reference distance, and $N_0(x', z')$ is the vertically-inhomogeneous background density profile given by (4.7), with the vertical slope scale height kept at $L_z = 20\text{ km}$ as before. A_{irreg} was set to be 0.05 to represent a maximum density depletion of 5% of the background. A smaller computational domain of dimensions $1280 \times 1 \times 1280$ was used to reduce computing time, with the discrete step sizes set to $\Delta_t = 9.17 \times 10^{-9}\text{ s}$ and $\Delta_x = 5.50\text{ m}$. L_{width} was varied to investigate a range of irregularity scale-sizes, from small-scale single striations with a width of tens of metres, up to larger ducts with widths of several kilometres. Examples of the 2D background electron density profiles for a selection of L_{width} can be seen in the upper panels of Figure 4.3. The effect of different perturbation widths on the position of the radio window is shown by the lower panel of Figure 4.3.

The presence of a duct-like inhomogeneity was found to have a strong effect on the O- to Z-mode conversion process, with the resulting radio window falling into one of several broad regimes depending on the irregularity width. Smaller-scale irregularities with widths $\lesssim 0.1\text{ km}$ were found to have a minimal effect on the Z-mode window shape, resulting in only a slight shift the radio window away from the Spitz position and towards vertical by $(0.5 - 1)^\circ$ measured. For duct widths in this range, the radio window was found to be broader than in the unperturbed case, with a full-width at

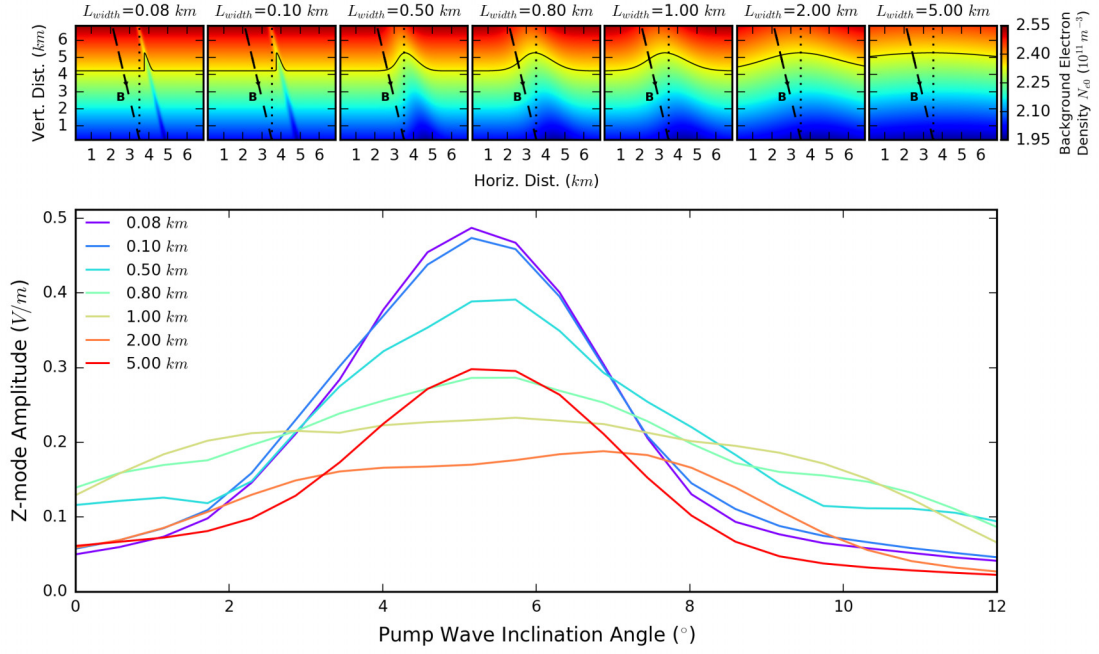


FIGURE 4.3: Simulated Z-mode window for varying duct width L_{width} when density perturbation of (4.10) is included in the background density profile. Initial amplitude of perturbation was set as 5% of the unperturbed background density given by (4.7). Smaller-width structures with $L_{width} \leq 0.1\text{km}$ can be seen to shift the distribution away from the Spitz direction towards vertical by $(0.5 - 1)^\circ$. As the irregularity width increases, the window broadens and loses its Gaussian shape. For widths $\geq 0.2\text{km}$, a significant fraction of incident wave amplitude was transmitted at all sampled angles, leading to a dramatic widening and flattening of the window. The background plasma density, magnetic field direction (dashed line), vertical direction (dotted line) and position of the O-mode reflection height (solid black line) used for each L_{width} are shown in upper panels. Computational grid parameters $\Delta_t = 9.17 \times 10^{-9} \text{ s}$ and $\Delta_x = 5.50 \text{ m}$ were used in these simulations.

half-maximum in the range $(4.0 - 4.5)^\circ$. Increasing the perturbation width in the range $0.1 \text{ km} \lesssim L_{width} \lesssim 2 \text{ km}$ was found to lead to an abrupt change in radio window shape, with a significant fraction of incident wave amplitude transmitted as a Z-mode for all sampled angles. This manifested as a broadening of the window as the scale size of the irregularity was increased, with the angular width of the window for a duct of 1 km width almost three times that of the 1D slope case. Increasing the irregularity width also had the effect of decreasing the Z-mode amplitude at each sampled angle, leading to a flattening of the window. For a 1 km width irregularity, the average amplitude transmitted of the Z-mode less than half that transmitted at the window central angle for the 1D slope regime. As the irregularity width was increased beyond 2 km , the shape of the Z-mode window was found to tend towards the unperturbed form measured for

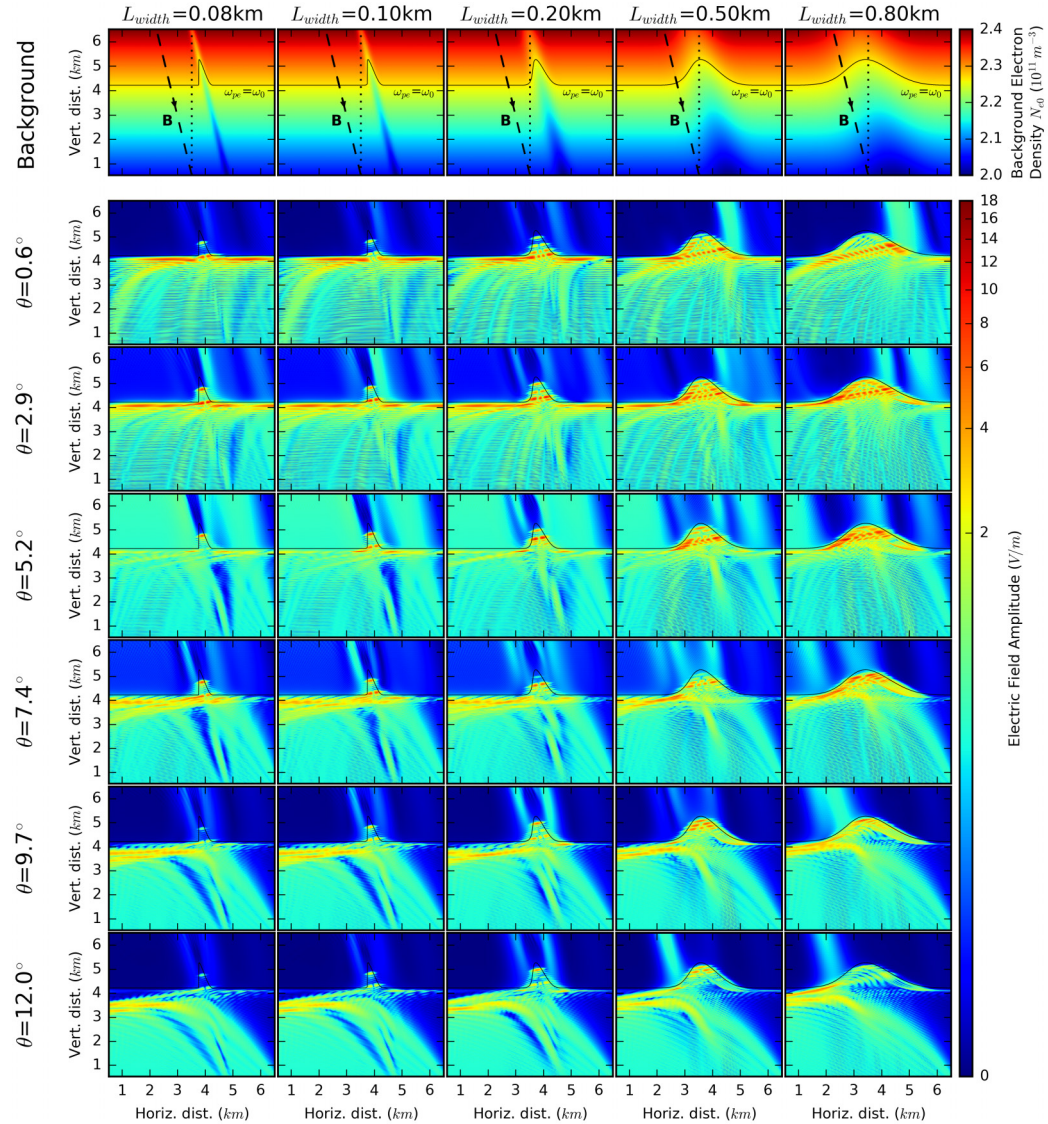


FIGURE 4.4: Time-averaged E-field amplitude for pump wave inclination angles of 0.6° , 2.9° , 5.2° , 7.4° , 9.7° and 12.0° when density perturbations of the form (4.10) and with L_{width} s of 0.08, 0.10, 0.20, 0.50 and 0.80 km are included in the background density profile. The position of the $X = 1$ O-mode reflection contour marked by a solid line. The colour range has been logarithmically-normalised to more clearly show the transmitted Z-mode waves passing beyond the O-mode reflection height. Upper panels show the background electron density, position of the O-mode reflection layer (solid black line), magnetic field direction (dashed black line) and vertical direction (dotted black line) for each L_{width} condition. Computational grid parameters $\Delta_t = 9.17 \times 10^{-9} s$ and $\Delta_x = 5.50 m$ were used in these simulations.

the case of a linear vertical slope only.

To understand the modification to the radio window caused by the presence of duct-like density irregularities, it was useful to examine the effect that an inhomogeneity of this nature has on EM wave propagation. 4.4 shows the E-field amplitude developed in

the simulation domain and averaged over $9.17 \times 10^{-4} s$ (1×10^5 time steps) for pump wave inclination angles of 0.6° , 2.9° , 5.2° , 7.4° , 9.7° and 12.0° and for the cases of irregularities of width 0.08 , 0.10 , 0.20 , 0.50 and $0.80 km$. The colour range of this plot has been logarithmically-normalised to more clearly show the transmitted Z-mode waves. The position of the $X = 1$ O-mode reflection contour is marked by a solid line. The Z-mode can be identified as signal which is able to penetrate beyond the O-mode reflection height. Around the region of the duct-like irregularity in each case, it can be seen that the Z-mode is transmitted as one or more narrow beams only, with the point(s) of transmission varying greatly according to the pump wave angle and duct geometry. For irregularities of width $> 0.1 km$, it can be seen that a strong Z-mode beam is transmitted for all angles shown (albeit emerging from very different points of the duct), leading to the flat, broad window profiles shown in Figure 4.3. Away from the region around the duct, behaviour reverts to that of the unperturbed case described above, with optimal O- to Z-mode conversion occurring at the Spitze angle. Only waves transmitted within a full width of the irregularity central axis were considered when calculating the shape of the window.

The irregular emission from the duct-like density features can likely be explained by considering the broad range of horizontal density gradients present in each duct profile. For the case of a linear horizontal density slope presenting a single gradient to the incoming wave, as explored above, different slope scale sizes were found to shift the inclination angle at which O-mode to Z-mode was most favourable. The duct-like irregularities investigated here present multiple horizontal density gradients simultaneously (the gradient between individual density nodes varies along the horizontal direction due to the Gaussian duct profile, unlike in the linear slope case), with changes in the duct width corresponding to changes in both the range of horizontal gradients present in the density profile and in their spatial distribution along the $X = 1$ contour (at which conversion may occur). Thus, for a given wave inclination angle and duct width, there may be a narrow range of points along the $X = 1$ contour at which the horizontal density gradient is favourable for O-to-Z-mode conversion, specific to that particular wave direction. This may lead to the irregular emission seen in Figure 4.4, and explain the broadening of the

window for certain duct widths. In the case of large-width ducts, only gentle horizontal density gradients with large scale-size are present in the profile, and thus O-to-Z-mode conversion would only be expected to occur for angles close to the Spitze angle; as the duct width is reduced, a broader range of individual gradients with increasing steepness (decreasing scale-size) would be introduced, allowing conversion to occur for a greater range of pump wave inclination angles.

The effect of including multiple periodically-arranged field-aligned density depletions was investigated by including density irregularities of the form (4.11) to the background density profile.

$$N_{irreg}(x', z') = N_0(x', z') \left\{ 1 - \frac{1}{2} A_{irreg} \left[1 - \cos \left(\frac{2\pi x'}{L_{width}} \right) \right] \right\} \quad (4.11)$$

Similarly to the duct-like irregularity simulation above, computational domain dimensions of $1280 \times 1 \times 1280$ were used, with the discrete step parameters set to $\Delta_t = 9.17 \times 10^{-9} \text{ s}$ and $\Delta_x = 5.50 \text{ m}$. The vertical slope scale size was set to be $L_z = 20 \text{ km}$ as before. Figure 4.5 shows the E-field amplitude developed in the simulation domain and averaged over $9.17 \times 10^{-4} \text{ s}$ (1×10^5 time steps) for pump wave inclination angles of 0.6° , 2.9° , 5.2° , 7.4° , 9.7° and 12.0° and for the cases of periodic irregularities of $L_{width} = 0.08$, 0.10 , 0.20 , 0.50 and 0.80 km . As with the single-irregularity case above, the $X = 1$ contour is shown by a solid line and the colour bar has been logarithmically-normalised to more clearly show any transmitted or trapped waves. The 2D background electron density profiles for each L_{width} can be seen in the upper panels of Figure 4.5. In the case of a single duct, the transmitted Z-mode wave can emerge from either side of the structure, or even multiple points simultaneously, depending on the inclination angle of the source wave, as shown by Figure 4.4. In the case of periodic structures, this resulted in a converted Z-mode wave potentially interacting with multiple adjacent irregularities. This had a strong effect on the propagation of the converted Z-mode, with transmitted waves multiply scattered by adjacent irregularities making it the Z-mode window shape almost impossible to measure in a meaningful way. In general, the scattering effect of periodic irregularities with spatial scales comparable to or smaller than the pump wave

wavelength ($\leq 0.08 \text{ km}$) had the consequence of attenuating the transmitted Z-mode amplitude at all angles while broadly maintaining the angular window shape measured for the unperturbed 1D density gradient case. As the irregularity width increased, multiple scattering of the Z-mode wave between adjacent irregularities resulted in the presence of high-amplitude E-field waves beyond the O-mode reflection height for all sampled pump wave angles. Scattered field beyond the reflection height was found to have amplitudes comparable to that found in the Airy field below the reflection height, and in some cases was well in excess of the maximum Z-mode amplitude obtained beyond $X = 1$ for the unperturbed 1D slope case.

4.4 Impact of Z-mode on Heating Effects

In the previous Section, the FDTD code was used to show that the O-to-Z-mode conversion process is strongly dependent on the electron plasma profile around the interaction height. In this Section, simulation results demonstrating that such behaviour can directly lead to an angular dependence in heating-induced effects such as electron temperature enhancement and the growth of density-depleted field-aligned irregularities are presented.

In an idealised heating experiment with a 1D linear vertical electron density gradient only, an O-mode wave launched at the Spitz angle will be almost fully converted to the Z-mode as it approaches the interaction height. The converted Z wave passes beyond the O-mode reflection barrier and, provided the ionospheric peak density is sufficiently high, is reflected at $X = Y + 1$. The reflected Z-mode wave can then freely propagate downwards, back towards the interaction region. As it approaches the point, close to the O-mode reflection height, at which $X = (1 - Y^2)/(1 - Y^2 \cos^2 \alpha)$, where α is the angle between the geomagnetic field direction and vertical, the reflected Z-mode wave encounters the X-mode resonance layer. This resonance is normally inaccessible to ground-launched fast X-mode waves which are reflected at $X = 1 - Y$, but when excited results in the very efficient conversion of the EM wave to upper-hybrid plasma waves [Gondarenko et al., 2002]. This process leads to a large increase in the E-field

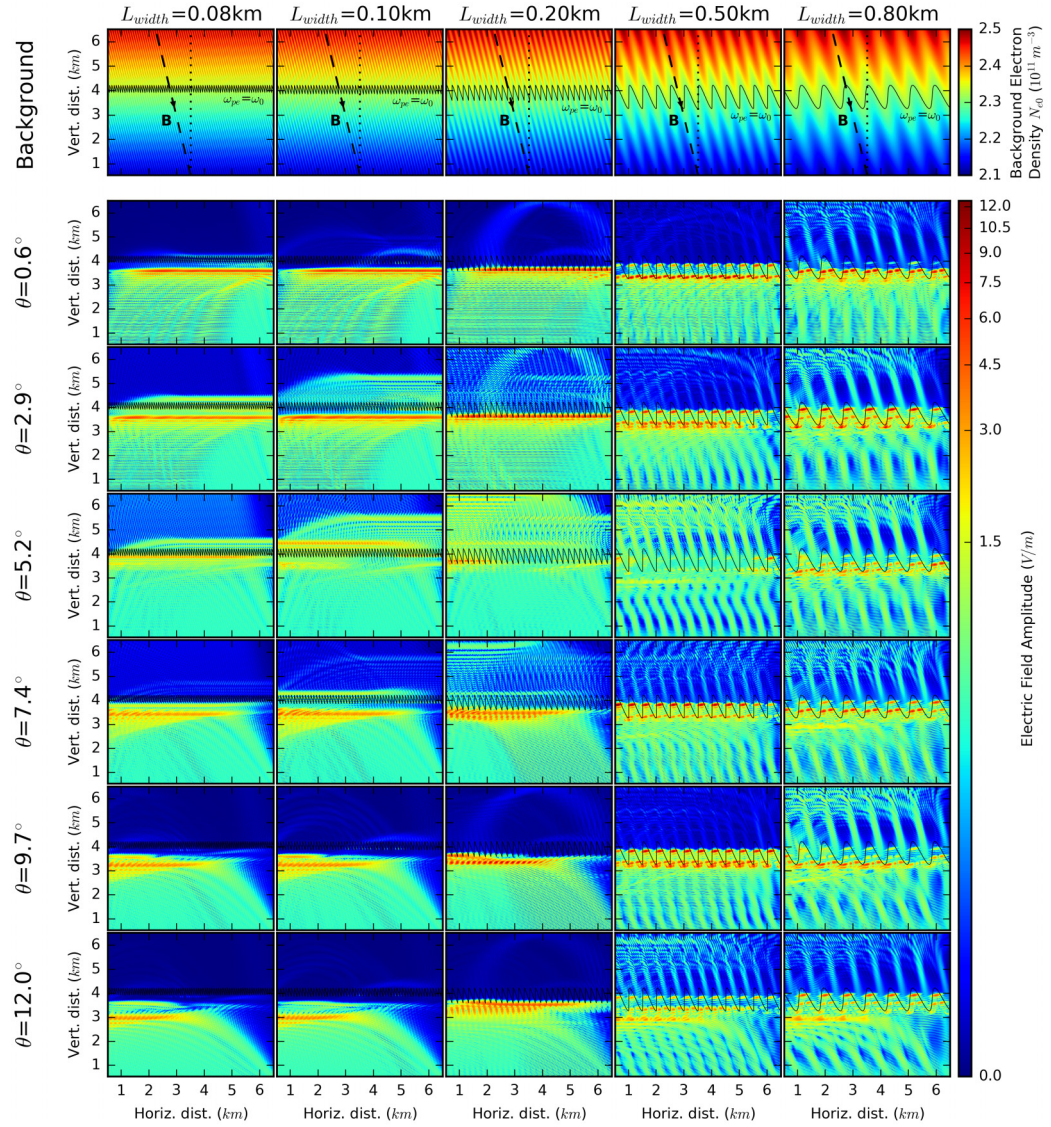


FIGURE 4.5: Time-averaged E-field amplitude for pump wave inclination angles of 0.6° , 2.9° , 5.2° , 7.4° , 9.7° and 12.0° when periodic density perturbations of the form (4.11) and with L_{width} s of 0.08, 0.10, 0.20, 0.50 and 0.80 km are included in the background density profile. The position of the $X = 1$ O-mode reflection contour is marked by a solid line. The colour range has been scaled to more clearly show the transmitted and scattered Z-mode waves beyond the O-mode reflection height. Upper panels show the background electron density, position of the O-mode reflection layer (solid black line), magnetic field direction (dashed black line) and vertical direction (dotted black line) for each L_{width} condition. Computational grid parameters $\Delta_t = 9.17 \times 10^{-9}$ s and $\Delta_x = 5.50$ m were used in these simulations.

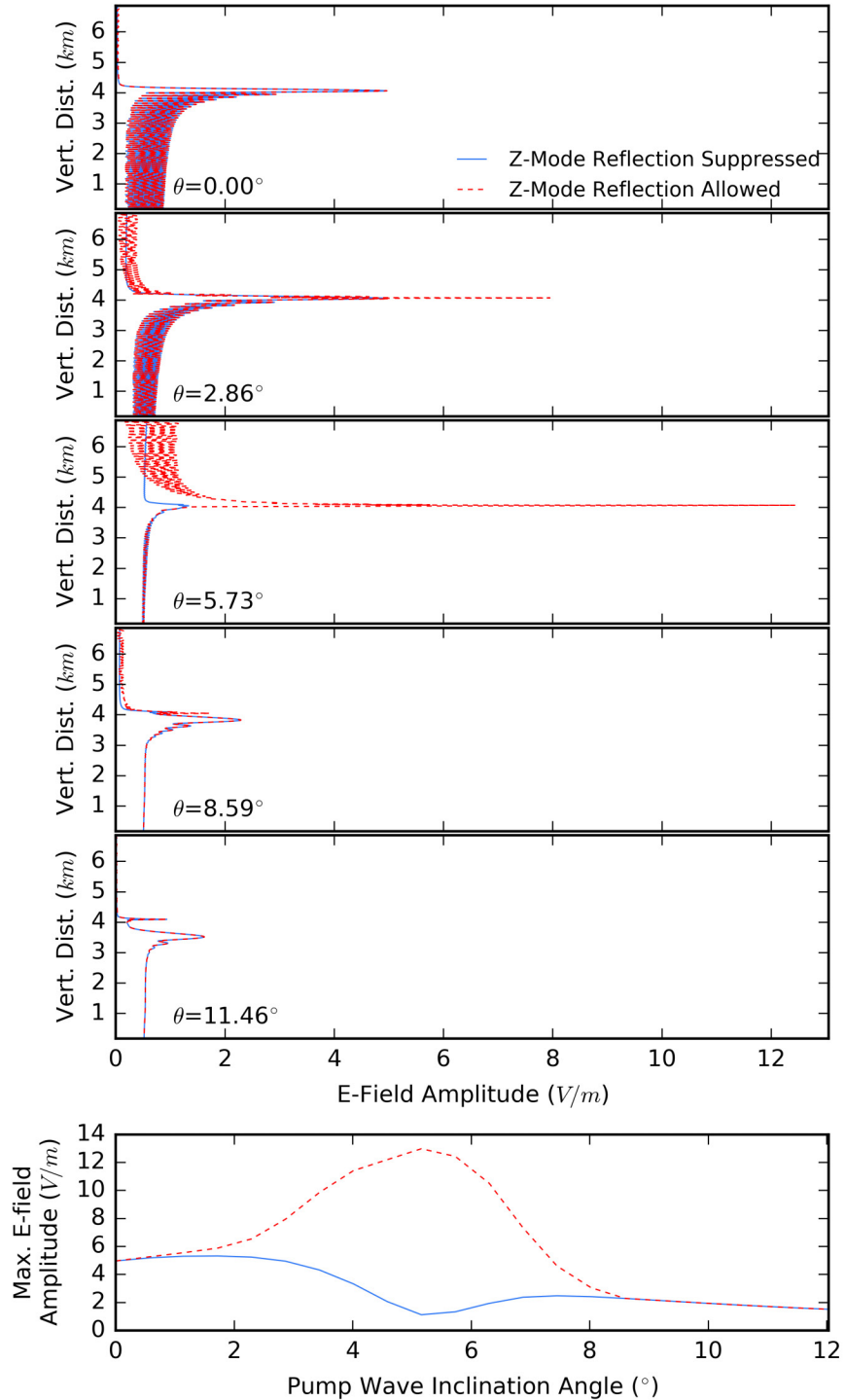


FIGURE 4.6: Upper panels show comparison of the E-field amplitude averaged over 1×10^5 time steps ($9.17 \times 10^{-4} \text{ s}$) for the case that the upwards boundary of the computational domain is terminated with an absorbing PML (blue) or a reflecting layer (red-dashed). Traces are shown for a selection of initial pump wave inclination angles. Lowermost panel shows the variation of maximum averaged E-field amplitude with inclination angle. It can be seen that allowing the Z-mode wave to reflect enhances the amplification of E-field around the interaction region, particularly for waves directed towards the centre of the radio window around 5.5° . Computational grid parameters $\Delta_t = 9.17 \times 10^{-9} \text{ s}$ and $\Delta_x = 5.50 \text{ m}$ were used in these simulations. The critical density for reflection of O-mode waves z_c was set to occur 4.1 km above the lower edge of the computational domain.

amplitude around the interaction region as shown in Figure 4.6. In this Figure, the time-averaged E-field amplitude measured along the direction of propagation is shown for a selection of inclination angles. The simulation parameters described in Section 4.3 for the case of an undisturbed 1D vertical density gradient were used, along with simple linear background electron and ion density profiles as given by (4.7), with $L_z = 20\text{ km}$. The blue curve shows E-field amplitude for the case when a PML was used to absorb the Z-mode wave as it reaches the upper boundary of the simulation, suppressing its reflection. The dashed-red curve shows the same signal, but for the case that the upper boundary of the simulation was set to be a reflecting boundary to simulate the reflection of the Z-mode wave at higher altitudes. A partial reflector was used in preference to a perfect reflector as the Z-mode wave would expect to experience partial attenuation due to collisional damping, particularly as it approaches $X = Y+1$. The variation in the peak E-field amplitude in the interaction region with pump wave inclination angle between the Z-mode-reflection-allowed and Z-mode-reflection-suppressed cases is shown in the lowermost panel of Figure 4.6. Allowing the Z-mode wave to reflect and propagate back towards the resonance layer was found to lead to a significantly enhanced amplification of the E-field around the interaction region. This effect was particularly pronounced for waves directed towards the centre of the radio window at around 5.5° from vertical, with the maximum magnitude of E-field amplitude found to be greater than 6 times that developed under similar conditions with Z-mode reflection suppressed.

The ability of the reflected Z-mode to excite large-amplitude plasma waves makes a clear difference to the magnitude of E-field standing wave that forms around the interaction region and can drive the formation of artificially-induced perturbations to the plasma medium. To investigate the impact of this effect on the growth of artificially-induced temperature and density perturbations in the heated region, two parallel simulations were performed: the first with Z-mode reflection suppressed using a PML layer at the upper boundary of the computational domain, the second with Z-mode reflection allowed through the inclusion of a reflecting boundary as described above. The simulation domain was set up with the smaller dimensions of $896 \times 1 \times 640$ Yee cells. The smaller size reduced the computing time required to calculate each simulation cycle and allowed

longer-duration runs to be performed. The time step size was set to be $1.83 \times 10^{-8} s$. The Courant number was maintained at 0.5 to preserve stability, and the discrete spatial step size set to be $11.0 m$ in all directions. A vertical gradient (4.7) was used as the background density profile, with $L_z = 20 km$ and $z_c = 4.46 km$ above the bottom edge of the simulation box, as indicated in the 2D background density profile shown in the uppermost panels of Figure 4.7 and Figure 4.8. Initially, no horizontal inhomogeneity was included. For this background density profile, the upper-hybrid resonance point occurred at $3.16 km$ above the bottom edge of the simulation. A similar 1D vertical gradient was used for the electron temperature, with the temperature at z_c set to be $1800 K$ and the slope scale-size set to be $L_z = 20 km$. This domain set-up was designed to include the important regions of interaction such as the reflection and upper hybrid resonance heights, while keeping the overall domain size small to reduce the computational run-time. An O-mode pump wave of frequency $\omega_0 = 2\pi \times 4.54 MHz$ was launched at an angle of 5.16° from the lower edge of the computational domain. As this inclination angle is close to the centre of the radio window, it was expected to lead to efficient conversion of the pump wave to the Z-mode. The beam was given a Gaussian profile to keep most of the source wave energy away from the domain boundaries. All other domain parameters were set as described in Section 4.3 for the case of an undisturbed 1D vertical density gradient.

Figures 4.7 and 4.8 illustrate the variation of E-field, electron density perturbation (expressed as a fraction of the background electron density, N_{e0}), fractional electron density irregularity amplitude $\delta N/N_{e0}$, and temperature perturbation evolved in the simulation after $1.83 \times 10^{-4} s$, $1.83 \times 10^{-2} s$, $9.17 \times 10^{-2} s$, $1.83 \times 10^{-1} s$, $2.93 \times 10^{-1} s$ and $1.10 s$ for the cases of Z-mode reflection suppressed (Figure 4.7) and allowed (Figure 4.8). The irregularity amplitude δN is calculated by subtracting a local average (taken along the horizontal x -direction) from the electron density perturbation, such that $\delta N = N_e - \langle N_e \rangle_x$. The temperature and density plots show the perturbations to the simulated medium only (initially zero everywhere) and do not include the background profiles. Both Figures show a rapid rise of the E-field amplitude at around $z_c = 4.46 km$ corresponding to the high-amplitude reflected standing wave, which results in significant rise of the E field

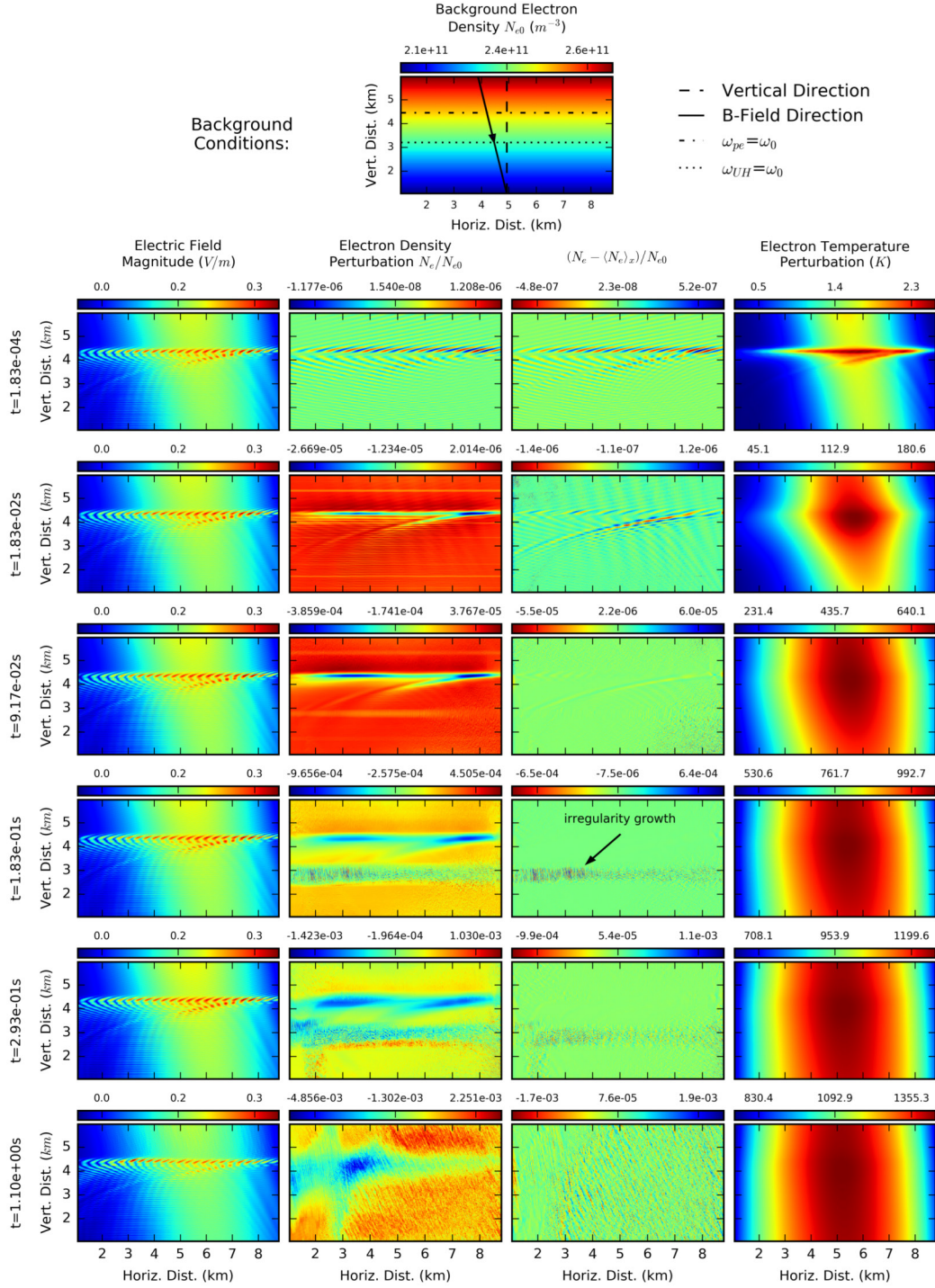


FIGURE 4.7: Change in the simulated E-field amplitude, electron density perturbation (expressed as a fraction of the background density N_{e0}), density irregularity amplitude $(N_e - \langle N_e \rangle_x)/N_{e0}$, and electron temperature perturbation with time, when Z-mode reflection was suppressed. Spatial snapshots of each quantity are shown for times $1.83 \times 10^{-4} s$, $1.83 \times 10^{-2} s$, $9.17 \times 10^{-2} s$, $1.83 \times 10^{-1} s$, $2.93 \times 10^{-1} s$ and $1.10 s$. Background conditions are shown in the uppermost panel. Computational grid parameters $\Delta_t = 1.83 \times 10^{-8} s$ and $\Delta_x = 11.0 m$ were used in this simulation. Field-aligned density irregularities with scale-sizes of approximately $30 - 40 m$ ($\sim 3 - 4 \Delta_x$) perpendicular to the geomagnetic field can be seen to grow with time around the upper-hybrid resonance height.

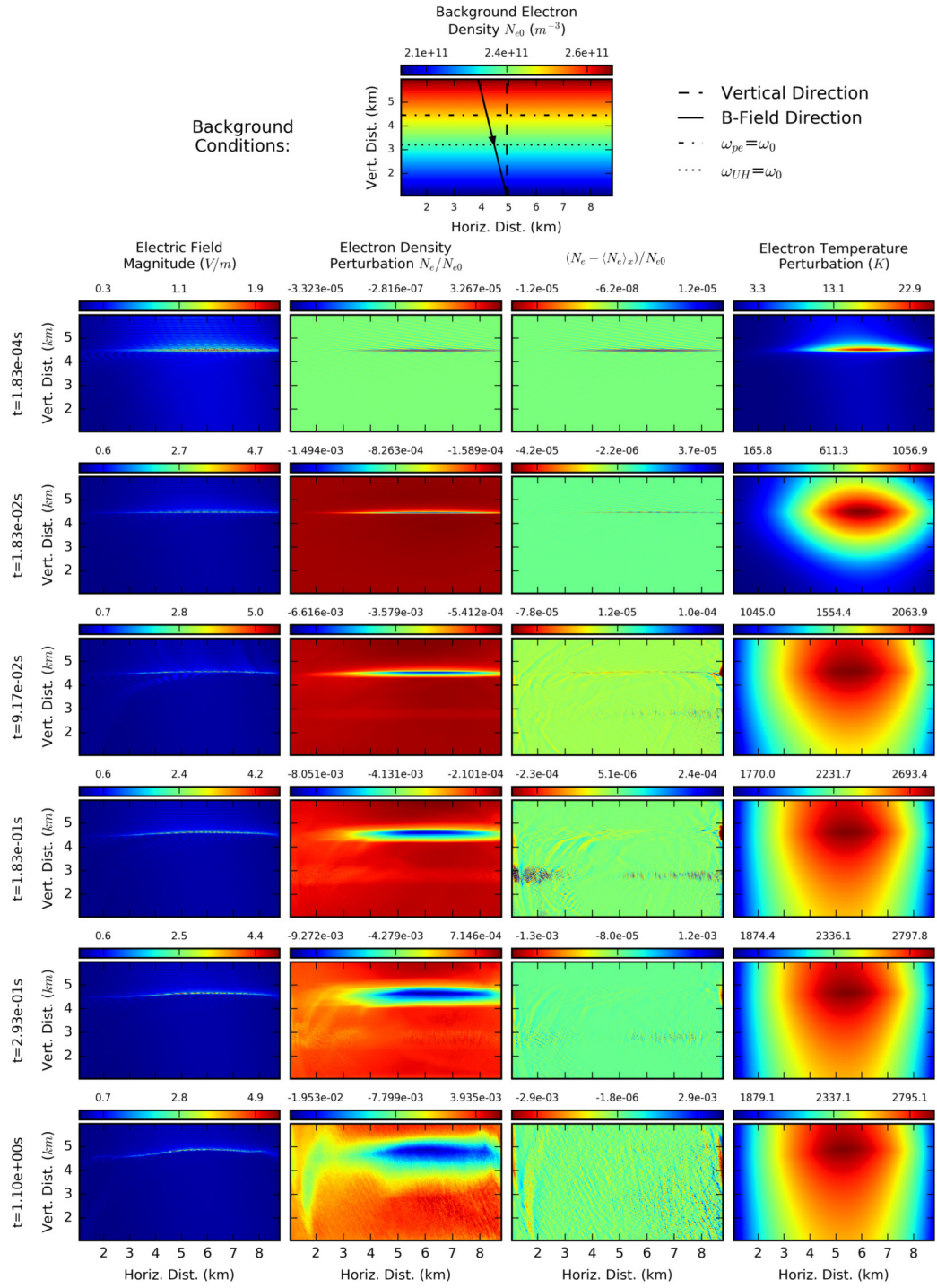


FIGURE 4.8: Change in the simulated E-field amplitude, electron density perturbation (expressed as a fraction of the background density N_{e0}), density irregularity amplitude $(N_e - \langle N_e \rangle_x)/N_{e0}$, and electron temperature perturbation with time, when Z-mode reflection was allowed. Spatial snapshots of each quantity are shown for times $1.83 \times 10^{-4} s$, $1.83 \times 10^{-2} s$, $9.17 \times 10^{-2} s$, $1.83 \times 10^{-1} s$, $2.93 \times 10^{-1} s$ and $1.10 s$. Background conditions are shown in the uppermost panel. Computational grid parameters $\Delta_t = 1.83 \times 10^{-8} s$ and $\Delta_x = 11.0 m$ were used in this simulation.

amplitude and an increase (due to the wave dissipation) of the electron temperature, which saturates after $\sim 0.3\text{ s}$. Allowing the Z-mode to reflect had a significant effect on the E-field strength developed in the simulation, with the saturation E-field amplitude achieved with reflection allowed over 10 times greater than with reflection suppressed. For the case of suppressed reflection, the highest field amplitudes were located around the reflection height at z_c and remained relatively steady for the duration of the simulation. By contrast, with reflection allowed, E-field amplitudes of up to 6 V/m were developed and located in a narrow band initially around z_c corresponding to the location of the resonance. This can be seen to move upwards in altitude with time as the simulation progresses, as shown by the leftmost panels of Figure 4.8. The Z-mode reflection allowed scenario was found to produce around double the increase in temperature compared to the reflection suppressed scenario. For both reflection suppressed and allowed cases, a strong electron density depletion is observed around the region of interaction. In the reflection-suppressed scenario, this takes the form of a pair of density depleted patches located on the shoulders of the Z-mode window. The density depletions are correlated with the regions where the pump wave is reflected and the reflection-induced standing wave forms (towards the edges of the beam, rather than towards the beam centre where the O-mode wave is transmitted as a Z-mode). This suggests that the formation of the density cavities may, in part, be due to a ponderomotive interaction or the excitation of a parametric instability. Around the peak of the window, the EM wave is mostly transmitted as the Z-mode and the swollen-amplitude reflected standing wave does not form; hence the density in this region is comparatively unperturbed. In the reflection-allowed scenario, the density perturbation takes the form of a single density-depleted cavity with a maximum depth of $N_e^{\min} \sim 0.02N_{e0}$. This is greater by almost a factor of 4 than the maximum magnitude of perturbation observed in the reflection-suppressed simulation. In this case, the site of maximum depletion can be seen to rise in altitude as the simulation progresses. This is caused by the downwards-travelling Z-mode wave encountering a region of plasma that matches the extraordinary-wave resonance condition $X = (1 - Y^2)/(1 - Y^2\cos^2\alpha)$ as it enters the depleted density patch. Due to the presence of the depletion, the resonance is encountered at a higher altitude than if there had been no density perturbation. High electric field amplitudes are excited as a result,

which accelerates the depletion of density around that region and leads to a gradual rise in altitude of the region of maximum density depletion as the simulation progresses. This process also explains why the band of maximum E-field amplitude moves upwards in altitude with time.

An interesting feature to note is the spontaneous formation of small-scale density structures aligned along the geomagnetic field, which become visible at after $\sim 0.1\text{ s}$ in the simulation. These are particularly clear in the plots of the density irregularity amplitude shown by Figure 4.7 for times of $t = 1.83 \times 10^{-1}\text{ s}$ and $t = 2.93 \times 10^{-1}\text{ s}$, and can also be seen at similar times for the reflection-allowed case in Figure 4.8. These appear to evolve naturally in the simulation, first appearing in a narrow band located just below the point at which the background upper-hybrid frequency matches with the pump wave frequency, and subsequently increase in both depth and elongation with time. At later times they can be seen to bunch together into larger-scale structures. Due to the location and orientation of these structures, it is clear that they are formed in the simulation due to the conversion of the pump wave to upper-hybrid waves; the altitude at which the structures initially form is located just below the upper-hybrid resonance height where the pump wave frequency matches the upper hybrid frequency, and the structures are exactly aligned along the geomagnetic field direction, consistent with a wave propagating in a direction perpendicular to this magnetic field. Changing the position of the upper-hybrid resonance height within the computational domain was found to change the position of this feature, with the initial location of the irregularity perturbation consistently found to originate in a band $\sim 400\text{ m}$ below the UH resonance height before extending with time to both higher and lower altitudes along the magnetic field direction. The density-depleted filaments were spatially resolvable under the grid resolution used here, with a typical spatial scale perpendicular to the geomagnetic field of $\sim 3 - 4\Delta_x$ when measured after $\sim 0.1\text{ s}$. The fact that the location at which these density structures formed within the simulation was found to change as the location of the UH resonance height was varied (rather than remaining at the same location in the computational domain) helped to give confidence that these were true plasma features and not numerical or averaging artefacts. That the individual irregularities were aligned

along the geomagnetic field and consistently appeared close to the UH resonance height also indicated that these features were linked to the excitement of UH waves, and were not numerical in nature.

Resolvable field-aligned density irregularities were visible after as little as 0.1 s ; this was unexpected as similar structures have been observed experimentally to require timescales of a few seconds or more to develop. This discrepancy may be partly due to the low amplitudes of the simulated irregularities: the maximum density irregularity amplitude developed over the simulation run was only $|N_e - \langle N_e \rangle_x| < 0.001N_{e0}$, which may be difficult to detect experimentally in a real heating experiment. The early onset of irregularity development may also be linked to the numerical noise level in the simulation. The linear mode conversion process understood to govern UH generation from an O-mode pump wave requires small-amplitude seed density irregularities to be present before it may proceed, however no such seed irregularities were included in the initial simulation density profiles. It is likely here that the seed for this process is provided by the low-amplitude numerical noise present in the simulated ion and electron densities. This is an artifact of the computational process and not physical in nature, however it may play an equivalent role to the seeding effect of low-amplitude density variations in the real ionosphere. If the numerical noise is of a higher amplitude or was to grow at a faster rate than seed perturbations in the real ionosphere, it may explain the unexpectedly early appearance of the field-aligned structures in the simulation.

To investigate this, the simulation was repeated for varying temporal and spatial step sizes, while keeping the Courant number constant. It was found that the field-aligned density structures become visible after approximately $6 \times 10^6 \Delta_t$, regardless of the magnitude of Δ_t , when test simulations were performed for $\Delta_t = 9.17 \times 10^{-9}\text{ s}$, $\Delta_t = 1.83 \times 10^{-8}\text{ s}$ and $\Delta_t = 3.67 \times 10^{-8}\text{ s}$. Subsequent to this, the growth rate of the irregularities was consistent with development due to a thermal physical process such as the resonance instability, and scaled with the simulated time in seconds rather than with the number of time steps. This implies that the onset time of irregularity growth was numerical in nature, dependent on the growth of numerical noise in the simulated plasma density, and thus was determined by the simulation time step number. After the

onset of the irregularities, their growth was physical in nature and progressed according to the physical timescale in the simulation rather than the numerical time step.

To investigate the dependence of artificially-induced heating effects on pump wave direction, the simulations above were repeated for pump wave launch angles θ of 0.1° , 1.7° , 3.4° , 5.2° , 6.9° and 8.6° . The electron density and temperature perturbation developed after 1.1 s for each wave direction is shown in Figure 4.9, with the Z-mode reflection-allowed case on the left and Z-mode reflection-suppressed case on the right. As before, these plots show only the perturbations to the plasma medium that developed during the simulation (initially zero everywhere), and do not include the background levels. In the reflection-allowed scenario, the strongest electron temperature enhancement was found to occur for an angle of 5.2° , which supports the argument that the pump wave that converts most effectively to the Z-mode (in this case, the wave with an inclination angle closest to the Spitz) should be able to produce the greatest temperature perturbation. For the reflection-suppressed scenario, the wave launched in a near-vertical direction produced the greatest temperature enhancement, as this wave lost the least energy to Z-mode transmission and thus resulted in a greater amplitude of standing wave below the O-mode reflection height. In this case, the Spitz-directed wave was almost fully transmitted through the reflection barrier and subsequently absorbed by the PML, hence causing the least temperature perturbation.

Summary plots showing how the maximum value of electron temperature perturbation and the minimum value of electron density perturbation in the simulation domain changed with time can be seen in the lowermost panels of Figure 4.9, for the cases of the pump wave directed above (8.6°), below (0.6°) and along the Spitz direction (5.2°). The Z-mode reflection-allowed scenario is shown by a solid line, with the reflection-suppressed case indicated by a dashed line. Allowing Z-mode reflection can be seen to lead to a higher eventual magnitude of heating induced effects by as much as a factor of 2 for the case of the Spitz-directed wave. Pump waves with initial inclination angles closer to the Spitz direction (for which conversion to Z-mode was more favourable) were found to achieve a greater magnitude of temperature enhancement and a greater variation between the reflection-allowed and reflection-suppressed cases.

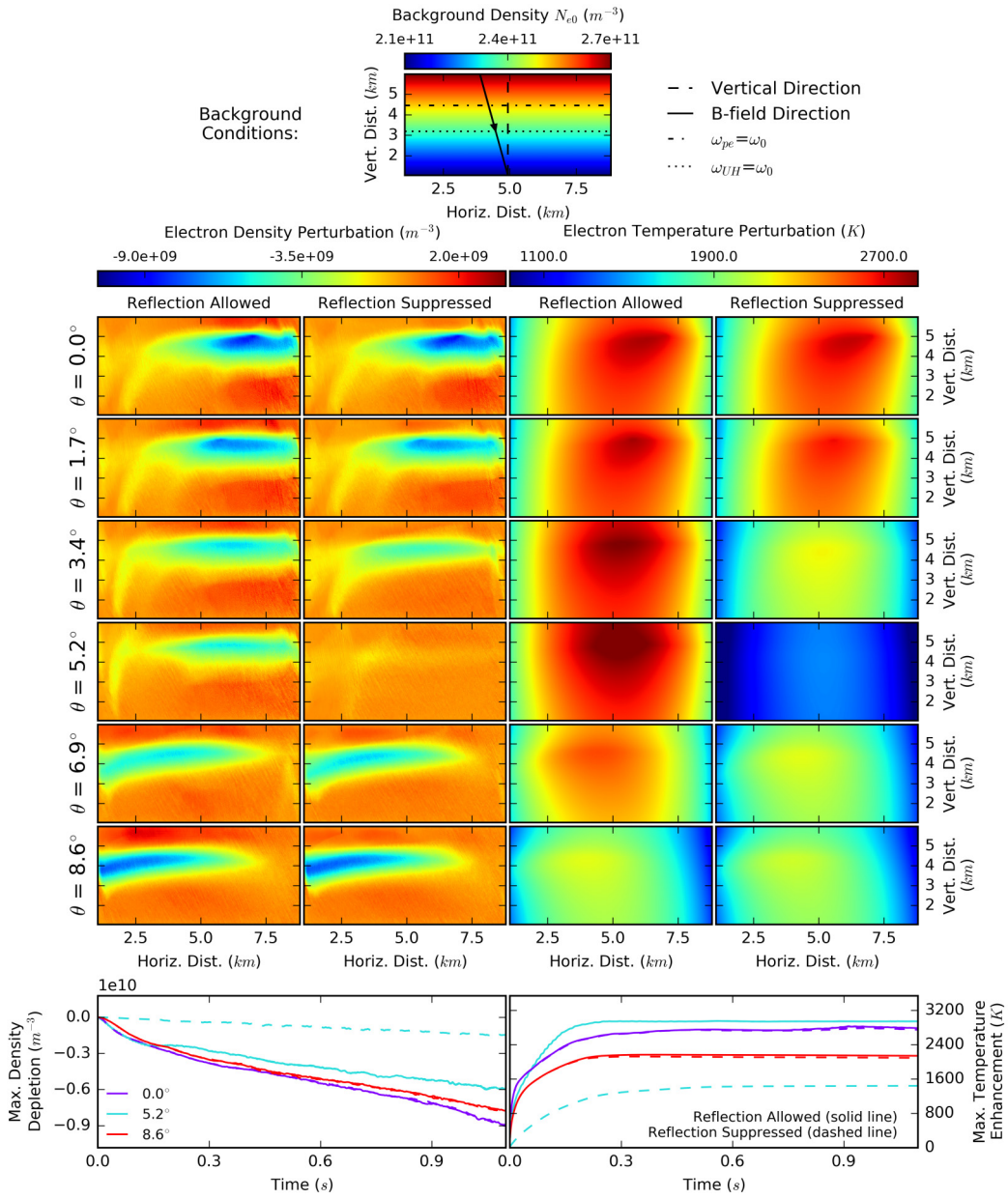


FIGURE 4.9: Variation of electron density and electron temperature perturbation with pump wave inclination angle, for the cases that Z-mode reflection is allowed and Z-mode reflection is suppressed. In the reflection-allowed scenario, the strongest electron temperature enhancement was found to occur for the pump wave inclined an angle of 5.2° (close to the Spitzer angle), supporting the argument that the pump wave that is most effectively converted the Z-mode excites the greatest temperature perturbation. In the reflection-suppressed scenario, the wave launched in a near-vertical direction produced the greatest temperature enhancement. The lowermost panels show the variation of the maximum value of electron temperature enhancement and electron density depletion in the simulation domain with time, for the Z-mode reflection allowed (solid lines) and suppressed (dashed lines) scenarios. Background conditions are shown in the uppermost panel. Computational grid parameters $\Delta_t = 1.83 \times 10^{-8} s$ and $\Delta_x = 11.0 m$ were used in these simulations.

The pump wave directed close to the Spitzee direction was also found to be most effective at exciting small-scale field aligned density irregularities around the upper-hybrid resonance height. This is shown by Figure 4.10 which displays the change in the fractional electron density irregularity amplitude, $(N_e - \langle N_e \rangle_x) / N_{e0}$, with time in a narrow band of altitude around the UH resonance level. Results are shown for pump waves directed along 0.0° , 5.2° and 8.6° to the vertical, after times of 0.11 s (uppermost panels), 0.13 s , 0.15 s , 0.17 s , and 0.18 s (lowermost panels). The UH resonance height at which the background upper-hybrid frequency matches the pump wave frequency ($\omega_{UH} = \omega_0$) is indicated by a dashed line. In each case, clear field-aligned density perturbations can be seen to grow with time, first visible from $\sim 0.1\text{ s}$ and persisting until they begin to collapse into less-ordered small-scale structures leaving a slight net density depletion. Initial growth of the irregularities in all cases occurs at an altitude $\sim 0.4\text{ km}$ below the UH height, after which they extend with time to both higher and lower altitudes. The rate of growth of striations can be seen to vary with pump wave angle, with the wave directed closest to the Spitzee angle (5.2°) causing the most rapid growth, both in terms of depletion depth and elongation along the magnetic field direction.

Panels in the left-hand column in Figure 4.10 show the 1D spatial Discrete Fourier Transform (DFT) of the magnitude of the fractional density irregularity amplitude $\delta N_e / N_{e0} = |N_e - \langle N_e \rangle_x| / N_{e0}$ for each angle, sampled along the horizontal axis of the simulation domain at the height at which the irregularities begin to develop. The DFT plots show that there is a clear increase in the perturbation amplitude for spatial frequencies around $k_x \sim 0.18\text{ m}^{-1}$, which increases in amplitude with time as the irregularities grow. This range of spatial frequencies corresponds to irregularity scale sizes in the range of $30 - 40\text{ m}$ ($\sim 3 - 4\Delta_x$) perpendicular to the geomagnetic field direction. The amplitude of density perturbation components in this scale-size range is highly dependent on pump wave angle, with the amplitude greater by a factor of 2 or more in the case of the Spitzee-directed wave. From this it follows that the UH wave excitation process is dependent on wave angle, with UH production occurring most favourably at the same range of angles for which the O- to Z-mode conversion process was most favourable.

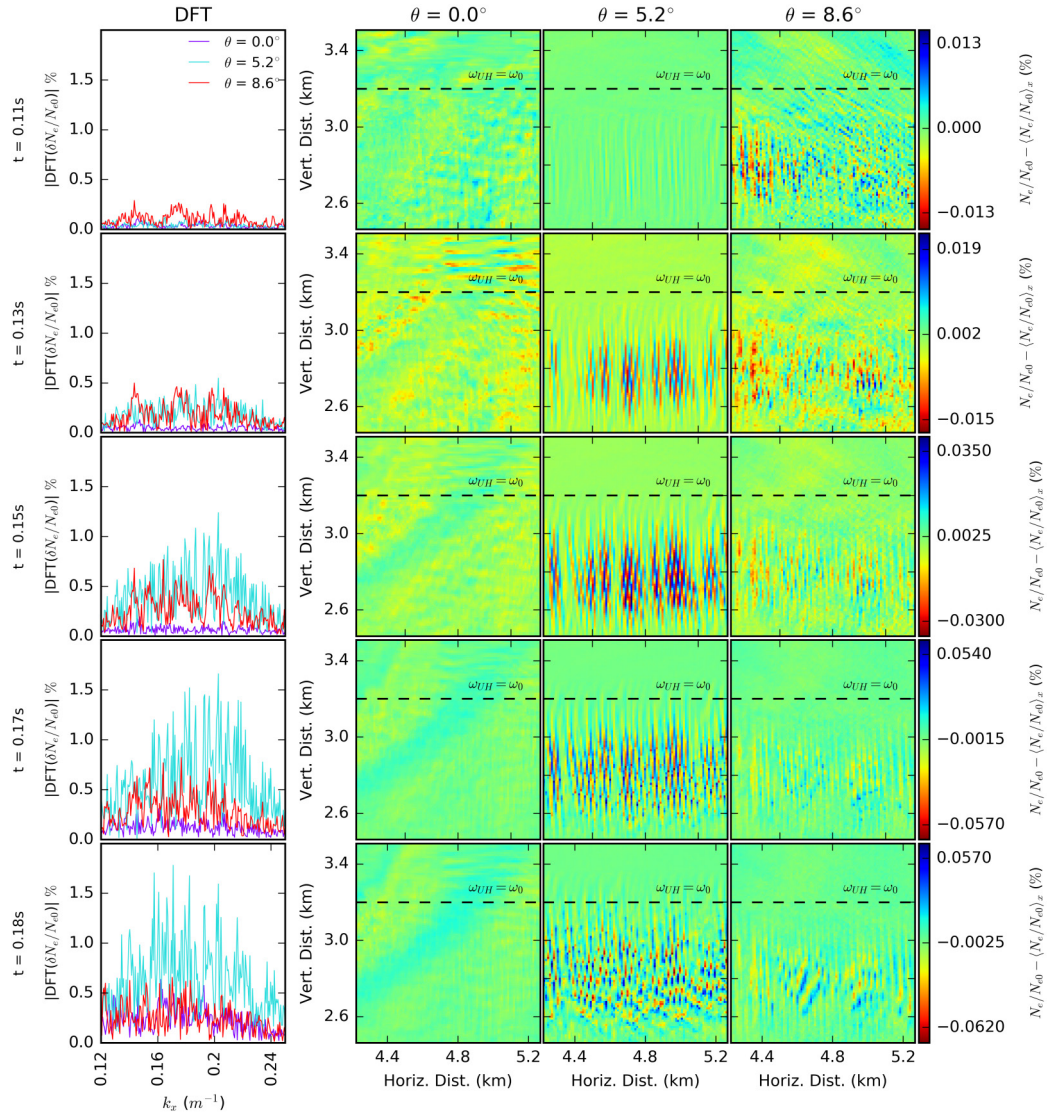


FIGURE 4.10: Right-hand three columns show the simulated growth of small-scale field-aligned density irregularities with time in a narrow band of altitude below the UH resonance level for pump waves directed along 0.0° , 5.2° and 8.6° to the vertical. The UH resonance height is indicated by a dashed line. Panels in the leftmost column show the 1D spatial discrete Fourier transform (DFT) of $\delta N/N_{e0}$ sampled along the horizontal axis of the simulation domain at the height at which the irregularities begin to develop ($\sim 2.8 \text{ km}$ above the lower boundary of the simulation). Amplitude of spatial frequency components around this value increases with time corresponding to the growth of irregularities and is greater by a factor of 2 or more in the case of the 5.2° -directed wave. Computational grid parameters $\Delta_t = 1.83 \times 10^{-8} \text{ s}$ and $\Delta_x = 11.0 \text{ m}$ were used in these simulations.

Production of UH waves and their dissipation in the associated field-aligned irregularities would be expected to make a significant contribution to the electron temperature enhancement via the resonance instability. As such, the dependence of irregularity production on pump wave angle demonstrated by these simulations could be expected to add a further contribution to the Magnetic Zenith Effect. Small-scale density irregularities such as this may also affect the development of large-scale plasma perturbations through anomalous attenuation of the pump wave. The code used here treats absorption of the pump wave through inclusion of an effective collision term ν_0 in a manner similar to that described by [Gondarenko et al., 2006]. The magnitude of irregularities developed over the simulation timescale is small ($< 0.001N_{e0}$), however, there is a small attenuation in the pump wave amplitude ($< 1 \text{ dB}$ for the vertically-directed wave) which may be due to absorption caused by irregularities.

The results presented in this Section show that the O-mode to Z-mode conversion process could be an important contributing mechanism behind the observed Magnetic Zenith Effect, with the observed angular dependence arising from the shape of the Z-mode window and the resonant excitation of large-amplitude electric fields via the reflected Z-mode contributing to the enhanced plasma perturbations.

4.5 Magnetic Zenith Effect with the Inclusion of Density Structures

The previous Section demonstrates that the O- to Z-mode conversion process can lead to an angular variation in the magnitude of artificial plasma perturbation with the inclination angle of an incident O-mode wave, for the case of a 1D linear vertical plasma density gradient. The addition of a component of horizontal inhomogeneity has been shown in Section 4.3 to significantly modify the Z-mode window, thus it is to be expected that the presence of a horizontally-inhomogeneous density feature will also affect the dependence of plasma perturbation on pump wave direction. This Section presents the results of simulations performed for various pump wave directions and for the cases that a linear horizontal density gradient, a single field-aligned density-depleted duct, or a

periodic distribution of field-aligned density-depleted irregularities are included in the background density profile.

Simulations were performed for pump wave initial inclination angles 0.0° , 2.9° , 5.7° , 8.6° , 11.5° with Z-mode reflection allowed. Computational domain dimensions were set to be $1024 \times 1 \times 768$. For increased accuracy, the time step size was reduced to $\Delta_t = 1.22 \times 10^{-8} s$ and the spatial step size to $\Delta_x = 7.33 m$ (keeping the Courant ratio $S_c = 0.5$ to maintain stability). The O-mode pump wave frequency (and hence the frequency of any excited Z-mode waves) was set to be $\omega_0 = 2\pi \times 4.54 MHz$ as before, meaning that, under the reduced step parameters used here, one pump wave (or Z-mode) oscillation period corresponded to $18\Delta_t$ and one pump wave (or Z-mode) wavelength to $9\Delta_x$ in free space. All other medium parameters were set as described in Section 4.4.

Figure 4.11 shows the electron density and temperature perturbation developed in the simulation after $0.23 s$ when a 2D density profile including a linear horizontal slope as given by (4.9) is used. Results for horizontal scale heights $L_x = 20 km$ and $L_x = 50 km$ are shown. In both cases the vertical slope scale-size was set to be $L_z = 20 km$. The lowermost panels show the variation of minimum density perturbation and maximum temperature perturbation recorded in the simulation with time. The $L_x = 20 km$ case is indicated by a solid line, and the $L_x = 50 km$ case by a dashed line.

The most striking difference between the results shown in Figure 4.11 and the unperturbed case with no horizontal inhomogeneity shown in Figure 4.9 is the shifting of the inclination angle responsible for the greatest temperature enhancement from the Spitzer position towards the magnetic zenith direction with decreasing L_x . For $L_x = 50 km$, the greatest temperature enhancement is produced by the wave launched at 8.6° . This is consistent with the modification of the Z-mode window found by the simulations presented in Section 4.3 for the case of a linear horizontal density inhomogeneity (as shown by the Z-mode window curves in Figure 4.2), which predicts maximum Z-mode transmission to occur for pump waves directed at an angle of 8.2° for the $L_x = 50 km$ case. Likewise, the analysis of Section 4.3 shows O- to Z-mode conversion to be more favourable as the pump wave direction approaches the zenith direction for the case of $L_x = 20 km$. This

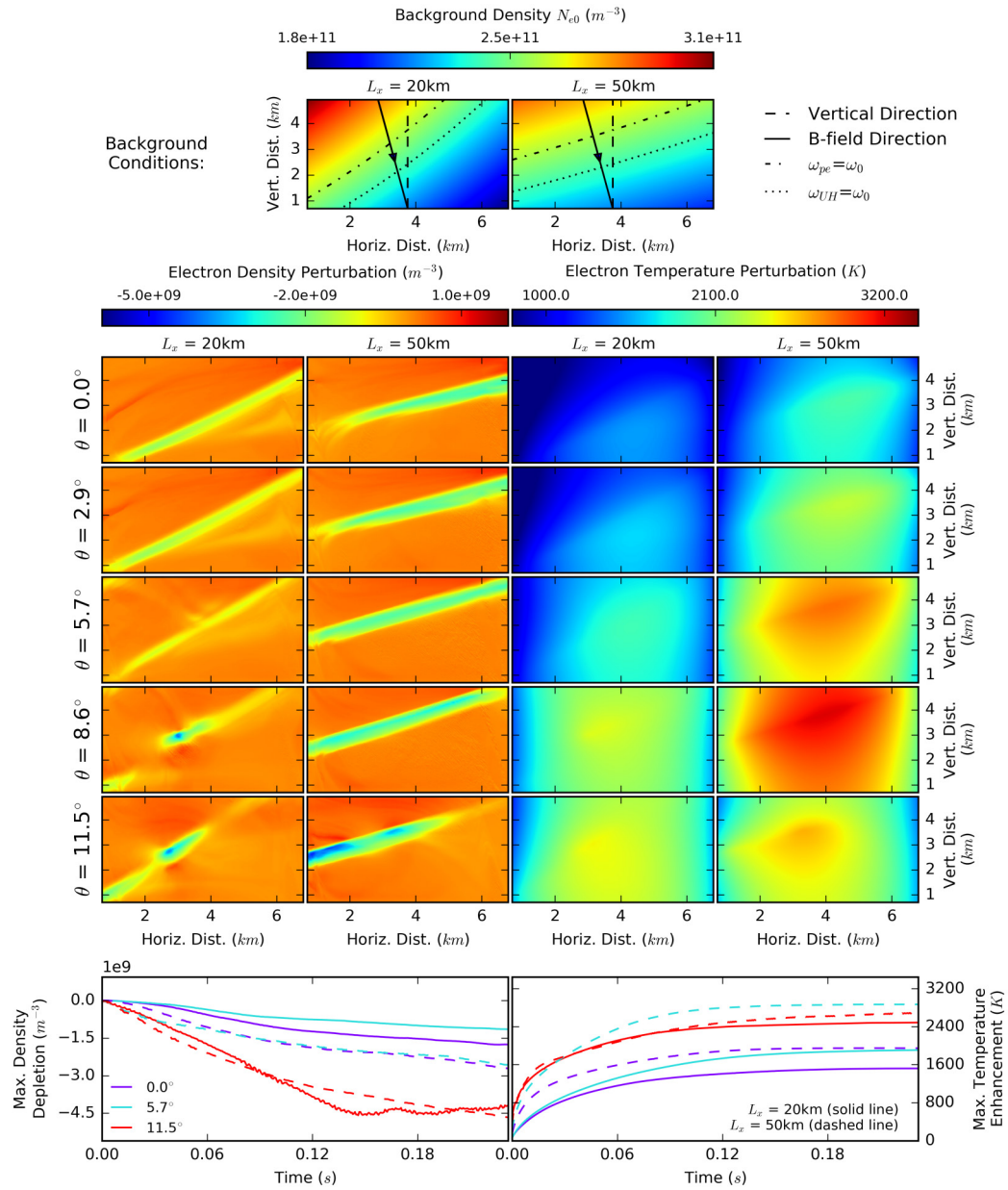


FIGURE 4.11: Variation in electron density perturbation and electron temperature perturbation with pump wave inclination angle when horizontal density slopes of the form (4.9) with $L_x = 20\text{ km}$ and $L_x = 50\text{ km}$ were included in the background density profile. Uppermost panels show the background conditions for each L_x case. Lowermost panels show the variation of minimum density perturbation and maximum temperature recorded in the simulation with time for $L_x = 20\text{ km}$ (solid line) and $L_x = 50\text{ km}$ (dashed line). The inclination angle responsible for the greatest temperature enhancement shifts from the Spitzer position towards the magnetic zenith direction with decreasing L_x , consistent with the modification of the Z-mode window simulated in Section 4.3 (shown in Figure 4.2). Computational grid parameters $\Delta_t = 1.22 \times 10^{-8}\text{ s}$ and $\Delta_x = 7.33\text{ m}$ were used in these simulations.

is in good agreement with the simulations presented here, which demonstrate that for a horizontal slope of scale size $L_x = 20\text{ km}$ the temperature enhancement increases as the pump wave inclination angle increases, with maximum enhancement found when the pump wave was directed at 11.5° .

Similar plots are shown in Figures 4.12 and 4.13 for the cases of a single density-depleted field-aligned duct and a periodic distribution of such irregularities respectively. In both scenarios, an inhomogeneities with scale parameters $L_{width} = 0.08\text{ km}$ and $L_{width} = 0.8\text{ km}$ are compared.

When the single, narrow (0.08 km) irregularity was included, the simulation behaved in a similar manner to the unperturbed case, as would be expected from Figure 4.3 which suggests that the Z-mode window would be relatively unmodified by irregularities of this scale, with only a slight ($< 1^\circ$) shift towards vertical. In this case, the maximum temperature enhancement occurred for the pump waves directed close to the Spitz angle (5.7°) and between the Spitz and vertical (2.9°) consistent with the small shift in the Z-mode window. The maximum stationary-state temperature was similar to that shown for the unperturbed 1D-slope case in Figure 4.9. For all angles, the largest density modification was found to occur away from the centre of the density duct (the position of the duct-like inhomogeneity in the simulation domain can be seen in the uppermost panels of Figure 4.12, which shows the background density profile). For the larger-scale (0.8 km) irregularity, the temperature perturbation at all angles was found to be greater than in the narrow-irregularity case at all sampled angles, due to the broadening of the window with increasing duct width (as shown in Figure 4.3). The greatest modifications to both temperature and density were found to occur for the wave directed between the Spitz angle and vertical ($\theta = 2.9^\circ$). Here, the maximum steady state temperature achieved was more than 10% greater than the maximum temperature developed in the unperturbed 1D-slope scenario shown in Figure 4.9. At all sampled angles, the site of greatest density perturbation can be seen to occur close to the centre of the duct; this had the effect of deepening the depletion with time in the region around the point at which the pump wave was reflected.

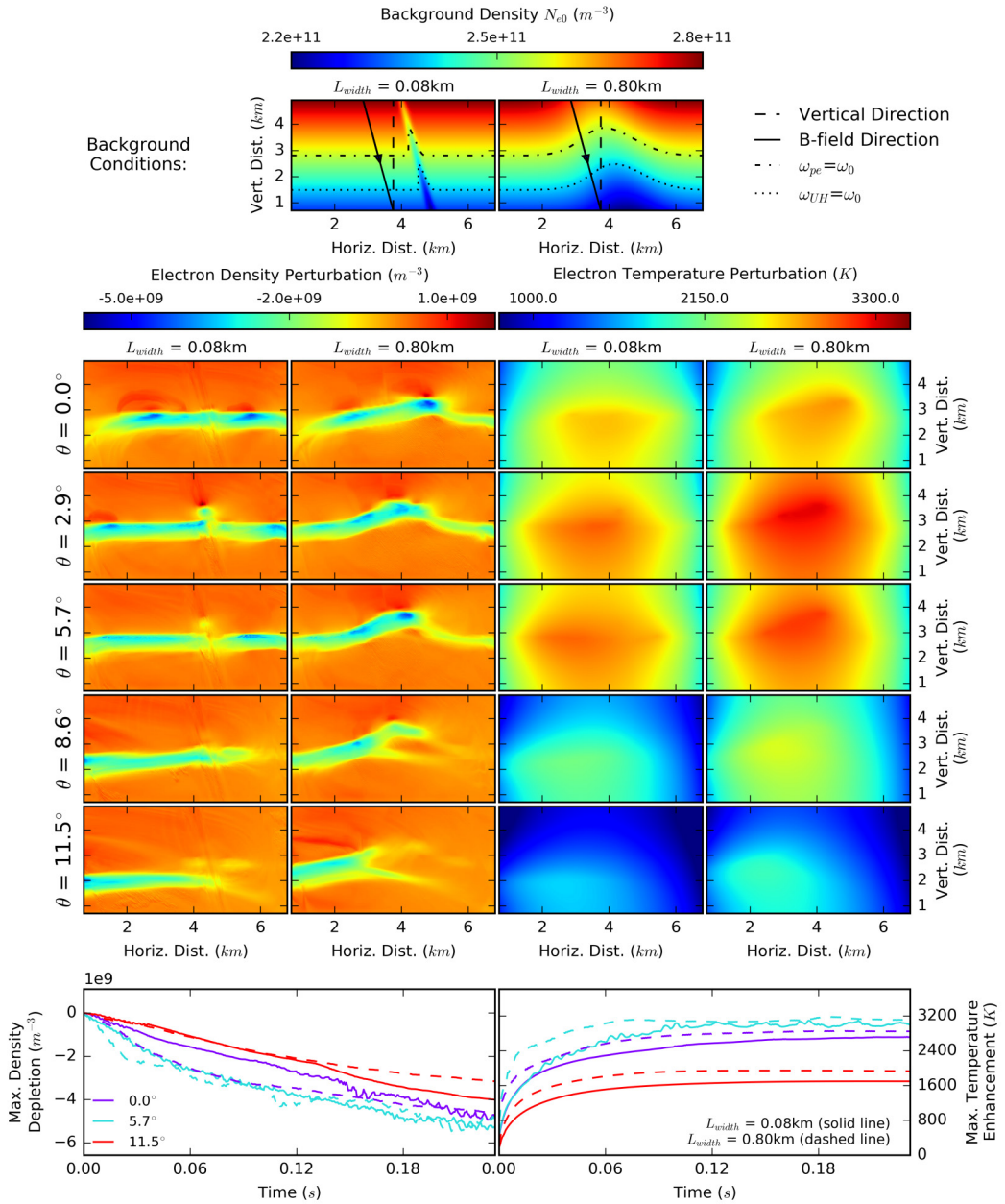


FIGURE 4.12: Variation in electron density perturbation and electron temperature perturbation with pump wave inclination angle when single density-depleted field-aligned irregularities of the form (4.10) with $L_{width} = 0.08\text{km}$ and $L_{width} = 0.8\text{ km}$ were included in the background density profile. Uppermost panels show the background conditions for each L_{width} . Lowermost panels show the variation of minimum density perturbation and maximum temperature perturbation recorded in the simulation with time, for $L_{width} = 0.08\text{ km}$ (solid line) and $L_{width} = 0.8\text{ km}$ (dashed line). Computational grid parameters $\Delta_t = 1.22 \times 10^{-8}\text{ s}$ and $\Delta_x = 7.33\text{ m}$ were used in these simulations.

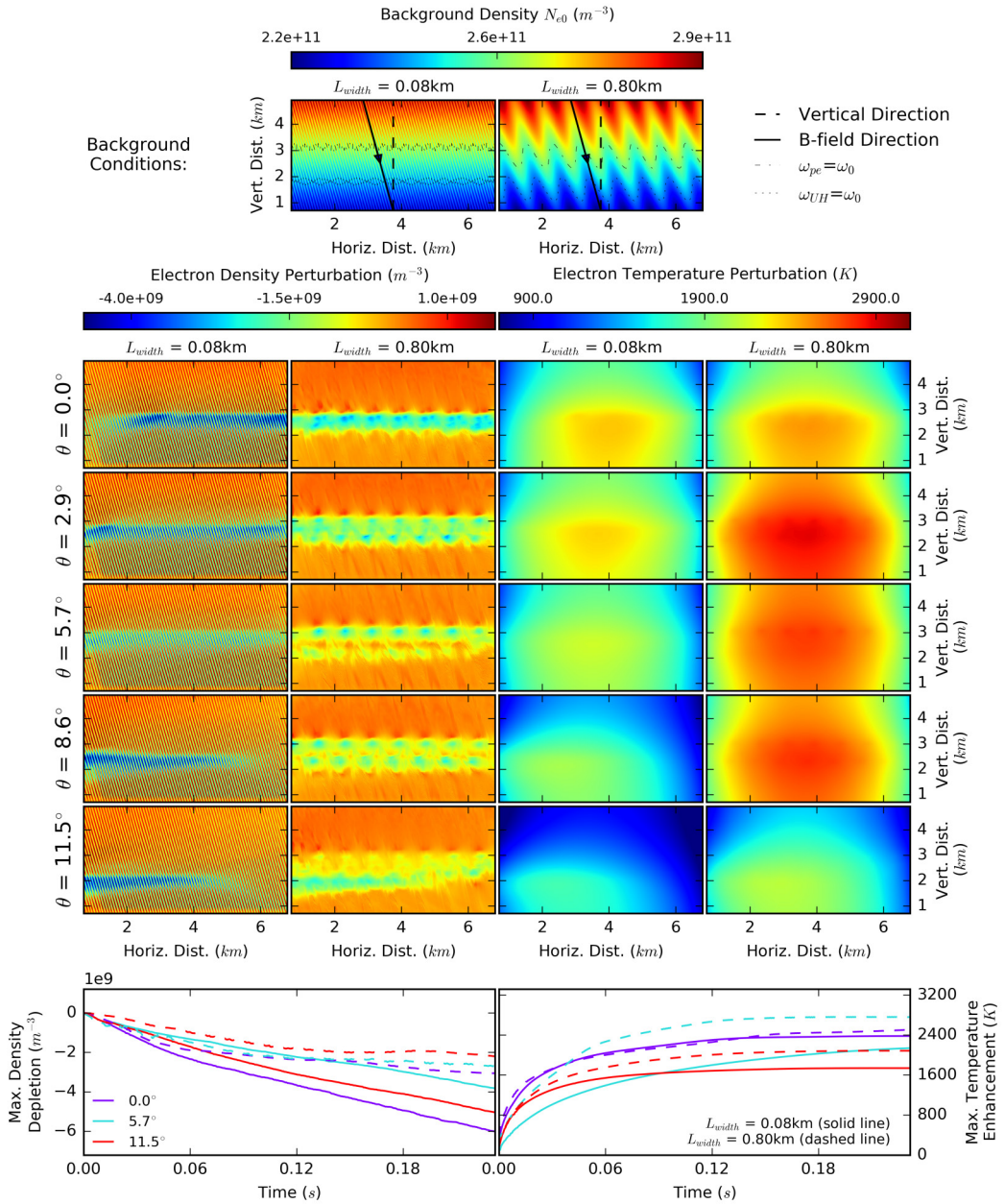


FIGURE 4.13: Variation in electron density perturbation and electron temperature perturbation with pump wave inclination angle when periodic density-depleted field-aligned irregularities of the form (4.11) with $L_{width} = 0.08\text{ km}$ and $L_{width} = 0.8\text{ km}$ were included in the background density profile. Uppermost panels show the background conditions for each L_{width} . Lowermost panels show the variation of minimum density perturbation and maximum temperature perturbation recorded in the simulation with time, for $L_{width} = 0.08\text{ km}$ (solid line) and $L_{width} = 0.8\text{ km}$ (dashed line). Computational grid parameters $\Delta_t = 1.22 \times 10^{-8}\text{ s}$ and $\Delta_x = 7.33\text{ m}$ were used in these simulations.

When multiple periodically-distributed irregularities were included, the growth of plasma perturbations was very different. As expected from Section 4.3, the smaller-scale (0.08 km) irregularities effectively attenuate the propagation of the Z-mode wave beyond the interaction region. As such, this narrow irregularity case behaves much like the unperturbed 1D density slope scenario with the effects due the Z-mode suppressed. Accordingly, the maximum temperature enhancement was found to occur for the vertically-directed pump wave, and was found to decrease as the wave inclination angle was increased towards the field-aligned direction. For the larger-width (0.8 km) irregularities, as in the single-irregularity case, the greatest modification to the plasma was found to occur for the pump wave inclined at 2.9° . The greatest perturbations can be seen to be localised at certain points within each density depletion. These “hot spots” correspond to the pump wave reflection point within each irregularity (indicated in the background profile plot in the uppermost panel of Figure 4.13). The maximum temperature in the large-irregularity case was greater than in the small-irregularity case for all pump wave angles aside from vertical (for which the steady state temperatures were approximately equal), due to the additional contribution provided by the Z-mode. By contrast, the magnitude of density depletions was greater in the case of narrow irregularities by a factor of 2 or greater at all sampled angles, corresponding to a more rapid growth of the depletions with time in this scenario.

The results presented in this Section demonstrate that the modification of the Z-mode window caused by inhomogeneities in the electron density profile (as explored in Section 4.3) can have a knock-on effect on the growth of artificially-induced thermal plasma perturbations. Changing the shape or position of Z-mode window via the inclusion of a 2D density inhomogeneity was found to lead to a corresponding variation in the dependence of electron temperature enhancement on pump wave inclination angle. This mechanism could explain why the greatest magnitudes of plasma heating have often been found to occur for non-Spitze directed waves during observations of the Magnetic Zenith Effect.

4.6 Summary and Conclusions

Ionospheric heating experiments have observed that the magnitude of artificial heating-induced plasma perturbations depend strongly on the inclination angle of the pump beam, with a greater modification to the plasma observed when the heating beam is directed close to or along the magnetic zenith direction. [Honary et al., 2011] proposed that this Magnetic Zenith Effect is due to the O-mode to Z-mode conversion process that can occur in the F-region for a narrow range of pump wave inclination angles. This conversion process has previously been investigated theoretically for the case of a 1D variation in electron density, however the case of a 2D variation had not been discussed before, and in this Chapter was investigated numerically for the first time. The full-wave FDTD code developed in Chapter 3 was used to numerically explore the effect of an O-mode polarised EM pump wave on the plasma around the ionosphere critical interaction region. In particular, the behaviour of the O- to Z-mode conversion process and Magnetic Zenith Effect was investigated for a variety of density profiles. These simulations show that the presence of ionospheric plasma density inhomogeneities can explain many of the features of the observed Magnetic Zenith Effect through modification of the angular window for O-mode to Z-mode conversion.

The fraction of the simulated pump wave field penetrating beyond the O-mode reflection height in the form of a Z-mode was measured for a range of launch angles and used to determine the angular shape of the window for which O-to-Z-mode conversion was favourable. For the case of a 1D vertical electron density gradient the simulation results (as shown in Figure 4.1) demonstrated good agreement with the predictions of [Mjølhus, 1984], with the conversion window centred on the Spitz angle (4.8). From this, one would expect that the Magnetic Zenith Effect would manifest most strongly for pump waves directed at the Spitz angle, however it has been reported that the maximum electron temperature enhancement at EISCAT can occur for inclination angles somewhere between the Spitz and field-aligned directions (for example, [Isham et al., 2005]). To explain this, [Honary et al., 2011] proposed that the shape of the Z-mode window can be modified by the presence of horizontal inhomogeneities in the electron

density, such as the large scale depleted regions or field-aligned irregularities that may be excited during the course of an ionospheric heating experiment. This problem cannot be fully treated theoretically using the techniques of geometric optics, however the numerical simulation techniques used here allowed 2D plasma profiles to be fully taken into account.

A varied hierarchy of electron density structures have been observed during heating experiments due to the formation of plasma irregularities of different scales. The FDTD code was used to investigate how the inclusion of 2D density inhomogeneities of this nature could influence the shape of the Z-mode window. Here three distinct cases were investigated: large-scale horizontal density slopes, medium-scale single density-depleted ducts and smaller-scale periodic field-aligned irregularities. The results demonstrate that the window is highly sensitive to the form of the density profile.

Adding a linear horizontal density gradient to represent a large-scale density-depleted patch was found to shift the centre of the Z-mode window away from the Spitze direction (see Z-mode window curves displayed in Figure 4.2), either towards the magnetic zenith direction or the vertical direction depending on the direction of the horizontal gradient. A steeper slope resulted in a greater shift of the window. Shifting the window all the way to the field-aligned direction was shown to require the presence of a horizontal density gradient of similar scale size to the vertical gradient.

Inclusion of a single field-aligned density-depleted irregularity to represent a duct-like structure led to a slight shifting of the window towards the vertical direction for irregularities with widths $< 0.1 \text{ km}$. Increasing the irregularity width in the range $0.1 \text{ km} - 2 \text{ km}$ was found to increasingly broaden the Z-mode window, with the angular width of the window for a duct of 1 km width almost three times that of the 1D slope case (see Z-mode window curves in Figure 4.3). For duct widths in this range, it could be seen that a narrow Z-mode beam was produced for every sampled pump wave direction, however the location with respect to the irregularity geometry at which conversion took place varied between inclination angles, as can be seen in Figure 4.4. For irregularity widths beyond 2 km , this broadening effect was found to decrease, and with increasing width

the shape of the Z-mode window tended towards the unperturbed form measured for the case of the 1D vertical density gradient.

Inclusion of multiple duct-like structures in the form of periodic field-aligned density-depleted irregularities had a strong effect on the propagation of the converted Z-mode (as shown in Figure 4.5), with transmitted waves multiply scattered by adjacent irregularities and making it difficult to measure the window shape. In general the effect of periodic irregularities with spatial scales comparable to or smaller than the pump wave wavelength had the effect of attenuating the transmitted Z-mode amplitude. As the irregularity scale size was increased, multiple scattering of the Z-mode wave between irregularities allowed significant E-field amplitude to propagate beyond the O-mode reflection height for all sampled pump wave angles.

A novel feature of the FDTD code used here is that it allowed the time-explicit evolution of thermal perturbations to the plasma density and temperature to be simulated on the timescale of the EM wave. This feature was used to investigate how the O-mode to Z-mode conversion process may lead to a modification of the plasma medium that is dependent on pump wave angle. In the F-region of the ionosphere, the Z-mode wave is reflected at a higher altitude than the O-mode wave at a point corresponding to $X = Y + 1$. If reflected, the Z-mode wave is able to propagate back towards the interaction region where it can excite a resonance that is inaccessible to fast X-mode waves and results in the efficient conversion of the EM wave to plasma waves. As the Z-mode wave approaches the resonance height, its k-vector approaches infinity and thus its group velocity decreases, leading to a sharp increase in electric field amplitude. The swelling in amplitude leads to the growth of local electron temperature, and thus an expansion of the local plasma. To investigate the impact of this process, simulations in which the Z-mode wave was allowed to reflect back towards the interaction height were compared with simulations in which the Z-mode was absorbed before reflection using an artificial PML, both for the case of a 1D linear density variation (see Figures 4.7 and 4.8). For a Spitzer-directed wave, the maximum E-field amplitude measured when the Z-mode wave was allowed to reflect was more than 4 times greater than in the reflection-suppressed case. Correspondingly, the magnitude of thermal perturbations to the plasma were

found to be greater in the reflection allowed scenario, with the electron temperature more enhanced by factor of 2 and the electron density more depleted by a factor of 4 compared to the Z-mode reflection-suppressed results.

In the reflection-allowed simulations, the angular dependence in O-to-Z-mode conversion translated to an angular dependence in plasma modification, demonstrated by the results presented in Figure 4.9. Pump waves with inclination angles more favourable for Z-mode conversion were found to achieve a greater magnitude of plasma perturbation, with the magnitude of steady-state temperature enhancement increasing as the wave inclination angle was increased from $2780K$ at vertical (0.0°) to $2940K$ at the Spitze (5.2°), before falling off as the inclination angle was increased further. By contrast, without Z-mode reflection the greatest electron temperature enhancement was seen for the vertically-directed ($2750K$) wave and the level of enhancement reduced as the inclination angle approached the Spitze ($1440K$). In addition, excitement of small-scale field-aligned density irregularities was found to occur most favourably for pump beams directed along the Spitze direction, as shown in Figure 4.10. These results support the idea that resonant excitation of large-amplitude electric fields via the reflected Z-mode can contribute to the enhanced plasma perturbations and pump wave inclination angle dependence associated with the Magnetic Zenith Effect.

The addition of a horizontal component to the linear density profile was shown to modify the Z-mode window by shifting its centre away from the Spitze direction; a density inhomogeneity of this type was also demonstrated to have a significant impact on the development of thermal plasma perturbations. Simulations were run using the density profile given by (4.9) for horizontal slope scale sizes of 50 km and 20 km (see results presented in Figure 4.11). Maximum temperature enhancement found to occur for pump wave inclination angles 8.6° and 11.5° respectively, corresponding closely to the centre of the Z-mode window for each scenario (8.3° and 12.4° respectively). Thus, by shifting the Z-mode window via a horizontal density inhomogeneity, the pump wave inclination angle resulting in the greatest heating was found to vary. This offers a potential mechanism to explain how the most substantial Magnetic Zenith Effect electron heating has been observed to occur for non-Spitze directed waves.

Simulations were run to compare the influence of duct-like irregularities of large (0.8 km) and smaller (0.08 km ; close to the pump wavelength) scale sizes on the growth of thermal plasma perturbations (see results presented in Figure 4.12). As would be expected from the simulated Z-mode window curves shown in Figure 4.3, the narrow irregularity behaves much like the unperturbed case with maximum temperature enhancement occurring at the Spitz angle. For the larger irregularity, greater stationary-state temperatures are achieved at all angles due to the broadening of the Z-mode window for irregularities of this type. Both the maximum temperature enhancement and the greatest depletion of density occurred for the wave directed between the Spitz angle and vertical. For a pump wave at this angle, the stationary temperature enhancement was 10% greater than in the unperturbed 1D-slope case shown in Figure 4.9.

For periodic irregularities of the same scale sizes ($L_{width} = 0.08\text{ km}$ and $L_{width} = 0.8\text{ km}$), the growth of plasma perturbations was very different (as shown in Figure 4.13). The narrow irregularities ($L_{width} = 0.08\text{ km}$) effectively attenuated conversion of the O-mode wave to the Z-mode, leading to the greatest plasma perturbations occurring when the pump wave was directed vertically. For the larger irregularities ($L_{width} = 0.8\text{ km}$), as in the single-irregularity case, the greatest modification to the plasma occurred for a pump wave inclination angle of 2.9° . The greatest perturbations can be seen to occur in highly-localised hot spots within the periodic density depletions. The magnitude of temperature in the large-irregularity case was greater than in the small-irregularity case for all pump wave angles aside from vertical (for which the steady state temperatures were approximately equal), due to the additional contribution from the Z-mode wave. By contrast, the magnitude of density depletions were greater in the case of narrow irregularities by a factor of 2 or more at all angles, corresponding to a more rapid growth of the depletions in this scenario.

The simulations presented in this Chapter demonstrate that the existence of 2D electron density inhomogeneities around the O-mode reflection height can have a significant impact on the development of perturbation to the plasma during a heating experiment. Large-scale linear density gradients, medium-scale duct-like density depletions and small-scale field-aligned irregularities were all found to affect the O-mode to Z-mode conversion

process and consequently modify the position of the Z-mode window. This was shown to have a knock-on effect on the growth of any thermal plasma perturbations caused via interaction of the heating wave, and offers a potential mechanism behind several features of the observed Magnetic Zenith Effect.

Chapter 5

Simulation of Density Irregularity Growth During O-Mode and X-Mode Heating

5.1 Introduction

Illumination of the F-region of the Earth's ionosphere with high-power radio-frequency radiation has been observed to excite a wide variety of often nonlinear plasma waves and instabilities, frequently resulting in significant modification of the plasma medium as described in Section 1.6. Energy from the incident wave can be deposited into the plasma both directly as a result of absorption processes related to the pump wave-field, or by so-called *anomalous* processes involving the excitement of plasma wave modes [Robinson, 1989]. In the former case, collisional interactions can lead to Ohmic dissipation of the pump wave energy. In the latter case, low-group-velocity electrostatic plasma waves are excited by the incident pump wave and subsequently dissipated into the local plasma. These excited plasma waves have a significantly shorter attenuation distance in the F-region than the electromagnetic pump wave and thus their energies are very efficiently absorbed into a small volume close to the interaction region. Anomalous heating of the ionosphere is often connected with the growth of small-scale electron density striations.

Transferral of the EM wave energy to ES plasma waves via striations has been observed to lead to a measurable decrease in the backscattered wave power, known as *anomalous absorption* of the pump wave [Graham and Fejer, 1976]. In F-region heating experiments, these anomalous wave-wave interactions are thought to be the dominant mechanism by which heater wave energy is transferred to the plasma medium.

Several plasma wave excitation processes are known to contribute to large-scale electron temperature enhancement in the case of ordinary-mode (O-mode) heating experiments. The *parametric decay instability* [Fejer, 1979], as described in Section 1.6.4, results in the decay of the EM pump wave to a high-frequency Langmuir electron plasma wave and a low-frequency ion-acoustic wave. The Langmuir wave then either undergoes further decay via the Langmuir decay instability or is collisionally absorbed into the volume local to the interaction region, heating the electron plasma. The E-field threshold for this instability close to the O-mode reflection height is of the order of 0.1 V/m [Stubbe and Kopka, 1981] and has been measured at EISCAT to be in the range of $0.25 - 0.3 \text{ V/m}$ [Bryers et al., 2013]; at decreasing altitudes, the effective threshold increases due to the effects of Landau damping (see Section 1.4.4.1). As such, this interaction occurs most favourably near to the O-mode reflection height where the pump wave frequency is closely matched with the local electron plasma frequency: here the E-field can be large due to the high-amplitude Airy-like periodic standing wave that develops due to the wave reflection and the effects of Landau damping are reduced, meaning that the instability threshold can easily be exceeded.

A second instability responsible for plasma-wave-driven heating in O-mode experiments is the *thermal resonance* or *thermal parametric instability* [Vaskov and Gurevich, 1975], as described in Section 1.6.5 above. This instability involves conversion of the EM pump wave to perpendicularly-propagating electrostatic upper-hybrid plasma waves via scattering from small-scale density irregularities aligned with the geomagnetic field close to the height where the pump wave frequency corresponds to the local UH frequency (upper-hybrid resonance height). The UH waves can become trapped and amplified within the density striations, resulting in an increase in the local electron temperature and an increase in the irregularity depletion amplitude due to thermal pressure. As the

irregularity grows, the trapping efficiency increases and explosive, nonlinear heating of the local electron plasma can result. The instability requires the presence of pre-existing density irregularities of a certain amplitude [Vaskov and Gurevich, 1975, Inhester et al., 1981], either naturally-occurring or created via another heating-induced process (for example the weak turbulence resulting from a cascade of decaying Langmuir waves); alternatively the instability can proceed with no seed irregularities as a consequence of pump-field non-uniformity, as described by [Das and Fejer, 1979]. The second, seedless mechanism requires an E-field threshold to be exceeded; [Robinson, 1989] reports that under characteristic F-region conditions this threshold is similar to that required for the PDI.

Production of the field-aligned density irregularities associated with the thermal resonance instability, and the resulting anomalous absorption of the EM pump wave, are known to be particularly sensitive to the proximity of the pump frequency to the harmonics of the electron gyrofrequency. [Stocker et al., 1993, Stubbe et al., 1994] reported a series of experiments performed at EISCAT in which the frequency of an O-mode polarised pump wave (ω_0) was systematically varied in small steps around the third, fourth and fifth harmonics of the electron gyrofrequency ($n\omega_{ce}$, $n = 3, 4, 5$). The observed anomalous absorption was found to vary significantly with the pump wave frequency, with a distinct minimum in anomalous absorption encountered as the pump frequency passed close to each of the gyroharmonic frequencies. Qualitative differences between each of the gyroharmonic frequencies were also observed: in particular, a strong asymmetry in the anomalous absorption was measured when the pump wave was varied around the third gyroharmonic, with significantly greater absorption recorded for pump frequencies above $3\omega_{ce}$ than below (see, for example, Figures 9 and 10 of [Stubbe et al., 1994]). The peak of the anomalous absorption in the $3\omega_{ce}$ case was found to occur $\sim 80\text{ kHz}$ above the absorption minimum. No consistent asymmetry in anomalous absorption was observed in either the $4\omega_{ce}$ or $5\omega_{ce}$ cases. [Honary et al., 1995] demonstrated that the variation in anomalous absorption observed for pump frequencies close to $3\omega_{ce}$ corresponded to a variation in the electron temperature enhancement around the O-mode interaction region.

The experiments described by [Stocker et al., 1993, Stubbe et al., 1994] also reported a drastic variation in the stimulated electron emission (SEE) spectrum as the pump frequency was stepped around each gyroharmonic frequency. Sensitivity of SEE features to the proximity of the pump frequency to $n\omega_{ce}$ had previously been extensively studied by, for example, [Leyser et al., 1990]. In particular, the downshifted maximum (DM) feature [Stubbe et al., 1984] was found to disappear as the pump frequency passed close to each gyroharmonic, corresponding to the frequencies at which the anomalous absorption minima were observed. This feature is commonly understood to be caused by the decay of upper-hybrid waves (such as those excited via the scattering of the EM wave by density striations) to frequency-downshifted EM waves that can then be measured on the ground, for example through the parametric decay $UH \rightarrow EM + LH$ [Leyser et al., 1990]. The disappearance of the DM features has been explained variously as cyclotron damping of the UH waves at $n\omega_{ce}$ [Leyser, 1991] or alternatively by conversion of the UH waves to non-propagating Bernstein modes for which the decay $EB \rightarrow EM + LH$ is not viable [Rao and Kaup, 1990]. Both theoretical explanations require the presence of density striations in order to excite UH waves, and are thus contradicted by the anomalous absorption minima observed by [Stocker et al., 1993]. Many of the observed anomalous absorption and SEE phenomena observed for pump frequencies close to the electron gyroharmonic frequencies have not been satisfactorily explained theoretically and would benefit from investigation via numerical simulation.

Ionospheric heating is predominantly carried out using O-mode rather than X-mode polarisation due to the differing reflection heights of O-mode and X-mode waves. In a vertically-increasing electron density gradient, a ground-launched X-mode wave reflects at the level corresponding to $X = 1 - Y$, where $X = \omega_{pe}^2/\omega_0^2$, $Y = \omega_{ce}/\omega_0$, and ω_{pe} , ω_{ce} and ω_0 are the electron plasma, electron cyclotron and pump wave frequencies respectively. This means that the X-mode wave will be reflected at a far lower altitude than the O-mode wave, which reflects around $X = 1$ (as demonstrated by the refractive index curves plotted in Figure 1.6 or the O-/X-mode propagation code validation test results shown in Figure 3.12). Practically, the consequence of this is that the X-mode wave reflects at a level of the ionosphere below that at which the plasma-wave driven

heating processes are favourable: a ground-launched X-mode wave cannot reach the UH resonance height and reflects at an altitude where Landau damping would be expected to render the PDI threshold infeasibly high. As such, one might expect that ionospheric heating using X-mode waves would be vastly inferior to heating using O-mode waves.

Several recent experiments carried out at EISCAT however have observed significant perturbation of the F-region electron plasma when X-mode polarised pump waves have been employed. In the experiments reported by [Blagoveshchenskaya et al., 2011], small-scale field-aligned density irregularities with perpendicular scales of $\sim 9 - 15\text{ m}$ were observed to be stimulated during X-mode heating. Irregularities of this nature have previously been associated with the excitation of upper-hybrid waves during O-mode experiments. [Blagoveshchenskaya et al., 2013] describe further X-mode heating experiments in which, in addition to field-aligned irregularity growth, substantial electron temperature and density modification was observed. The temperature perturbation took the form of large-scale enhancements around the X-mode reflection height, with magnitudes measured to be as high as 100% of the background temperature level. The strong temperature enhancement would seem to indicate that Ohmic dissipation of the pump wave is not the only process leading to large scale heating of the plasma. The most significant large-scale density modifications observed during this campaign took the form of enhancements $\sim 30\%$ of background in magnitude; these were observed at an altitude $\sim 35 - 50\text{ km}$ above the altitude of maximum temperature modification. Both the production of density irregularities and the large-scale modification of the electron plasma were found to occur most favourably when the heater frequency f_0 was in the range $f_0 - (f_{ce}/2) \leq f_{xF2} \leq f_0 + (f_{ce}/2)$, where f_{xF2} is the maximum X-mode frequency that can be reflected by the ionosphere (an X-mode wave with $f_0 = f_{xF2}$ will reflect at the F-region peak; frequencies higher than this will pass through the peak and beyond without reflection, so-called *underdense* heating). In a further experiment reported by [Blagoveshchenskaya et al., 2014], X-mode heating was observed to excite strong artificial optical emissions at the red (630.0 nm) and green (557.7 nm) lines, in addition to strong irregularity generation, for magnetic-zenith aligned pump waves with frequencies $f_0 \leq f_{oF2}$ (where f_{oF2} is the maximum O-mode frequency that can be reflected

by the ionosphere). These measurements were accompanied by the observation of HF-enhanced ion and plasma lines, indicative of the excitation of ion-acoustic and Langmuir waves. [Blagoveshchenskaya et al., 2015] investigated X-mode heating-induced effects for a further range of frequencies and observed that the HF-enhanced ion and plasma lines continue to be excited for pump wave frequencies in the range $f_{oF2} \leq f_0 \leq f_{xF2}$, however are not apparent for frequencies beyond f_{xF2} : this suggests that the process responsible for these features requires the reflection or associated amplitude-swelling of the pump wave to proceed (the ability of a pump wave to meet the threshold for various instabilities as it approaches the X-mode reflection height will be investigated further through numerical simulation in Chapter 6). The excitement of field-aligned irregularities was observed to occur even when the pump frequency exceeded f_{xF2} and the wave was not reflected. An angular dependence of X-mode heating-induced effects, similar to the magnetic zenith effect seen during O-mode experiments, was also reported. From these results, it is clear that X-mode polarised waves are capable of perturbing the F-region plasma medium significantly, however determining the underlying process behind these interactions requires further investigation.

In a situation where the mechanism behind a particular observed phenomenon is not apparent, it can be useful to augment experimental findings with numerical simulations that accurately replicate the underlying plasma physics. In this Chapter, the GPU-accelerated FDTD numerical simulation code described in detail in Chapter 3 was used to simulate ionospheric modification experiments using both O-mode and X-mode polarised waves to look for similarities in plasma response and attempt to determine a mechanism responsible for both the enhanced X-mode heating observed at EISCAT and the variation in anomalous absorption observed when the pump frequency is systematically stepped around a harmonic of the electron gyrofrequency. As described in Chapter 4, this code is capable of exciting small-scale field-aligned electron density irregularities associated with the excitement of upper-hybrid electrostatic plasma waves. In the case of O-mode heating, waves of this nature are understood to be connected with strong temperature enhancement of the electron plasma close to the upper-hybrid resonance height via the thermal resonance instability and anomalous absorption of the pump

wave; in this Chapter, simulation results are presented which show that upper-hybrid-like field-aligned features can be excited by both O- and X-mode polarised waves at a range of altitudes closely corresponding to the heights at which the background electron plasma frequency is close to one of the electron gyroharmonics. Production of these irregularities is potentially caused by a parametric process involving the pump wave and one or more of the electron Bernstein wave modes (see Section 1.4.4.3). Coupling of the electrostatic wave fields due to these irregularities to the electron temperature evolution is included in the simulation update algorithm to estimate the effect this wave excitation could have on plasma heating, and the results compared to theoretical values for the anomalous plasma-wave driven heating.

This Chapter is structured as follows: Section 5.2 briefly introduces the FDTD code, highlighting features that make it suitable for investigation of plasma wave excitation and irregularity growth. Section 5.3 presents the results of simulations performed to study and compare the growth of small-scale density irregularities in the case of both O-mode and X-mode polarisation. Section 5.4 describes how the simulation code was modified to provide an estimation of the electrostatic wave-fields due to the excited density irregularities; this additional E-field calculation is included in the simulation algorithm and coupled to the plasma temperature time-advancement scheme, allowing the contribution of the ES waves to electron heating to be evaluated. Section 5.5 provides a summary of the numerical simulation results presented in this Chapter.

5.2 Methodology

Numerical simulations were performed using the GPU-accelerated FDTD code described and validated in Chapter 3 and [Cannon and Honary, 2015]. The FDTD code was shown in Section 3.4.2 to correctly model the propagation of both O-mode and X-mode polarised EM pump waves; here equivalent simulations were run for each polarisation to compare the effect of each wave mode. A two-fluid plasma model containing electrons and singly-ionised O^+ ions was employed. Of particular interest were the modifications to electron plasma density and temperature induced by waves of each polarisation. Both

density and temperature were incorporated into the FDTD scheme as single scalar nodes located at the corners of each Yee cell. Each quantity was modelled as a combination of a time-independent background component and a relatively small dynamic perturbation component, such that $N_a(t) = N_{a0} + N_{a1}(t)$ and $T_a(t) = T_{a0} + T_{a1}(t)$. As described in 3.2.2.4, time-explicit updates to the perturbed component of fluid density and temperature for each species were performed using discretised versions of the governing F-region continuity and energy balance equations [Robinson, 1989], reproduced respectively by equations (5.1) and (5.2) below:

$$\frac{\partial N_{a1}}{\partial t} + \nabla \cdot (N_a \mathbf{U}_a) = 0 \quad (5.1)$$

$$\frac{3}{2}k_B \left[T_a \frac{\partial N_{a1}}{\partial t} + N_a \frac{\partial T_{a1}}{\partial t} \right] + \nabla \cdot \mathbf{Q}_a - N_a e_a \mathbf{E} \cdot \mathbf{U}_a - \Delta \varepsilon_a = 0 \quad (5.2)$$

The full form of the FDTD update equations are given by (3.14) and (3.15) in Chapter 3. Wave-based heating contributions to the plasma temperature modification were incorporated through the $N_a e_a \mathbf{E} \cdot \mathbf{U}_a$ term in (5.2). Plasma transport was handled via the diffusion term $\nabla \cdot (N_a \mathbf{U}_a)$ in (5.1), and the heat flux term $\nabla \cdot \mathbf{Q}_a$ in (5.2). The heat flux term was taken to be:

$$\nabla \cdot \mathbf{Q}_a = \nabla \cdot [\kappa_a k_B \nabla T_a] = k_B^2 \nabla \cdot \left[\left(\frac{N_a T_a}{m_a \nu_a} \right) \nabla T_a \right] \quad (5.3)$$

Particle-neutral collisional contributions to plasma modification were incorporated into the term $\Delta \varepsilon_a$, expressed here as:

$$\Delta \varepsilon_a = -\frac{N_a m_a \nu_a}{m_a + m_0} [3(T_0 - T_a) + m_0 U_a^2] \quad (5.4)$$

where m_0 and T_0 represent the average mass and temperature of background neutral species (oxygen atoms). A further term taking into account inelastic collisions $\frac{3}{2}N_e R(T_e - T_0)$ was included in the electron temperature update equation, where R is the heat loss per electron to the background species [Robinson, 1989]. As in the previous Chapter, no plasma source or loss processes such as ionisation or recombination were

included in the simulation scheme, and it was assumed that the background plasma conditions would remain broadly stable for the short duration of the simulations described below. In future investigations, it would be desirable to improve the numerical code through inclusion of these processes.

The time-discretised version of the momentum equation, as used to update the fluid velocity for each species in the FDTD time-stepping algorithm was described previously in 3.2.2.3 and is reproduced by (5.5) below:

$$\mathbf{U}_a^{q+1/2} = \mathbf{R}_a \cdot \mathbf{U}_a^{q-1/2} + \left(\frac{e_a \Delta t}{m_a} \right) \mathbf{S}_a^{-1} \cdot \mathbf{E}^q + \left(\frac{k_B \Delta t}{m_a N_a^q} \right) \mathbf{S}_a^{-1} \cdot \nabla (N_a^q T_a^q) \quad (5.5)$$

where the update matrices S and R are given in equations (3.10) and (3.11) and Δ_t is the discrete time step. In this scheme, coupling of the plasma density and temperature to the fluid velocity was achieved via the $\mathbf{S}_a^{-1} \cdot \nabla (N_a^q T_a^q)$ term. In the simulations described here, as in Chapter 4, a 2D geometry was assumed with wave propagation, geomagnetic field and plasma variation limited to the xz -plane. Under this restriction, the pressure coupling term can be expressed as:

$$\mathbf{S}_a^{-1} \cdot \nabla (N_a^q T_a^q) = \left\{ \mathbf{I} - \frac{1}{2} \Delta t \begin{pmatrix} -\nu_a & -\omega_{ca} b_z & 0 \\ \omega_{ca} b_z & -\nu_a & -\omega_{ca} b_x \\ 0 & \omega_{ca} b_x & -\nu_a \end{pmatrix} \right\}^{-1} \cdot \begin{pmatrix} N_a \frac{\partial T_{a1}}{\partial x} + T_a \frac{\partial N_{a1}}{\partial x} \\ 0 \\ N_a \frac{\partial T_{a1}}{\partial z} + T_a \frac{\partial N_{a1}}{\partial z} \end{pmatrix} \quad (5.6)$$

where \mathbf{I} is the identity matrix and the unit vector $\hat{\mathbf{b}} = (b_x, 0, b_z)$ lies along the direction of the geomagnetic field.

5.3 Excitation of Density Irregularities

Experiments performed at EISCAT, as reported by [Blagoveshchenskaya et al., 2015] and the references therein, have demonstrated that substantial electron temperature enhancement may be induced by incident X-mode-polarised pump waves with a range of frequencies. The observed temperature gains have often been of a sufficiently high magnitude to suggest that a heating mechanism beyond the simple Ohmic dissipation of

the pump wave energy is at work. The temperature modification is often accompanied by the excitement of field-aligned density irregularities and HF-enhanced plasma lines, both of which are indicative of the excitation of plasma waves. An HF-enhanced plasma line in particular is often seen as a characteristic signature of the PDI process, and hence the excitation of Langmuir plasma waves. Taken together, these observations suggest that a plasma-wave-driven heating mechanism may be contributing to the observed electron temperature enhancement. Anomalous heating of this nature has been observed to be particularly sensitive to the pump wave frequency, with anomalous absorption minima observed when the pump wave is close to an electron gyroharmonic, and a strong asymmetry in absorption observed for pump waves above and below $3\omega_{ce}$ [Stubbe et al., 1994].

To investigate both of these effects, the FDTD code was used to perform a series of simulations to compare the response of an F-region-style plasma to O-and X-mode irradiation. The primary aim of these simulations was to search for possible mechanisms by which the polarised pump wave could excite plasma waves at an altitude below the X-mode reflection height, and hence help to explain some of the observed but as-yet unexplained X-mode heating phenomena. The simulations were also used to investigate the observed asymmetry in anomalous plasma-wave-driven processes observed when the pump wave frequency was close to the third gyroharmonic. Each simulation was initialised with a 2-dimensional computational domain of dimensions 256×1920 Yee cells, with all wave propagation confined to the xz -plane. A background magnetic field of magnitude $4.5 \times 10^{-5} T$ was directed at an angle of 0.1 rad to the vertical z -axis in the xz -plane, to represent the geomagnetic field. This set the value of the electron and ion cyclotron frequencies in the domain to be $\omega_{ce} = 7.9 \times 10^6 \text{ rad/s}$ and $\omega_{ci} = 2.7 \times 10^2 \text{ rad/s}$ respectively. Simulations were repeated for pump wave frequencies varying in $0.1\omega_{ce}$ steps in the ranges $\omega_0 = (2 - 3)\omega_{ce}$, $\omega_0 = (3 - 4)\omega_{ce}$, and $\omega_0 = (4 - 5)\omega_{ce}$. Spatial and temporal step sizes were chosen such that the period and wavelength of each pump wave could be accurately resolved. For each range of ω_0 , the spatial step size was kept constant to allow for easy comparison of features. The resulting Courant numbers $S_c = c\Delta_t/\Delta_x$ were kept sufficiently small such that numerical stability was maintained. The discrete

$\omega_0 = (2 - 3)\omega_{ce}$				$\omega_0 = (3 - 4)\omega_{ce}$			
ω_0	Δ_x (m)	Δ_t (s)	S_c	ω_0	Δ_x (m)	Δ_t (s)	S_c
$2.0\omega_{ce}$	11.91	1.986×10^{-8}	0.500	$3.0\omega_{ce}$	11.34	1.892×10^{-8}	0.500
$2.1\omega_{ce}$	11.91	1.892×10^{-8}	0.476	$3.1\omega_{ce}$	11.34	1.831×10^{-8}	0.484
$2.2\omega_{ce}$	11.91	2.006×10^{-8}	0.505	$3.2\omega_{ce}$	11.34	1.910×10^{-8}	0.505
$2.3\omega_{ce}$	11.91	1.919×10^{-8}	0.483	$3.3\omega_{ce}$	11.34	1.852×10^{-8}	0.490
$2.4\omega_{ce}$	11.91	2.069×10^{-8}	0.521	$3.4\omega_{ce}$	11.34	1.947×10^{-8}	0.515
$2.5\omega_{ce}$	11.91	1.986×10^{-8}	0.500	$3.5\omega_{ce}$	11.34	1.892×10^{-8}	0.500
$2.6\omega_{ce}$	11.91	1.910×10^{-8}	0.481	$3.6\omega_{ce}$	11.34	1.839×10^{-8}	0.486
$2.7\omega_{ce}$	11.91	2.102×10^{-8}	0.529	$3.7\omega_{ce}$	11.34	1.952×10^{-8}	0.516
$2.8\omega_{ce}$	11.91	2.027×10^{-8}	0.510	$3.8\omega_{ce}$	11.34	1.901×10^{-8}	0.502
$2.9\omega_{ce}$	11.91	1.957×10^{-8}	0.493	$3.9\omega_{ce}$	11.34	1.852×10^{-8}	0.490
$3.0\omega_{ce}$	11.91	1.892×10^{-8}	0.476	$4.0\omega_{ce}$	11.34	1.806×10^{-8}	0.477

$\omega_0 = (4 - 5)\omega_{ce}$			
ω_0	Δ_x (m)	Δ_t (s)	S_c
$4.0\omega_{ce}$	8.821	1.419×10^{-8}	0.482
$4.1\omega_{ce}$	8.821	1.491×10^{-8}	0.507
$4.2\omega_{ce}$	8.821	1.455×10^{-8}	0.495
$4.3\omega_{ce}$	8.821	1.421×10^{-8}	0.483
$4.4\omega_{ce}$	8.821	1.505×10^{-8}	0.511
$4.5\omega_{ce}$	8.821	1.471×10^{-8}	0.500
$4.6\omega_{ce}$	8.821	1.439×10^{-8}	0.489
$4.7\omega_{ce}$	8.821	1.409×10^{-8}	0.479
$4.8\omega_{ce}$	8.821	1.505×10^{-8}	0.511
$4.9\omega_{ce}$	8.821	1.474×10^{-8}	0.501
$5.0\omega_{ce}$	8.821	1.444×10^{-8}	0.491

TABLE 5.1: List of computational grid parameters used for each simulated pump wave frequency ω_0 .

step sizes and Courant parameter used for each pump frequency are listed in Table 5.1. Equal spatial step sizes were used for the horizontal and vertical directions, as in previous Chapters ($\Delta_x = \Delta_z$). Equivalent simulations were performed for both O-mode and X-mode wave polarisations.

The effective collision frequency for each species was calculated independently at each grid cell using (5.7), where ν_0 was set to be 500 s^{-1} for electrons and 6 s^{-1} for ions.

$$\nu_a(N_a, T_a) = \nu_{a0} \left(\frac{N_a}{N_{a0}} \right) \left(\frac{T_a}{T_{a0}} \right)^{-3/2} \quad (5.7)$$

A linear background temperature gradient was set for both plasma species, with $T_{e0}/T_{i0} = 2$, representative of daytime conditions in the F-region at Tromsø. The electron temperature profiles used in each simulation are shown by the blue lines in Figure 5.1. Typical conditions were obtained using IRI-2012 [Bilitza et al., 2014]. Termination of the EM fields was accomplished using a 32-cell perfectly-matched layer on each side, designed to absorb any outgoing waves with minimal numerical reflection. Plasma perturbations were terminated by setting their spatial gradients to zero at the upper / lower boundaries and setting their magnitudes to zero at the left / right boundaries (to approximate plasma transport in the vertical direction, almost along the geomagnetic field).

Previously, the FDTD code has demonstrated the ability to simulate the growth of small-scale field aligned density striations associated with the excitation of upper-hybrid waves. In the simulations presented in Chapter 4 (see in particular: Figure 4.10), the irregularities were thought to form via the interaction between the pump wave and numerical noise present in the simulated density; the low-amplitude noise variations acted as seed irregularities which allowed the thermal resonance instability to proceed. Those simulations focused only on the small range of altitude close to the O-mode reflection height, beyond the reach of a ground-launched X-mode wave.

Here, a much greater variation in plasma density was considered. In a vertically-varying plasma, the spectrum of plasma waves that each layer can support changes drastically with altitude; the inclusion of a background plasma density profile that corresponded to a wide range of plasma frequencies allowed for the possibility of the simulated pump wave coupling to many different regimes of plasma wave. As such, background profiles were chosen to accommodate as great a range of background plasma frequencies as possible in the computational domain, while maintaining a realistic profile shape. The need to keep simulation runtimes acceptably low restricted the maximum domain dimensions; because of this, the profiles were made artificially steep, however not to such a degree that this would affect the qualitative results. Figure 5.1 shows how the background plasma frequency profile used in the simulations described below varies with vertical distance from the lower edge of the computational domain. The points where the electron plasma frequency matched a harmonic of the electron cyclotron frequency are indicated by 'x'

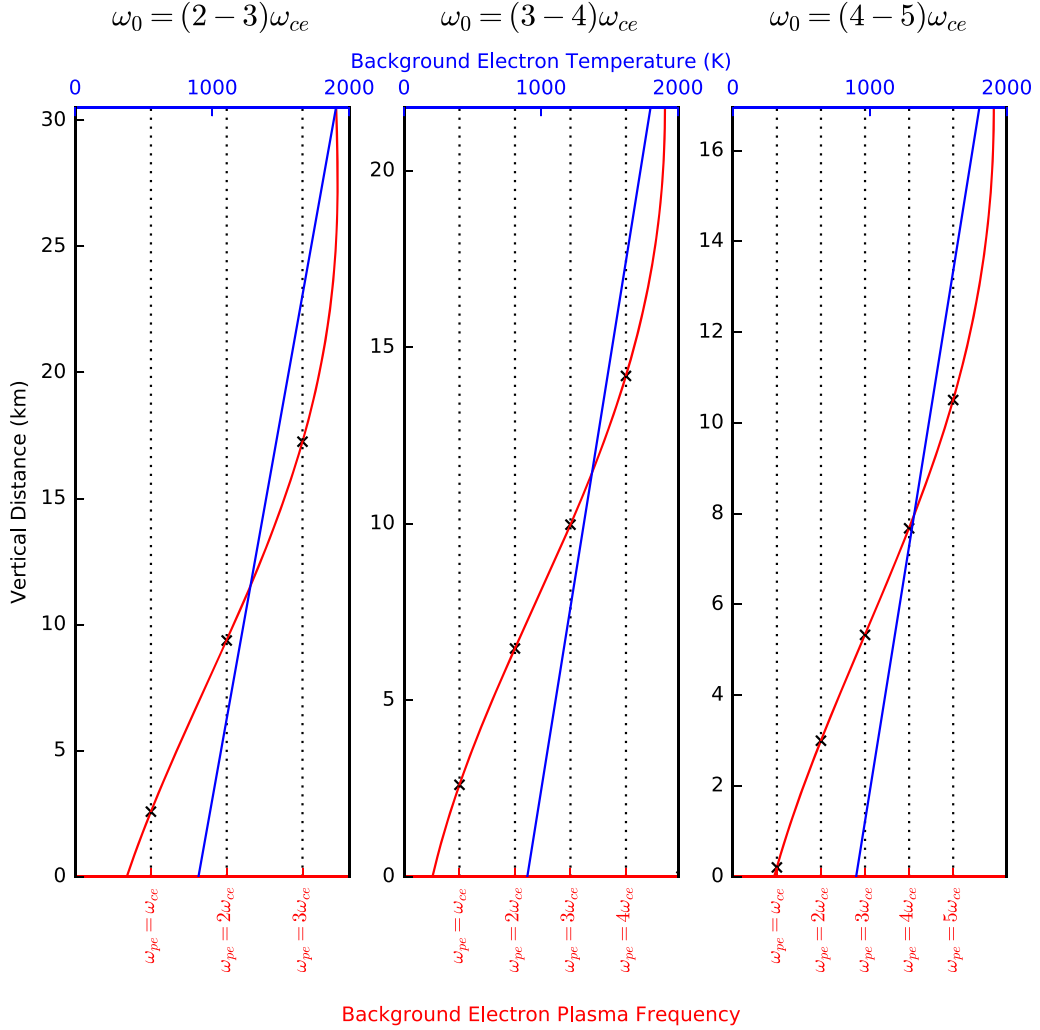


FIGURE 5.1: Variation of background electron plasma frequency (red) and background electron temperature (blue) with vertical distance from lower edge of the computation domain. From left to right these represent the profiles used in the case of simulated pump wave frequency in the ranges $\omega_0 = (2 - 3)\omega_{ce}$, $\omega_0 = (3 - 4)\omega_{ce}$, and $\omega_0 = (4 - 5)\omega_{ce}$ respectively. The points where the electron plasma frequency matches one of the electron gyroharmonics are indicated by 'x' symbols.

symbols. The background density profile was varied depending on the frequency of the simulated pump wave; from left to right, Figure 5.1 shows the profile utilised for the cases of pump frequency in the ranges $\omega_0 = (2 - 3)\omega_{ce}$, $\omega_0 = (3 - 4)\omega_{ce}$, and $\omega_0 = (4 - 5)\omega_{ce}$ respectively.

The evolution of the simulated perturbation to the plasma density was examined in search of evidence of plasma wave excitation. An example of the development of the electron density perturbation with simulation time is shown in Figure 5.2 for the case

of an O-mode wave with $\omega_0 = 4.8\omega_{ce}$. The upper panel of this plot shows the variation in the background electron plasma frequency (solid line) and upper-hybrid frequency (dashed line) with vertical distance from the lower edge of the computational domain (increasing from left to right). The pump wave frequency and gyroharmonic frequencies are also indicated. The panels below this show a snapshot of the simulated electron density perturbation in the domain for increasing values of simulation time from top to bottom. Indicated are the O-mode and X-mode reflection levels, and the positions where the background electron plasma frequency matches with an integer multiple of the electron cyclotron frequency (referred to from here onwards as the “gyroharmonic heights”).

Several density features are seen to develop with time: most prominent is the large density-depleted region which forms at the O-mode reflection height. This feature has been encountered previously in the simulations performed as part of Chapter 4 and can be attributed to thermal pressure from the enhanced electron temperature close to the reflection height acting to reduce the electron density. The high-amplitude standing wave below the reflection height results in a large spatial variation in the E-field amplitude; this may cause expulsion of electrons from the region via the ponderomotive force and contribute further to the density depletion. The spatial asymmetry of this feature arises from the Gaussian profile of the incident pump wave.

Below this a pattern of density depletions can be seen to grow around the height where the background plasma density matches the upper-hybrid frequency, corresponding to the excitement of upper-hybrid waves. As expected from irregularities in this region, these perturbations are elongated along the geomagnetic field direction. The irregularities in the UH region begin to be visible after $\sim 0.15\text{ s}$, consistent with the observations of similar features in the previous Chapter.

In the plasma below this, a range of additional features emerge. At early times, a series of pale bands are visible. Below the O-mode reflection height, there is a general trend towards an increase in electron plasma density with time throughout the heated volume of

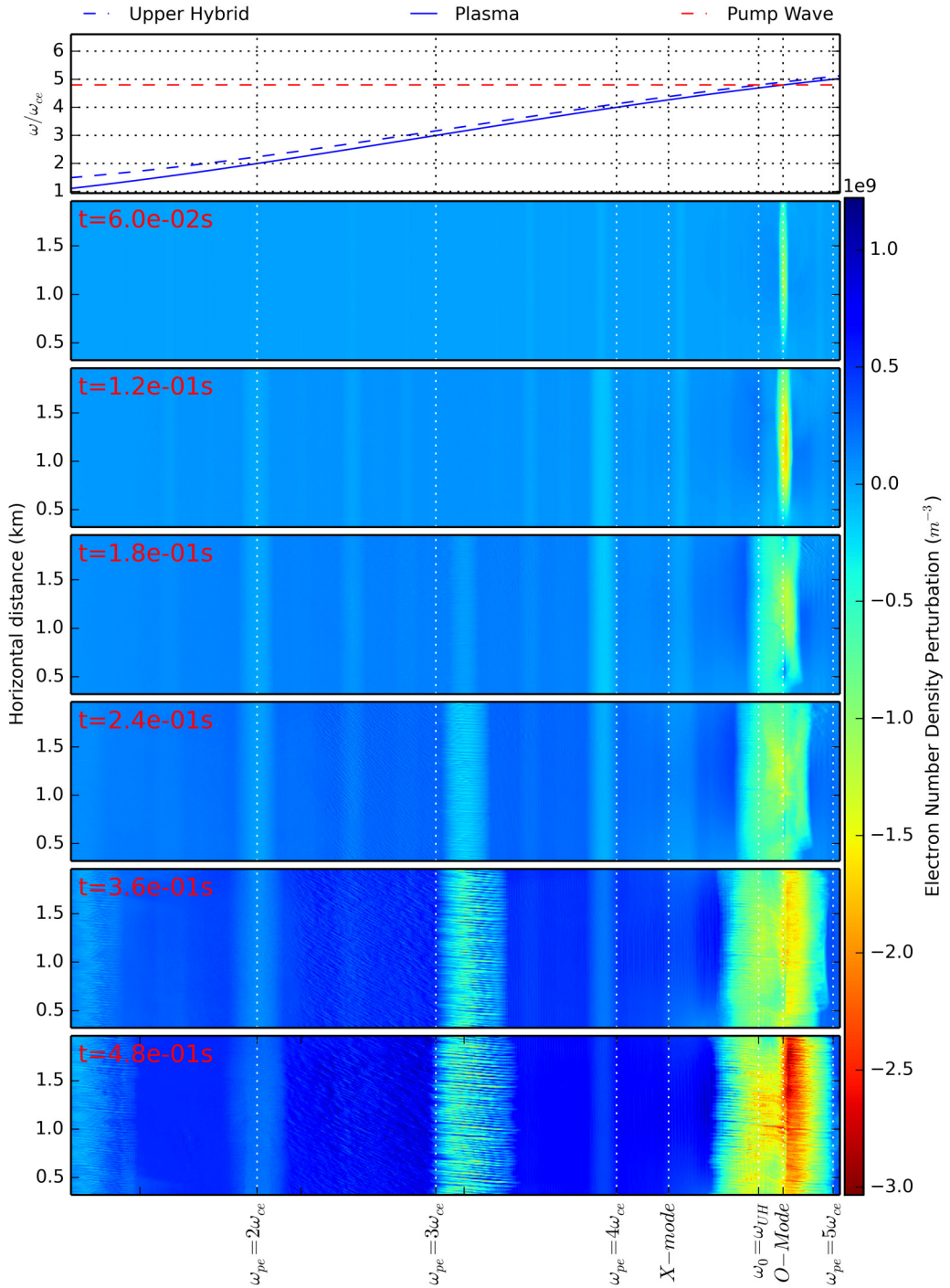


FIGURE 5.2: Evolution of density perturbation with time for the case of an O-mode pump wave with frequency $\omega_0 = 4.8\omega_{ce}$. Top panel shows spatial variation of ω_{pe} and ω_{UH} with altitude in the simulation domain. Lower panels show density perturbation snap-shots at various simulation times (increasing downwards). Large-amplitude density depletion can be seen at the O-mode reflection height. Below this, several populations of small-scale density irregularities can be seen to emerge and grow with time, particularly when ω_{pe} and ω_{UH} approach an electron gyroharmonic. Computational grid parameters $\Delta_t = 1.51 \times 10^{-8} \text{ s}$, $\Delta_x = 8.82 \text{ m}$ were used in this simulation. The particularly clear irregularities which form just above $\omega_{pe} = 3\omega_{ce}$ have horizontal spatial scales in the range $\sim 20 - 40 \text{ m}$ ($\sim 3 - 5\Delta_x$).

the domain, however these bands correspond to layers where the plasma is relatively depleted instead. Depleted regions close to the gyroharmonic heights where the background electron plasma frequency matches a harmonic of the electron cyclotron frequency can be seen to grow with time, increasing in depletion relative to the surrounding plasma perturbations as the simulation progresses. At later times several distinct populations of features are apparent close to these regions. Most striking is the strong growth of density-depleted irregularities that forms just above the 3rd gyroharmonic height. These features are aligned with the geomagnetic field direction, and are similar in appearance and formation-timescale to the irregularities that form close to the upper-hybrid layer, suggesting that a similar production process may be responsible. Like the upper-hybrid features, these 3rd-gyroharmonic irregularities increase in both depth of depletion and elongation along the geomagnetic field direction with simulation time. After 0.5 s, the amplitude of these features is $\sim 0.7\%$ of the background level. Close to the 2nd and 4th gyroharmonic heights, further distinct bands of strong depletion with amplitudes $\sim 0.5\%$ and $\sim 0.1\%$ of background density respectively can be seen to form. The depletion close to $\omega_{pe} = 2\omega_{ce}$ is made up of a population of faint field-aligned irregularities (these are difficult to resolve in the Figure in question due to their relatively small amplitudes; a clearer picture of these can be seen in Figure 5.6 below for the X-mode case, in which the plot colour-map has been logarithmically normalised). No irregularities are apparent in the depleted region close to $\omega_{pe} = 4\omega_{ce}$, however this may be due to the simulation spatial resolution being insufficiently fine to resolve them. A striated fine-structuring also appears to develop in the large-scale depletion at the O-mode reflection height at late times: this may be due to the proximity of this feature to the upper-hybrid resonance region below or at the 5th gyroharmonic layer above (which may be accessed via the Z-mode).

A further population of faint small-scale density irregularities are visible in the region between the 2nd and 3rd gyroharmonic heights. The irregularities in this region form on the same timescale as the strongly-depleted features above $\omega_{pe} = 3\omega_{ce}$, but are much smaller in amplitude ($\sim 0.25\%$ of N_{e0} after 0.5 s) and do not appear to be field aligned; instead these features appear to elongate in a direction approximately $\sim 0.45 \text{ rad}$ to

the vertical. Features of this nature appear confined to the altitudes corresponding to $\omega_{pe} = (2 - 3)\omega_{ce}$ only, and are not found anywhere else in the perturbed density profile.

When the simulation was repeated using X-mode polarisation, an equivalent, diverse set of electron density irregularities was found to develop. Figure 5.3 shows the evolution of electron density perturbations with time for the case of the X-mode pump wave. All other simulation parameters, including the pump wave frequency of $\omega_0 = 4.8\omega_{ce}$, were unchanged from the O-mode case shown in Figure 5.2. A large-scale depletion can be seen to grow at the X-mode wave reflection height (indicated by the “X-mode” label in the Figure), similar to that seen to develop at a higher altitude in the O-mode case. The magnitude of this depletion was found to be greater than the equivalent depletion caused via O-mode reflection by a factor of $\sim 20\%$ after 0.5 s of simulated time.

The density irregularities found to develop close to the gyroharmonic heights in the O-mode case were also found to occur in the X-mode case, including the population of small-scale density filaments in the range $\omega_{pe} = (2 - 3)\omega_{ce}$. The respective amplitudes of the density irregularities relative to the background were similar to those found in the O-mode case, with a particularly strong population of field-aligned striations with amplitude $\sim 0.7\%$ of the background level after 0.5 s found to grow just above $\omega_{pe} = 3\omega_{ce}$. Prior to the recent experimental findings at EISCAT, it was expected that an X-mode wave would be unable to generate field-aligned irregularities as it is unable to reach the upper-hybrid resonance height from the ground. The simulation results presented here indicate that populations of field-aligned density irregularities can form not only at the UHR height, but also at heights associated with the 2nd, 3rd and 4th electron gyroharmonics, all of which are accessible to a ground-launched X-mode wave of sufficiently high frequency.

Varying the pump wave frequency was found to lead to differences in the excited density features. Figures 5.4, 5.5 and 5.6 show examples of the electron density perturbation developed in the simulation for various examples of X-mode pump wave frequency in the ranges $(2 - 3)\omega_{ce}$, $(3 - 4)\omega_{ce}$, and $(4 - 5)\omega_{ce}$ respectively. For each frequency, the upper panel displays a spatial snapshot of the simulated density perturbation developed

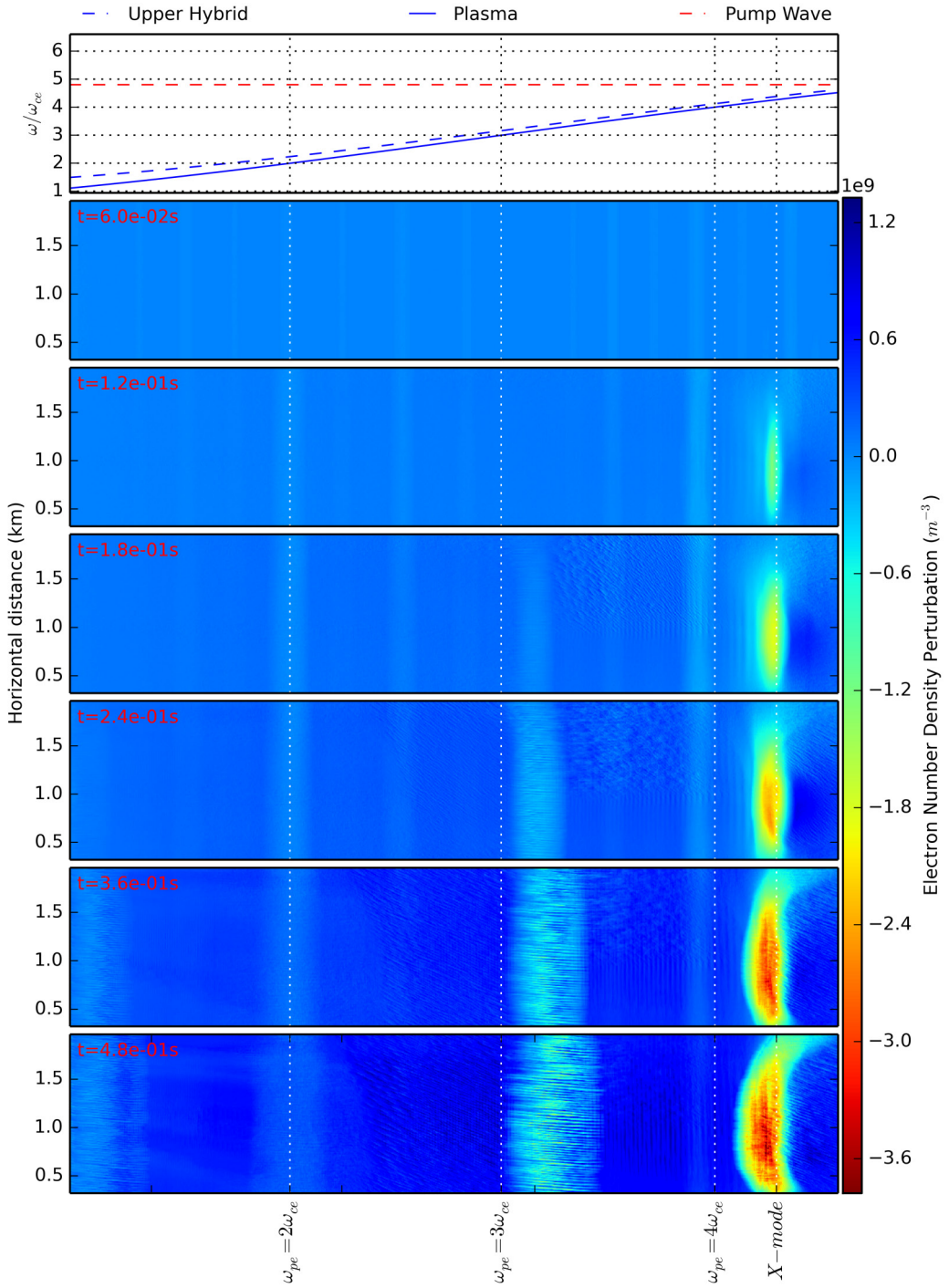


FIGURE 5.3: Evolution of density perturbation with time for the case of an X-mode pump wave with frequency $\omega_0 = 4.8\omega_{ce}$. Top panel shows spatial variation of ω_{pe} and ω_{UH} with altitude in the simulation domain. Lower panels show density perturbation snap-shots at various simulation times (increasing downwards). Large-amplitude density depletion can be seen at the X-mode reflection height. As in the O-mode case depicted in Figure 5.2, several populations of small-scale density irregularities can be seen to emerge and grow with time, located close to the layers where ω_{pe} and ω_{UH} approach an electron gyroharmonic. Computational grid parameters $\Delta_t = 1.51 \times 10^{-8} \text{ s}$, $\Delta_x = 8.82 \text{ m}$ were used in this simulation.

after 0.75 s (Figure 5.4), 0.72 s (Figure 5.5) and 0.56 s (Figure 5.6), with the background plasma frequency increasing from left to right. The colour-map in these plots has been logarithmically-normalised to better reveal small-amplitude density variations. The lower panel shows line plots of the vertical electron density perturbation profile averaged in the horizontal direction, and plotted for a range of simulation times. In each case the horizontally-averaged perturbation profile from the corresponding O-mode simulation is indicated by the dotted line (the O-mode profile was measured after 0.75 s in Figure 5.4, 0.72 s in Figure 5.5 and 0.56 s in Figure 5.6).

The main source of variation in density structure evolution between simulation runs using different pump wave frequencies was caused by the variation in reflection height: pump waves which were reflected at a higher altitude were able to access more of the plasma and potentially excite additional populations of plasma waves. For the examples of pump waves between $(2 - 3)\omega_{ce}$ shown in Figure 5.4, the altitude at which the large-amplitude density depletion associated with reflection occurs can be seen to increase with pump wave frequency. Again, the spatial asymmetry in this feature can be attributed to the Gaussian shape of the incident pump wave. For lower pump frequencies, a population of density-depleted irregularities - elongated along the background magnetic field and with a perpendicular scale size $\sim 30\text{ m}$ - developed below the point where $\omega_{pe} = \sqrt{2}\omega_{ce}$. These were found to decrease in relative amplitude as the pump frequency was increased, and are barely visible for $\omega_0 = 2.8\omega_{ce}$ and above. For sufficiently high pump frequencies, a further band of field-aligned irregularities were formed at the 2nd gyroharmonic height. These can also be seen in the $\omega_0 = 2.0\omega_{ce}$ plot despite this pump wave reflecting far below $\omega_{pe} = 2\omega_{ce}$: this may be due to a small fraction of the pump wave leaking beyond the X-mode reflection height as the O-mode and exciting irregularities at higher altitudes. Low-amplitude irregularities below $\omega_{pe} = \omega_{ce}$ were also formed during the higher-frequency $\omega_0 = 2.8\omega_{ce}$ example, as were small-scale, non-field-aligned density variations located between $\omega_{pe} = \sqrt{2}\omega_{ce}$ and $\omega_{pe} = 2\omega_{ce}$. There were visually similar to those seen between the 2nd and 3rd gyroharmonic heights in Figures 5.2 and 5.3 above, and Figure 5.6 below.

For the examples using pump waves of frequencies in the range $(3 - 4)\omega_{ce}$ shown in

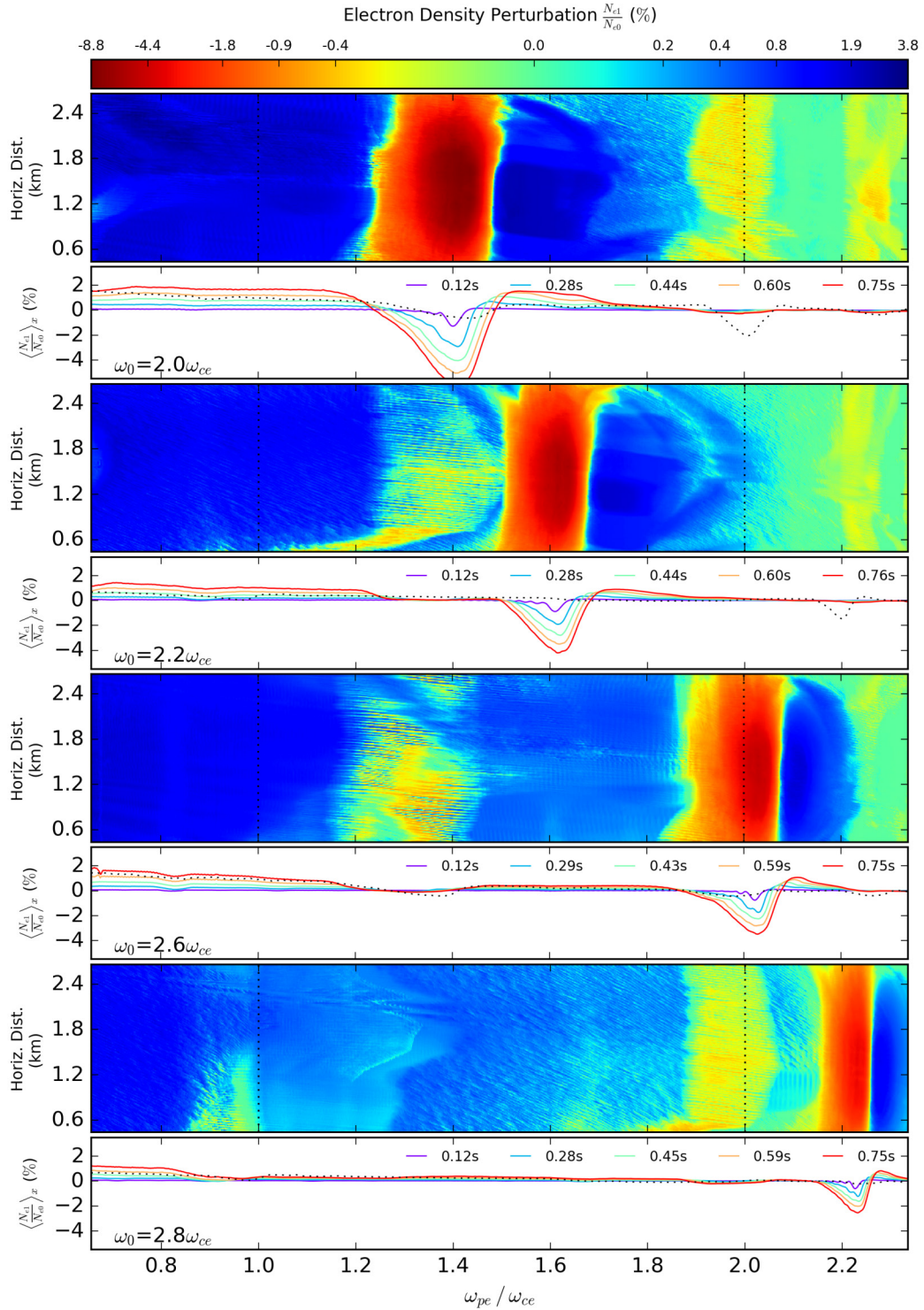


FIGURE 5.4: Examples of the density perturbations developed in the simulation using pump wave frequencies in the range $(2 - 3)\omega_{ce}$. For each frequency, the upper panel displays the spatial snapshot of the electron density perturbation developed after 0.75s . Note that the colour-map has been logarithmically-normalised. The gyroharmonic heights are indicated by dotted lines. The lower panel for each frequency shows horizontally-averaged vertical profiles of the density perturbation for a range of heights (solid lines). The horizontally-averaged profile from the corresponding O-mode simulation is indicated by the dotted line (recorded after 0.75s simulated time). Computational grid parameters used in these simulations can be found in Table 5.1.

Figure 5.5, field-aligned irregularities located at $\omega_{pe} = 2\omega_{ce}$ were found to develop in all cases. A slight increase in the amplitude of these irregularities with pump frequency was observed, with a depletion of $\sim 0.5\% N_{e0}$ relative to the background and surrounding density perturbation for $\omega_0 = 3.0\omega_{ce}$ increasing to $\sim 0.7\% N_{e0}$ for $\omega_0 = 3.8\omega_{ce}$. The population of irregularities at $\omega_{pe} = \sqrt{2}\omega_{ce}$ - as seen in the lower-frequency simulations in the $\omega_0 = (2 - 3)\omega_{ce}$ range - was no longer apparent, with only a faint band of depletion visible in this region. Low-amplitude irregularities below $\omega_{pe} = \omega_{ce}$ were visible for all pump wave frequencies. For pump waves with sufficiently-high reflection heights, a strong band of irregularities could be seen to grow around the region corresponding to $\omega_{pe} = 3\omega_{ce}$. These could also be seen to manifest weakly in the lower-frequency examples due to O-mode leakage.

In the examples of simulations using pump waves with frequencies in the range $(4 - 5)\omega_{ce}$ shown in Figure 5.6, the density irregularities around the 2nd gyroharmonic height are only weakly apparent as a low-amplitude density depletion. Some fine structure is visible in this region which suggests the existence of field-aligned striations of very small perpendicular scale ($\sim 2 - 3\Delta_x$) compared to the higher-amplitude and more easily identifiable structures just above $\omega_{pe} = 3\omega_{ce}$ ($\sim 3 - 5\Delta_x$). The field-aligned irregularity population around the 3rd gyroharmonic height was found to manifest very strongly for all pump wave frequencies in this range. The amplitude of density depletion of these irregularities was found to be $\sim 50\%$ greater than those found at the corresponding location in the simulations with pump waves in the range $\omega_0 = (3 - 4)\omega_{ce}$ (this contrast may be due to differing background density gradients between the two simulation regimes). At sufficiently high frequency, a low-amplitude band of depletion was visible close to $\omega_{pe} = 4\omega_{ce}$, however no evidence of field-aligned structures was visible in this region. A population of small-scale non-field-aligned density filaments can be seen to develop between $\omega_{pe} = 2\omega_{ce}$ and $\omega_{pe} = 3\omega_{ce}$.

The locations and relative amplitudes of simulated electron density structures appeared to vary only very weakly with pump wave frequency. For all pump frequencies, the characteristics of the density perturbations could be seen to be more closely associated with the background plasma properties; populations of density irregularities were found

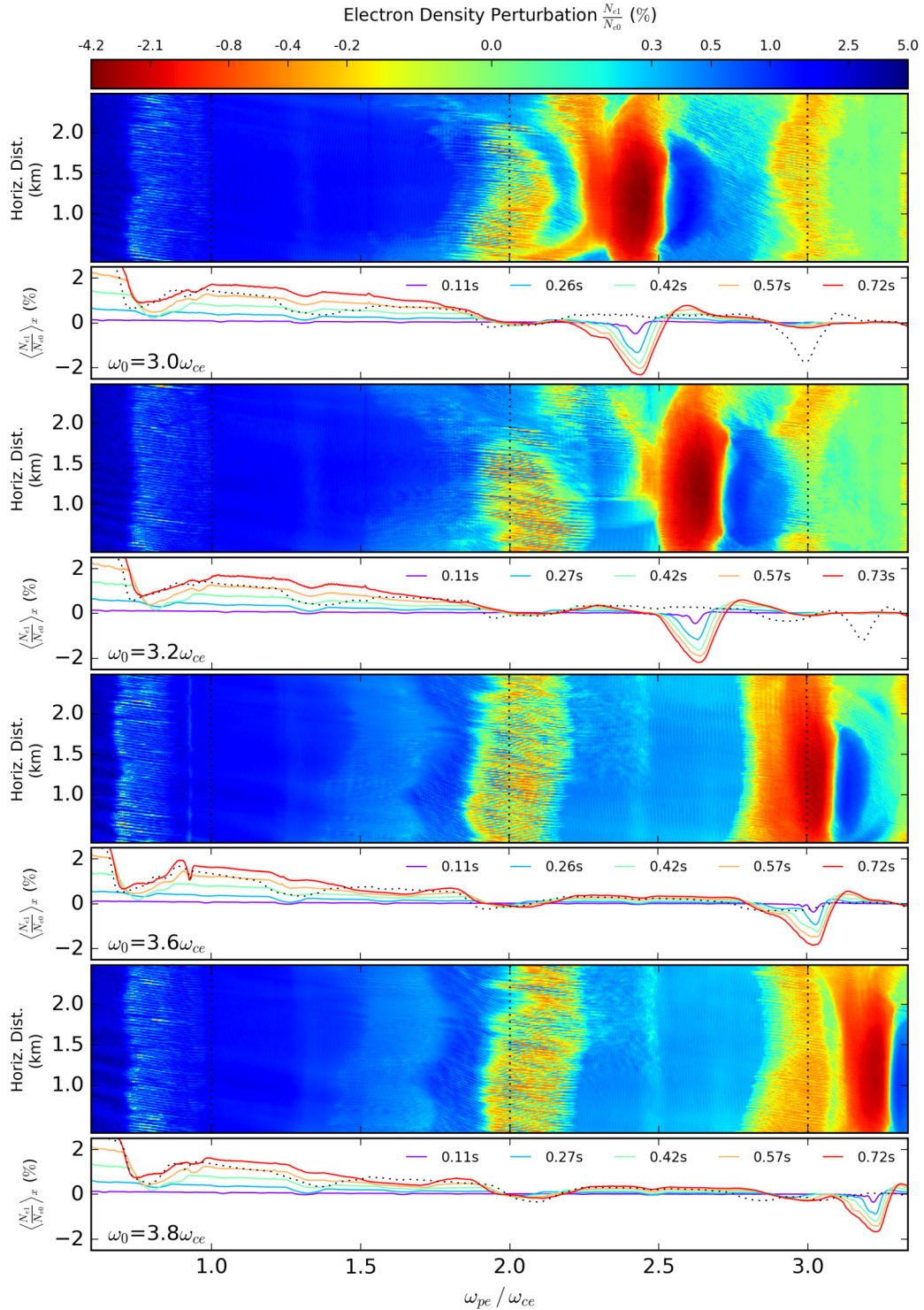


FIGURE 5.5: Examples of the density perturbations developed in the simulation using pump wave frequencies in the range $(3 - 4)\omega_{ce}$. For each frequency, the upper panel displays the spatial snapshot of the electron density perturbation developed after 0.72 s . Note that the colour-map has been logarithmically-normalised. The gyroharmonic heights are indicated by dotted lines. The lower panel for each frequency shows horizontally-averaged vertical profiles of the density perturbation for a range of heights (solid lines). The horizontally-averaged profile from the corresponding O-mode simulation is indicated by the dotted line (recorded after 0.72 s simulated time). Computational grid parameters used in these simulations can be found in Table 5.1.

to be organised in bands located close to the gyroharmonic heights, with a variation in the pump wave frequency determining only which bands could be accessed and excited. It was found that for all cases where the X-mode pump wave frequency was in the range $(n-0.2)\omega_{ce} \lesssim \omega_0 \lesssim (n+0.2)\omega_{ce}$, where n is an integer, a population of particularly strong field-aligned irregularities was excited in the region just below the X-mode reflection height.

The mechanism responsible for these simulated density features is likely to be connected with the excitation of plasma waves. Many of the irregularities bear a clear resemblance to the field-aligned density structures generated around the upper-hybrid resonance height, in spatial distribution and orientation, and in developmental timescale; the similarities suggest a process analogous to the thermal-resonance class of instabilities understood to drive the formation of the irregularities at the UHR height. For this process to occur, electrostatic plasma waves propagating in a direction close to perpendicular to the background geomagnetic field - such as upper-hybrid or electron Bernstein waves - must be excited by the pump wave.

Although small variations in the location of irregularity populations with pump wave frequency were found, the density features were consistently found to develop near to regions where the background plasma frequency was close to matching a harmonic of the electron cyclotron frequency; the position of field-aligned irregularity growth appeared to be more closely tied to background plasma conditions than to pump wave parameters. This observation implies that a multi-step decay process in which the pump wave first excites an electron plasma wave was more likely to be accountable for the simulated irregularities than the direct conversion of the electromagnetic pump wave to upper-hybrid or Bernstein modes. The latter mechanism, perhaps occurring via a parametric process such as two-plasmon decay instability, would be reliant on the combined frequencies of the daughter wave-products matching the EM pump wave frequency and hence the altitude at which this matching occurred in a vertically-inhomogeneous plasma may be expected to vary as the pump frequency was varied. In the former mechanism, a Langmuir plasma wave at the local electron plasma frequency could be excited via a process similar to the parametric decay instability, and would then decay to further

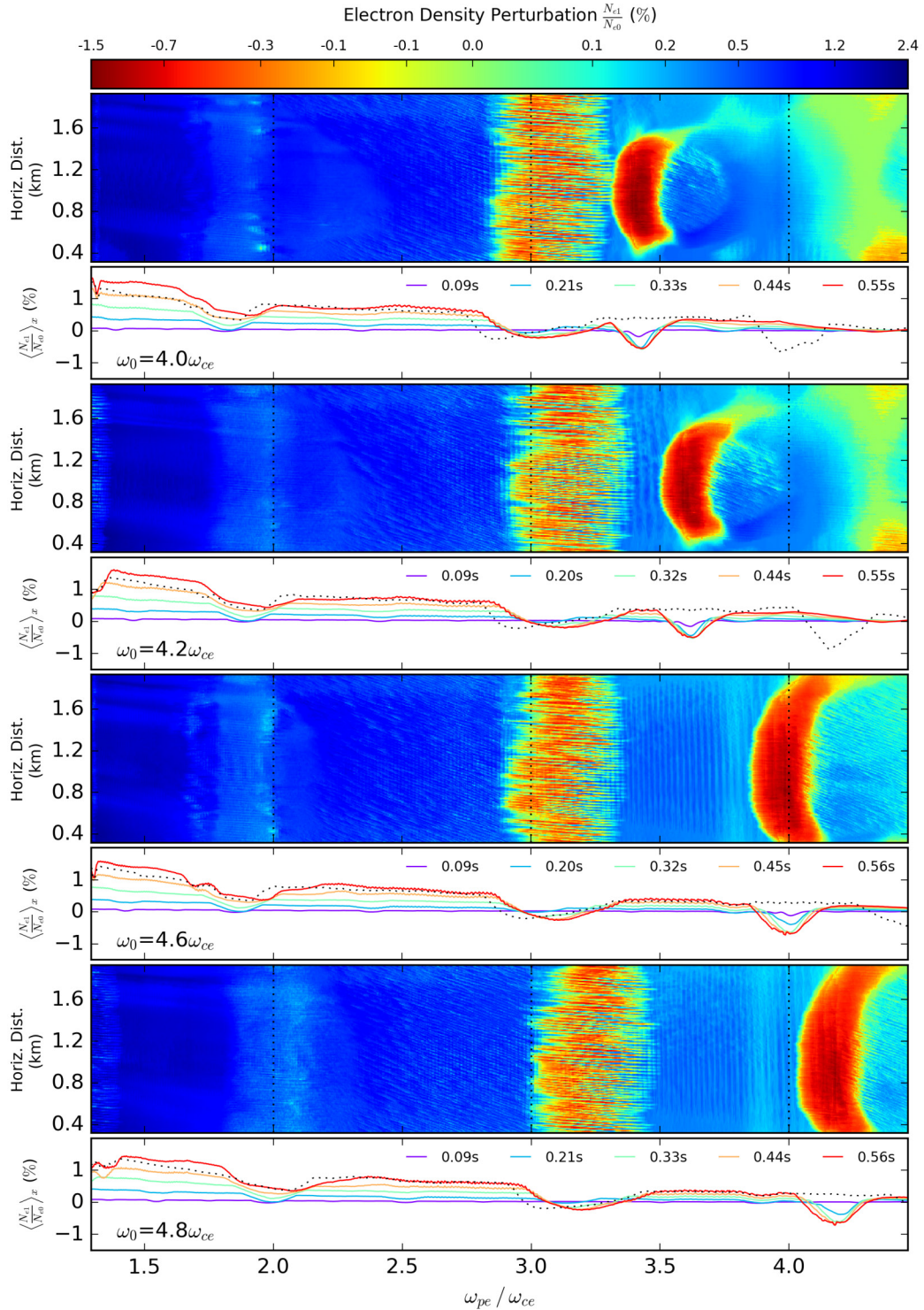


FIGURE 5.6: Examples of the density perturbations developed in the simulation using pump wave frequencies in the range $(4 - 5)\omega_{ce}$. For each frequency, the upper panel displays the spatial snapshot of the electron density perturbation developed after $0.56, s$. Note that the colour-map has been logarithmically-normalised. The gyro-harmonic heights are indicated by dotted lines. The lower panel for each frequency shows horizontally-averaged vertical profiles of the density perturbation for a range of heights (solid lines). The horizontally-averaged profile from the corresponding O-mode simulation is indicated by the dotted line (recorded after $0.56, s$ simulated time). Computational grid parameters used in these simulations can be found in Table 5.1.

plasma waves. The mechanism behind the non-field-aligned density striations visible between $\omega_{pe} = 2\omega_{ce}$ and $\omega_{pe} = 3\omega_{ce}$ is not clear, however it could be due to turbulence caused by multiple decays of Langmuir or other plasma waves in this region.

Until recently, the notion of a PDI process being excited in the F-region via X-mode irradiation would have been thought to be unlikely. This process is known to be suppressed at altitudes more than $\sim 10\text{ km}$ below the O-mode reflection height [Stubbe and Kopka, 1981] due to Landau damping effects and the poor matching between the pump wave and plasma wave frequencies. Further, due to the X-mode wave having no component of its E-field vector parallel to the magnetic field, the threshold for this instability would be unlikely to be met. However, the calculations of [Wang et al., 2016], discussed and investigated via numerical simulation in Chapter 6 below, have shown that under certain conditions the PDI *can* be excited at and below the X-mode reflection height, enabling the excitation of Langmuir plasma waves in this region. This theoretical prediction is supported by the experimental observations of HF-enhanced plasma and ion lines during X-mode heating by [Blagoveshchenskaya et al., 2015], a feature understood to be indicative of the excitement of the PDI and OTSI processes. In the fluid simulation, there is no Landau damping to suppress the PDI process and thus the threshold for this instability may be low; conceivably, electron plasma waves could be excited by the pump wave at all altitudes in the numerical domain. Excited plasma waves could then decay further to produce perpendicularly-propagating electrostatic upper-hybrid or electron Bernstein waves, which could then go on to drive the growth of the field-aligned density structures found in the simulated density data. A mechanism such as this could explain why the development of these features predominantly occurs close to the gyroharmonic heights: in these regions, an excited Langmuir plasma wave will be closely-matched in frequency to one of the electron Bernstein modes. Bernstein waves thus excited could then potentially generate or enhance field aligned irregularities through a thermal-resonance-style interaction, or decay further to upper-hybrid modes that could themselves produce or amplify the observed irregularity structures.

The proposed mechanism for the formation of field-aligned irregularities relies on the excitation of electron plasma waves via the PDI process. This instability, as described

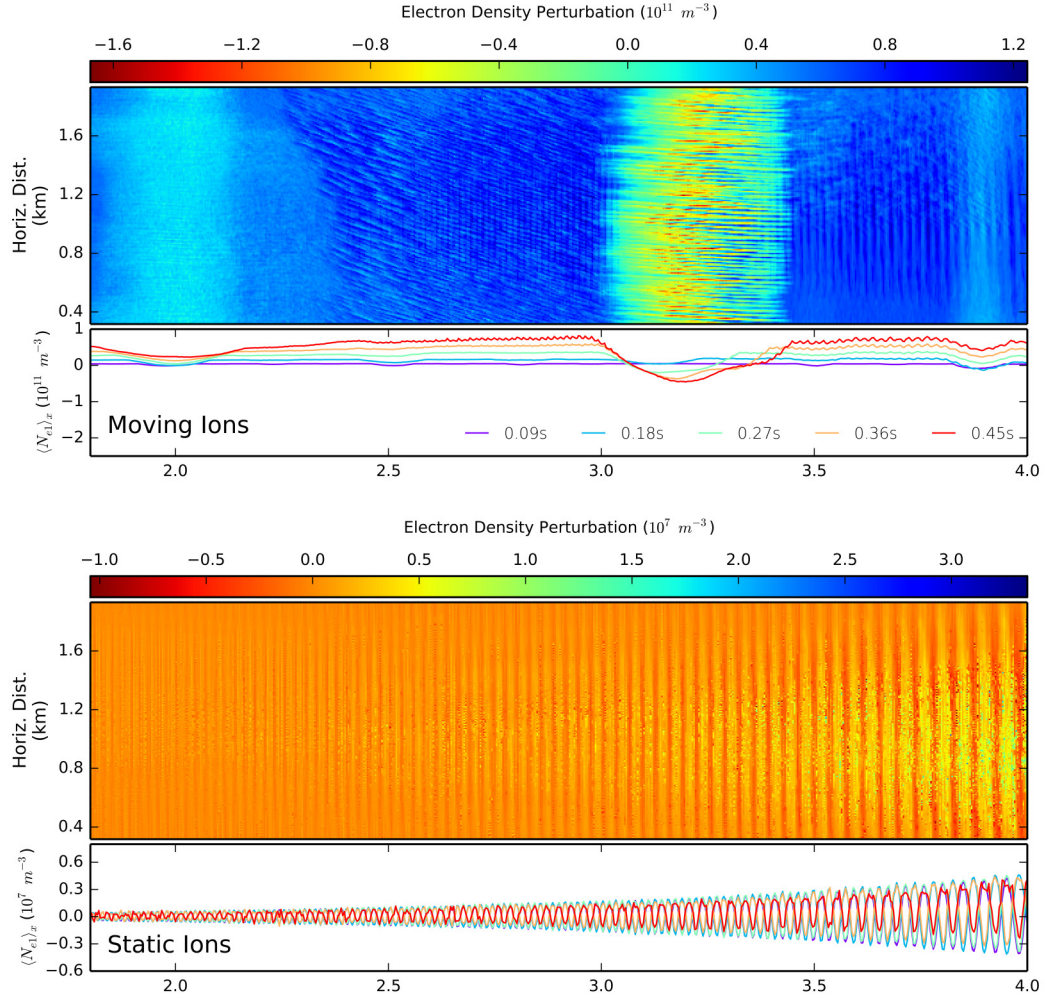


FIGURE 5.7: Comparison of the electron density perturbation simulated after 0.4 s for the cases of dynamic O^+ ions with time-varying density (upper panels) and static ions with no variation in density with time (lower panels) for the case of an X-mode polarised pump wave with $\omega_0 = 4.8\omega_{ce}$. In the static-ion case, plasma waves that rely on oscillation of the ion fluid such as lower-hybrid or ion-acoustic waves cannot exist in the simulation. Similar results were found for the O-mode case. Computational grid parameters $\Delta_t = 1.51 \times 10^{-8} \text{ s}$, $\Delta_x = 8.82 \text{ m}$ were used in this simulation.

in Section 1.6.4 requires the production of a low-frequency wave component involving an oscillation of the ion density, for example an ion-acoustic or lower-hybrid wave. In Figure 5.7, the electron density perturbation produced for the cases of dynamic O^+ ions with a time-varying density (upper panels) and static ions with no time-variation in density (lower panels) are compared. In the latter case, an ion fluid is still present to provide a neutralising and restorative background to the electron motion, however no ion oscillations or waves can exist in the simulation. The former is the approach used in all other simulations described above. It can be seen that allowing the ions to move and vary

in density makes a significant difference to the development of density structures in the simulation; with ion motion “turned off”, the field-aligned density structures discussed above do not manifest and the electron plasma experiences only weak perturbation. Similar results were found for the equivalent O-mode simulations. This provides further indication that a PDI-type process may be at least partially involved in the irregularity formation: when the ion waves crucial to the instability are suppressed, growth of the irregularities is also suppressed.

In reality, the effects of Landau damping would be likely to drive the threshold for the PDI process to infeasibly high levels over most of the altitude range covered by the simulation: observation of field-aligned density structures at multiple gyroharmonic heights (as was found in the Landau-free numerical simulation results) during X-mode heating would not be expected. However, the simulation results demonstrate that, under some circumstances at least, the excitation of field-aligned density irregularities by an X-mode pump wave is indeed possible. As will be discussed further in Chapter 6, under certain conditions it is possible for the X-mode wave to exceed the threshold for the parametric decay or oscillating two-stream instabilities, particularly when the field-aligned component of the pump wave E-field is enhanced near to the X-mode wave reflection layer or by the effect of density inhomogeneities. This would allow the mechanism proposed here to proceed under experimental conditions.

In the O-mode case, parametric processes leading to the excitation of Langmuir plasma waves are known to occur in a narrow range of altitudes below the O-mode reflection height, in which the EM wave amplitude is almost always sufficiently high to exceed the threshold for the PDI or OTSI [Stubbe and Kopka, 1981]. Thus, the production of field-aligned irregularities via the mechanisms proposed above may be expected to occur when the O-mode wave reflects at an altitude close to but above a gyroharmonic height. For the case of pump waves with frequencies around the third gyroharmonic, the emergence of a strong population of field-aligned density features close to the altitude where $\omega_{pe} = 3\omega_{ce}$ could contribute to an asymmetry in anomalous absorption. In the experiments reported by [Stocker et al., 1993, Stubbe et al., 1994], the anomalous absorption fell to a minimum at a frequency thought to closely correspond to $\omega_0 = 3\omega_{ce}$, before rising to

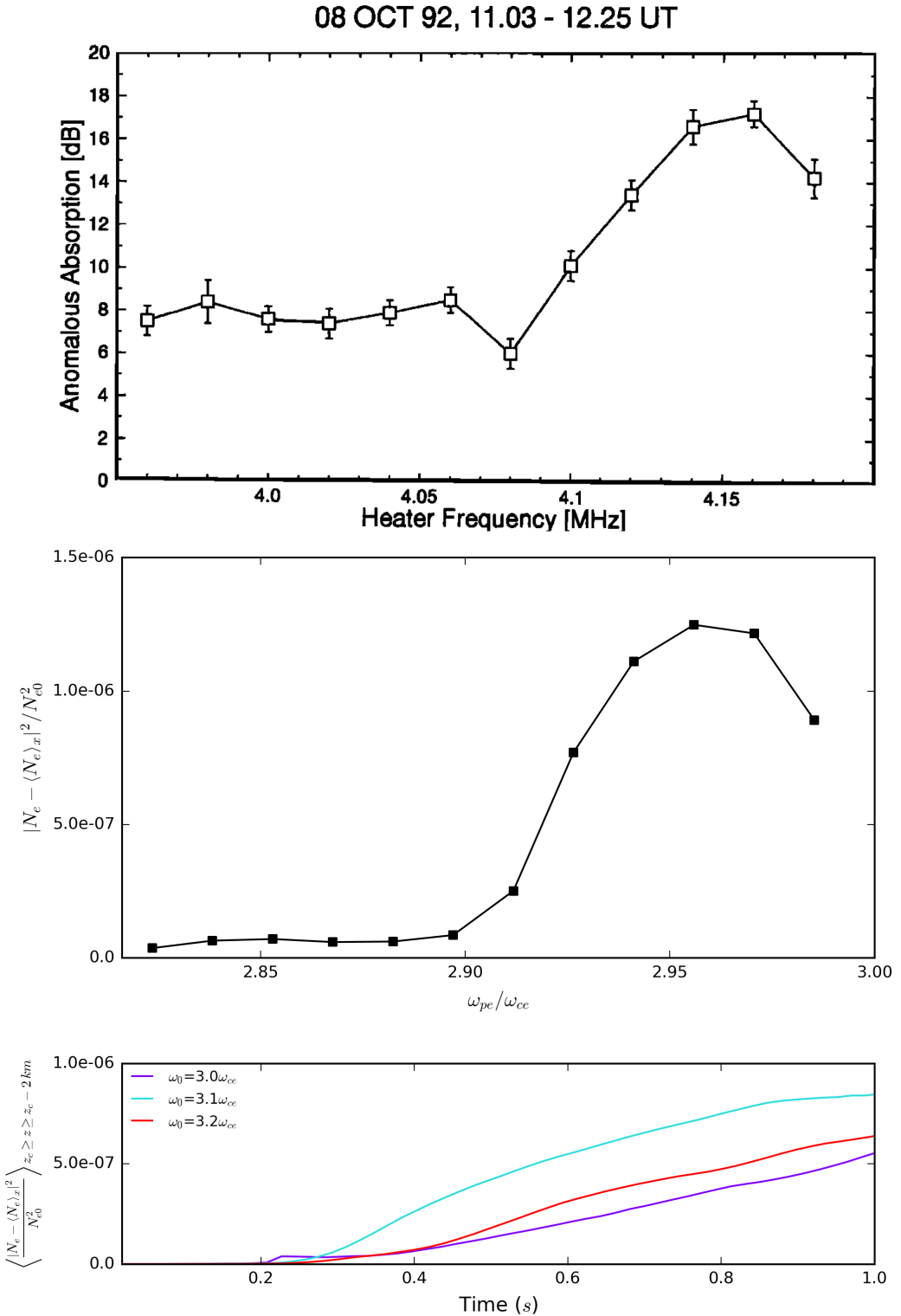


FIGURE 5.8: Top panel shows an example of the anomalous absorption asymmetry for pump wave frequencies $\omega_0 \simeq 3\omega_{ce}$ measured at EISCAT (plot adapted from the upper panel in Figure 10 of [Stubbe et al., 1994]). Central panel shows the variation of the mean-squared irregularity amplitude $\langle |\delta N|^2 \rangle / N_0^2$ with ω_{pe} close to the third gyro-harmonic height, sampled at similar frequency steps to those used in the upper panel. Bottom panel shows the temporal evolution of $\langle |\delta N|^2 \rangle / N_0^2$, averaged over the altitude range $z_c \geq z \geq z_c - 2 \text{ km}$. The greatest irregularity amplitude, and hence the greatest expected anomalous absorption, can be seen to occur for $3.1\omega_{ce}$. Computational grid parameters used in these simulations can be found in Table 5.1.

Image credit (upper panel): [Stubbe et al., 1994].

a distinct peak at a frequency $\sim 80\text{ kHz}$ above this. This asymmetry can be seen in the upper panel of Figure 5.8, which has been adapted from the upper panel of Figure 10 in [Stubbe et al., 1994]. The simulation results suggest that pump waves which reflect above but sufficiently close to $\omega_{pe} = 3\omega_{ce}$ may be able to excite irregularities, and hence stimulate anomalous absorption. Pump waves which reflect below this region may not excite irregularities, and thus are unlikely to induce the same level of absorption, leading to an asymmetry. In the simulations described here, O-mode pump waves with reflection heights far above $\omega_{pe} = 3\omega_{ce}$ excited strong irregularities in this region, however in a real experiment the effects of Landau damping would be expected to inhibit the parametric decay of the pump wave to plasma waves (and thus the generation of irregularities) in all but a narrow region below the reflection height, thus the anomalous absorption would be expected to reduce as the frequency was increased far beyond $\omega_0 = 3\omega_{ce}$. The possibility of Bernstein modes being favourably excited close to the gyroharmonic heights via this method may also help to explain the disappearance of the downshifted maximum feature observed in SEE spectra for $\omega_0 \sim n\omega_{ce}$.

An analytical expression for the anomalous absorption (Γ) due to a population of irregularities at the upper-hybrid resonance height was calculated by [Robinson, 1989], in which $\Gamma \propto \langle |\delta N|^2 \rangle / N_0^2$, where $\langle |\delta N|^2 \rangle$ is the mean-squared irregularity amplitude. To investigate the possibility of the simulated density features seen to grow close to the third gyroharmonic height contributing to anomalous absorption, the mean-squared irregularity amplitude was calculated for the O-mode simulations with pump wave frequencies $\omega_0 = 3.0\omega_{ce}$, $3.1\omega_{ce}$ and $3.2\omega_{ce}$, with δN obtained by subtracting a horizontal average from the simulated electron density perturbation such that $\delta N = N_e - \langle N_e \rangle_x$. The temporal evolution of this quantity, averaged over an altitude range $z_c \geq z \geq (z_c - 2\text{ km})$ (over which the parametric excitement of plasma waves may be expected to occur), is shown in the bottom panel of Figure 5.8 for each pump frequency. From this it can be seen that the anomalous absorption due to the simulated irregularities would be expected to be greatest for $\omega_0 = 3.1\omega_{ce}$. This matches well with the observed results of [Stubbe et al., 1994] shown in the upper panel of Figure 5.8, which show a peak in absorption $\sim 0.1\omega_{ce}$ above the pump frequency thought to be $\sim 3\omega_{ce}$. The central panel

shows the variation of $\langle |\delta N|^2 \rangle / N_0^2$ with ω_{pe} observed close to the third gyroharmonic height for an example case of $\omega_0 = 3.6\omega_{ce}$ (chosen as an example because the reflection and UH resonance heights for this wave were sufficiently far away that they did not disturb the irregularity population; in a real experiment a wave of this frequency would no be expected to generate irregularities in this region) and sampled at similar-sized frequency intervals to the experimental results displayed in the upper panel. A very close correspondence to the qualitative shape of the irregularity profile and the observed anomalous absorption distribution can be seen in this case. Close to the fourth gyroharmonic height, only very weak density features were seen in the simulations; when the above process was repeated for O-mode pump waves with reflection heights close to $\omega_{pe} = 4\omega_{ce}$, no significant asymmetry in the simulated mean-squared irregularity amplitude was found, in agreement with the experimental observations reported by [Stubbe et al., 1994].

For the EISCAT experiment described by [Blagoveshchenskaya et al., 2015], the X-mode pump wave frequency used during heating was $\omega_0 \simeq 5.17\omega_{ce}$ (using geomagnetic field values from IGRF-12 [Thébault et al., 2015] to obtain ω_{ce}). In the above simulations, X-mode waves with frequencies in the corresponding range $(n - 0.2)\omega_{ce} \lesssim \omega_0 \lesssim (n + 0.2)\omega_{ce}$ (for integer n) were found to reflect at a layer just above a strong population of irregularities. This suggests that the region in which this heater beam would most favourably excite Langmuir waves (where the E-field is enhanced close to the reflection height) would occur close to a region in which strong field-aligned irregularity production is possible, offering a potential explanation as to why this experiment generated particularly strong X-mode heating effects. This mechanism does not necessarily require reflection on the X-mode pump wave, and thus also provides a possible explanation for the continued observation of field-aligned irregularities during underdense heating ($f_0 > f_{xF2}$) observed during the same campaign. The creation of density irregularities close to the X-mode reflection height also suggests that if a future experiment was to vary the frequency of an X-mode pump wave in small steps in the range $(n - 0.2)\omega_{ce} \lesssim \omega_0 \lesssim (n + 0.2)\omega_{ce}$, it may expect to observe an asymmetry in the anomalous absorption similar to that found

for the O-mode case around the third gyroharmonic by [Stubbe et al., 1994]. The simulation results indicate that this effect may be particularly apparent for X-mode pump waves in the range $3.8\omega_{ce} \lesssim \omega_0 \lesssim 4.2\omega_{ce}$, due to the strong growth of simulated density irregularities occurring just above $\omega_{pe} = 3\omega_{ce}$.

5.4 Contribution of Electrostatic Fields to Temperature

The simulation results presented in the previous section demonstrate that the numerical code is capable of exciting density irregularities associated with a variety of plasma waves. Excitation of irregularities of this nature has often been associated with heating of the electron plasma via anomalous absorption of the pump wave (see, for example, [Honary et al., 1995]). The update algorithm however does not include an explicit evaluation of the Poisson equation and only calculates numerical solutions to Maxwell's curl equations; consequently the electric fields associated with any regions of charge difference in the simulation are not explicitly calculated. Due to this, the electrostatic fields due to plasma waves generated through the action of the pump wave are not fully modelled by the simulation, and not included in the calculation of the $\mathbf{E} \cdot \mathbf{U}$ term in the electron temperature update step. In this section, the numerical code is modified to take into account an estimation of the electrostatic fields due to any excited density irregularities.

In the multi-fluid scheme used here, the evolution of ion and electron densities are calculated independently. It is therefore a simple matter to find the net charge density at each grid cell by summing the charge density contribution due to each species:

$$\rho[m, p] = \sum_{a=e,i} e_a N_a[m, p] = eN_i[m, p] - eN_e[m, p] \quad (5.8)$$

where ρ is the charge density and the notation $[m, p]$ refers to a node with horizontal position $m\Delta_x$ and vertical position $p\Delta_z$ in the 2-dimensional computational grid, where m and p are integers. Here as above, the spatial step size was set to be equal in all directions $\Delta_x = \Delta_z = \Delta$. The charge density node was situated at the corner of the Yee

cell, collocated with the density nodes for ease of calculation. This positioning was also amenable to calculation of the electric fields without spatial averaging of the charge or potential.

Calculation of the charge density was added into the time-stepping algorithm to occur every cycle following immediately after the density perturbation update. Following this, the electrostatic potential in each cell resulting from any non-zero charge density was calculated using a discretised version of the Poisson equation:

$$\nabla^2 \phi = \frac{\partial^2 \phi}{\partial x^2} + \frac{\partial^2 \phi}{\partial z^2} = -\frac{\rho}{\varepsilon_0}$$

$$\frac{\left(\phi[m-1, p] - 2\phi[m, p] + \phi[m+1, p] \dots \right.}{\Delta^2} \left. \dots + \phi[m, p-1] - 2\phi[m, p] + \phi[m, p+1] \right) = -\left(\frac{\rho[m, p]}{\varepsilon_0} - \nabla \cdot \mathbf{E}_{EM} \right) \quad (5.9)$$

A correction term $\nabla \cdot \mathbf{E}_{EM}$ to remove any contribution from the EM field was subtracted. The classic Yee electromagnetic scheme is divergence-free, however, since the FDTD code used here couples the current due to the moving plasma fluid to the E-field updates (see Chapter 3), this scheme has a non-zero electric divergence. This correction term is an attempt to remove the contribution from this coupling, and leave only the contribution to the charge density due to modifications to the plasma distribution such as small-scale irregularities. Many methods to computationally solve the discrete Poisson equation exist (see examples in [Birdsall and Langdon, 1985]) however these are often difficult to implement efficiently using GPU architecture. Solving this equation exactly every cycle would be restrictively time-consuming; instead the potential was updated every time-step using past nearest-neighbour values in a *Jacobi* update scheme:

$$\phi^{q+1}[m, p] \simeq \frac{1}{4} \left(\phi^q[m-1, p] + \phi^q[m+1, p] + \phi^q[m, p-1] + \phi^q[m, p+1] + \frac{\Delta^2}{\varepsilon_0} \rho^{q+1}[m, p] \right) \quad (5.10)$$

where q represents the integer simulation timestep, and ρ^{q+1} was calculated using (5.9) immediately prior to the ϕ^{q+1} update. This approximation proved to be adequate provided that the simulation time step was short compared to the timescales at which density features in the simulation evolved, and was found to yield potentials similar to

those calculated using more rigorous techniques, such as successive over-relaxation [Press et al., 1992].

From this estimate of the potential distribution, “ES” contributions to the electric field due to regions of charge separation could be found each cycle using a discrete form of Gauss’ Law:

$$\mathbf{E}_{ES} = -\nabla\phi$$

$$\Rightarrow E_{ESx}^q[m + \frac{1}{2}, p] = -\frac{1}{\Delta} (\phi^q[m+1, p] - \phi^q[m, p]) \quad (5.11)$$

$$E_{ESz}^q[m, p + \frac{1}{2}] = -\frac{1}{\Delta} (\phi^q[m, p+1] - \phi^q[m, p]) \quad (5.12)$$

These field components are collocated in time and spatially within the Yee cell with the “EM” field nodes calculated from Maxwell’s curl equations using (3.7). The E-field input to the electron temperature update equation was then modified to include the ES contribution via $\mathbf{E}_{Tot} = \mathbf{E}_{EM} + \mathbf{E}_{ES}$. The approximations used in this calculation are finite-differences of 2nd-order accuracy (similar to Yee scheme), however the results below should be treated as a somewhat-crude estimate only. The method described above does not accurately model the ES plasma wave fields, and should not be expected to give a quantitative prediction that can be compared to experimental observations; at best this method gives an indication that the presence of additional ES fields due to the formation of irregularities can lead to additional enhancement of the electron temperature. The estimated field calculations also do not take into account the possibility that changes in plasma distribution may generate a fluctuating current, and hence perturb the magnetic field in the simulation domain, leading to an additional EM contribution and a perturbation to the plasma velocities. A more thorough treatment would require inclusion of this additional magnetic contribution, a finer spatial grid resolution, and ideally a kinetic approach to the simulation of plasma dynamics.

The modified code was run for a selection of pump frequencies using X-mode polarised pump waves. The density perturbations developed after 3×10^7 timesteps (~ 0.5 s) were used as the initial perturbation profile in each case, and the simulations run for a further 8×10^6 steps with the E-fields estimated from the excited density irregularities

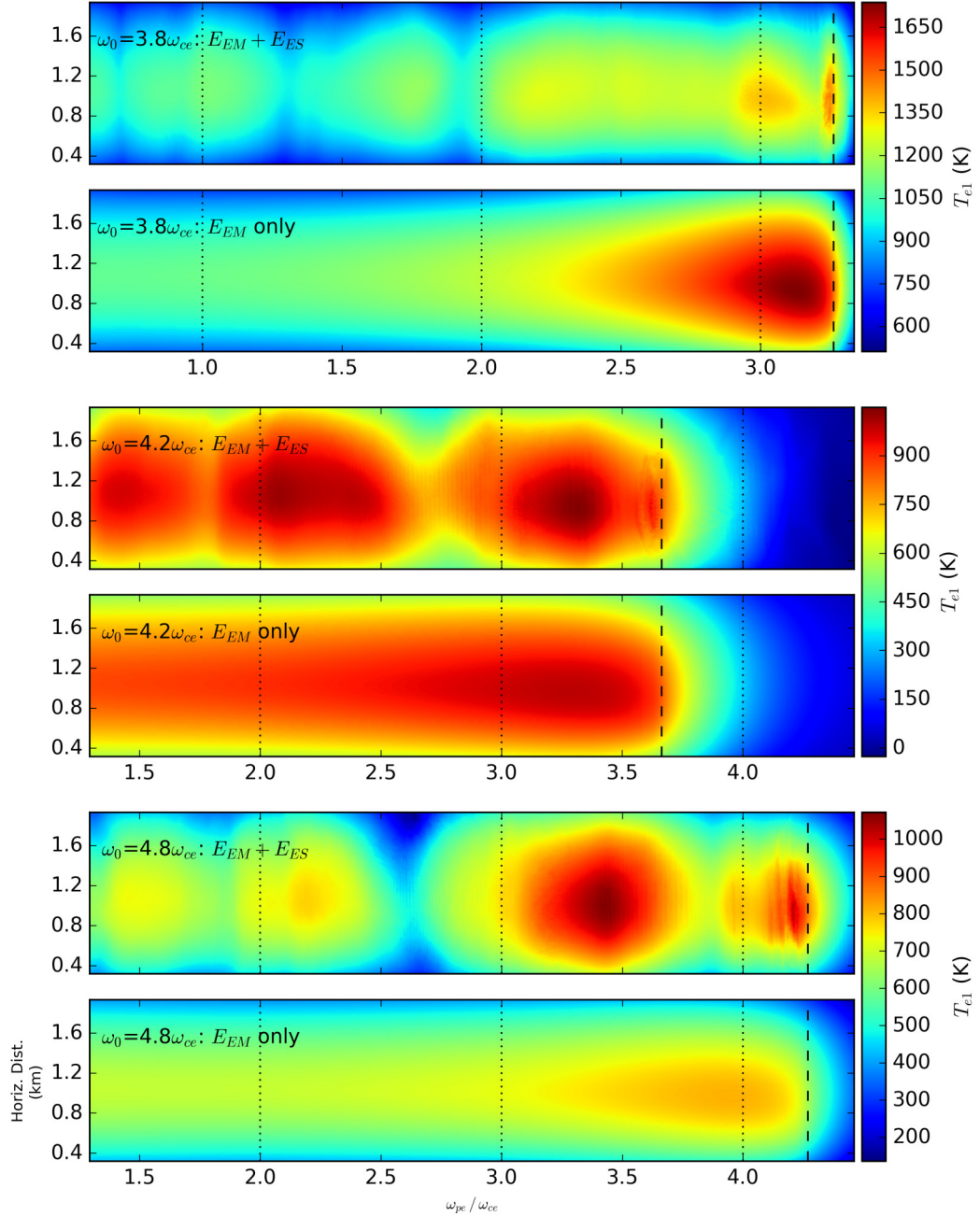


FIGURE 5.9: Comparison of the electron temperature perturbations developed in the simulation domain with and without the inclusion of estimated E-fields due to excited density irregularities in the electron temperature update calculation. Spatial snap-shots of temperature perturbation with and without E_{ES} are shown for example pump wave frequencies $\omega_0 = 3.8\omega_{ce}$, $\omega_0 = 4.2\omega_{ce}$ and $\omega_0 = 4.8\omega_{ce}$ (from top to bottom respectively). The gyroharmonic heights are indicated by dotted lines. The more coarsely-dashed line indicates the X-mode reflection layer for each case. Computational grid parameters used in these simulations can be found in Table 5.1.

included in the electron temperature update. The impact of the inclusion of these fields on the evolution of electron temperature in the simulation domain is shown in Figure 5.9 for the examples of X-mode pump waves with frequencies $\omega_0 = 3.8\omega_{ce}$, $\omega_0 = 4.2\omega_{ce}$ and $\omega_0 = 4.8\omega_{ce}$ (displayed from top to bottom respectively). With only the fluid EM E-fields contributing to the electron temperature calculation, the perturbation takes the form of a large-scale enhancement located below the X-mode reflection height. The inclusion of the estimated E_{ES} field adds a great deal more altitude variation to the simulated temperature and in most cases increased the maximum temperature recorded during the simulation. Localised regions of enhancement can be seen to form close to populations of irregularities; the magnitude of temperature perturbation found in these enhanced patches often exceeded the maximum temperature perturbation for the case of E_{EM} fields only. The enhancement in electron temperature due to E_{ES} is particularly apparent around the strong irregularity growth seen above $\omega_{pe} = 3\omega_{ce}$ for pump wave frequencies in the range $(4 - 5)\omega_{ce}$. In this region, the perturbation to electron temperature relative to the E_{EM} -only case was found to be up to 5% greater for $\omega_0 = 4.2\omega_{ce}$, and as large as 33% greater for $\omega_0 = 4.8\omega_{ce}$.

The theoretical heating rate (Q) due to both collisional and anomalous processes can be calculated using $Q \propto |E|^2 e^{-\Gamma_c - \Gamma_a}$, where Γ_c refers to the collisional absorption and Γ_a to the anomalous absorption [Honary et al., 1995]. The equations (5.18) and (6.11) of [Robinson, 1989] were used to find Γ_a and Γ_c respectively, and thus calculate the gain in heating rate that would be expected from inclusion of both collisional and anomalous absorption (equivalent to including both ES and EM wave fields) compared to the inclusion of collisional absorption only (equivalent to including EM wave fields only) in the region above $\omega_{pe} = 3\omega_{ce}$. By this method, inclusion of the ES fields due to irregularities would be expected to increase the heating rates by $\sim 39\%$ and $\sim 12\%$ for the $\omega_0 = 4.2\omega_{ce}$ and $\omega_0 = 4.8\omega_{ce}$ cases respectively, in surprisingly good agreement with the simulated gains in temperatures of 33% and 5%.

While these somewhat-crude estimates of the electrostatic fields due to the growth of density irregularities do not accurately replicate the plasma wave fields and cannot be used to provide quantitative predictions of the resulting temperature enhancement, the

results presented above do indicate that the presence of substantially high-amplitude E-fields around the site of the irregularities can lead to significant electron heating. Such large-amplitude wave fields could be developed through a thermal resonance process, in which upper-hybrid or electron Bernstein waves are trapped in the density depletions and amplified. To address this in future investigations, these simulations should be repeated at a far greater resolution to allow short-wavelength plasma waves to be accurately represented. Ideally, a full or partial kinetic implementation such as a hybrid particle-in-cell / FDTD approach could be used, which would allow important kinetic effects such as Landau and cyclotron damping to be included. Perturbations to the background magnetic field should also be included in the update algorithm, to account for the possibility that the changes to plasma distribution lead to fluctuations in current, and therefore in magnetic field. These approaches would require significantly more processing time and capacity than the simulations presented in this Chapter.

5.5 Summary and Conclusions

Experiments performed at the EISCAT ionospheric heating facility in Tromsø have often observed significant perturbation to the plasma medium when the F-region of the ionosphere is illuminated using an O-mode polarised heating beam. The processes understood to be predominantly responsible for this modification are known to occur close to the O-mode reflection layer and upper-hybrid resonance height. These include both collisional absorption of the pump wave, particularly in the region of high field amplitude due to the Airy-like reflected standing wave, and anomalous processes through which the EM pump wave may excite low-group-velocity plasma waves that are subsequently dissipated in the local medium, resulting in efficient transfer of the pump wave energy to the plasma. Anomalous plasma-wave-driven effects have been observed to be particularly sensitive to the proximity of the pump wave frequency to harmonics of the electron gyrofrequency. These processes occur in regions of the F-region of the ionosphere where it is impossible under normal conditions for a ground-launched X-mode wave to access. Recently however, experiments performed at EISCAT using X-mode

heater waves have achieved significant modification of the F-region plasma, with observed effects including large-scale electron temperature and density variations and the production of small-scale field-aligned density irregularities similar to those often associated with upper-hybrid wave excitation and the thermal resonance instability 1.6.5. In this Chapter, numerical simulations were carried out to address several of the exciting and unexplained plasma phenomena recently observed both during X-mode heating experiments and during experiments in which the EM pump wave frequency was varied close to one of the electron gyroharmonics.

The multiple-fluid FDTD code developed in Chapter 3 was used to simulate the ionospheric heating process for the cases of both O-mode and X-mode polarised electromagnetic pump waves with a range of frequencies. The numerical algorithm contained time-explicit update steps for both the plasma temperature and density, allowing the evolution of perturbations to the plasma medium to be investigated. It was found that each pump wave frequency excited a wide variety of electron density features, including regions of depletion and bands of density-depleted structures elongated along the background magnetic field direction. The simulation results presented in this Chapter demonstrate that both O- and X-mode polarised pump waves are capable of exciting several bands of field-aligned density-depleted irregularities, predominantly located at points where the background electron plasma frequency was closely matched with a harmonic of the electron cyclotron frequency. These irregularities were often alike in spatial distribution and developmental timescale to the irregularities found to grow at the upper-hybrid resonance height during O-mode simulations, suggesting that a similar formation mechanism was at work. Increasing the pump wave frequency allowed a greater range of the background plasma to be accessed and enabled the excitement of additional bands of density structures. Plasma-wave driven anomalous heating processes associated with the growth of structures of this nature could contribute to the large electron temperature enhancements observed during X-mode experiments at EISCAT. The growth of irregularities close to the third gyroharmonic height could also potentially explain the observed asymmetry in anomalous absorption observed by [Stubbe et al., 1994].

The mechanism behind the growth of field-aligned electron density irregularities close to gyroharmonic heights is proposed to begin with the excitation of Langmuir plasma waves by the pump wave. Until recently this process would have been expected to be suppressed for X-mode waves due to the effects of Landau damping and the fact that they typically have little or no component of their E-field directed along the geomagnetic field direction, however the calculations of [Wang et al., 2016] as discussed in the following Chapter show that the parametric decay and oscillating two-stream instabilities may proceed for X-mode waves under certain conditions. Experimental observations of HF-enhanced ion and plasma lines by [Blagoveshchenskaya et al., 2015] suggest that excitation of Langmuir waves via X-mode heating does indeed occur. Excited Langmuir waves could then decay to a perpendicularly-propagating electrostatic plasma waves such as one of the electron Bernstein modes, provided their frequencies were of a sufficiently close match. These electrostatic waves could then go on to drive density irregularity growth through a thermal-resonance-style process or similar. A mechanism such as this would explain why in the simulation the bands of irregularities appeared to be more closely associated with background plasma properties than pump wave parameters. Simulations performed with ion motion “switched off”, and thus the electrostatic ion waves crucial to the PDI and OTSI suppressed, were found to produce no growth of field-aligned irregularities. Once excited, these plasma waves could drive electron temperature enhancement and contribute to the observed temperature increases.

The numerical code was modified to take into account an estimation of the electrostatic fields due to any excited density irregularities. Subtracting the number density of electrons from that of ions allowed the charge difference in each computational grid cell to be calculated; it was found that the populations of field-aligned density irregularities located close to the gyroharmonic heights were associated with substantial variations between the electron and ion densities, and thus regions of non-zero charge density. The inferred charge distribution was used to estimate the electrostatic potential at each grid node, and from this the contribution to the E-field corresponding to the density variations. The calculated E-fields were then coupled to the temperature update step through the $\mathbf{E} \cdot \mathbf{U}$ heating term to provide an estimation of the temperature enhancement

due to the growth of irregularities. Inclusion of the electrostatic fields led to significant increases in the electron temperature in the region of the excited irregularities. Close to the gyroharmonic heights, the temperature enhancement was found to be as much as 33% greater than the corresponding temperatures in simulations using the FDTD EM fields only, in reasonably good agreement with the theoretical gain in heating rates expected when anomalous processes are included. These results indicate that the presence of substantially-high-amplitude electrostatic E-fields around the site of the irregularities can potentially lead to significant heating of the electron plasma.

Chapter 6

Comparison of Simulated X-mode Wave Fields with Theoretical Parametric Instability Thresholds

The work presented in this Chapter has been published as part of:

[Wang et al., 2016] X. Wang, P. D. Cannon, C. Zhou, F. Honary, B. Ni, Z. Zhao, 2016, *A Theoretical Investigation on the Parametric Instability Excited by X-mode Polarized Electromagnetic Wave at Tromsø*, Journal of Geophysical Research: Space Physics, 121 (4), 3578-3591, doi:10.1002/2016JA022411.

P. D. Cannon was responsible for the numerical simulations presented in Section 6.3 below (Section 4 of the above article). The theoretical calculations and comparisons with experimental observations described in Sections 6.1-6.2 below and Sections 1-3 of the above article were performed by X. Wang and colleagues.

6.1 Introduction

Modification experiments in which high-power, high-frequency EM waves are used to artificially perturb the ionosphere have been discussed in the preceding Chapters. Ground-launched waves of both ordinary-mode (O-mode) and extraordinary-mode (X-mode) polarisation have been observed to excite a wide range of plasma phenomena including high-frequency-enhanced ion and plasma lines, artificial field-aligned density irregularities, large scale electron density and temperature perturbations and stimulated electromagnetic emission.

The excitation of the parametric decay instability (PDI) and oscillating two-stream instability (OTSI) has been extensively studied for the case of an O-mode pump wave (see, for example, [Fejer, 1979]). Until recently, it was thought that pump waves with X-mode polarisation would not be capable of exciting parametric processes such as those observed in the ionosphere. As discussed in Chapter 5 above, reflection of the X-mode pump wave in the ionosphere occurs at a level where the background plasma frequency is far below the pump frequency, such that the parametric matching conditions (see Section 1.6.4) are poorly satisfied. At these altitudes the effects of Landau damping would also act to raise the thresholds required for excitation of parametric instabilities [Stubbe and Kopka, 1981]. Further, a perfect X-mode wave has no component of its E-field directed along the geomagnetic field direction, meaning that the thresholds for either the PDI or OTSI would not be expected to be met. However, a series of experiments at EISCAT [Blagoveshchenskaya et al., 2013, Blagoveshchenskaya et al., 2014] have demonstrated that X-mode waves are capable of generating both HF-enhanced plasma lines and zero-frequency-offset HF-enhanced ion lines, indicative of the excitation of the PDI and OTSI processes respectively. The numerical simulations presented previously in Chapter 5 also provide a further indication that waves of X-mode polarisation are capable of exciting plasma waves in the ionosphere.

The thresholds for excitation of the PDI and OTSI have been analysed for the case of an X-mode polarised pump wave by [Wang et al., 2016]. This calculation is described briefly in Section 6.2 below. The resulting expressions demonstrate that it is possible

for these processes to be excited during X-mode heating, however a minimum fraction of the pump wave power is required to be directed along the geomagnetic field direction; in Section 6.3, full-wave numerical simulations using the GPU-accelerated FDTD code developed in Chapter 3 are used to test if this criterion could be met under certain experimental conditions.

6.2 Threshold Calculation and Comparison to Experiment and Observation

The thresholds for excitation of the PDI and OTSI via an X-mode polarised pump were calculated by [Wang et al., 2016] assuming a magnetised plasma fluid of electrons and ions. The full calculation of the thresholds is very involved, and therefore is only briefly summarised here. In the PDI case, a pump wave of parameters (ω_0, \mathbf{k}_0) was assumed to decay to a high-frequency plasma wave with parameters (ω, \mathbf{k}) and a low-frequency plasma wave (for example an ion-acoustic wave) with parameters $(\Delta\omega, \Delta\mathbf{k})$. In the OTSI case, the pump wave decays to a pair of high-frequency plasma waves propagating in opposite directions $(\omega_{\pm}, \pm\mathbf{k})$ and a low-frequency purely-growing mode $(\Delta\omega, \Delta\mathbf{k})$.

The derivation of the threshold begins with the coupled fluid expressions describing particle continuity (6.1), particle momentum (6.2-6.3) and electric potential (6.4) :

$$\frac{\partial N_{e,i}}{\partial t} + \nabla \cdot (N_{e,i} \mathbf{v}_{e,i}) = 0 \quad (6.1)$$

$$\left(\frac{\partial}{\partial t} + \nu_e \right) (N_e \mathbf{v}_e) + \omega_{ce} N_e \mathbf{v}_e \times \hat{\mathbf{z}} = -\nabla \cdot (N_e \mathbf{v}_e \mathbf{v}_e) - \frac{e}{m_e} N_e (\mathbf{E}_0 - \nabla \phi) - \gamma_e v_{Te}^2 N_{e1} \quad (6.2)$$

$$\left(\frac{\partial}{\partial t} + \nu_i \right) (N_i \mathbf{v}_i) - \omega_{ci} N_i \mathbf{v}_i \times \hat{\mathbf{z}} = -\nabla \cdot (N_i \mathbf{v}_i \mathbf{v}_i) + \frac{e}{m_i} N_i (\mathbf{E}_0 - \nabla \phi) - \gamma_i v_{Ti}^2 N_{i1} \quad (6.3)$$

$$\nabla^2 \phi = -\frac{1}{\epsilon_0} \sum_a e_a N_a \quad (6.4)$$

Here \mathbf{E}_0 is the E-field of the EM pump wave and ϕ is the potential due to the excited electrostatic waves. The geomagnetic field is assumed to lie along the z -direction such that $\mathbf{B}_0 = B_0 \hat{\mathbf{z}}$. The cyclotron frequencies for each species are given by $\omega_{ce,ci}$ and the thermal velocities by $v_{Te,Ti} = \sqrt{k_B T_{e,i}/m_{e,i}}$. As in previous Chapters, N_e and N_i

represent the number density of electrons and ions respectively, and can be split into a non-varying background part $N_{e0,i0}$ and a perturbed part $N_{e1,i1}$. Here the perturbed part is further broken down into a disturbance due to the high-frequency ($N_{\pm k}$) and low-frequency ($N_{\pm \Delta k}$) decay modes such that $N = N_0 + N_{\pm k} + N_{\pm \Delta k}$ for each species. Similarly, the particle velocities $\mathbf{v}_{e,i}$ can be broken down into components driven by the pump wave and high/low frequency electrostatic wave fields, such that $\mathbf{v} = \mathbf{v}_0 + \mathbf{v}_{\pm k} + \mathbf{v}_{\pm \Delta k}$ for each species. $\gamma_{e,i}$ are adiabatic indices. Effective collision frequencies are expressed as $\nu_e = \nu_{ei} + \nu_{en} + \nu_{eL}$ for electrons and $\nu_i = \nu_{ie} + \nu_{in} + \nu_{iL}$ for ions, where ν_{ei} , ν_{ie} , ν_{en} and ν_{in} are the electron-ion, ion-electron, electron-neutral and ion-neutral collision frequencies respectively. Landau damping for electrons and ions is included through collision frequency components ν_{eL} and ν_{iL} [Baumjohann and Treumann, 1996], given by:

$$\nu_{eL} = \frac{\omega}{k^3 \lambda_D^3} \left(\frac{\pi}{8} \right)^{\frac{1}{2}} \Lambda_0^{\frac{3}{2}}(b) e^{\left[-\frac{3}{2} - \frac{\Lambda_0(b)}{2k^2 \lambda_D^2} \right]} \quad (6.5)$$

$$\nu_{iL} = \Delta\omega \left(\frac{\pi}{8} \right)^{\frac{1}{2}} \left[\left(\frac{m_e}{m_i} \right)^{\frac{1}{2}} + \left(\frac{T_e}{T_i} \right)^{\frac{3}{2}} e^{\left(-\frac{T_e}{2T_i} - \frac{3}{2} \right)} \right] \quad (6.6)$$

where $\Lambda_0(b) = I_0(b) e^{-b}$, I_0 is the modified Bessel function, $b = k_\perp^2 v_{Te}^2 / 2\omega_{ce}^2$ and λ_D is the Debye length. Inclusion of these terms in the effective collision frequency allows Landau damping effects to be represented in the fluid-scheme calculation.

The pump wave field is assumed to be a plane wave of the form $\mathbf{E}_0 = \frac{E_0}{2} e^{-i(\mathbf{k}_0 \cdot \mathbf{r} - \omega_0 t)}$. As $k_0 \simeq 0$, this could be split into components perpendicular and parallel to the geomagnetic field, such that $\mathbf{E}_0 = E_\perp (\hat{\mathbf{x}} + i\hat{\mathbf{y}}) e^{-i\omega_0 t} + E_\parallel \hat{\mathbf{z}} e^{-i\omega_0 t}$. Each physical quantity was treated as a sum of plane wave components, for example in the case of particle velocity:

$$\begin{aligned} \mathbf{v} &= \mathbf{v}_{k_0, \omega_0} + \mathbf{v}_{\pm k, \pm \omega} + \mathbf{v}_{\pm \Delta k, \pm \Delta \omega} \\ &= \mathbf{v}_0 e^{-i(\mathbf{k}_0 \cdot \mathbf{r} - \omega_0 t)} + \mathbf{v}_k e^{i(\mathbf{k} \cdot \mathbf{r} - \omega t)} + \mathbf{v}_{-k} e^{-i(\mathbf{k} \cdot \mathbf{r} - \omega t)} + \dots \\ &\quad \dots + \mathbf{v}_{\Delta k} e^{i(\Delta \mathbf{k} \cdot \mathbf{r} - \Delta \omega t)} + \mathbf{v}_{-\Delta k} e^{-i(\Delta \mathbf{k} \cdot \mathbf{r} - \Delta \omega t)} \end{aligned} \quad (6.7)$$

Physical quantities made up of frequency components appropriate to each instability were incorporated into the governing fluid equations (6.1-6.4). Due to the arbitrary

nature of the \mathbf{r} and t parameters, the coefficient in front of each exponent term should equal zero. Thus, by collecting the coefficients for each exponent and summing to zero, dispersion relations relating to the parametric coupling processes could be obtained.

For the case of the PDI instability, in which the pump wave decays to a Langmuir wave and low-frequency ion-acoustic wave, this calculation resulted in a dispersion relation for the parametric coupling given by (6.8):

$$\left. \begin{aligned} & \left\{ -k_{\parallel}^2 [(\Delta\omega - i\gamma)(\Delta\omega - i\gamma - i\nu_i) - k^2 c_s^2] \dots \right. \\ & \left. \dots - \frac{k_{\perp}^2}{\omega_{ce}^2} (\Delta\omega - i\gamma - i\nu_e)^2 [-(\Delta\omega - i\gamma)(\Delta\omega - i\gamma - i\nu_i) + k^2 c_s^2] \dots \right\} \times \dots \\ & \left. \dots - \frac{k_{\perp}^2}{\omega_{ce}^2} \omega_{ce} \omega_{ci} (\Delta\omega - i\gamma - i\nu_e) (\Delta\omega - i\gamma) \right. \\ & \left. \dots \left\{ (\omega + i\gamma)^2 - \omega_L^2 + i\nu_e (\omega + i\gamma) \dots \right. \right. \\ & \left. \left. \dots + \frac{e^2}{m_e^2} \frac{1 - \frac{\omega_{ce}^2}{\omega^2}}{\omega^2 \left(1 - \frac{\omega_{ce}^2}{\omega^2} \cos^2 \theta\right)} \left[k_{\parallel}^2 E_{\parallel}^2 + \frac{k_{\perp}^2 E_{\perp}^2}{\left(1 + \frac{\omega_{ce}}{\omega_0}\right) \left(1 - \frac{\omega_{ce}^2}{\omega_0^2}\right)} \right] \right\} \dots \right. \\ & \left. \dots - \frac{m_e}{m_i} \frac{e^2 k^2}{m_e^2 \omega_0^2} \left\{ (\mathbf{k} \cdot \mathbf{E}_{\parallel})^2 + \frac{\Delta\omega - i\gamma}{\omega_{ce}} \frac{(\mathbf{k} \cdot \mathbf{E}_{\perp})^2}{\left(1 - \frac{\omega_{ce}^2}{\omega_0^2}\right)} \right\} \times \dots \right. \\ & \left. \dots \left\{ (\omega + i\gamma)^2 - \omega_L^2 + i\nu_e (\omega + i\gamma) \dots \right. \right. \\ & \left. \left. \dots + \frac{e^2}{m_e^2} \frac{1 - \frac{\omega_{ce}^2}{\omega_0^2}}{\omega_0^2 \left(1 - \frac{\omega_{ce}^2}{\omega_0^2} \cos^2 \theta\right)} \left[(\mathbf{k} \cdot \mathbf{E}_{\parallel})^2 + \frac{(\mathbf{k} \cdot \mathbf{E}_{\perp})^2}{\left(1 + \frac{\omega_{ce}}{\omega}\right) \left(1 - \frac{\omega_{ce}^2}{\omega^2}\right)} \right] \right\} = \dots \right. \\ & \left. \dots \frac{e^2 k^2}{m_e m_i} \frac{\left(1 - \frac{\omega_{ce}^2}{\omega_0^2}\right) \left(1 - \frac{\omega_{pe}^2}{\omega_0^2}\right)}{\left(1 - \frac{\omega_{ce}^2}{\omega_0^2} \cos^2 \theta\right)} \times \dots \right. \\ & \left. \dots \left\{ (\mathbf{k} \cdot \mathbf{E}_{\parallel})^2 + \frac{\Delta\omega}{\omega_{ce}} \frac{\left[-(\omega + i\gamma + i\nu_e)^2 + \omega_{ce}^2 - \omega_{pe}^2\right] (\mathbf{k} \cdot \mathbf{E}_{\perp})^2}{\left(1 - \frac{\omega_{ce}^2}{\omega_0^2}\right) \left(1 + \frac{\omega_{ce}}{\omega_0}\right) \left[-(\omega + i\gamma + i\nu_e)^2 - \omega_{pe}^2\right]} \right\} \end{aligned} \right\} \quad (6.8)$$

where $c_s^2 = k_B (T_e + 3T_i) / m_i$ is the ion acoustic speed, ω_L is the Langmuir frequency, and θ is the angle between the high-frequency (Langmuir) plasma wave and the geomagnetic field. The frequencies of the electrostatic wave components have been expressed in terms of a growth-rate, γ , as $\omega = \omega + i\gamma$ and $\Delta\omega = \Delta\omega + i\gamma$. For a heater pump wave directed close to the magnetic field direction almost all the X-mode pump wave power is dispersed in a direction perpendicular to the direction of propagation, thus the $(\mathbf{k} \cdot \mathbf{E}_{\perp})$ terms could be approximated to zero and neglected. The threshold was obtained from

(6.8) by allowing the growth rate γ to tend to zero:

$$E_{Th\parallel}^2 = \frac{4m_e m_i}{e^2 k^2 \cos^2 \theta} \frac{\omega_0^3 \Delta \omega \nu_e \nu_i}{(\omega_0^2 + \omega_{pe}^2)} \left[1 + \frac{(\omega_0^2 - \omega^2)}{\omega_0^2 \nu_e^2} \right] \frac{1 - \frac{\omega_{ce}^2}{\omega_0^2} \cos^2 \theta}{1 - \frac{\omega_{ce}^2}{\omega_0^2}} \quad (6.9)$$

where $\Delta \omega^2 = k^2 c_s^2 - \Delta \omega \nu_i (\omega^2 - \omega^2) / \omega_0 \nu_e$, and ω is the frequency of the Langmuir wave in the interaction region. As expected, this threshold reaches a minimum value when $\omega_0^2 - \omega^2 = 0$ and $\Delta \omega = k c_s$.

For the case of the OTSI, the EM pump wave decays to a pair of oppositely-propagating Langmuir waves and a low-frequency purely-growing mode. Following the same process as above, this resulted in a dispersion relation for the parametric coupling given by (6.10):

$$\begin{aligned} & k_{\parallel}^2 \omega_{ce}^2 [\gamma(\gamma + \nu_i) + k^2 c_s^2] + k_{\perp}^2 \left\{ \omega_{ce} \omega_{ci} \gamma (\gamma + \nu_e) + (\gamma + \nu_e)^2 [\gamma(\gamma + \nu_i) + k^2 c_s^2] \right\} = \dots \\ & \dots + \frac{e^2 \omega_{ce}^2 k^2}{m_e m_i \omega_0^2} \left[(\mathbf{k} \cdot \mathbf{E}_{\parallel})^2 + \frac{i\gamma}{\omega_{ce} \left(1 - \frac{\omega_{ce}^2}{\omega_0^2} \right)} (\mathbf{k} \cdot \mathbf{E}_{\perp})^2 \right] \dots \\ & \dots + \frac{e^2 k^2}{m_e m_i} \left(\frac{1 - \frac{\omega_{ce}^2}{\omega_0^2}}{1 - \frac{\omega_{ce}^2}{\omega_0^2} \cos^2 \theta} \right) \frac{\frac{2\omega_{ce}^2}{\omega_0^2} (\omega_0^2 - \omega_L^2 + \Sigma) \left[(\omega_0 + i\gamma + i\nu_e)^2 + \omega_{pe}^2 \right]}{(\omega^2 - \omega_L^2 + \Sigma)^2 + \omega^2 \nu_e^2} \times \dots \\ & \dots \left\{ (\mathbf{k} \cdot \mathbf{E}_{\parallel})^2 + \frac{\omega_0^2 (i\gamma + i\nu_e) \left[\omega_0^2 - \omega_L^2 + \Sigma + \frac{i\nu_e \omega_{pe}^2 (\omega_0 + i\gamma)}{\omega_0^2 - \omega_{ce}^2} \right]}{\omega_{ce} \left(1 + \frac{\omega_{ce}}{\omega_0} \right) (\omega_0^2 - \omega_L^2 + \Sigma) \left[(\omega_0 + i\gamma + i\nu_e)^2 + \omega_{pe}^2 \right]} (\mathbf{k} \cdot \mathbf{E}_{\perp})^2 \right\} \end{aligned} \quad (6.10)$$

where:

$$\Sigma = \frac{e^2}{m_e^2 \omega_0^2} \frac{1 - \frac{\omega_{ce}^2}{\omega_0^2}}{1 - \frac{\omega_{ce}^2 \cos^2 \theta}{\omega_0^2}} \left[(\mathbf{k} \cdot \mathbf{E}_{\parallel})^2 + \frac{(\mathbf{k} \cdot \mathbf{E}_{\perp})^2}{\left(1 + \frac{\omega_{ce}}{\omega_0} \right) \left(1 - \frac{\omega_{ce}^2}{\omega_0^2} \right)} \right]$$

Here the frequencies of the electrostatic wave components were expressed in terms of growth rate γ as $\omega = \omega + i\gamma$ and $\Delta \omega = i\gamma$. As with the PDI equation, the $(\mathbf{k} \cdot \mathbf{E}_{\perp})$ terms could be approximated to zero and neglected, and the instability threshold obtained by allowing γ to approach zero:

$$E_{Th\parallel}^2 = \frac{2m_e m_i}{e^2} \frac{c_s^2 \omega_0^2}{(\omega_0^2 + \omega_{pe}^2)} \left[(\omega_0^2 - \omega^2) + \frac{\omega_0^2 \nu_e^2}{(\omega_0^2 - \omega^2)} \right] \frac{1 - \frac{\omega_{ce}^2}{\omega_0^2} \cos^2 \theta}{1 - \frac{\omega_{ce}^2}{\omega_0^2}} \quad (6.11)$$

Equations (6.8) and (6.10) provide the thresholds for the parametric decay of an X-mode polarised pump wave into Langmuir waves via the PDI or OTSI. These thresholds require a component of the pump wave E-field (E_{\parallel}) to be aligned with the geomagnetic field. In general it is assumed that E_{\parallel} equals zero in the X-mode heater field due to the small magnitude of E_{\parallel} compared to E_{\perp} as the wave approaches the reflection height (allowing the $(\mathbf{k} \cdot \mathbf{E}_{\perp}) \sim 0$ approximation to be made in the calculations above). However, a non-zero parallel component of the pump field can arise due to the dispersion or refraction of the wave by the ionospheric plasma medium; it is possible that this small component may still be sufficiently large to exceed the threshold for one of the parametric instabilities.

These equations were employed by [Wang et al., 2016] to analyse the thresholds required for the excitement of parametric instabilities during three X-mode heating experiments performed at EISCAT. The first two experiments, as reported by [Blagoveshchenskaya et al., 2014], were performed on 19 October 2012 and 22 October 2013, both from 16-18 UT. The X-mode pump wave was directed along the geomagnetic field direction in each case, with a frequency of 6.2 MHz and an effective radiated power (ERP) of 458 MW on 19 October 2012 and an increased frequency of 7.1 MHz and ERP of 548 MHz on 22 October 2013. Calculation of the parametric instability thresholds revealed that a far lower fraction of the pump wave power was required to be directed along the geomagnetic field direction to excite the PDI compared to the threshold required for excitation of the OTSI. For both sets of experimental conditions, it was found that excitation of the PDI required approximately 3% of the heater ERP to be aligned with the geomagnetic field while the OTSI required approximately 12% of the heater EPR to be aligned with the geomagnetic field. In both experiments, HF-enhanced plasma lines were observed, indicative of excitation of the PDI. The zero-frequency-offset HF-enhanced ion line indicative of OTSI excitation was observed during the 19 October 2012 experiment but not the 22 October 2013 experiment; the effect of the inhomogeneous ionosphere on the wave power distribution may have led to the threshold for this instability being exceeded in the 19 October 2012 case but not the 22 October 2013 case.

The parametric thresholds were calculated for a further experiment performed on 8 March 2010 [Blagoveshchenskaya et al., 2013], in which a field-aligned X-mode pump

wave with frequency 5.423 MHz and an ERP of 123 MW was employed. Under these experimental conditions, parametric instabilities would be excited only when in excess of 50% of the pump wave ERP was directed parallel to the geomagnetic field. As parallel wave fields of this magnitude are highly unlikely for X-mode pump waves, this calculation would suggest that parametric instabilities could not be excited under those conditions. This prediction was confirmed by the lack of any observed HF-enhanced plasma or ion lines during this experiment.

6.3 Numerical Simulation Results

A perfect X-mode polarised EM wave has no component of electric field directed parallel to the geomagnetic field direction. This suggests that it should be impossible for such a wave to excite longitudinal plasma waves, as the parametric decay instability or the oscillating two-stream instability require a non-zero fraction of the pump wave E-field to be along the magnetic field near the reflection height. However, because the ionosphere is an inhomogeneous and dispersive medium, it is possible that during propagation the wave may develop a small parallel field component of sufficient magnitude to exceed the instability threshold. To test this, the full-wave GPU-accelerated FDTD simulation code described in Chapter 3 and [Cannon and Honary, 2015] was used to model the propagation of an X-mode polarised EM wave for the experimental conditions described in Section 6.2 above. The code simulates the interaction of the wave with the background plasma in a fully time-explicit manner, allowing the effect of plasma inhomogeneity and anisotropy on wave propagation to be determined.

The simulation domain was set up as a 2D box aligned with the geomagnetic field and terminated on all sides by a perfectly-matched absorbing layer. The domain dimensions were set as 30.9 km parallel to the field and 15.5 km perpendicular to the field. A continuous pump wave source with X-mode polarisation (E-field perpendicular to the geomagnetic field) was injected from the lower edge of the domain. Pump beam parameters were set to replicate the experiments described in Section 6.2. A linear electron density gradient in the vertical direction was used as a background profile, with a scale

size of 60 km . For each simulation, the density profile was set such that the X-mode reflection height would occur around 28 km above the bottom edge of the simulation domain.

Figure 6.1 shows the E_{\parallel} amplitude developed in the simulation for each set of experimental conditions, averaged over 2×10^5 timesteps ($\sim 2.67\text{ ms}$). The traces are measured along the pump beam direction, and show how the amplitude varies with distance from the lower edge of the simulation domain. In all cases it can be seen that there is a non-zero E_{\parallel} component, due to the dispersive or refractive effects of the inhomogeneous plasma medium on the propagation of the wave. As the pump wave approaches the X-mode reflection height, corresponding to $\omega_{pe}^2 = \omega_0(\omega_0 - \omega_{ce})$, the wave group velocity decreases and a standing wave develops. This leads to a swelling of the amplitude in all components including the parallel field, which can be seen to increase in amplitude with increasing altitude. The parallel field component manages to exceed the amplitude threshold equivalent to $\sim 3\%$ of EPR (indicated in the figure by a dashed line) required for the PDI to proceed in the simulations representing the 22 October 2012 and 19 October 2013 experiments. This only occurs for a narrow range of altitudes below the reflection height, where the field has been amplified by the swelling effect of the standing wave. For the case of the simulation representing the 8 March 2010 experiment, the parallel field amplitude is lower and the required threshold amplitude (equivalent to $\sim 50\%$ of EPR) is not achieved. This agrees well with the experimental observations which report the HF-enhanced plasma line signature indicative of PDI on 19 October 2012 and 22 October 2013 but not on 8 March 2010, and supports the theoretical analysis of Section 6.2. The simulation results suggest that, under certain conditions, the effect of the inhomogeneous plasma background is capable of redirecting a sufficiently large fraction of the X-mode pump energy along the parallel direction for the PDI to be excited.

To excite the OTSI, a parallel E-field amplitude corresponding to $\sim 12\%$ of the pump wave EPR would be required for the 19 October 2012 and 22 October 2013 experiments. The simulation results indicate that this is unlikely to be achieved due to the action of the background plasma density gradient alone. To realize E_{\parallel} fields of this magnitude, more

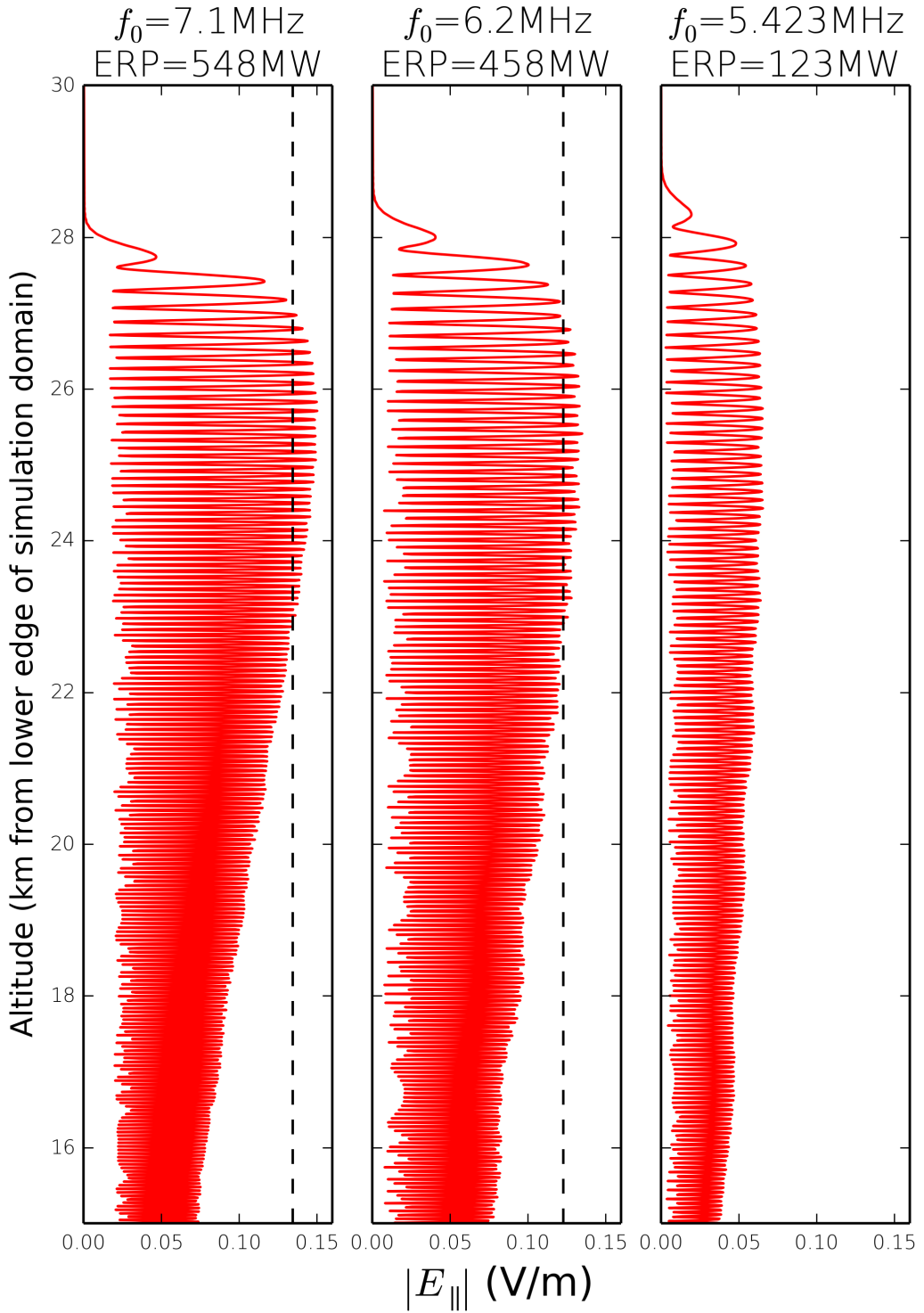


FIGURE 6.1: The simulated E_{\parallel} amplitude around the X-mode reflection height for each set of experimental conditions, averaged over 2×10^5 timesteps (~ 2.67 ms). The field amplitude corresponding to 3% of the pump wave ERP is indicated by a dashed line for the cases of the 19 October 2012 and 22 October 2013 experiments. For the remaining experiment, the PDI threshold corresponded to $\sim 50\%$ of EPR and therefore was much higher than the maximum simulated E-field amplitude shown here.

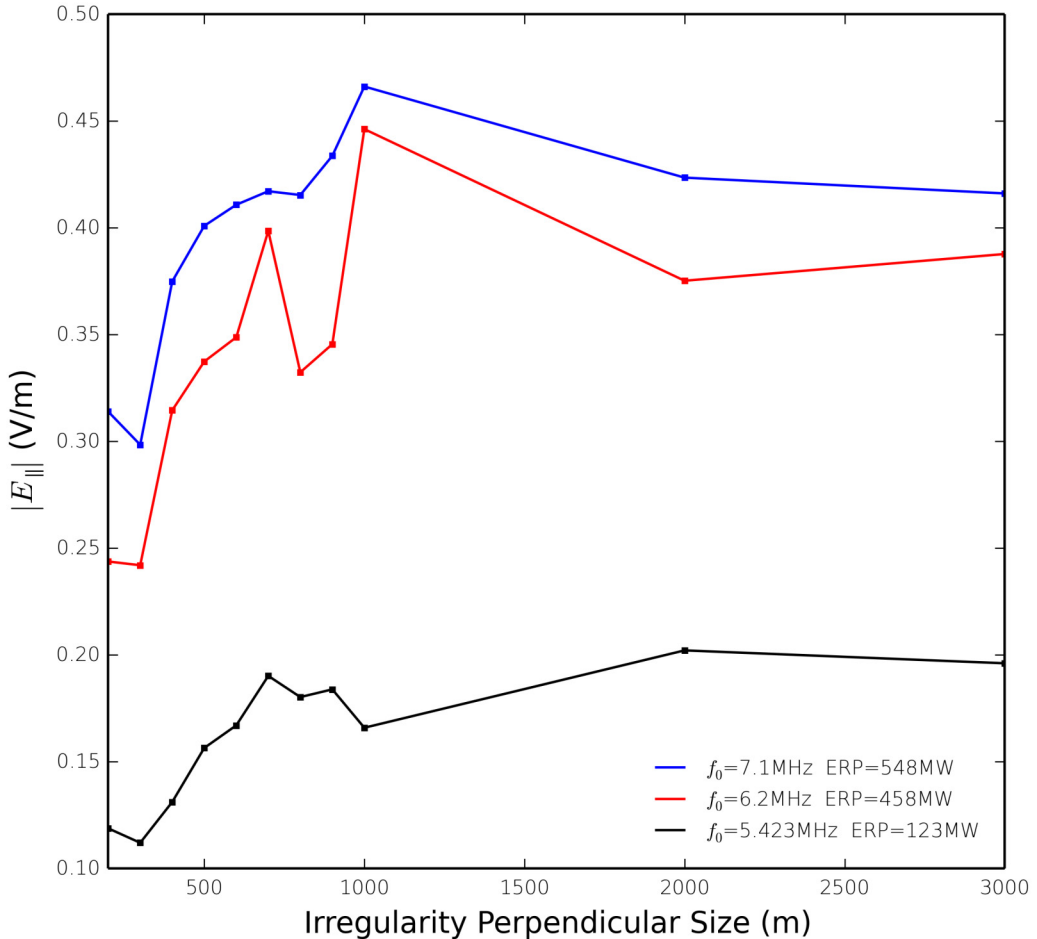


FIGURE 6.2: The variation of maximum simulated E_{\parallel} amplitudes with irregularity perpendicular scale-size when field-aligned density depletions with amplitude 5% of background density were included in the simulation. Results are shown for the pump wave conditions of 22 October 2013 (blue), 19 October 2012 (red) and 8 March 2010 (black). For the cases of the 19 October 2012 and 22 October 2013 experiments, the maximum simulated E_{\parallel} for most irregularity scale sizes is well in excess of the amplitude corresponding to $\sim 12\%$ EPR ($\sim 0.25 \text{ V/m}$) threshold required for the OTSI.

complicated inhomogeneities such as field-aligned density structures must be included in the background density profile. When field-aligned density depletions of maximum amplitude 5% of the background plasma were included in the simulation, this was found to significantly modify the propagation of the X-mode pump wave, with large parallel E-fields developing within the irregularities. Figure 6.2 shows the maximum E_{\parallel} amplitudes recorded in the simulation for a range of irregularity perpendicular scale sizes, for each set of pump wave conditions discussed above. For the cases of the 19 October 2012 and 22 October 2013 experiments, the maximum simulated E_{\parallel} for most irregularity scale sizes is well in excess of the amplitude corresponding to $\sim 12\%$ EPR ($\sim 0.25 \text{ V/m}$)

threshold required for the OTSI, particularly for depletions with perpendicular scale size $\sim 1\text{ km}$. Medium-scale irregularities of this scale have previously been observed to form during X-mode heating (see, for example [Kosch et al., 2007]). The enhancement of the pump electric field through interaction with density irregularities offers a potential mechanism by which sufficient pump energy could be directed along the magnetic field direction to exceed the instability threshold.

6.4 Summary and Conclusions

Until recently, it has been assumed that ground-launched EM waves with X-mode polarisation would be incapable of exciting parametric instabilities such as the PDI or OTSI, since the parametric matching conditions are poorly satisfied over the range of ionospheric plasma accessible to the X-mode wave, and the effects of Landau damping would act to raise the E-field thresholds to prohibitively-high amplitudes. However, as has been discussed in Chapter 5 above, several experiments at EISCAT have observed significant perturbation of the F-region plasma during X-mode heating and the HF-enhancement of plasma and ion lines indicative of the excitation of parametric processes. Further, the numerical simulations presented in Chapter 5 demonstrate that an X-mode pump wave is able to stimulate the growth of a diverse range of geomagnetic-field-aligned electron density irregularities; this effect could be readily explained if the X-mode wave was capable of exciting plasma waves such as the Langmuir wave via a parametric process.

The thresholds for excitation of both the PDI and OTSI were analysed for the case of an X-mode polarised pump wave by [Wang et al., 2016]. The calculations demonstrate that it is possible for these processes to be excited during X-mode heating, provided a minimum fraction of the pump wave power was directed along the geomagnetic field direction. A perfect X-mode wave would have no component of its wave field directed along the geomagnetic field direction. However, the ionosphere is an inhomogeneous, dispersive and anisotropic medium, and it is possible that a non-zero parallel component of the pump field can arise due to the dispersion or refraction of the wave by the

ionospheric plasma. This component may be sufficiently large to exceed the threshold for one of the parametric instabilities.

To test the modification of the pump wave field by the ionospheric plasma, numerical simulations were performed using the full-wave FDTD code developed in Chapter 3. The experimental conditions experienced during EISCAT X-mode heating experiments performed on 19 October 2012, 22 October 2013 and 8 March 2010 were investigated. The simulation results demonstrated that, for the conditions of the 19 October 2012 and 22 October 2013 experiments, the E-field threshold required for the excitation of the PDI was exceeded in a region below the X-mode reflection height. For the conditions of 8 March 2010, the threshold was much higher and hence was not exceeded at any point in the simulation domain. These findings were in good agreement with the experimental observations, which reported HF-enhanced plasma lines (and thus excitation of the PDI) on 19 October 2012 and 22 October 2013, but not 8 March 2010.

Further simulations demonstrated that the presence of medium-scale ($\sim 1\text{ km}$) field-aligned density irregularities around the X-mode reflection altitude could significantly enhance the parallel component of the pump electric field within the irregularities. This provides a potential mechanism by which the high E-field threshold required for the OTSI to proceed could be exceeded by an X-mode wave.

The results presented in this Chapter demonstrate that, under certain experimental conditions, an X-mode wave is capable of exciting parametric instabilities which would lead to the conversion of the EM wave to electrostatic plasma waves, particularly in the region close to the X-mode reflection layer. This process could contribute to the large scale plasma modification recorded during X-mode heating experiments at EISCAT and explain the observation of HF-enhanced plasma and ion lines. Parametric decay of the pump wave to plasma waves could also help explain the excitation of density irregularities by X-mode waves seen in the numerical simulations presented in Chapter 5.

Chapter 7

Summary and Conclusions

Investigating the fundamental mechanics of the ionosphere is an important and active area of Space Physics research. Ionospheric plasma physics is crucial to the communications industry: radio waves must cope with its reflective and refractive properties, satellite signals must pass through it; without a thorough understanding of the manner in which the ionosphere affects electromagnetic wave propagation, technology such as GPS would not be viable. Study of the ionosphere also presents the opportunity to investigate fundamental plasma physics over vast scale lengths and observe the diverse multitude of plasma waves and instabilities the ionosphere is capable of supporting. To this end, the ionosphere has been extensively studied though illumination via high-power, radio-frequency electromagnetic “pump” beams. Artificial ionospheric modification experiments of this type have observed of a wide range of complicated and often nonlinear plasma processes, many of which are highly sensitive to the polarisation, frequency or inclination angle of the incident electromagnetic waves, and all of which are greatly influenced by the background plasma density profile. The mechanisms behind many of these interactions are not fully understood, and would benefit from accurate numerical simulation of the underlying physical processes. Although substantial approximation and assumption is necessary in any simulation code, time-explicit computational experiments can offer a greatly enhanced time and spatial resolution when compared to real ionospheric measurements, allowing fine-detail investigation of wave and plasma behaviour.

In a simulation, the initial conditions can be easily set and controlled; observation of a particular phenomenon is not reliant or contaminated by unpredictable background variability. Numerical calculations allow certain processes to be arbitrarily “switched on/off” by addition or removal of terms from the update equations, meaning that the dominant process responsible for a particular observed feature can be more easily disentangled from the many coupled processes involved in a wave-plasma interaction.

The work presented in this thesis explored the use of a numerical simulation code to investigate several of the exciting but as-yet unexplained plasma phenomena observed during artificial ionospheric modification experiments. Below, the conclusions of the preceding Chapters are summarised. These results have been discussed previously in this thesis, but are repeated here as an overview.

7.1 Development of a GPU-Accelerated FDTD Scheme

Chapter 3 described the development of a high-performance finite-difference time-domain code designed to simulate the response of a dynamic, magnetised and inhomogeneous ionospheric plasma to an incident radio-frequency electromagnetic wave. The effect on wave propagation due to the presence of plasma was introduced through the coupling of Maxwell’s wave equations with the Lorentz equations of motion, with fluid velocity component nodes spatially co-located with the electric field component nodes in the Yee cell and offset in time. Anisotropy was introduced through inclusion of a static externally-applied magnetic field. The scheme built on well-established FDTD techniques with the addition of new time-advancement equations for the plasma fluid density and temperature, allowing perturbations to the multiple-fluid plasma medium to be included in the time-explicit update algorithm. The accuracy and stability of this scheme was analysed and found to be dependent on both the choice of discrete time and space step parameters and the properties of the background plasma.

Accelerating the code using graphical processing unit technology was demonstrated to significantly boost code performance: a dual-GPU implementation of the code was found to achieve a rate of node update almost two orders of magnitude faster than a serial CPU

implementation. Optimisation techniques such as memory coalescence were shown to have a significant effect on the performance of the GPU code, and it was demonstrated that large performance gains could be achieved through careful choice of the GPU work group dimensions.

Numerical validation tests were performed in which FDTD scheme was shown to achieve a good agreement with both the predictions of plasma theory and the results computed using the Tech-X VORPAL 4.2.2 software package, which was used as a benchmark. In particular, the propagation characteristics of ordinary-mode and extraordinary-mode electromagnetic waves in an inhomogeneous, magnetised plasma were accurately replicated, including the formation of a high-amplitude Airy-like standing wave below the O-mode reflection height. The FDTD algorithm was found to run the validation tests considerably more quickly than the benchmark software using equivalent hardware.

Once validated, this code was used to investigate several unexplained plasma processes observed during recent ionospheric modification experiments, including: the influence of variations in the 2D plasma density profile on the O-mode to Z-mode conversion process and the Magnetic Zenith Effect; the excitation of density irregularities by O-mode and X-mode polarised EM waves, and the anomalous heating caused by the associated electrostatic waves; and the excitation of parametric instabilities by X-mode polarised EM waves.

7.2 Simulation of the Radio Window and Magnetic Zenith Effect

The magnitude of artificially-induced plasma perturbation has been observed to depend strongly on the inclination angle of the electromagnetic pump beam. [Honary et al., 2011] proposed that this *Magnetic Zenith Effect* is due to the O-mode to Z-mode conversion process that can occur in the F-region for a narrow range of pump wave inclination angles. However, the greatest plasma perturbations have often been observed to occur not for pump waves inclined at the Spitze angle (at which conversion to the Z-mode

is theoretically most favourable), but for wave angles somewhere between the Spitze and the magnetic field directions (see, for example, [Isham et al., 2005]). This suggests that the conversion process, and the “Z-mode window” for which conversion is likely to occur, may be modified by the presence of 2D inhomogeneities in the ionospheric plasma density close to the interaction region.

In the second body of research, presented in Chapter 4, the FDTD code was used to investigate influence of 2D density variations on the O-mode to Z-mode conversion process, and the contribution of this process to several aspects of the observed Magnetic Zenith Effect. This conversion process has previously been investigated theoretically for the case of a 1D variation in electron density, and in this Chapter was investigated numerically for the case of a 2D electron density profile for the first time.

A varied hierarchy of electron density structures have been observed during heating experiments due to the formation of plasma irregularities of different scales. The FDTD code was used to simulate the O-mode to Z-mode conversion process for three distinct cases of inhomogeneity: large-scale horizontal density slopes representative of large-scale plasma depletions, medium-scale single density-depleted ducts and smaller-scale periodic field-aligned irregularities. The results demonstrated that the window is highly sensitive to the form of the density profile. Addition of a linear horizontal gradient was found to shift the centre of the conversion window away from the Spitze direction and towards the geomagnetic field-aligned direction, with a steeper slope found to produce a greater shift in position. A shift of this kind could explain why the most significant plasma modification has been experimentally observed for pump wave directions between the Spitze and field-aligned angles. Inclusion of a single field-aligned duct-like structure led to a slight shifting of the window towards the vertical direction for irregularities with widths $< 0.1 \text{ km}$. Increasing the irregularity width in the range $0.1 \text{ km} - 2 \text{ km}$ was found to increasingly broaden the Z-mode window, with the angular width of the window for a duct of 1 km width almost three times that of the 1D slope case. The addition of periodic field-aligned density-depleted irregularities had a strong effect on the propagation of the converted Z-mode, with transmitted waves multiply scattered

by adjacent irregularities resulting in the propagation of significant E-field amplitude beyond the O-mode reflection height for irregularity widths $> 0.2\text{ km}$.

The contribution of the O-mode to Z-mode conversion process to the large-scale modification of ionospheric plasma was investigated by comparing simulations in which the Z-mode wave was allowed to reflect back towards the interaction region to simulations in which the Z-mode was absorbed before reflection by an artificial PML. Allowing the Z-mode wave to reflect was found to cause resonant enhancement of the electric field and a substantial increase in electron temperature enhancement around the interaction region. For the case of a vertical electron density profile and a Spitze-directed wave, electron temperature enhancement was found to be more than a factor of 2 greater in the Z-mode reflection-allowed simulation than in the reflection-suppressed simulation. The O-mode to Z-mode conversion process was shown to result in an angular dependence in electron temperature enhancement: the angles for which conversion of the pump wave to the Z-mode were more favourable were found to correspond to greater temperature gains, in the case that Z-mode reflection was allowed. In addition, excitement of small-scale field-aligned density irregularities was found to occur most favourably for pump beams directed along the Spitz direction. The inclusion of 2D inhomogeneities was found to further influence the variation of electron plasma perturbation with pump wave angle.

The simulation results demonstrated that the presence of 2D density inhomogeneities around the O-mode reflection height can significantly modify the angular shape of the Z-mode conversion window, and that the excitement and subsequent reflection of Z-mode waves can lead to substantial enhancements in artificially-induced plasma perturbations. In combination, these processes cause the magnitude of thermal plasma perturbation to depend strongly on both the pump wave inclination angle and the 2D electron density profile. This offers a potential mechanism behind several features of the observed Magnetic Zenith Effect.

7.3 Simulation of Density Irregularity Growth During O-Mode and X-Mode Heating

Anomalous processes involving the excitation of electrostatic plasma waves are a key component of F-region ionospheric modification when using O-mode waves. These processes have been shown to be particularly sensitive to the proximity of the pump wave frequency to harmonics of the electron gyrofrequency (see, for example, [Stubbe et al., 1994]). Recent ionospheric heating experiments performed at EISCAT using X-mode waves have also observed several anomalous plasma effects previously associated with O-mode waves only, including large-scale temperature enhancement and generation of field-aligned density irregularities (see, for example, [Blagoveshchenskaya et al., 2015]). In the third body of research, presented in Chapter 5, the FDTD code was employed to simulate ionospheric modification experiments using both O-mode and X-mode polarised pump waves of varying frequencies, with the aim of investigating several of the unexplained plasma phenomena recently observed both during X-mode heating experiments and during experiments in which the EM pump wave frequency was varied close to one of the electron gyroharmonics.

Both O-mode and X-mode polarised pump waves were found capable of exciting several bands of field-aligned density-depleted irregularities, predominantly located at points where the background electron plasma frequency was closely matched with a harmonic of the electron cyclotron frequency. These irregularities were often alike in spatial distribution and developmental timescale to the irregularities found to grow at the upper-hybrid resonance height during O-mode simulations, suggesting that a similar formation mechanism was at work. Increasing the pump wave frequency allowed a greater range of the background plasma to be accessed and enabled the excitement of additional bands of density structures. Comparing simulations in which ion motion was allowed or suppressed indicated that a parametric process was responsible for the production of these irregularities, possibly involving parametric excitement of Langmuir plasma waves by the EM pump wave, and their subsequent decay to perpendicularly-propagating electrostatic waves such as Bernstein or upper-hybrid modes. A mechanism such as this would

explain why the bands of simulated irregularities appeared to be more closely associated with background plasma properties than pump wave parameters, and tended to occur close to the altitudes where the local Langmuir frequency was close to the frequency of a Bernstein wave mode.

The numerical code was modified to take into account an estimation of the electrostatic fields associated with any excited density irregularities. Inclusion of these fields as a source term in the temperature update equation was shown to result in a greater increase in the simulated electron temperature than was produced in simulations performed where only the FDTD electromagnetic E-fields were considered. These temperature enhancements were found to be in reasonably good agreement with the anomalous heating predicted using the equations of [Robinson, 1989].

Plasma-wave driven anomalous heating processes associated with the growth of structures of this nature could potentially contribute to anomalous electron heating and explain the observations of both significant temperature enhancements and the growth of field-aligned density irregularities during X-mode experiments at EISCAT. The growth of irregularities close to the third gyroharmonic height could also explain the observed asymmetry in anomalous absorption observed by [Stubbe et al., 1994] during O-mode experiments.

7.4 Comparison of Simulated X-mode Wave Fields with Theoretical Parametric Instability Thresholds

The thresholds for excitation of both the parametric decay instability and oscillating two-stream instability were analysed for the case of an X-mode polarised pump wave by [Wang et al., 2016]. The calculations demonstrated that it is possible for these processes to be excited during X-mode heating, provided a minimum fraction of the pump wave power was directed along the geomagnetic field direction. A perfect X-mode wave would have no component of its wave field directed along this direction. However, the ionosphere is an inhomogeneous, dispersive and anisotropic medium, and

it is possible that a non-zero parallel component of the pump field can arise due to the dispersion or refraction of the wave by the ionospheric plasma. This component may be sufficiently large to exceed the threshold for one of the parametric instabilities.

In the final body of research, presented in Chapter 6, the FDTD code was used to simulate the modification of the pump wave field by the ionospheric plasma for the experimental conditions experienced during EISCAT X-mode heating experiments performed on 19 October 2012, 22 October 2013 and 8 March 2010. The simulation results demonstrated that, for the conditions of the 19 October 2012 and 22 October 2013 experiments, the theoretical E-field threshold required for the excitation of the PDI was exceeded in a region below the X-mode reflection height. For the conditions of 8 March 2010, the threshold was much higher and hence was not exceeded at any point in the simulation domain. These findings were in good agreement with the experimental observations, which reported HF-enhanced plasma lines (and thus excitation of the PDI) on 19 October 2012 and 22 October 2013, but not 8 March 2010.

Further simulations demonstrated that the presence of medium-scale ($\sim 1\text{ km}$) field-aligned density irregularities around the X-mode reflection altitude could significantly enhance the parallel component of the pump electric field within the irregularities. This provides a potential mechanism by which the high E-field threshold required for the OTSI to proceed could be exceeded by an X-mode wave.

The simulation results demonstrated that, under certain experimental conditions, an X-mode wave is capable of exciting parametric instabilities which would lead to the conversion of the EM wave to electrostatic plasma waves, particularly in the region close to the X-mode reflection layer. This process could contribute to the large scale plasma modification recorded during X-mode heating experiments at EISCAT and explain the observation of HF-enhanced plasma and ion lines. Parametric decay of the pump wave to plasma waves could also help explain the excitation of density irregularities by X-mode waves seen in the numerical simulations presented in Chapter 5.

7.5 Further Investigation

The scientific investigations described in this thesis focus on several specific plasma phenomena observed during artificial ionospheric modification experiments, with each area of investigation chosen in the hope that the numerical simulations could contribute to an area of active interest to the ionospheric research community. These studies consider only a fraction of the many and varied plasma processes observed over decades of experimental study in this field, and there are many interesting topics around which future investigations using this numerical code could be based. Possible areas of future study may include (but are by no means limited to):

- The numerical investigation of the Stimulated Electron Emission (SEE) spectra commonly observed during heating experiments (see, for example, [Leyser et al., 1990] for a review of SEE observations). Many SEE features are thought to be formed via the excitation of ES plasma waves close to the interaction layer by the EM pump wave. These plasma waves subsequently decay to frequency-shifted EM waves that can be detected by ground-based spectral analysers as peaks or broad continua offset from the pump wave input frequency. The exact mechanisms behind many spectral features are not fully understood, and it would be interesting to use the code to attempt to reproduce a SEE spectrum, and investigate how perturbing the initial plasma conditions would translate to changes in the identity and characteristics of the observed SEE features. Simulation of SEE in conjunction with the simulation of perturbations to the plasma density would allow the theory that certain SEE features are associated with the growth of density structures to be tested (for example, the downshifted maximum feature is thought to be linked to the formation of small-scale irregularities close to the upper-hybrid resonance layer).
- An extension of the work described in Chapter 5 to directly and in greater detail investigate the anomalous absorption of the pump wave caused by the growth of density irregularities, and how this varies with pump wave frequency (particularly

when the frequency is close to an electron gyroharmonic). The simulations described in Chapter 5 employ somewhat-idealised and simplified initial conditions; it would be desirable to repeat these using parameters that replicate the conditions of the experiments described in [Stubbe et al., 1994] and others as accurately as possible, such that the numerical results could be more readily compared to the experimental observations. It would also be of interest to perform these investigations at far greater spatial resolution, such that the excitation and trapping of plasma modes within density irregularities, the effect of such a process on absorption, and its dependence on the proximity of pump frequency to a gyroharmonic, could be simulated accurately.

- An investigation into the possibility of enhanced heating of the ionospheric top-side due to O-mode to Z-mode conversion. Heating of the top-side has been observed to be sensitive to the inclination angle of an O-mode pump wave by [Kosch et al., 2011], and may be linked to the O-to-Z-mode conversion process. In Chapter 4, it was demonstrated numerically that the reflected Z-mode, when encountering the resonance close to the O-mode reflection layer, enhances the local electric field and leads to an increase in the electron temperature. It would be of interest to investigate whether a corresponding process may occur on the ionospheric top-side, for the case that O-mode to Z-mode conversion occurs sufficiently close to the ionospheric peak that the Z-mode wave does not reflect but propagates beyond the peak and can access the resonance layer in top-side.

Further development to the numerical code would also be desirable, and would aid future investigations. These improvements would incur considerable additional computational costs, but would allow more accurate and more powerful scientific simulations to be performed. As has been mentioned in the preceding Chapters, it would be useful to augment future versions of the code with realistic plasma source and loss mechanisms, such as ionisation and recombination. These would help maintain steady-state background conditions and result in more accurate simulation of the interactions between the charged plasma components and the neutral background. Ideally, these additions would model the local ionospheric chemistry, and would allow the impact of different

neutral components and compositions on artificially-induced plasma perturbations to be investigated. The code used here considers only a static, uniform background magnetic field; in future it would be of interest to allow this to vary both spatially and temporally, and to allow any perturbations to this field due to changes in the plasma distribution to be considered and incorporated into the FDTD update algorithm. Finally, it would be particularly desirable to include either a hybrid or full particle-in-cell mechanism in the simulation algorithm. This approach would be non-trivial to implement on GPU hardware, but would potentially allow kinetic phenomena not adequately described by the current fluid treatment to be accurately simulated, and in particular would enhance the ability of the code to simulate electrostatic plasma wave modes.

Bibliography

- [Antani et al., 1996] Antani, S. N., Kaup, D. J., and Rao, N. N. (1996), Excitation of upper hybrid waves from ordinary-mode electromagnetic waves via density gradient in the ionosphere, *Journal of Geophysical Research: Space Physics*, 101(A12), 27035–27041, doi:10.1029/96JA02634.
- [Baumjohann and Treumann, 1996] Baumjohann, W. and Treumann, R. A. (1996). *Basic space plasma physics*. Imperial College Press, London.
- [Berenger, 1994] Berenger, J. P. (1994), A perfectly matched layer for the absorption of electromagnetic waves, *Journal of Computational Physics*, 114(2), 185–200, doi:10.1006/jcph.1994.1159.
- [Berenger, 2002] Berenger, J. P. (2002), Finite-difference computation of VLF-LF propagation in the earth-ionosphere waveguide, *Annales Des Télécommunications*, 57(11), 1059–1090, doi:10.1007/BF02999454.
- [Bilitza et al., 2014] Bilitza, D., Altadill, D., Zhang, Y., Mertens, C., Truhlik, V., Richards, P., McKinnell, L.-A., and Reinisch, B. (2014), The international reference ionosphere 2012 a model of international collaboration, *Journal of Space Weather and Space Climate*, 4, A07, doi:10.1051/swsc/2014004.
- [Birdsall and Langdon, 1985] Birdsall, C. K. and Langdon, A. B. (1985). *Plasma Physics via Computer Simulation*. McGraw-Hill, New York.
- [Blagoveshchenskaya et al., 2014] Blagoveshchenskaya, N. F., Borisova, T. D., Kosch, M., Sergienko, T., Brändström, U., Yeoman, T. K., and Häggström, I. (2014),

- Optical and ionospheric phenomena at EISCAT under continuous X-mode HF pumping, *Journal of Geophysical Research: Space Physics*, 119(12), 10483–10498, doi:10.1002/2014JA020658.
- [Blagoveshchenskaya et al., 2015] Blagoveshchenskaya, N. F., Borisova, T. D., Yeoman, T. K., Häggström, I., and Kalishin, A. S. (2015), Modification of the high latitude ionosphere F region by X-mode powerful HF radio waves: Experimental results from multi-instrument diagnostics, *Journal of Atmospheric and Solar-Terrestrial Physics*, 135, 50–63, doi:10.1016/j.jastp.2015.10.009.
- [Blagoveshchenskaya et al., 2013] Blagoveshchenskaya, N. F., Borisova, T. D., Yeoman, T. K., Rietveld, M. T., Häggström, I., and Ivanova, I. M. (2013), Plasma modifications induced by an X-mode HF heater wave in the high latitude F region of the ionosphere, *Journal of Atmospheric and Solar-Terrestrial Physics*, 105–106, 231–244, doi:10.1016/j.jastp.2012.10.001.
- [Blagoveshchenskaya et al., 2011] Blagoveshchenskaya, N. F., Borisova, T. D., Yeoman, T. K., Rietveld, M. T., Ivanova, I. M., and Baddeley, L. J. (2011), Artificial small-scale field-aligned irregularities in the high latitude F region of the ionosphere induced by an X-mode HF heater wave, *Geophysical Research Letters*, 38(8), L08802, doi:10.1029/2011GL046724.
- [Boris, 1970] Boris, J. P. (1970). The acceleration calculation from a scalar potential. Technical Report MATT-152, Plasma Physics Laboratory, Princeton University.
- [Borisov and Robinson, 2003] Borisov, N. and Robinson, T. (2003), Transformation of an EM pump wave into upper hybrid resonance oscillations in striations in a vertically inhomogeneous ionosphere, *Physics Letters A*, 315(1–2), 126–135, doi:10.1016/S0375-9601(03)00978-2.
- [Brekke, 1997] Brekke, A. (1997). *Physics of the upper polar atmosphere*. Wiley-Praxis.

- [Bryers et al., 2013] Bryers, C. J., Kosch, M. J., Senior, A., Rietveld, M. T., and Yeoman, T. K. (2013), The thresholds of ionospheric plasma instabilities pumped by high-frequency radio waves at EISCAT, *Journal of Geophysical Research: Space Physics*, 118(11), 7472–7481, doi:10.1002/2013JA019429.
- [Budden, 1961] Budden, K. G. (1961). *Radio Waves in the Ionosphere: the mathematical theory of the reflection of radio waves from stratified ionised layers*. Cambridge University Press.
- [Cannon and Honary, 2015] Cannon, P. D. and Honary, F. (2015), A GPU-accelerated finite-difference time-domain scheme for electromagnetic wave interaction with plasma, *IEEE Transactions on Antennas and Propagation*, 63(7), 3042–3054, doi:10.1109/TAP.2015.2423710.
- [Cannon et al., 2016] Cannon, P. D., Honary, F., and Borisov, N. (2016), Two-dimensional numerical simulation of O-mode to Z-mode conversion in the ionosphere, *Journal of Geophysical Research: Space Physics*, 121(3), 2755–2782, doi:10.1002/2015JA022105.
- [Chen, 1984] Chen, F. F. (1984). *Introduction to Plasma Physics and Controlled Fusion*. Plenum Press, New York, 2nd edition.
- [Chen et al., 1998] Chen, Q., Katsurai, M., and Aoyagi, P. H. (1998), An FDTD formulation for dispersive media using a current density, *IEEE Transactions on Antennas and Propagation*, 46(11), 1739–1746, doi:10.1109/8.736632.
- [Courant et al., 1967] Courant, R., Friedrichs, K., and Lewy, H. (1967), On the partial difference equations of mathematical physics, *IBM Journal of Research and Development*, 11(2), 215–234, doi:10.1147/rd.112.0215.
- [Cummer, 1997] Cummer, S. A. (1997), An analysis of new and existing FDTD methods for isotropic cold plasma and a method for improving their accuracy, *IEEE Transactions on Antennas and Propagation*, 45(3), 392–400, doi:10.1109/8.558654.

- [Das and Fejer, 1979] Das, A. and Fejer, J. (1979), Resonance instability of small-scale field-aligned irregularities, *Journal of Geophysical Research: Space Physics*, 84(A11), 6701–6704, doi:10.1029/JA084iA11p06701.
- [Dhillon and Robinson, 2005] Dhillon, R. S. and Robinson, T. R. (2005), Observations of time dependence and aspect sensitivity of regions of enhanced UHF backscatter associated with RF heating, *Annales Geophysicae*, 23(1), 75–85, doi:10.5194/angeo-23-75-2005.
- [Djuth et al., 1987] Djuth, F. T., Thidé, B., Ierkic, H. M., and Sulzer, M. P. (1987), Large F-region electron-temperature enhancements generated by high-power HF radio waves, *Geophysical Research Letters*, 14(9), 953–956, doi:10.1029/GL014i009p00953.
- [Dysthe et al., 1982] Dysthe, K. B., Mjølhus, E., Pécseli, H., and Rypdal, K. (1982), Thermal cavitons, *Physica Scripta*, 1982(T2B), 548–559, doi:10.1088/0031-8949/1982/T2B/040.
- [Eliasson and Stenflo, 2008] Eliasson, B. and Stenflo, L. (2008), Full-scale simulation study of the initial stage of ionospheric turbulence, *Journal of Geophysical Research: Space Physics*, 113(A2), A02305, doi:10.1029/2007JA012837.
- [Engquist and Majda, 1977] Engquist, B. and Majda, A. (1977), Absorbing boundary conditions for the numerical simulation of waves, *Mathematics of Computation*, 31(139), 629–651, doi:10.1090/S0025-5718-1977-0436612-4.
- [Fejer, 1979] Fejer, J. A. (1979), Ionospheric modification and parametric instabilities, *Reviews of Geophysics*, 17(1), 135–153, doi:10.1029/RG017i001p00135.
- [Ginzburg, 1970] Ginzburg, V. L. (1970). *The propagation of electromagnetic waves in plasmas*. Pergamon Press, New York, 2nd edition.
- [Gondarenko et al., 2002] Gondarenko, N. A., Guzdar, P. N., Milikh, G. M., and Os-sakow, S. L. (2002), Modification of the electron density profile near the upper hybrid layer during radio wave heating of the ionosphere, *Geophysical Research Letters*, 29(11), 5–1–5–4, doi:10.1029/2002GL014934.

- [Gondarenko et al., 2003] Gondarenko, N. A., Guzdar, P. N., Ossakow, S. L., and Bernhardt, P. A. (2003), Linear mode conversion in inhomogeneous magnetized plasmas during ionospheric modification by HF radio waves, *Journal of Geophysical Research: Space Physics*, 108(A12), 1470, doi:10.1029/2003JA009985.
- [Gondarenko et al., 2005] Gondarenko, N. A., Ossakow, S. L., and Milikh, G. M. (2005), Generation and evolution of density irregularities due to self-focusing in ionospheric modifications, *Journal of Geophysical Research: Space Physics*, 110(A9), A09304, doi:10.1029/2005JA011142.
- [Gondarenko et al., 2006] Gondarenko, N. A., Ossakow, S. L., and Milikh, G. M. (2006), Nonlinear evolution of thermal self-focusing instability in ionospheric modifications at high latitudes: Aspect angle dependence, *Geophysical Research Letters*, 33(16), L16104, doi:10.1029/2006GL025916.
- [Gordon and Carlson, 1974] Gordon, W. E. and Carlson, H. C. (1974), Arecibo heating experiments, *Radio Science*, 9(11), 1041–1047, doi:10.1029/RS009i011p01041.
- [Graham and Fejer, 1976] Graham, K. N. and Fejer, J. A. (1976), Anomalous radio wave absorption due to ionospheric heating effects, *Radio Science*, 11(12), 1057–1063, doi:10.1029/RS011i012p01057.
- [Gurevich et al., 2002] Gurevich, A., Fremouw, E., Secan, J., and Zybin, K. (2002), Large scale structuring of plasma density perturbations in ionospheric modifications, *Physics Letters A*, 301(3–4), 307–314, doi:10.1016/S0375-9601(02)00901-5.
- [Gurevich et al., 1998] Gurevich, A., Hagfors, T., Carlson, H., Karashtin, A., and Zybin, K. (1998), Self-oscillations and bunching of striations in ionospheric modifications, *Physics Letters A*, 239(6), 385–392, doi:10.1016/S0375-9601(98)00006-1.
- [Gurevich, 1978] Gurevich, A. V. (1978). *Nonlinear Phenomena in the Ionosphere*. Springer Berlin Heidelberg, 1st edition.
- [Gurevich et al., 2001] Gurevich, A. V., Carlson, H., and Zybin, K. P. (2001), Nonlinear structuring and southward shift of a strongly heated region in ionospheric modification, *Physics Letters A*, 288(3–4), 231–239, doi:10.1016/S0375-9601(01)00516-3.

- [Gurevich et al., 1995] Gurevich, A. V., Lukyanov, A. V., and Zybin, K. P. (1995), Stationary state of isolated striations developed during ionospheric modification, *Physics Letters A*, 206(3–4), 247–259, doi:10.1016/0375-9601(95)00595-T.
- [Gurevich et al., 2005] Gurevich, A. V., Zybin, K. P., and Carlson, H. C. (2005), Magnetic-zenith effect, *Radiophysics and Quantum Electronics*, 48(9), 686–699, doi:10.1007/s11141-005-0113-7.
- [Hawkins and Kallman, 1993] Hawkins, R. J. and Kallman, J. S. (1993), Linear electronic dispersion and finite-difference time-domain calculations: a simple approach, *Journal of Lightwave Technology*, 11(11), 1872–1874, doi:10.1109/50.251186.
- [Honary et al., 2011] Honary, F., Borisov, N., Beharrell, M., and Senior, A. (2011), Temporal development of the magnetic zenith effect, *Journal of Geophysical Research: Space Physics*, 116(A6), A06309, doi:10.1029/2010JA016029.
- [Honary et al., 1995] Honary, F., Stocker, A. J., Robinson, T. R., Jones, T. B., and Stubbe, P. (1995), Ionospheric plasma response to hf radio waves operating at frequencies close to the third harmonic of the electron gyrofrequency, *Journal of Geophysical Research: Space Physics*, 100(A11), 21489–21501, doi:10.1029/95JA02098.
- [Honary et al., 1993] Honary, F., Stocker, A. J., Robinson, T. R., Jones, T. B., Wadh, N. M., Stubbe, P., and Kopka, H. (1993), EISCAT observations of electron temperature oscillations due to the action of high power HF radio waves, *Journal of Atmospheric and Terrestrial Physics*, 55(10), 1433–1448, doi:10.1016/0021-9169(93)90109-C.
- [Hu and Cummer, 2006] Hu, W. and Cummer, S. (2006), An FDTD model for low and high altitude lightning-generated EM fields, *IEEE Transactions on Antennas and Propagation*, 54(5), 1513–1522, doi:10.1109/TAP.2006.874336.
- [Hunsucker and Hargreaves, 2002] Hunsucker, R. D. and Hargreaves, J. K. (2002). *The high-latitude ionosphere and its effects on radio propagation*. Cambridge atmospheric and space science series. Cambridge University Press.

- [Inan and Golkowski, 2011] Inan, U. S. and Golkowski, M. (2011). *Principles of Plasma Physics for Engineers and Scientists*. Cambridge University Press.
- [Inhester et al., 1981] Inhester, B., Das, A. C., and Fejer, J. A. (1981), Generation of small-scale field-aligned irregularities in ionospheric heating experiments, *Journal of Geophysical Research: Space Physics*, 86(A11), 9101–9106, doi:10.1029/JA086iA11p09101.
- [Isham et al., 2005] Isham, B., Hagfors, T., Khudukon, B. Z., Yurik, Y., Tereshchenko, E. D., Rietveld, M. T., Belyey, V., Grill, M., La Hoz, C., Brekke, A., and Heinselman, C. (2005), An interferometer experiment to explore the aspect angle dependence of stimulated electromagnetic emission spectra, *Annales Geophysicae*, 23(1), 55–74, doi:10.5194/angeo-23-55-2005, 2005.
- [Joseph et al., 1991] Joseph, R. M., Hagness, S. C., and Taflove, A. (1991), Direct time integration of Maxwell's equations in linear dispersive media with absorption for scattering and propagation of femtosecond electromagnetic pulses, *Optics Letters*, 16(18), 1412–1414, doi:10.1364/OL.16.001412.
- [Kelley, 1989] Kelley, M. C. (1989). *The Earth's Ionosphere*. International Geophysics Series. Elsevier Academic Press, 2nd edition.
- [Kelley et al., 1995] Kelley, M. C., Arce, T. L., Salowey, J., Sulzer, M., Armstrong, W. T., Carter, M., and Duncan, L. (1995), Density depletions at the 10-m scale induced by the Arecibo heater, *Journal of Geophysical Research: Space Physics*, 100(A9), 17367–17376, doi:10.1029/95JA00063.
- [Kim and Park, 2012] Kim, K.-H. and Park, Q.-H. (2012), Overlapping computation and communication of three-dimensional FDTD on a GPU cluster, *Computational Physics Communications*, 183(11), 2364–2369, doi:10.1016/j.cpc.2012.06.003.
- [Kivelson and Russell, 1995] Kivelson, M. G. and Russell, C. T. (1995). *Introduction to space physics*. Cambridge University Press.

- [Kosch et al., 2000] Kosch, M., Rietveld, M. T., Hagfors, T., and Leyser, T. B. (2000), High-latitude HF-induced airglow displaced equatorwards of the pump beam, *Geophysical Research Letters*, 27(17), 2817–2820, doi:10.1029/2000GL003754.
- [Kosch et al., 2011] Kosch, M. J., Mjølhus, E., Ashrafi, M., Rietveld, M. T., Yeoman, T., and Nozawa, S. (2011), Angular dependence of pump-induced bottomside and topside ionospheric plasma turbulence at EISCAT, *Journal of Geophysical Research: Space Physics*, 116(A3), A03322, doi:10.1029/2010JA016014.
- [Kosch et al., 2007] Kosch, M. J., Pedersen, T., Mishin, E., Starks, M., Gerken-Kendall, E., Sentman, D., Oyama, S., and Watkins, B. (2007), Temporal evolution of pump beam self-focusing at the High-Frequency Active Auroral Research Program, *Journal of Geophysical Research: Space Physics*, 112(A8), A08304, doi:10.1029/2007JA012264.
- [Kuzuoglu and Mittra, 1996] Kuzuoglu, M. and Mittra, R. (1996), Mesh truncation by perfectly matched anisotropic absorbers in the finite-element method, *Microwave and Optical Technology Letters*, 12(3), 136–140, doi:10.1002/(SICI)1098-2760(19960620)12:3;136::AID-MOP5;3.0.CO;2-I.
- [Landau, 1946] Landau, L. (1946), On the vibrations of the electronic plasma, *J. Phys. (USSR)*, 10, 25–34, *English translation in JETP* 16, 574.
- [Lee and Kalluri, 1999] Lee, J. H. and Kalluri, D. K. (1999), Three-dimensional FDTD simulation of electromagnetic wave transformation in a dynamic inhomogeneous magnetized plasma, *IEEE Transactions on Antennas and Propagation*, 47(7), 1146–1151, doi:10.1109/8.785745.
- [Leyser, 1991] Leyser, T. B. (1991), Parametric interaction between upper hybrid and lower hybrid waves in heating experiments, *Geophysical Research Letters*, 18(3), 408–411, doi:10.1029/91GL00136.
- [Leyser and Nordblad, 2009] Leyser, T. B. and Nordblad, E. (2009), Self-focused radio frequency L wave pumping of localized upper hybrid oscillations in

- high-latitude ionospheric plasma, *Geophysical Research Letters*, 36(24), L24105, doi:10.1029/2009GL041438.
- [Leyser et al., 1990] Leyser, T. B., Thidé, B., Derblom, H., Hedberg, A., Lundborg, B., Stubbe, P., and Kopka, H. (1990), Dependence of stimulated electromagnetic emission on the ionosphere and pump wave, *Journal of Geophysical Research: Space Physics*, 95(A10), 17233–17244, doi:10.1029/JA095iA10p17233.
- [Leyser et al., 1989] Leyser, T. B., Thidé, B., Derblom, H., Hedberg, A., Lundborg, B., Stubbe, P., Kopka, H., and Rietveld, M. T. (1989), Stimulated electromagnetic emission near electron cyclotron harmonics in the ionosphere, *Physics Review Letters*, 63(11), 1145–1147, doi:10.1103/PhysRevLett.63.1145.
- [Livesey et al., 2012] Livesey, M., Stack, J. F., Costen, F., Nanri, T., Nakashima, N., and Fujino, S. (2012), Development of a CUDA implementation of the 3D FDTD method, *IEEE Antennas and Propagation Magazine*, 54(5), 186–195, doi:10.1109/MAP.2012.6348145.
- [Luebbers and Hunsberger, 1992] Luebbers, R. J. and Hunsberger, F. (1992), FDTD for Nth-order dispersive media, *IEEE Transactions on Antennas and Propagation*, 40(11), 1287–1301, doi:10.1109/8.202707.
- [Luebbers et al., 1991] Luebbers, R. J., Hunsberger, F., and Kunz, K. S. (1991), A frequency-dependent finite-difference time-domain formulation for transient propagation in plasma, *IEEE Transactions on Antennas and Propagation*, 39(1), 29–34, doi:10.1109/8.64431.
- [Lundborg and Thidé, 1986] Lundborg, B. and Thidé, B. (1986), Standing wave pattern of HF radio waves in the ionospheric reflection region: 2. applications, *Radio Science*, 21(3), 486–500, doi:10.1029/RS021i003p00486.
- [Meltz et al., 1974] Meltz, G., Holway, L. H., and Tomljanovich, N. M. (1974), Ionospheric heating by powerful radio waves, *Radio Science*, 9(11), 1049–1063, doi:10.1029/RS009i011p01049.

- [Mjølhus, 1984] Mjølhus, E. (1984), Coupling to Z mode near critical angle, *Journal of Plasma Physics*, 31(01), 7–28, doi:10.1017/S0022377800001392.
- [Mjølhus, 1990] Mjølhus, E. (1990), On linear conversion in a magnetized plasma, *Radio Science*, 25(6), 1321–1339, doi:10.1029/RS025i006p01321.
- [Mjølhus and Flå, 1984] Mjølhus, E. and Flå, T. (1984), Direct access to plasma resonance in ionospheric radio experiments, *Journal of Geophysical Research: Space Physics*, 89(A6), 3921–3928, doi:10.1029/JA089iA06p03921.
- [Mur, 1981] Mur, G. (1981), Absorbing boundary conditions for the finite-difference approximation of the time-domain electromagnetic-field equations, *IEEE Transactions on Electromagnetic Comparability*, EMC-23(4), 377–382, doi:10.1109/TEMC.1981.303970.
- [Nieter and Cary, 2004] Nieter, C. and Cary, J. R. (2004), VORPAL: a versatile plasma simulation code, *Journal of Computational Physics*, 196(2), 448–473, doi:10.1016/j.jcp.2003.11.004.
- [Nordblad and Leyser, 2010] Nordblad, E. and Leyser, T. B. (2010), Ray tracing analysis of L mode pumping of the ionosphere, with implications for the magnetic zenith effect, *Annales Geophysicae*, 28(9), 1749–1759, doi:10.5194/angeo-28-1749-2010.
- [Parker, 1958] Parker, E. N. (1958), Dynamics of the Interplanetary Gas and Magnetic Fields., *Astrophysical Journal*, 128, 664–676, doi:10.1086/146579.
- [Pedersen et al., 2003] Pedersen, T. R., McCarrick, M., Gerken, E., Selcher, C., Sentman, D., Carlson, H. C., and Gurevich, A. (2003), Magnetic zenith enhancement of HF radio-induced airglow production at HAARP, *Geophysical Research Letters*, 30(4), 1169, doi:10.1029/2002GL016096.
- [Press et al., 1992] Press, W. H., Teukolsky, S. A., Vetterling, W. T., and Flannery, B. P. (1992). *Numerical Recipes in C: The Art of Scientific Computing*. Cambridge University Press, 2nd edition.

- [Rao and Kaup, 1990] Rao, N. N. and Kaup, D. J. (1990), Upper hybrid mode conversion and resonance excitation of Bernstein modes in ionospheric heating experiments, *Journal of Geophysical Research: Space Physics*, 95(A10), 17245–17252, doi:10.1029/JA095iA10p17245.
- [Rietveld et al., 1993] Rietveld, M., Kohl, H., Kopka, H., and Stubbe, P. (1993), Introduction to ionospheric heating at Tromsø – I. Experimental overview, *Journal of Atmospheric and Terrestrial Physics*, 55(4–5), 577–599, The Fifth International EISCAT Workshop, doi:10.1016/0021-9169(93)90007-L.
- [Rietveld et al., 2003] Rietveld, M. T., Kosch, M. J., Blagoveshchenskaya, N. F., Kornienko, V. A., Leyser, T. B., and Yeoman, T. K. (2003), Ionospheric electron heating, optical emissions, and striations induced by powerful HF radio waves at high latitudes: Aspect angle dependence, *Journal of Geophysical Research: Space Physics*, 108(A4), 1141, doi:10.1029/2002JA009543.
- [Robinson, 1989] Robinson, T. R. (1989), The heating of the high-latitude ionosphere by high-power radio waves, *Phys. Reports*, 79(2-3), 79–209, doi:10.1016/0370-1573(89)90005-7.
- [Schneider, 2004] Schneider, J. (2004), Plane waves in FDTD simulations and a nearly perfect total-field/scattered-field boundary, *IEEE Transactions on Antennas and Propagation*, 52(12), 3280–3287, doi:10.1109/TAP.2004.836403.
- [Schneider, 2010] Schneider, J. B. (2010). Understanding the FDTD method. www.eecs.wsu.edu/~schneidj/ufdtd.
- [Stefaski et al., 2012] Stefaski, T., Benkler, S., Chavannes, N., and Kuster, N. (2012), OpenCL-based acceleration of the FDTD method in computational electromagnetics, *International Journal of Numerical Modelling*, 26(4), 355–365, doi:10.1002/jnm.1862.
- [Stocker et al., 1993] Stocker, A. J., Honary, F., Robinson, T. R., Jones, T. B., and Stubbe, P. (1993), Anomalous absorption during artificial modification at harmonics of the electron gyrofrequency, *Journal of Geophysical Research: Space Physics*, 98(A8), 13627–13634, doi:10.1029/93JA00878.

- [Stocker et al., 1992] Stocker, A. J., Honary, F., Robinson, T. R., Jones, T. B., Stubbe, P., and Kopka, H. (1992), EISCAT observations of large scale electron temperature and electron density perturbations caused by high power HF radio waves, *Journal of Atmospheric and Terrestrial Physics*, 54(11–12), 1555–1572, doi:10.1016/0021-9169(92)90163-F.
- [Stubbe and Kopka, 1981] Stubbe, P. and Kopka, H. (1981). *Exploration of the Polar Upper Atmosphere: Proceedings of the NATO Advanced Study Institute held at Lillehammer, Norway, May 5–16, 1980*, chapter Modification of the F Region by Powerful Radio Waves, pages 83–98. Springer Netherlands, Dordrecht, doi:10.1007/978-94-009-8417-2_6.
- [Stubbe et al., 1984] Stubbe, P., Kopka, H., Thidé, B., and Derblom, H. (1984), Stimulated electromagnetic emission: a new technique to study the parametric decay instability in the ionosphere, *Journal of Geophysical Research: Space Physics*, 89(A9), 7523–7536, doi:10.1029/JA089iA09p07523.
- [Stubbe et al., 1994] Stubbe, P., Stocker, A. J., Honary, F., Robinson, T. R., and Jones, T. B. (1994), Stimulated electromagnetic emissions and anomalous HF wave absorption near electron gyroharmonics, *Journal of Geophysical Research: Space Physics*, 99(A4), 6233–6246, doi:10.1029/94JA00023.
- [Sypekand et al., 2009] Sypekand, P., Dziekonski, A., and Mrozowski, M. (2009), How to render FDTD computations more effective using a graphics accelerator, *IEEE Transactions on Magnetics*, 45(3), 1324–1327, doi:10.1109/TMAG.2009.2012614.
- [Taflove and Hagness, 2000] Taflove, A. and Hagness, S. C. (2000). *Computational Electrodynamics: the Finite-Difference Time-Domain Method*. Artech House, Boston, MA, 2nd edition.
- [Thébault et al., 2015] Thébault, E., Finlay, C., Beggan, C., Alken, P., Aubert, J., Barrois, O., Bertrand, F., Bondar, T., Boness, A., Brocco, L., Canet, E., Chambodut, A., Chulliat, A., Coisson, P., Civet, F., Du, A., Fournier, A., Fratter, I., Gillet, N., Hamilton, B., Hamoudi, M., Hulot, G., Jager, T., Korte, M., Kuang, W., Lalanne, X.,

- Langlais, B., Léger, J.-M., Lesur, V., and Lowes, F. (2015), International Geomagnetic Reference Field: the 12th generation, *Earth, Planets and Space*, 67(1), 1–19, doi:10.1186/s40623-015-0228-9.
- [Thidé, 1990] Thidé, B. (1990), Stimulated scattering of large amplitude waves in the ionosphere: experimental results, *Physica Scripta*, 1990(T30), 170, doi:10.1088/0031-8949/1990/T30/023.
- [Vaskov and Gurevich, 1975] Vaskov, V. and Gurevich, A. (1975), Nonlinear resonant instability of a plasma in the field of an ordinary electromagnetic wave, *Journal of Soviet Physics*, 69(1), 176–188, *English Translation in JETP*, 42(1), 91–97.
- [Wang et al., 2016] Wang, X., Cannon, P. D., Zhou, C., F. Honary, B. N., and Zhao, Z. (2016), A theoretical investigation on the parametric instability excited by X-mode polarized electromagnetic wave at Tromsø, *Journal of Geophysical Research: Space Physics*, 121(4), 3578–3591, doi:10.1002/2016JA022411.
- [Wong et al., 1981] Wong, A. Y., Morales, G. J., Eggleston, D., Santoru, J., and Behnke, R. (1981), Rapid conversion of electromagnetic waves to electrostatic waves in the ionosphere, *Physics Review Letters*, 47(18), 1340–1343, doi:10.1103/PhysRevLett.47.1340.
- [Yee, 1966] Yee, K. S. (1966), Numerical solution of initial boundary value problems involving Maxwell's equations in isotropic media, *IEEE Transactions on Antennas and Propagation*, 14(3), 302–307, doi:10.1109/TAP.1966.1138693.
- [Young, 1994] Young, J. L. (1994), A full finite difference time domain implementation for radio wave propagation in a plasma, *Radio Science*, 29(6), 1513–1522, doi:10.1029/94RS01921.
- [Young and Brueckner, 1994] Young, J. L. and Brueckner, F. P. (1994), A time domain numerical model of a warm plasma, *Radio Science*, 29(2), 451–463, doi:10.1029/93RS03443.

[Yu and Simpson, 2010] Yu, Y. and Simpson, J. J. (2010), An E-J collocated 3-D FDTD model of electromagnetic wave propagation in magnetized cold plasma, *IEEE Transactions on Antennas and Propagation*, 58(2), 469–478, doi:10.1109/TAP.2009.2037706.

[Yu and Simpson, 2012] Yu, Y. and Simpson, J. J. (2012), A 3-D global earth-ionosphere FDTD model including an anisotropic magnetized plasma ionosphere, *IEEE Transactions on Antennas and Propagation*, 60(7), 3246–3256, doi:10.1109/TAP.2012.2196937.

[Yusheng and Wenbing, 1996] Yusheng, Z. and Wenbing, W. (1996), The studies of the stability of FDTD with Mur's absorbing boundary condition of second order in 3-D scattering problems, *Microwave and Guided Wave Letters, IEEE*, 6(3), 120–122, doi:10.1109/75.481086.